Response to Stratospheric Forcing and Its Dependence on the State of the Troposphere

by

Cegeon J Chan

B.S. Meteorology (2003), Lyndon State College
B.S. Mathematics (2003), Lyndon State College

Submitted to the Department of Earth, Atmospheric,
and Planetary Sciences
in partial fulfillment of the requirements for the Degree of

Doctor of Philosophy

at the

MASSACHUSETTS INSTITUTE OF TECHNOLOGY

September 2009

Signature of Author...
Department of Earth, Atmospheric, and Planetary Sciences
August 21, 2009

Certified by...
R. Alan Plumb
Professor of Earth, Atmospheric and Planetary Sciences
Thesis Supervisor

Accepted by...
Maria T. Zuber
E.A. Griswold Professor of Geophysics
Head, Department of Earth, Atmospheric and Planetary Sciences

Response to Stratospheric Forcing and Its Dependence on the State of the Troposphere

by

Cegeon J Chan

B.S., Meteorology (2003), Lyndon State College
B.S., Mathematics (2003), Lyndon State College

Submitted to the Department of Earth, Atmospheric, and Planetary Sciences
on August 21, 2009, in partial fulfillment of the
requirements for the degree of
Doctorate in Philosophy

Abstract

There is increasing evidence that changes in the stratosphere can have an impact on the surface. While observational results show a surface response of about 0.5 - 1 m/s, modeling studies can show a signal two times and in a particular extreme, four to eight times larger. In this thesis, an investigation of this extreme result revealed the model's characteristic timescale associated with the leading mode of variability was unrealistically large, which ultimately led to the exaggerated responses. Numerous experiments confirmed the tropospheric setup lay in a transition zone in the model's parameter space, teetering between an eddy-driven jet (1) coexisting with or (2) being well-separated from the subtropical jet. Modest shifts in the peak equilibrium temperature profile in either direction removed the bimodal behavior reducing the timescale associated with the internal variability. Subsequently, the response associated with a stratospheric perturbation was greatly reduced and consistent with those found in observations.

Composites of the observed mid-tropospheric Northern Annular Mode (NAM) anomalies persisting much longer than normal reveal a lower stratospheric signal, while there was a much weaker signal under normal conditions, suggesting the lower stratosphere has a role in increasing the persistence of the NAM. Using this framework, the following mechanism was proposed. When the lower stratospheric winds sufficiently weaken, there is an increased wave drag in the lower stratosphere which then projects onto the annular modes. The negative phase of the annular mode can continue as long as both the lower stratospheric winds remain weak and the wave source is sufficient.

Model runs with lower stratospheric winds that were always sufficiently weak or always too strong showed no significant tropospheric response to any extreme stratospheric events. Similarly, shifting mountains into the polar region appeared to shift the wave drag away from synoptic eddy feedback region. In either of these two cases, none of the model runs exhibited signs of a tropospheric response, consistent with the wave drag projection onto the annular mode having a key role in allowing the stratosphere to affect the tropospheric circulation.

Thesis Supervisor: R. Alan Plumb
Title: Professor of Meteorology

Acknowledgments

Particularly at an university like MIT, graduate programs are setup to test and challenge the students' ability to perform independently. However, one cannot earn a degree without the support from others. The following are the people who have helped me along the way.

First and foremost, I would like to thank my advisor, Alan Plumb for our frequent insightful discussions. We've probably met over a hundred times, but not once did he force upon his own ideas, while remaining remarkably patient to guide me through wrong turns. Despite his busy schedule, I appreciated his generosity to always find time for me.

Of course, the help from my research group – Ivana Cerovecki, Gang Chen, Mary Elliff, Will Heres, Linda Meinke, Nikki Privé, Mike Ring and Angela Zalucha – was greatly appreciated. Besides teaching me the basics of bridge, Mike shared a lot of code that made this thesis possible including the zonally-symmetric model and EOF analysis. Nikki was my "mentor" and was an excellent resource for advice as a first-year graduate student. Ivana always had an answer for any question I had pertaining to the model output and the MIT-GCM itself. Gang provided valuable feedback whenever I needed some perspective on my ideas. Angela always helped with the aesthetics of my conference practice talks. Mary could always give suggestions to my grammar. Also none of the model results would have happened without the help of Will and Linda.

Besides the research component, the first couple of years was a tough transition due to the difficult classes and the daunting General Exam, but, with friendly supportive classmates, this was made bearable. In particular, I would like to thank Yang Zhang, Daniel Enderton, Ian Fenty and Bhaskar Gunturu for helping me prepare for the General Exam and various problem sets. Also, my officemates – Dave Flagg, Vikram Khade, and Kelly Klima – were pleasant to talk with when a break was needed.

This thesis was also greatly aided by many of the WxChallenge (formerly known as the National College Weather Forecast Contest) team members: Lodovica Illari, Rob Korty, Greg Lawson, Garrett Marino, Jon Moskaitis, Jeff Scott and Brian Tang. Besides their help in improving my general scientific base in a comfortable informal setting, figures like 7.8 originated with the help of Jon Moskaitis and many visual aesthetics were inspired by Brian Tang.

Outside of this department, a special thanks go to Jason Furtado and Vivian Cheng. As a friend and colleague from our undergraduate days and now graduate school, Jason has not only helped contribute insightful comments to this thesis, but I have also benefitted from many fruitful discussions about a variety of topics in our field. Finally, Vivian Cheng, my girlfriend has had to put up with the roller coaster ride associated with being a graduate student and its time constraints. She has always been right beside me and been able to provide balance to my often idealistic views of the world with much needed practical perspectives.

This material is based upon work supported by the National Science Foundation under Grants ATM-0314094 and ATM-0808831. Any opinions, findings, and conclusions or recommendations expressed in this material are those of the author and do not necessarily reflect the views of the National Science Foundation. Lastly, I also acknowledge the financial support from the NASA's Earth Science Enterprise Graduate Fellowship.

Contents

List of Figures

Chapter 1

Introduction

Since the seminal work by Charney and Drazin (1961), theories of upward wave propagation led to research on the impact of tropospheric waves on the stratospheric flow. Their work showed that waves only propagated upward through a certain "window" of wind speeds, which can be derived from the QG index of refraction for atmospheric waves:

$$n^2 = \frac{N^2}{f_0^2}\left[\frac{\beta}{\bar{u} - c} - k^2\right] - \frac{1}{4H^2} \tag{1.1}$$

where N^2 is the Brunt-Vaisalla frequency, f_o is Coriolis parameter at a fixed latitude, β is the meridional gradient of the Coriolis parameter, c is the phase speed of the wave, k is the zonal wavenumber and H is the scale height. For propagating waves, n^2 must be greater than zero. Therefore, a necessary condition for vertically propagating waves is as follows.

$$0 < \bar{u} - c < \beta\left[k^2 + \frac{f_o^2}{4N^2H^2}\right]^{-1} \equiv U_c \tag{1.2}$$

From this equation, we can see that the flow has to be eastward, but not past a certain critical westerly wind speed. Since this upper bound in wind speed is determined by the length scale of the wave, this explains why disturbances in the stratosphere have a much larger scale than those in the troposphere. In addition, the Charney-Drazin theory explains why there is very little variability during the summer season, when stratospheric winds are easterly.

So during the winter season when the polar region receives little to no sunlight, the radiational and geostrophic constraints require stratospheric westerlies poleward of the subtropics. However Matsuno (1971) showed that these westerly winds can undergo a dramatic oscillation and at times, turn easterly because of dynamical reasons. Using a simple QG numerical model, the author found waves 1 and 2 as the key drivers in producing these stratospheric sudden warming events.

More specifically, a two-way interaction between the mean flow and Rossby waves can drive changes away from radiative equilibrium. With sufficient wave drag, the winds turn easterly, and as described above, Rossby waves are shielded from any further vertical penetration. With the lack of dynamical forces at play, the winds are relaxed towards radiative equilibrium and the strong westerlies reappear again. This extratropical process is analogous to the tropical phenomenon, the quasi-biennial oscillation, described by Plumb (1977).

Until the early 1990s, the focus was centered around this one-way dynamical effect: the troposphere providing the source of Rossby waves, which subsequently drive changes in the stratosphere. Recently, however, there has been an increasing amount of evidence suggesting stratospheric processes have an effect on the surface climate as well.

Understanding this coupling between the troposphere and stratosphere is not only of academic interest, but it also has implications on the current climate. With anthropogenic forcing cooling the stratosphere (*e.g.* Fu et al. 2004) and the development of the Southern Hemisphere stratospheric ozone hole (*e.g.* Solomon 1999), there is great importance in understanding the role stratospheric processes play in the overall tropospheric climate.

1.1 Internal Variability

1.1.1 Annular Modes

Observational studies have shown that the largest low-frequency variability in the troposphere is associated with the latitudinal movement of the mid-latitude jet (e.g. Baldwin and Dunkerton 1999; Thompson and Wallace 2000; Lorenz and Hartmann 2001). Often calculated using empirical orthogonal function (EOF) analysis, the leading mode (EOF1) reveals a spatial pattern that is almost zonally symmetric, and as a result, is often referred to as the annular modes. Thompson and Wallace (2000) noted that these spatial structures were found regardless of season and had opposite signs between the mid-latitudes and the polar region. This dipolar characteristic is often interpreted as a "see-saw" exchange of mass, *e.g.* when the geopotential anomalies are anomalously high in the mid-latitudes, they are anomalously low in high-latitudes, as shown in the bottom panel of Fig. 1.1.

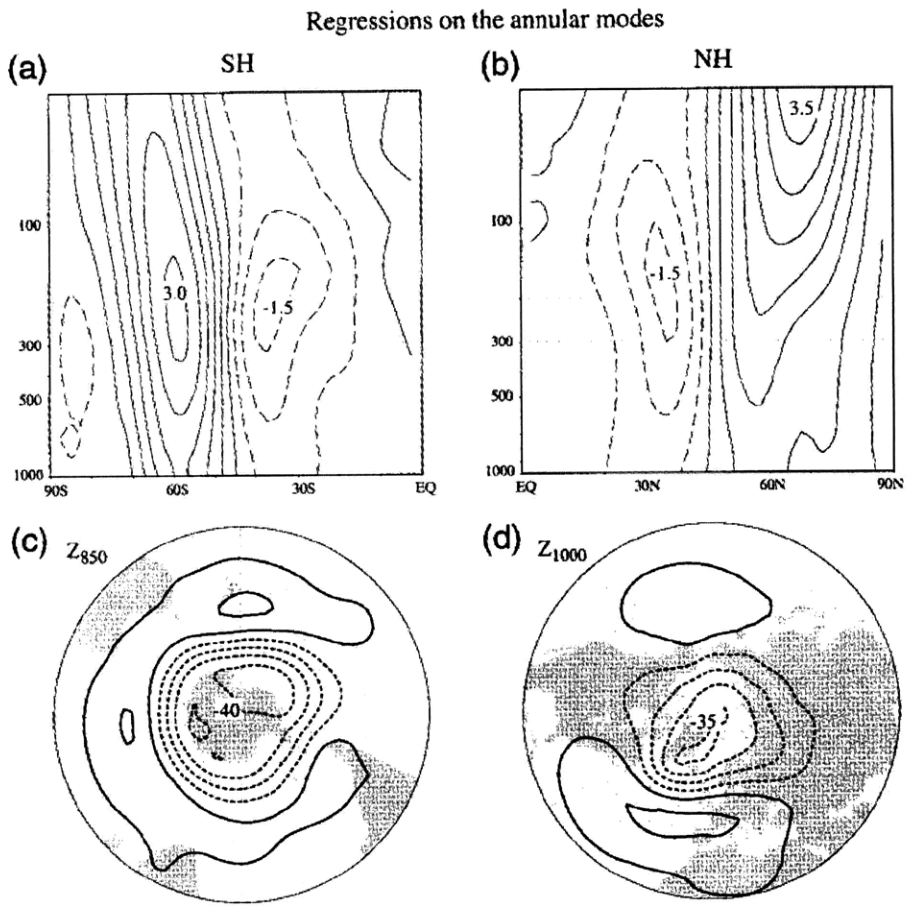

FIG. 1. (top) Zonal-mean geostrophic wind and (bottom) lower-tropospheric geopotential height regressed on the standardized indices of the annular modes (the AO and its SH counterpart) based upon monthly data, Jan 1958–Dec 1997. Left panels are for the SH, right panels are for the NH. Units are m s^{-1} (top) and m per std dev of the respective index time series (bottom). Contour intervals are 10 m (-15, -5, 5, . . .) for geopotential height and 0.5 m s^{-1} (-0.75, -0.25, 0.25) for zonal wind.

Figure 1.1: Reproduced from Thompson and Wallace (2000).

Although "annular modes" generally refers to the characteristics described above, there are specific names for particular regions around the globe. Since this thesis will refer to many of these, we will describe them here. The annular modes in the northern and southern hemispheres are referred to the Northern Annular Mode (NAM) and Southern Annular Mode (SAM), respectively. As discussed in Eichelberger and Hartmann (2007) and in Chapter 7, the Atlantic and Pacific ocean basins have different characteristics, so a delineation is made between the two sectors. For the former, the annular modes are referred to the North Atlantic Oscillation (NAO) and for the latter, the Pacific North-American (PNA).

Regardless of their name, they have similar dynamics. Ring and Plumb (2007)'s modeling study suggested that these annular modes are the preferred extratropical response to generic forcing. Using a simple GCM, regardless of the shape, location and intensity of the explicit extratropical forcing, the response would be that of the annular mode pattern. Changes to the number, location, and type of forcing from other studies (*e.g* Polvani and Kushner 2002; Song and Robinson 2004; Chen and Zurita-Gotor 2008; Butler et al. 2009) yielded similar results.

Lorenz and Hartmann (2001) and Ring and Plumb (2007) attributed this variability in the troposphere to eddy feedback processes. Applying the same forcings in a zonally-symmetric model, Ring and Plumb (2007) noted the responses no longer resembled those from the full 3-dimensional simulation. Not only were the changes significantly weaker, the dipole structure was absent. They concluded the direct forcing could not reproduce the response, instead, it was the changes to the eddy fluxes that were primarily responsible for the annular mode structures. More specifically, Lorenz and Hartmann (2001) argued that anomalous baroclinic wave activity, generated from a region with anomalous temperature gradient, had a net propagation away from the jet. Since the momentum fluxes are opposite to wave propagation, this leads to an anomalous convergence of eddy momentum fluxes, which would further amplify the temperature gradient and thus, creating a positive eddy feedback.

1.2 Stratosphere / Troposphere Coupling

Although the dynamical causes of the annular modes are different in the troposphere than the stratosphere, there is a significant correlation of the annular mode index between the stratosphere and troposphere. To illustrate this point, Thompson and Wallace (2000) calculated the annular mode index from the leading principal component of the lower-tropospheric geopotential height. This index is then regressed with the zonal wind anomalies to obtain the zonally-averaged spatial pattern shown in the top panel of Fig. 1.1. As shown, the annular mode pattern extends into stratosphere during the winter season. Combined with the climatological winds (not shown), this figure suggests a correlation between the latitudinal movement of the tropospheric eddy-driven jet and the intensification of the stratospheric polar night jet. With this relationship holding for both hemispheres, this feature appears robust.

Prompted by the apparent correlation in the annular modes between the troposphere and stratosphere, Baldwin and Dunkerton (2001) looked at the evolution of the NAM index as a function of pressure and time. First, at each pressure level, the NAM index was defined to be the leading principal component of the geopotential height anomalies for that level. Second, a composite of the indices were taken during the onset of the weak and strong vortex events and is shown in the top and bottom panel of Fig. 1.2, respectively.

As shown, there are three points of interest. First, following the onset of the weak stratospheric polar vortex, the tropospheric NAM anomalies follow the same sign. Second, the persistence of the NAM index following the event is noteworthy, since the typical timescale is approximately 10 days (cf. Feldstein 2000). Here, the composite shows that the phase persists for about six times this timescale after the onset of these extreme stratospheric events.

The third key point lies in the troposphere between lags of -20 and 0 day. Since this feature is prior to the extreme stratospheric event, this was likely a tropospheric signal of the "burst" of planetary waves prior to the sudden warming discussed in the last section. As shown by Polvani and Waugh (2004), indeed, at 100 mb there are anomalous eddy heat fluxes prior to the sudden warming, consistent with the mechanism thought to produce the sudden warming as described in the previous section.

So even though Baldwin and Dunkerton (2001) seem to suggest the stratosphere (under certain conditions) exerted a significant control in the tropospheric weather, this does not necessarily imply that "information" is being transmitted downward. There is the possibility

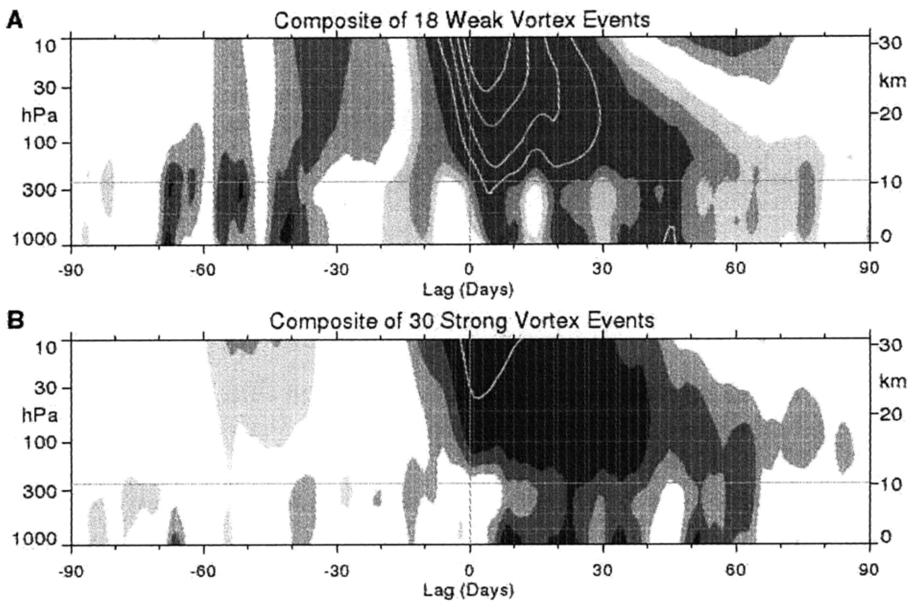

Fig. 2. Composites of time-height development of the northern annular mode for (**A**) 18 weak vortex events and (**B**) 30 strong vortex events. The events are determined by the dates on which the 10-hPa annular mode values cross −3.0 and +1.5, respectively. The indices are nondimensional; the contour interval for the color shading is 0.25, and 0.5 for the white contours. Values between −0.25 and 0.25 are unshaded. The thin horizontal lines indicate the approximate boundary between the troposphere and the stratosphere.

Figure 1.2: Reproduced from Baldwin and Dunkerton (2001).

of the tropospheric burst of planetary waves *causing* the stratospheric extreme event *and* the persistence of the tropospheric NAM anomalies. Similar to the idea of the quasi-biennial oscillation (Plumb 1977), Plumb and Semeniuk (2003) showed that wave-mean flow interaction from forcing at low levels could generate the same downward propagating structures generated by Baldwin and Dunkerton (2001) even when both wave reflection and meridional circulations were "turned off." Hence, downward propagation of stratospheric anomalies into the troposphere does not necessarily imply the stratosphere has control over the troposphere.

However, in numerical models, variations in only stratospheric parameters have demonstrated to have significant effects in the tropospheric climate. Using a simple GCM, Polvani and Kushner (2002) changed the stratospheric equilibrium temperature profile, and in effect, could control the strength of the stratospheric polar vortex. Although this thermodynamic forcing was only applied to the stratosphere, by "turning on" the polar vortex, the tropospheric jet was displaced poleward, consistent with the observational result found by Thompson and Wallace (2000) discussed above: as the strength of the stratospheric winds increase, the annular mode pattern requires a poleward shift in the eddy driven jet. At least for this particular case, downward propagation of information would be difficult to discount.

While the Polvani and Kushner (2002) study revealed a steady-state tropospheric response to a stratospheric perturbation under a perpetual-solstice (i.e. time-independent) forcing, the transient response was examined in Kushner and Polvani (2004). The stratospheric adjustment to the cooling takes about a hundred days, while the troposphere takes over several hundred days. This raises the question of whether there is enough time for the troposphere to respond when a realistic seasonal cycle is applied. So in Kushner and Polvani (2006), they found that there was still (albeit weaker) tropospheric response.

The dynamics of the stratosphere/tropospheric interaction was investigated in Kushner and Polvani (2004). Their goal was to determine whether eddy feedbacks described in the previous section were responsible for the tropospheric response. Using a zonally symmetric model, eddy terms from their (full) atmospheric GCM control run can be explicitly inserted into the model. Thus by forcing the eddies to behave as they did in the control run, the eddy feedback processes were effectively suppressed. When a stratospheric perturbation was applied in this case, unlike in the full model, there was no tropospheric response. Thus, Kushner and Polvani (2004) argued that transient eddy mean-flow interactions are crucial to the stratosphere-troposphere system.

Also recognizing the importance of the transient eddies in the troposphere, Song and Robinson (2004) hypothesized that the stratosphere could influence the troposphere through a process termed by the authors as downward-control with eddy feedback (DCWEF). From downward control theory (Haynes 2005), a forcing in the stratosphere typically would not be strong enough to account for the tropospheric response. However, the Song and Robinson (2004) argued that a stratospheric forcing could "tickle" the troposphere enough for transient eddies to respond. The result is an initial weak forcing that gets amplified through eddy feedbacks (e.g. Lorenz and Hartmann 2001) that projects on the model's intrinsic annular modes. However, Song and Robinson (2004) increased the wind speed of the stratospheric jet (presumably affecting the vertical propagation of Rossby waves), the same forcing resulted in a considerably weaker tropospheric response. Since downward control theory does not depend on the background state, DCWEF cannot be a complete explanation for downward influence, suggesting planetary waves has an important role in the coupling.

In a modeling study, Chen and Robinson (1992) looked at the determining factors on whether planetary waves propagated into the stratosphere. They found that as the vertical shear increased (*i.e.* the stronger the stratospheric winds), the more wave activity is trapped in the troposphere. Therefore, there is less left to propagate into the stratosphere. This was later confirmed by observational results from Perlwitz and Harnik (2003), where they also discussed how planetary waves (zonal wave number 1) reflected in the upper stratosphere can affect the behavior of planetary waves in the troposphere. Consequently, this could affect the synoptic-scale eddies responsible for eddy zonal flow feedback. Perlwitz and Harnik (2004) then extended their initial study to cases where planetary waves were able to propagate into the stratosphere. In that study, they found planetary waves were non-reflective during the conditions in which NAM anomalies migrated downward (Baldwin and Dunkerton 2001), consistent with the idea that tropospheric planetary waves are important in initiating the polar vortex weakening.

However, other results suggest that eddy feedback processes may not be important at all. Thompson et al. (2006) found the amplitude of the tropospheric anomalies is quantitatively similar to the balanced response to a stratospheric wave drag. The authors mention that anomalous radiative heating at stratospheric levels is a simple but yet previously overlooked mechanism in communicating stratospheric variability towards the troposphere. Although their model was able to represent the amplitude of the surface wind anomalies, their mechanism could not explain the latitudinal structure. In addition, with only a stratospheric wave drag, there was no accompanying wave source in the troposphere. By neglecting the westerly forcing in the troposphere, easterly anomalies would be too large. This would likely affect wave propagation important to the tropospheric circulation. In fact, when a westerly forcing was applied in the troposphere (in addition to the stratospheric wave drag forcing), the anomalies at the surface associated with the balanced response were too weak (Furtado 2005). Thus, their results on whether the balanced response is sufficient in explaining anomalous activity at the surface seem to be sensitive to tropospheric wave forcing.

1.3 Role of Stratosphere in Climate Change

Thus far, we have discussed how the annular modes arise from eddy-mean flow interaction and thus are free, internal modes of tropospheric variability. Since this variability is associated with a timescale of about ten days and is also considered a white-noise process (cf. Feldstein (2000)), long-term trends of the NAM or SAM can be attributed to external forcing, *i.e.* climate signals become more evident when the short-term noise averages out on sufficiently long timescales. Observational studies (*e.g.* Hurrell and van Loon 1997; Meehl et al. 1998; Feldstein 2000; Thompson and Wallace 2000) have shown that there has been an increase in the polarity of both indices over the last 30 years.

Hartmann et al. (2000) argued that this trend can largely be attributed to both the stratospheric ozone depletion and greenhouse warming. Since the former is an absorber of incoming radiation, ozone depletion in the polar stratosphere will lead to cooler temperatures at high latitudes and increase the latitudinal temperature gradient. Through the thermal wind relation, this will strengthen the polar night jet. Similarly, greenhouse gases cool the lower stratosphere. However, since the tropopause is lower at the pole than the equator, this effect will also increase the temperature gradient and strengthen the stratospheric winds. The authors then described how this would lead to a decrease in both the poleward transport of ozone and stratospheric wave drag in high latitudes. In turn, the polar vortex strengthens, perpetuating the feedback.

The observational study by Thompson and Solomon (2002) is consistent with this described feedback. Further, the modelling study by Gillett and Thompson (2003) indicate that stratospheric ozone depletion alone may be the cause in the southern hemisphere. Using the Hadley Centre slab model and a prescribed stratospheric ozone depletion as the forcing, their results captures both the magnitude and spatial structure of the changes in the near-surface zonal winds shown to be occurring in observations.

With the expected ozone recovery, Son et al. (2008) looked at whether there is a difference in the climate predictions between climate models which have a fully interactive stratospheric chemistry (the Chemistry-Climate Model Validation (CCMVal) models) and ones that do not resolve the future changes to stratospheric ozone (certain of the Intergovernment Panel on Climate Change / Fourth Assessment Report (IPCC/ AR4) models). The climate predictions between the CCMVals, AR4s with ozone recovery and the AR4s with no ozone recovery revealed a glaring difference. In the first two cases, the models predicted an equatorward shift in the mid-latitude surface westerlies, while the latter case showed a perpetuation of current poleward trend. So even in the most sophisticated types of models, the role of the stratosphere in climate has never been more evident.

1.4 Fluctuation-Dissipation Theorem

One of the approaches to understand and predict climate change in recent years is to make use of the fluctuation-dissipation theorem (FDT). Although the original formulation and proof required nonlinear dynamical systems to be in thermodynamic equilibrium (Kraichnan 1958, 1959), Leith (1975) showed that the response to an external force can be related to its unforced natural variability in a climate system. So even though the system may only be in statistical equilibrium, Ring and Plumb (2007) and Gerber et al. (2008) found a fairly linear response to an increase in forcing, as shown in Fig. 1.3, suggesting this framework appears sufficient in gauging climate responses.

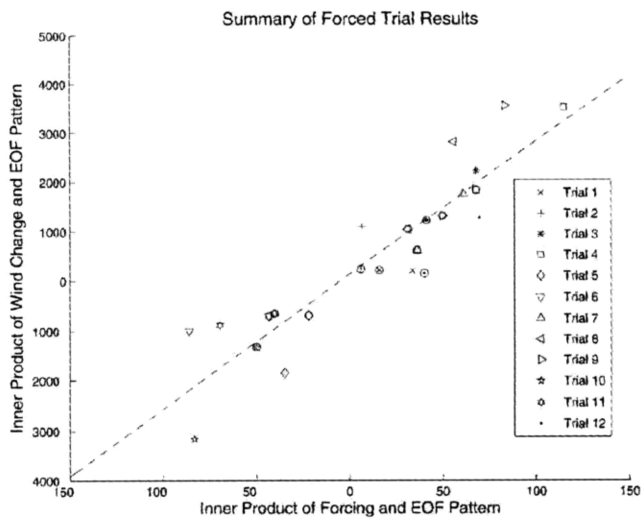

FIG. 14. Inner product of zonal wind change and EOF pattern plotted against inner product of forcing and EOF pattern. Plot contains points for both Southern Hemisphere and Northern Hemisphere; NH points are enclosed with a circle and rotated to appear in same quadrant as similar SH trial. Dashed line is best least squares linear fit.

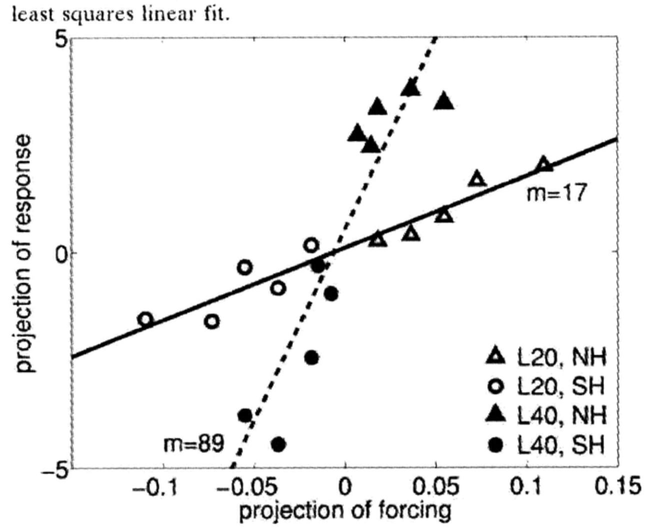

FIG. 8. The response as a function of the forcing for the first EOF of zonal mean zonal wind in the T42L20 and T42L40 models. The forcing and response are quantified by projecting the torque and the resulting change in the zonal mean zonal wind onto the first EOF of zonal wind, respectively. The magnitude of the response in the L40 model is on average 89/17 ≈ 5 times that in the L20 model, as determined by the slopes of the best-fit lines. In other words, the L40 configuration of the model is roughly 5 *times* as sensitive as the L20 model to the same external perturbation.

Figure 1.3: Reproduced from (top panel) Ring and Plumb (2007) and (bottom panel) Gerber et al. (2008).

As the top panel shows, the changes in the climatology were proportional to the projection of the forcing and the mode. As intuition would suggest, either amplifying the forcing or improving its projection onto the annular mode would increase the response. However, less intuitively, the slope of the line is determined by the timescale associated with the leading mode of variability. For example, for a timescale that is much shorter, the system's response would be much less sensitive to forcing. This can be clearly seen in the bottom panel of Fig. 1.3. Using a similar model, Gerber et al. (2008) varied the model's horizontal and vertical resolution. In this particular figure, changes to the vertical resolution produced two different decorrelation times for the annular mode. Since the internal variability had a longer timescale in the model with 40 vertical levels, these experiments had a larger response than the model with 20 vertical levels.

Since the response is closely tied with the persistence of the variability, models with unrealistically large timescales would give unrealistically large responses. Thus, one interpretation of the results from the bottom panel of Fig. 1.3 is that models with too long of a timescale are overly sensitive to forcings, and thus exaggerate the responses. Such a problem has large implications, since the literature is full of simple models with timescales longer than those observed (Gerber and Vallis 2007; Gerber and Polvani 2009).

Likely the primary reason for the long persistence in these simple models is related to the unrealistically strong and persistent eddy-zonal flow feedback. Without topography producing undulations in the latitude of the jet, waves are less likely to break as they travel around latitude circles. As a result, wave-mean flow interaction can have longer "memory" than what is observed (Son et al. 2008). Along those lines, Son et al. (2008) also found that the meridional propagation of waves was crucial in reducing the timescale. If waves were confined to the mid-latitudes, the momentum flux convergence in that regions would only strengthen the eddy feedback. The authors argued that if the PV gradient was too strong, waves would be confined to the mid-latitudes, while weaker PV gradient in the subtropics would be more susceptible for mid-latitude waves to propagate and break far away from the source. Again, with more wave breaking, the shorter the timescale will be.

As Son and Lee (2006) demonstrates cleanly, there an interesting feature when the PV gradient is weakened: baroclinic waves penetrate further into the subtropics and the eddy-mean flow feedback processes significantly weakens (Son et al. 2008). In addition, the variability is no longer described as a jet oscillation. Instead, the anomalies undergo a poleward propagation and are associated with much shorter timescales (Chan and Plumb 2009), consistent with the eddy-feedback playing a large role in determining the timescale of the internal variability. With the timescale playing such a crucial factor in the fluctuation-dissipation theorem, we will take a closer look at this behavior in the next section.

1.4.1 Poleward propagation

As described earlier (e.g. Song and Robinson 2004; Kushner and Polvani 2004), the stratosphere might be able to perturb the troposphere enough for eddies to excite an annular mode-like response. This variability associated with the tropospheric jet is often referred to as the zonal index and first discussed by Rossby (1939) and Namias (1950). However, other observational studies have documented another form of variability. Although their study was limited to seven months of data, Riehl et al. (1950) first described a poleward propagation of the zonal wind anomalies. With a considerable improvement in observations, Feldstein (1998) examined a similar quantity, the anomalous vertically integrated angular momentum and a similar and robust pattern emerged. Independent of hemisphere and season, starting in the tropics, the described quantity migrated into high latitudes.

Whether the tropospheric variability behaves as poleward propagation (with two EOFs needed to capture the variability) or as an oscillating jet (with only one EOF needed) is not just of academic interest. When the variability to the zonal-mean zonal wind was dominated by EOF1 in their control runs, Son and Lee (2006) showed that a tropospheric thermal perturbation resulted in changes in the zonal wind that had the same spatial pattern as EOF1. This result is not extremely novel, as other studies have obtained similar results (e.g. Kushner and Polvani 2004; Song and Robinson 2004; Ring and Plumb 2007). However, in a regime where the variability is dominated by poleward propagation, Son and Lee (2006) performed similar perturbations and found EOF1 performed worse. The spatial structure to EOF1 could not capture the changes to the zonal-mean zonal wind. In other words, for this particular model, "climate predictability" was relatively lower in a poleward propagating regime.

This raises the question of the dynamical processes involved in driving the poleward propagation. Lee et al. (2007) proposed such a mechanism. Waves originating from mid-latitudes propagate equatorward. Eventually, they break in the tropics and negative anomalies arise. This would presumably shift the critical latitude poleward. Thus, as future waves propagate equatorward, they must break poleward relative to the earlier waves. As long as the source of wave bombardment is sustained, this process allows the zonal wind anomalies to continuously propagate poleward. Meanwhile equatorward of the critical latitude, the Hadley circulation can reestablish subtropical jet without the influence of eddies. Once the critical latitude has shifted poleward of the source of wave activity, the process starts over.

1.5 Motivation

As discussed above, changes in the stratosphere can drive changes in the troposphere. The most compelling pieces of evidence have been observational and modeling studies that have shown that these changes take on the the form of the annular modes. Both bodies of work describe an equatorward shift in the tropospheric mid-latitude jet following a stratospheric sudden warming event.

However, the extent in which the changes in the surface wind can be attributed to stratospheric processes differs greatly. In the observational studies (*e.g.* Baldwin and Dunkerton 2001; Baldwin 2003; Thompson et al. 2006) the difference in the surface zonal winds between weak and strong stratospheric polar vortex events were only about 0.4 - $1\ m\ s^{-1}$, while results from simple models (*e.g.* Polvani and Kushner 2002; Kushner and Polvani 2004; Song and Robinson 2004) show changes in the surface winds four to eight times larger. The question we would like to address is: *how can this discrepancy be reconciled between these simple models and observations?* or similarly, *what causes these large responses in simple models but not in observations?*

I will make use of the fluctuation-dissipation theorem (FDT) to answer these questions. FDT relates the system's response to the forcing and the timescale of the intrinsic variability. In order to show the large responses are related to this unrealistically large timescale, we will systematically alter the tropospheric equilibrium temperature, T_{eq}, profile and show that modest latitudinal shifts in either direction of the peak T_{eq} reduces this timescale considerably. Besides altering the tropospheric T_{eq} profile, changes to the topographical profile also decreased the timescale associated with the annular modes. Consequently, in both cases, the response to changes in the stratosphere are significantly weaker.

On a related note, we will also examine the following question. *Why do some stratospheric sudden warmings yield changes in the troposphere, while others do not?* or more generally, "What is the dynamical mechanism involved in communicating stratospheric wave drag to a change in the tropospheric circulation?" Given evidence of the importance of the lower stratosphere (*e.g.* Sigmond et al. 2008), I will focus on the intensity of the winds and its connection with the unusual persistence of the tropospheric NAM anomalies.

In Chapter 2, the models mentioned above will be discussed in further detail. The climatology and its internal variability will be shown in Chapter 3. With this reference state, Chapter 4 applies systematic changes to the tropospheric and stratospheric equilibrium temperature profile in order to map out a parameter space and isolate the region where the setup is particularly sensitive to perturbations. In Section 4.3, we continue to change the tropospheric setup by varying the topographical profile to examine how these changes affect the response to stratospheric sudden warming events. These modeling studies show that changes in the stratosphere can affect the behavior of the tropospheric variability and one particular type, poleward propagation, will be investigated in Chapter 6. In order to provide an observational context, Chapter 7 will make comparisons to some of our key findings from the modeling work. Finally, the conclusions will be presented in Chapter 8.

Chapter 2

Models

2.1 Introduction

As described in the last section, the main purpose of this thesis is to understand what influences the stratosphere has on the troposphere. Since there is such difficulty in determing cause and effects from observations, the use of general circulation models (GCMs) will be used here.

The first one is the GFDL GCM dynamical core model, described in section 2.2, and is utilized for most of the thesis. Using a similar setup, the second one is the same model, but with no stratosphere. Hence this model will be referred to as a "tropospheric-only" model, detailed in section 2.3. With some minor adjustments, the model will be run in only two-dimensions, consisting of only the meridional and vertical directions. This setup, detailed in Section 2.4, will be referred to as the zonally-symmetric model. Finally, a small portion of the thesis will be interested in the variability generated by an oceanic model, the MITGCM, and will be outlined in section 2.5.

2.2 GFDL GCM dynamical core

To investigate how the stratosphere interacts with the troposphere, we use the dynamical core of the Geophysical Fluid Dynamical Laboratory (GFDL) atmospheric general circulation model (GCM). Using this model, other studies (e.g. Polvani and Kushner (2002); Song and Robinson (2004); Gerber and Polvani (2009)) have also looked into the interactions between the stratosphere and troposphere. Here, we will employ many of the same characteristics used in the studies above.

The GFDL dynamical core is a dry, hydrostatic primitive equation model in σ coordinates, where equations are solved using spectral transforms in the horizontal and Simmons and Burridge (1981) finite difference in the vertical. The prognostic variables are temperature, vorticity, the divergence of the horizontal flow and the logarithm of the surface pressure. Surface drag is parameterized as Rayleigh friction, and radiation is represented by Newtonian cooling toward an equilibrium temperature profile.

In the rest of the section, I will discuss the particular details in the model setup.

2.2.1 Resolution

For all the results using the GFDL GCM, we use a T30 resolution with a grid spacing of 3.75° in latitude and longitude. In the stratosphere-troposphere model, we use 40 vertical sigma levels, with about 15 levels in the troposphere and 18 in the stratosphere and 7 above the stratopause as shown in Fig. 2.1. They are approximately spaced equally in log-pressure coordinates, with the precise location of the kth grid point defined as follows.

$$\sigma_k = \left(\frac{k+3}{44}\right)^5 \quad \text{where} \quad 2 \leq k \leq 41 \tag{2.1}$$

with σ_1=0. All model output is then interpolated onto pressure levels.

A time step of 1800 seconds is used for experiments where the stratospheric winds are expected to be weak. However, for model runs where the stratospheric polar vortex was of moderate strength (50 ms^{-1}), the time step was decreased to 1600 seconds in order to meet the CFL condition. Finally, when the polar vortex was strong (90 ms^{-1}), the time step was decreased further to 1440 seconds.

In addition to the experiments run at T30 resolution, certain key experiments were re-run at a higher horizontal resolution (T42 and T60) to show results were robust to changes in resolution. As shown in Fig. 2.2, the runs conducted at higher resolution were very similar

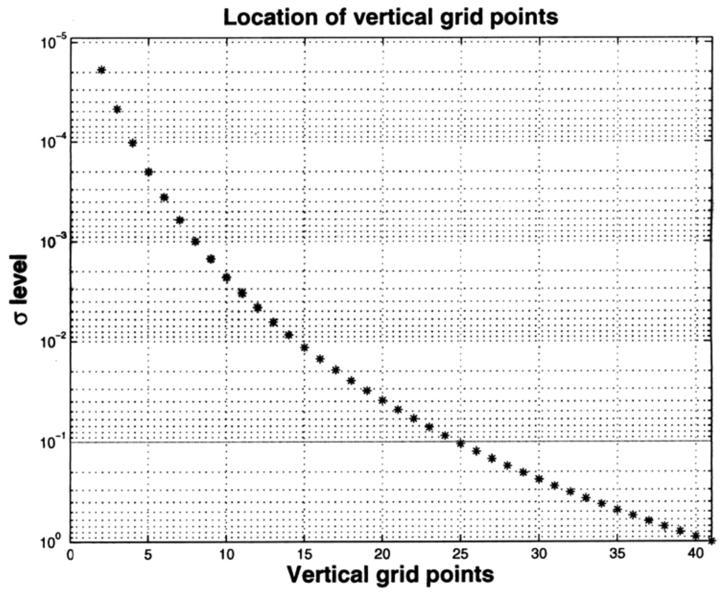

Figure 2.1: Location of the vertical grid points in σ coordinates. Thin gray line represents the nominal height of the tropopause.

to those of T30 resolution. In terms of the size and strength, both the tropospheric and stratospheric jets look very similar. The T30 resolution shows slightly higher wind speeds in the winter tropospheric and stratospheric jet.

Fig. 2.3 provides a closer look into the troposphere. As shown, in both cases, the westerly jet peaks at about 40 $m\ s^{-1}$. at 45°S in the winter hemisphere and have essentially the same climatological structure.

With the time-average characteristics being nearly identical, the T30 resolution seems sufficient for our purposes. However, under certain setups using this simple GCM, Gerber et al. (2008) have shown that the timescale representing the internal variability can vary when the horizontal and vertical resolution are changed (or more precisely, the ratio of the two). For completeness, we will examine the internal variability between two identical runs with two different resolutions. A more thorough analysis will be given in the next chapter. Here, only a cursory description will be provided.

Figs. 2.4a and 2.4b show the spatial pattern that captures the greatest variability for the model with T30 and T42 resolution, respectively. This is calculated by first removing the time-mean, weighing the data by the square root of cosine and the square root of pressure

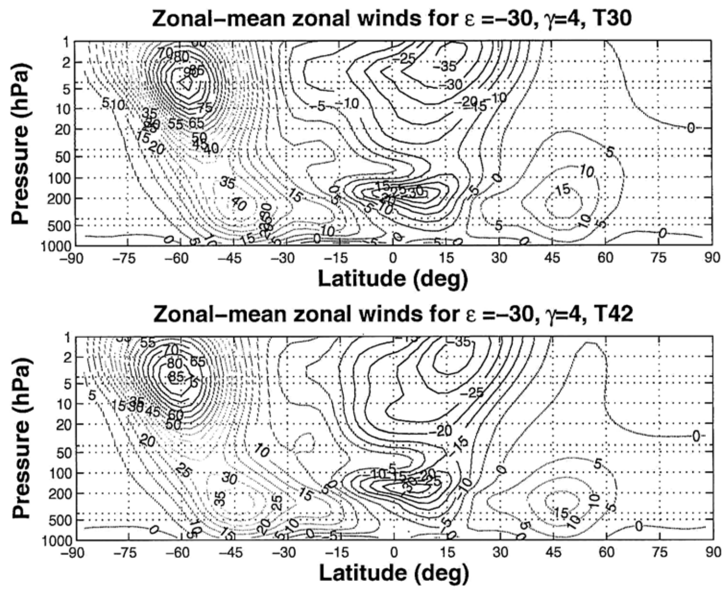

Figure 2.2: A comparison of the climatological zonal-mean zonal wind for the standard T30 resolution (top) and the higher T42 resolution (bottom) Contour interval is 5 $m\ s^{-1}$.

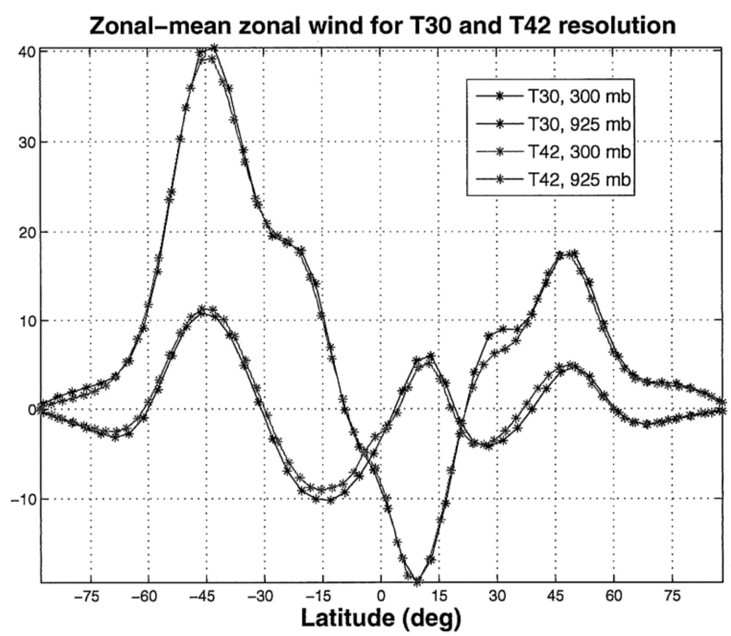

Figure 2.3: A comparison of the climatological zonal-mean zonal wind for the standard T30 resolution and the higher T42 resolution at the pressure levels of 300 mb and 925 mb.

and then doing an EOF analysis poleward of 20°S. In both cases, the EOF structure reveals a tripole in the troposphere and a dipole in the stratosphere. With the same spatial pattern, this figure suggests that changing the resolution did not change the behavior of the variability. For instance, when the tropospheric mid-latitude jet shifts poleward (compare Fig. 2.4 with Fig. 2.2), the subtropical jet is enhanced and the stratospheric jet is displaced equatorward.

Although the spatial pattern is approximately the same, the amount of what one standard deviation represents in the stratosphere differs between the two models. The T42 case is weaker in magnitude (by about a factor of 2) in the stratosphere than the T30 case. However, in the troposphere, the magnitudes are nearly the same. As shown in Fig. 2.4c, at 300mb, where the time-mean and internal variability maximizes, the two runs are not completely identical, but they do broadly have the same shape and phase. Finally, the autocorrelation of the leading principal component for both cases is shown in Fig. 2.4d. The timescale related to the leading mode of internal variability did not vary greatly switching from T30 to T42.

Other meteorological variables including temperature and meridional wind were compared between the T30 and the T42 run and all were found to be similar. Since the T42 case would take about 15 days for the system to run a 5000-day experiment, while at T30 resolution, only half the time is needed, the T30 truncation will be chosen to minimize computing time while being able to capture the essential features.

2.2.2 Radiation

In this model, radiation is represented by Newtonian cooling, essentially a parameterization for thermodynamic processes. At every time step, the temperature is relaxed linearly toward a prescribed equilibrium temperature profile at a rate described by the damping coefficient. Thus, there are two "switches" one can adjust. The first is the damping rate and the second is the equilibrium temperature profile. The former is identical to Held and Suarez (1994) – $\frac{1}{40}$ day^{-1} above $\sigma = 0.7$ and increases linearly to $\frac{1}{4}$ day^{-1} at the surface, multiplied by the fourth power of the cosine of the latitude. Unlike the damping coefficient being identical throughout all experiments, changes to the equilibrium temperature profile will be performed.

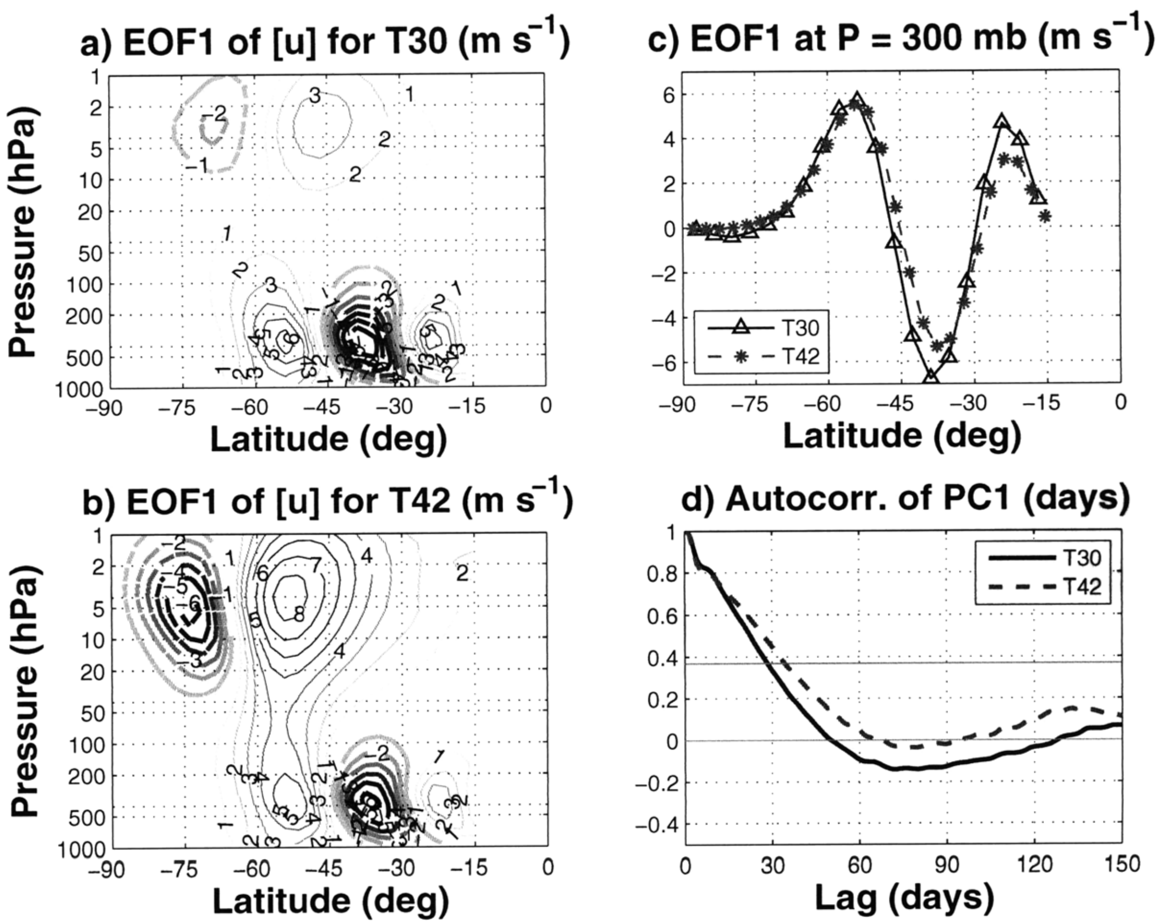

Figure 2.4: The leading EOF structure using a resolution of (a) T30, (b) T42 and (c) the comparison of the two at 300 mb. In (d), the autocorrelation is shown for the leading principal component for both T30 and T42. Light gray horizontal lines a correlation of zero and $1/e$. In (a) and (b), intervals are contoured every 1 $m\ s^{-1}$, thick heavy dashed lines are negative, thin continuous lines are positive and the zero contour is omitted.

Following Polvani and Kushner (2002), temperatures are relaxed toward this specified profile in the troposphere.

$$T_{eq}^{trop}(p,\phi) = max[T_T, (T_0 - \delta T)(p/p_0)^{\kappa}] \tag{2.2}$$

$$\delta T = \delta_y sin^2(\phi) + \epsilon \cdot sin(\phi) + \delta_z \cdot \log(p/p_0) \cdot cos^2(\phi) \tag{2.3}$$

where ϕ is the latitude, p is the pressure, T_T, T_0, p_0,δ_y,δ_z and ϵ are constants listed in Table 2.1. (2.2) and (2.3) are identical to that of Held and Suarez (1994) except for the addition of the second term in (2.3). This has been modified to represent a solstitial pattern. With the first and third terms symmetric about the equator, only the second term determines the strength of the seasonality. When $\epsilon = 0$, the equilibrium temperature profile is symmetric about the equator. As the magnitude of ϵ increases, the peak of the T_{eq} is shifted to the summer hemisphere.

In the experiments described in Chapter 4, multiples of 10K ranging from 0 to -30 K will be used for ϵ. The different latitudinal surface equilibrium temperature structures are shown in Fig. 2.5. As the magnitude of ϵ is increased, there are two characteristics to note. First, the peak temperature is displaced away from the equator and into the Northern Hemisphere; this profile is broadly representative of a Northern Hemisphere summer and a Southern Hemisphere winter. Second, the equator to pole temperature difference increases; for instance, when ϵ changes from 0 K to -10 K, the temperature difference changes from 60 K to 70 K.

Following Polvani and Kushner (2002), the stratospheric equilibrium temperature profiles are governed by the following equations.

$$T_{eq}^{strat}(p,\phi) = [1 - W(\phi)]T_{US}(p) + W(\phi)T_{PV}(p) \tag{2.4}$$

$$W(\phi) = \frac{1}{2}(1 - tanh[(\phi - \phi_0)/\delta\phi]) \tag{2.5}$$

$$T_{PV} = T_{US}(p_T)(p/p_T)^{-R\cdot\gamma/g} \tag{2.6}$$

where T_{US} is the US Standard Temperature, $W(\phi)$ weighs the cooling over the stratospheric

Constant	Description	Value
T_T	Top of the troposphere temperature	216.65 K
T_0	Reference temperature	315 K
p_0	Reference surface pressure	1000 mb
δ_y	Eq. to pole temp. diff. when ϵ=0	60 K
δ_z	Controls static stability in the Tropics	10 K
κ	R/c_p	2/7
R	Ideal gas constant	287 $J\ kg^{-1}\ K^{-1}$
c_p	Specific heat at constant pressure	1004 $J\ kg^{-1}\ K^{-1}$
ϕ_0	Defines center of largest gradient	$-50°$
$\delta\phi$	Controls width of str. temp. grad.	10°
p_T	nominal pressure level for the tropopause	100 mb

Table 2.1: Constants used in the equilibrium temperature profile.

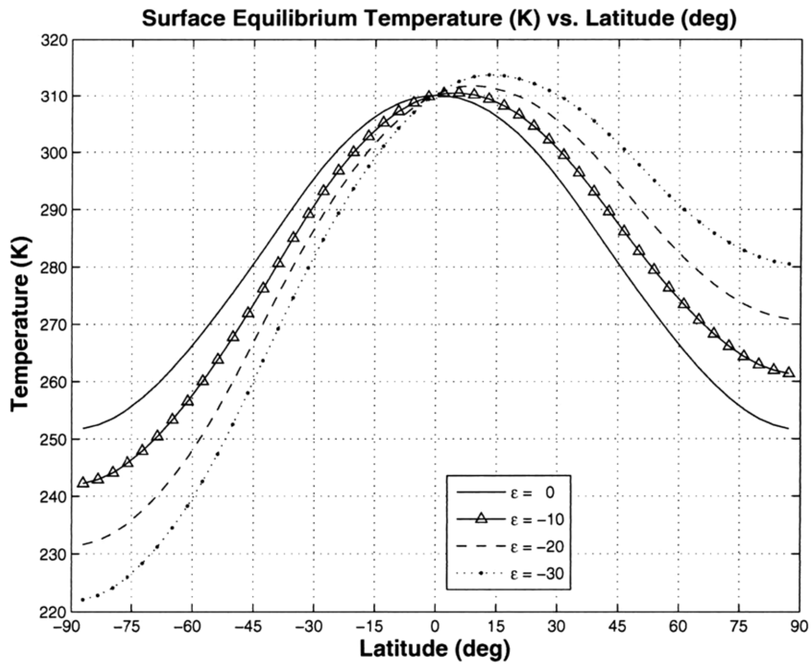

Figure 2.5: Surface equilibrium temperature (K) for ϵ=0,-10,-20,-30 K as described in equation 2.3.

winter pole, T_{PV} is the temperature with a constant lapse rate γ, ϕ_0, p_T and $\delta\phi$ are constants defined in Table 2.1.

Similar to the changes of the tropospheric equilibrium temperature profile, where changes to ϵ will be made, variations of γ (in units of K/km) will be used to alter the strength of the polar vortex. To illustrate the different stratospheric temperature profiles, Fig. 2.6 shows three examples. Going from $\gamma = 2\ K/km$ to $\gamma = 4\ K/km$ greatly increases the equilibrium temperature gradient near the stratospheric winter poles (compare Fig. 2.6a and Fig. 2.6b). Finally, to get a full range of experiments, there will be experiments performed with no stratosphere temperature gradient in the equilibrium profile. This is done by setting $W = 0$ and will be referred to as the "no polar vortex" case. In this setup, Fig. 2.6 shows the equilibrium temperature profile as a function of pressure only.

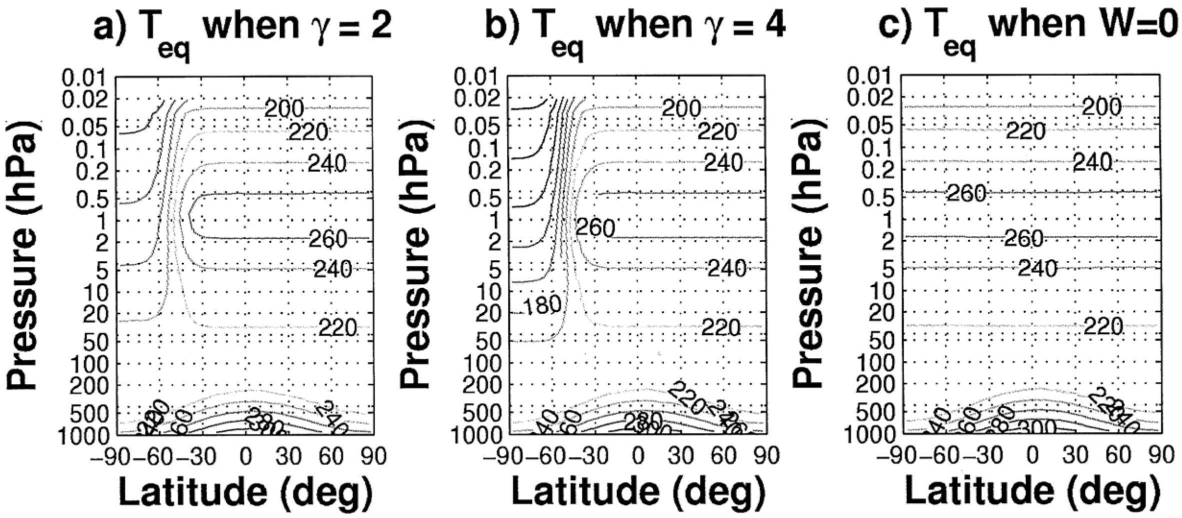

Figure 2.6: Equilibrium temperature (K) profile for (a) $\gamma = 2$, (b) $\gamma = 4$ and (c) $W = 0$. Contour intervals are every 20 K.

2.2.3 Friction, hyperdiffusion and the sponge layer

Following Held and Suarez (1994), to represent friction, below $\sigma = 0.7$, a linear drag is applied to the momentum equations. The coefficient of friction is zero above this level and increases linearly to 1 day^{-1} at the surface. In addition, a ∇^6 hyperviscosity is applied to minimize numerical diffusion. Here, the smallest wavenumber is damped on a timescale of half a day.

Finally, to prevent false wave reflections at the top of the model, we have employed a sponge layer.

$$
\begin{aligned}
k_{sp}(p) &= k_{max}[(p_{sp} - p)/p_{sp}]^2 \qquad \text{for} \quad p < p_{sp} \\
k_{sp}(p) &= 0 \qquad \text{for} \quad p \geq p_{sp}
\end{aligned}
\tag{2.7}
$$

where k_{max}= $(0.5\ day)^{-1}$ and $p_{sp} = 0.5\ mb$. This sponge layer is applied as a linear damping term on the momentum equations with the damping coefficient described in (2.7). As shown, the sponge starts above 0.5 mb and increases with height to a maximum value of a damping rate of half a day.

2.3 Tropospheric version

As we will discuss in Chapter 6.1, the primary reason for using this particular model is to understand a particular tropospheric variability and whether or not it depends on the stratosphere. As an added bonus, a comparison can be made between the stratosphere-troposphere model with the troposphere-only model. In terms of the setup, the two models are similar. The friction, hyperdiffusion and horizontal resolution are the same. However, there are two main differences: the placement of the vertical levels and the equilibrium temperature profile.

Unlike the stratosphere-troposphere model, where the vertical levels are approximately spaced equally in log-pressure coordinates, here, the grid points are placed evenly in sigma coordinates, as shown in Fig. 2.7. With only two layers above the nominal height of the tropopause, the stratospheric equilibrium temperature profile described by (2.4)-(2.6) is replaced by a "stratospheric" formalization from Held and Suarez (1994). In this case, the equilibrium temperature profile never drops below 216 K. This value was chosen to match the temperature at the tropopause in the U.S. Standard Atmosphere (1976). Fig. 2.8 shows an example of the equilibrium profile using $\epsilon = -10K$. Note the profiles are identical to Fig. 2.6a-c in the troposphere, but with only two layers representing the stratosphere, the equilibrium temperatures representing the stratosphere are 216 K everywhere.

2.4 Zonally-symmetric model

In the previous two sections, the GFDL GCM is, of course, run in three spatial dimensions. Here, we replace the 96 grid points with only 1 grid point in the west-east direction, constraining any variations in the longitudinal direction. Instead of solving for the three dimensional primitive equations, a two dimensional form will be used, and hence, the setup described here is referred to as the zonally-symmetric model. The purpose of this exercise is to determine the relative role of the eddy heat and momentum fluxes in setting the mean flow. By explicitly inputting the eddies from the control run, an analysis can be made of their relative importance.

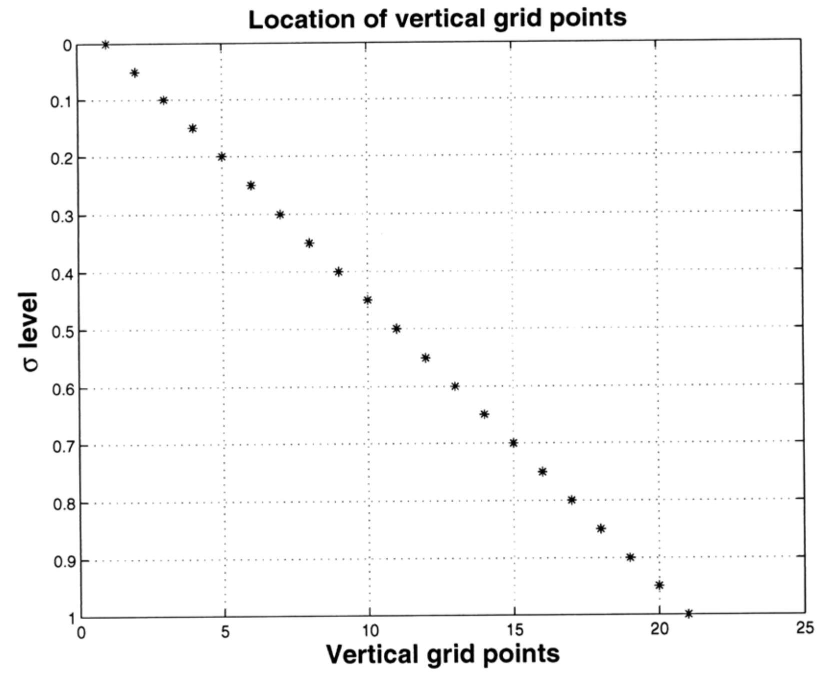

Figure 2.7: Location of the vertical grid points in σ coordinates.

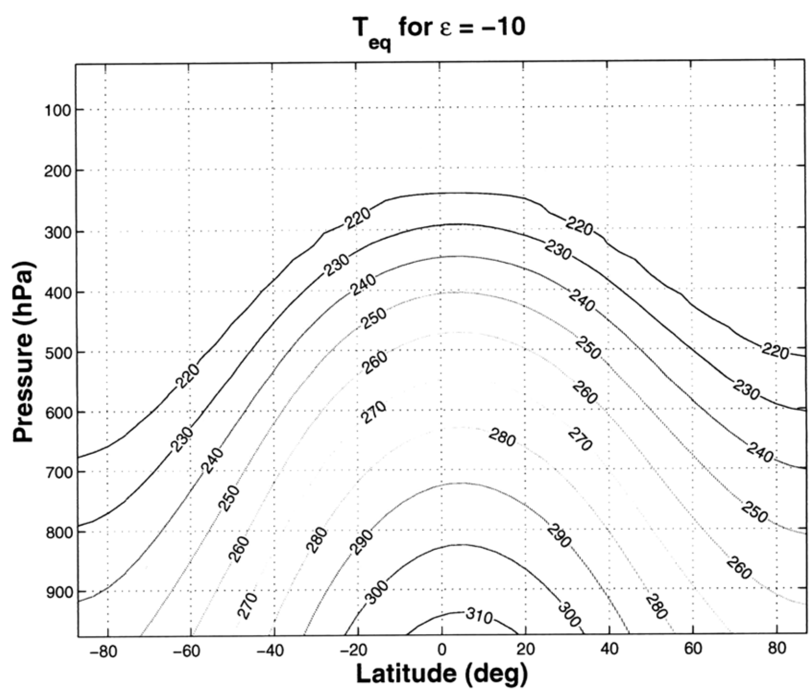

Figure 2.8: Equilibrium temperature profile for troposphere model using $\epsilon = -10K$.

As we will describe in Chapter 6.1, the primary reason for using this model is to understand a particular variability exhibited by the previous two models. Thus, the setup here is nearly identical to what was described in the previous section, except the model is now constrained to the latitudinal and vertical directions. We will then explicitly input the eddy forcing terms into the zonal momentum and heating equations. These eddy forcing terms are calculated off-line from a previous run using the "full" model.

Following Ring (2008), the eddy forcing terms in sigma coordinates are calculated as follows.

$$\frac{\partial \overline{u}}{\partial t}_{eddy\ tend.} = \frac{1}{\overline{p_s}}\left[\frac{-1}{a\cos^2\phi}\frac{\partial}{\partial\phi}\overline{\left((vp_s)'\,u'\cos^2\phi\right)} - \frac{\partial}{\partial\sigma}\overline{\left((\dot{\sigma}p_s)'\,u'\right)} - \frac{\partial}{\partial t}\overline{(u'p_s')}\right] \tag{2.8}$$

$$\begin{aligned}\frac{\partial \overline{T}}{\partial t}_{eddy\ tend.} &= -\frac{1}{a\cos\phi}\frac{\partial}{\partial\phi}\overline{\left((vp_s)'\,T'\cos\phi\right)} - \frac{\partial}{\partial\sigma}\overline{\left((\dot{\sigma}p_s)'\,T'\right)} - \kappa\overline{\left(\left(\frac{\partial\dot{\sigma}}{\partial\sigma}p_s\right)'T'\right)} \\ &\quad -\kappa\overline{(p_sD)'\,T'} + \kappa\left(\frac{\overline{(p_s\dot{\sigma})'\,T'}}{\sigma}\right),\end{aligned} \tag{2.9}$$

where

$$\dot{\sigma} = \frac{D\sigma}{Dt} = -\frac{\sigma}{p_s}\left(\frac{\partial p_s}{\partial t} + \vec{v}\cdot\nabla p_s\right) + \frac{\omega}{p_s}, \tag{2.10}$$

D is the horizontal divergence and p_s is the surface pressure.

Unlike in Ring (2008) where they were interested in the climatological changes, here, we will be interested in the internal variability of zonal-mean zonal wind timeseries. Therefore, for each day, we calculate the eddy momentum and eddy heat fluxes from the full 3-D model, shown on the right hand side of (2.8) and (2.9) respectively. We then explicitly input the former into the zonally-symmetric model's zonal-mean wind and the latter into the zonal-mean temperature equations. As expected, Fig. 2.9 shows that a comparison between the climatological model output of the full and zonally-symmetric model are virtually the same.

We will later see in Chapter 6.1 that the timeseries of the internal variability of both models are nearly identical and will exhibit characteristics of poleward propagation. By calculating the eddy forcing terms off-line, we can select and choose which eddy terms to feed into the zonally-symmetric model to determine which ones are responsible for this behavior.

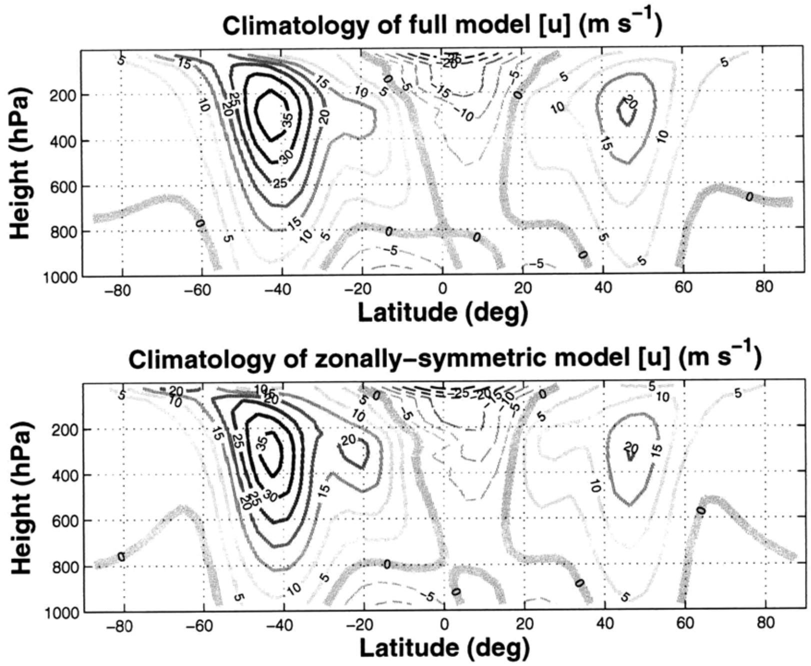

Figure 2.9: Climatological zonal-mean zonal wind for the full model (top) and the zonally-symmetric model (bottom) using ϵ = -20 K.

2.5 MIT GCM

As discussed in the previous section and in 1.4.1, the zonal-mean zonal wind variability goes through periods of poleward propagation. But the propagation of zonal-mean zonal flows does not appear limited to the atmosphere. In a semi-hemispheric, zonally-reentrant oceanic GCM, *equatorward* propagation is shown to exist. In Chapter 6.3, a more detailed analysis of this behavior will be discussed. Here, we provide the details involving the setup.

The full details of the MITGCM can be found in Marshall et al. (1997b) and Marshall et al. (1997a) and the particular setup was described in Chan (2006) and Chan et al. (2007).

Here, we just provide a cursory description. This is a zonally reentrant, semi-hemispheric model ranging from 50.67°S to 0.17°S and 0°E to 10° E on a $\frac{1}{6}^{\circ} \times \frac{1}{6}^{\circ}$ latitude/longitude grid with 15 vertical levels. The model does not include salinity; density is simply a linear function of temperature. The model-imposed forcings are shown in Fig. 2.10. The wind stress is eastward everywhere with weak winds near the equator. The heat forcing is applied to the upper surface layer, with a relaxation time of 30 days. Both forcings are constant in time and functions only of latitude. With the flow reaching statistically steady state by year 500, the model was integrated for a total of 1285 years, of which the last 313 years were examined for this study.

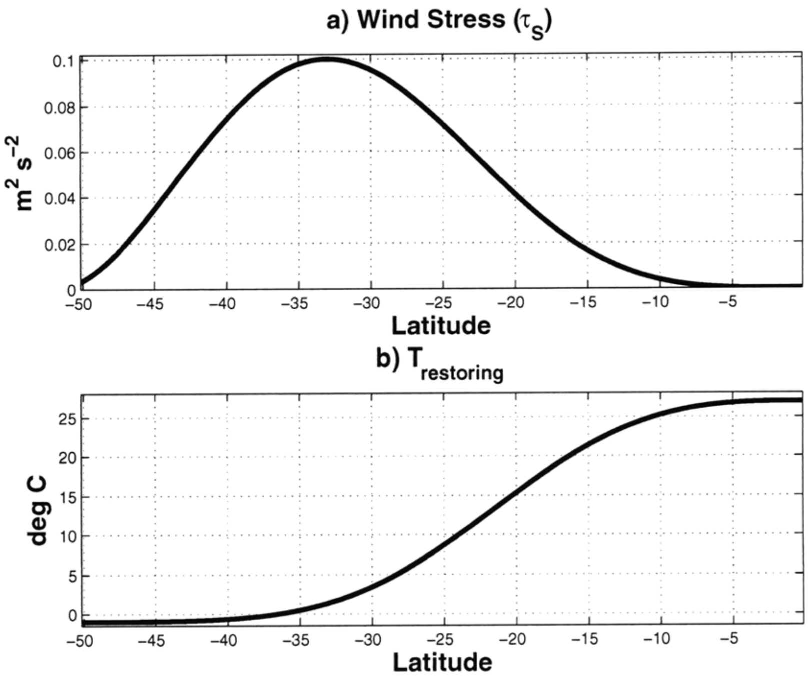

Figure 2.10: The prescribed model forcings are an (a) atmospheric wind stress and (b) heat forcing with a relaxation time of order one month. Both are constant in time, only a function of latitude, and applied to the top surface layer (22m). Adapted from Cerovecki et al. (2009).

Chapter 3

Stratosphere-troposphere coupling

The purpose of this chapter is to introduce a reference state and demonstrate the characteristics behind the stratosphere-troposphere coupling. This starting point will allow us to branch off into many directions in later chapters to see how the coupling is sensitive to the tropospheric setup. Therefore, the setup to our reference point will be examined in the next section. In an attempt to describe the internal variability, many issues arise and this will be discussed in section 3.2. Finally, in section 3.3, through thermal and momentum forcings, we will then show more definitively that the model's stratosphere has an impact in the troposphere.

3.1 Setup and characteristics of control run

The setup here is nearly identical to that of Polvani and Kushner (2002) and is described in Section 2.2. This stratosphere-troposphere model is run with $\epsilon = -10K$ and $\gamma = 4K/km$. These parameters would be representative of a Southern Hemisphere winter and Northern Hemisphere summer, as depicted in a time-average of the zonal-mean zonal wind shown in Fig. 3.1.

There are many features that are broadly similar to observations. First, there are surface easterlies in the tropics that extend throughout the troposphere. Second, the peak surface westerlies occur in mid-latitudes in both the winter and summer hemispheres. Third, with

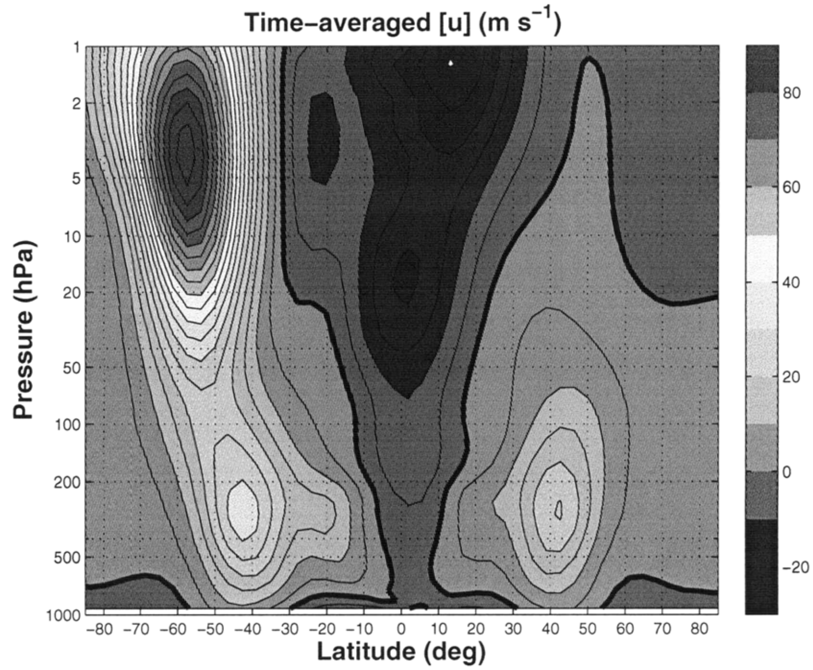

Figure 3.1: Time-average of the zonal-mean zonal wind for specified parameters $\gamma = 4K/km$ and $\epsilon = -10K$. Contour intervals are every 5 ms^{-1} with the thick black line representing the zero contour.

surface easterlies at 25°and strong westerlies at 300 hPa, this would suggest a subtropical jet (associated with the tropical meridional overturning circulation), roughly consistent with the location described in observations. Fourthly, the eddy-driven jet and its associated peak of the surface westerlies, occurring near 45°S, appear well-removed from the location of this subtropical jet. Finally, the speed of the stratospheric jet maximizes at about 90 $m\ s^{-1}$ and is located roughly near 55°S; all these traits are nearly the same as observations.

Although there are many qualitative features in common with observations, the most obvious difference in Fig. 3.1 is the relative magnitudes between the subtropical and eddy-driven jets. In observations, during the winter months, the greatest wind speeds at 300 mb occur near the subtropics with a local maxima in the mid-latitudes (cf. Peixoto and Oort 1992). In this model, the opposite is true: there is a hint of a local maxima in the subtropical winds, while the greatest wind speeds occur in the mid-latitudes. This would suggest that the relative strengths between the subtropical and eddy-driven jets may not be accurately captured. In other words, in our model, the subtropical jet is either too weak or the eddy-driven jet is too strong. As we will see in Section 4.1, this discrepancy may a major role in examining the tropospheric response to stratospheric perturbations.

On any given day, the winds can be much stronger than the climatological- and zonal-average. Fig. 3.2a shows the stereographic planar projection of the zonal winds at 4 mb for a particular day. In the polar region, zonal wind speeds approach zero. While at the jet, wind speeds are in excess of 110 $m\ s^{-1}$, all consistent with Fig. 3.1. We will refer to these strong winds circum-navigating the sub-polar region as the polar vortex.

Besides the similarities in both the magnitude and spatial structure of the stratospheric jet to observations, the "isolation" of the polar vortex can also be seen. In Fig. 3.2b, the daily-averaged quasi-geostrophic potential vorticity (q_p) is shown corresponding to Fig. 3.2a. In the immediate polar region, there is low q_p and is nearly homogenized. However, near the jet (approximately 60°S), there is a strong PV gradient, which acts as a strong barrier (Dritschel and McIntyre 2008) separating the high PV from the low PV.

Matsuno (1970) and Matsuno (1971) have shown that the planetary waves are crucial in triggering stratospheric sudden warmings (SSW). However, with flat topography, planetary waves are weak. Thus, not surprisingly, there are no SSW during the 12000 day run as shown

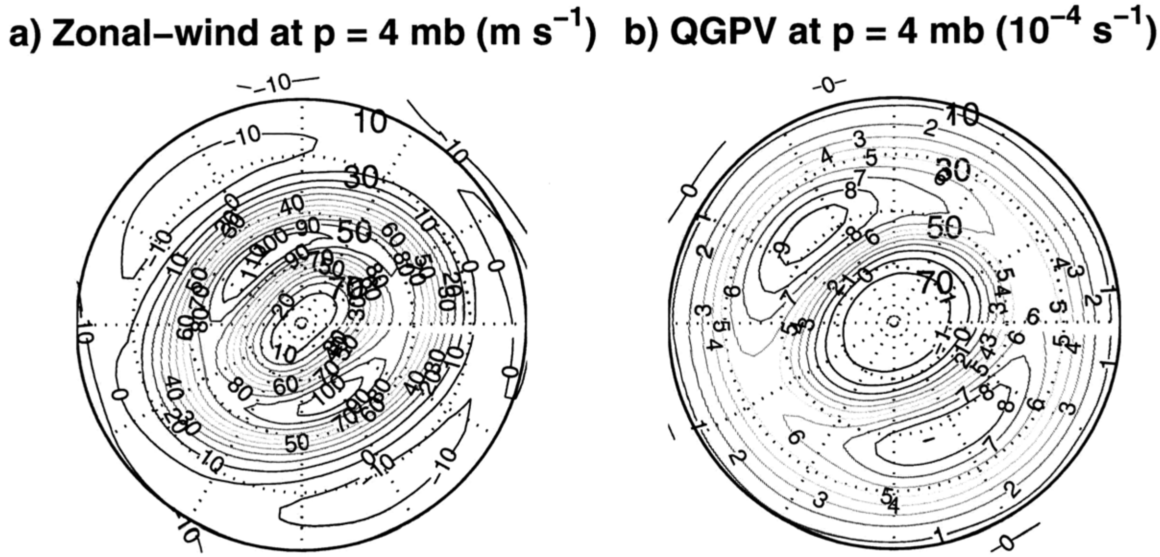

Figure 3.2: Stereographic projection of the southern hemisphere. Plot of the daily- averaged (a) zonal wind and (b) quasi-geostrophic potential vorticity at $p = 4$ mb for $t = 3751$ day. Contours are every 10 $m\ s^{-1}$ for (a) and 1 x 10^{-4} s^{-1} for (b). The center is the SH pole and every concentric circle outward is 20° latitude with every angular sector representing 30° of longitude.

in Fig. 3.3. The WMO definition of a major SSW is the appearance of a wind reversal (from westerlies to easterlies) at 10 mb and 60°S. After the model gets spun up between days 0 and 500, the zonal wind oscillates around 65 $m\ s^{-1}$ and never drops below 50 $m\ s^{-1}$. Given this timeseries, it is clear that the present model does not adequately represent any SSW. (However, this will change when we include topography in Section 4.3.)

Consistent with the wind speeds being never too far from "radiative" equilibrium, we will show that there is little wave dissipation in the stratosphere, and as a result, there is insufficient wave drag to drive the stratospheric temperatures from this equilibrium illustrated in Fig 2.6b. To show this, we use the Eliassen-Palm (EP) fluxes, which illustrate wave propagation. Following Edmon et al. (1980), the EP fluxes can be decomposed to the following meridional and vertical directions.

$$F_\phi = -a \cos\phi \overline{u'v'} \tag{3.1}$$

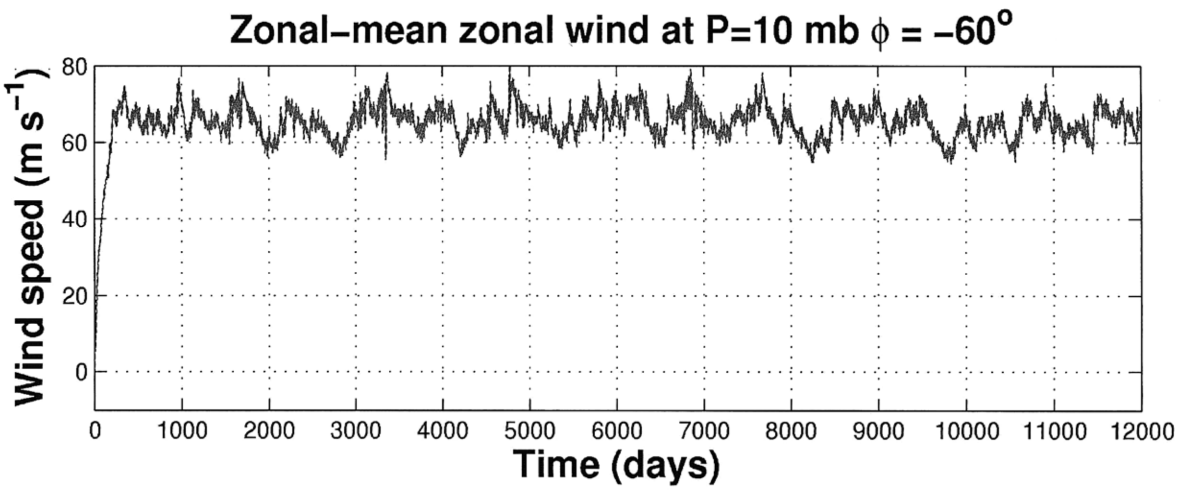

Figure 3.3: Timeseries of the zonal-mean zonal wind at $p = 10\ mb$ and 60°S for days.

$$F_p \quad = \quad f \cdot a \cos\phi \overline{v'\theta'} \left(\frac{\partial\overline{\theta}}{\partial p}\right)^{-1} \tag{3.2}$$

where the overbars indicate zonal means, the primes departures from the zonal mean, and the notation of meteorological variables standard.

Fig. 3.4 shows the EP fluxes and its divergence for the winter hemisphere. Not surprisingly, most of the divergence is near the surface and convergence is in the middle to upper parts of the troposphere. This pattern suggests eddies are generated at the low levels, propagate upward (and equatorward), then dissipate away from the surface. As shown in this time-average plot, only a small fraction of the waves get dissipated in the stratosphere, consistent with the model's inability to reproduce SSW as shown in Fig. 3.3. (We will see in Chapter 4.3, the EP fluxes will change markedly in the stratosphere.)

3.2 Defining the leading mode

In the previous section, with the sole exception of Fig. 3.3, we went through snapshots and time-averages of some of the main characteristics of this model. One of the more important features is trying to understand the internal variability. As described in Section 1.1.1, these annular modes are important in not only describing the greatest variability, but also can

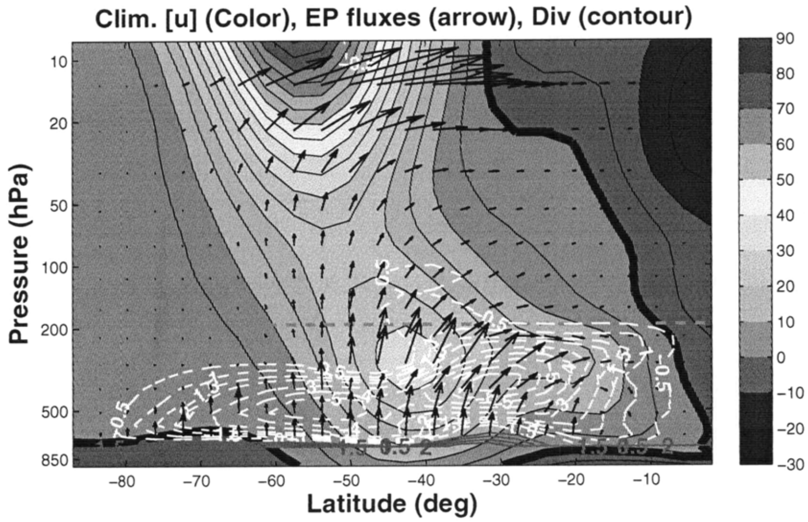

Figure 3.4: Climatological zonal-mean zonal wind (filled contours), EP fluxes (arrows), EP flux convergence and divergence (white and red contours respectively). EP flux divergence contours are every 1 $m\ s^{-1}\ day^{-1}$ for values less -2 $m\ s^{-1}\ day^{-1}$ and 0.5 $m\ s^{-1}\ day^{-1}$ elsewhere, with the zero contour omitted. EP fluxes have been scaled by $1/\rho$. Zonal wind contour intervals are every 5 ms^{-1} with the thick black line representing the zero contour.

be used to predict climate change. Thus, having the correct representation of the mode is important, but yet, a universal method remains absent (Baldwin and Thompson 2009). In this section, we will detail four methods in describing how the zonal-mean zonal wind varies as a function of latitude and height.

Since this thesis examines the relationship of the stratospheric impact on the troposphere, we will be concerned about the hemisphere in which the stratosphere is active, hence the remaining part of the thesis will only show calculations of the southern winter hemisphere. In the following figures, we will make extensive use of EOF analysis (Wilks 2005). Since our focus is on the extra-tropics, our calculations will be constrained to the region poleward of 20°S.

The first four figures show results of an EOF analysis, with the covariance matrix weighted by the cosine of the latitude to account for the convergence of longitudinal grid points at the poles. However, the first two apply different weightings to the covariance matrix, while the third performs a level-by-level calculation. The fourth analysis is done by finding the principal component (PC) of a particular level and regressing the zonal-mean zonal wind anomalies to obtain the regressed spatial pattern.

The first method uses a pressure-weighted EOF analysis on the zonally-averaged zonal wind as a function of height, latitude and time. This convention was used by Thompson and Wallace (2000) when the analysis was performed over multiple heights and essentially accounts for the density variations in the vertical direction. More specifically, we multiply the data by the square root of the normalized pressure interval, e.g. $\sqrt{\Delta P/(\Delta P)_{max}}$.

In a troposphere-only world, results are likely insensitive to the precise weighting scheme since density has the same order of magnitude between the tropopause and the surface. However, when the stratosphere is included, density varies by several orders of magnitude between the stratopause and the surface. Thus, unlike a tropospheric-only world, the leading EOFs will be duly sensitive to the choices made in the vertical weighting scheme as we will see when we compare Figs. 3.5a and 3.5b.

In Fig. 3.5a, the first method is used. Not surprisingly, in the case where the tropospheric variability is weighted so that it accounts for most of the total variability (Fig. 3.5a), most of the signal is below the tropopause. Comparing the jet's climatological tropospheric location in Fig. 3.1, this structure describes the jet's meridional oscillation. Besides the latitudinal shift, this tripole structure also suggests a link with the subtropics. When the mid-latitude jet shifts poleward, the subtropical jet is enhanced, and conversely, when the mid-latitude shifts equatorward, the subtropical jet is weakened.

Although most of the leading EOF structure is dominated below the stratosphere, the tropospheric poleward lobe does extend into the stratosphere. Taken literally, this figure describes a statistical correlation between an increase in the stratospheric winds and the mid-latitude jet shifting poleward, suggesting a coupling between the troposphere and the stratosphere.

However, using the second method, where there's no vertical weighting, *i.e.* each vertical layer is equally accounted for in the covariance matrix, the results change markedly (Fig. 3.5b). In this case, all the tropospheric signal found in Fig. 3.5a is now absent. Instead, the stratospheric dipole structure depicts an oscillation of the stratospheric polar vortex with little connection to the troposphere. So this particular choice of calculating the internal variability suggests that there is no coupling between the two layers.

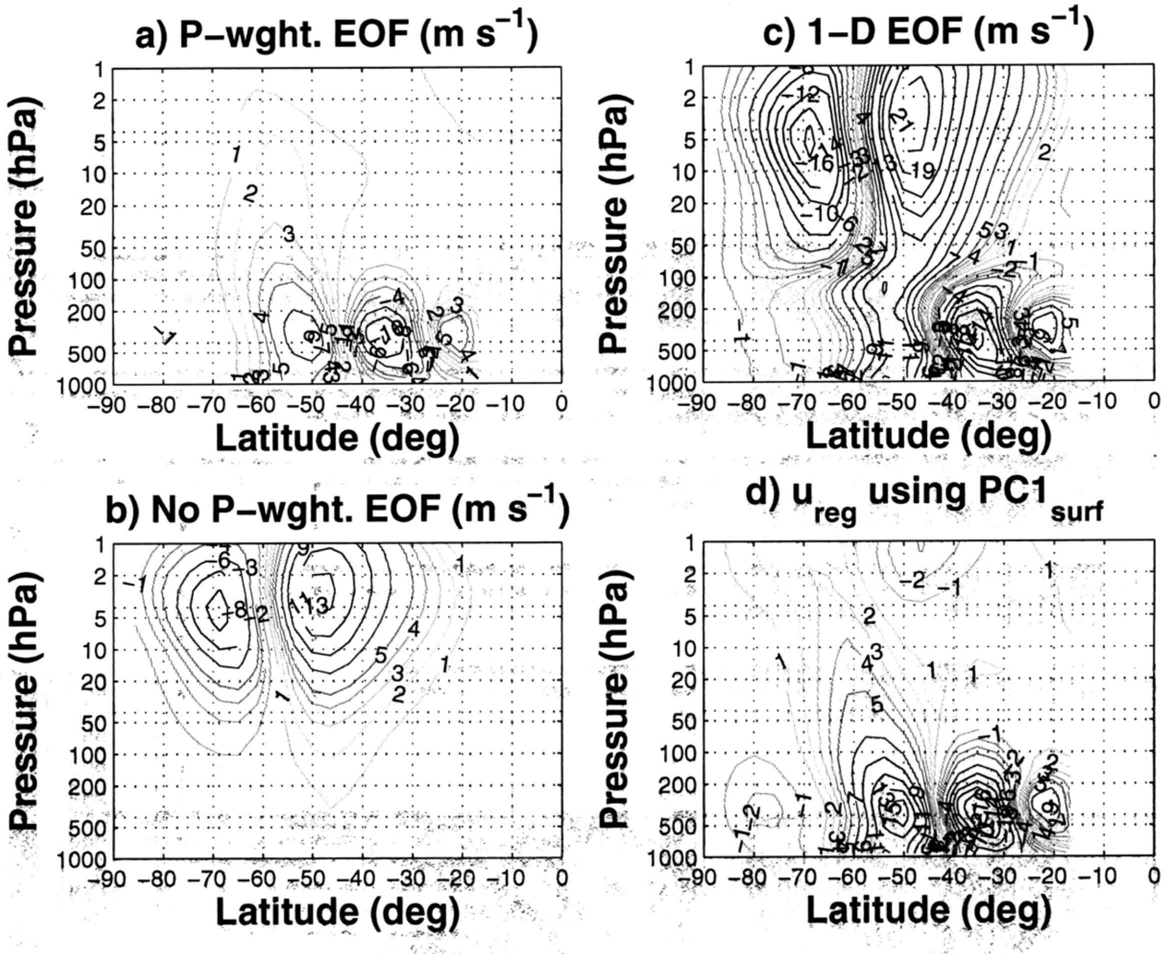

Figure 3.5: Leading spatial patterns. The leading EOF is calculated in (a) by weighing the vertical mass variations in [u](y,p,t) (b) by no vertical weighting in [u](y,p,t) (c) by doing an EOF analysis of [u](y,t) at each model level. In (d), using the leading principal component from the surface, a regression is made from the [u] anomalies. Contour intervals are 1 m s^{-1} with the zero contour omitted. The magnitudes in plots (a), (b) and (c) correspond to anomalies associated with a standard deviation of one from the time-mean.

Comparing Figs. 3.5a and 3.5b show that an EOF analysis extending several orders of magnitude in density is sensitive to the vertical weighting. However, the next two calculations do not require a weighting in the vertical direction. In the first example, Fig. 3.5c is determined by the leading EOF of each layer. Since the sign and amplitude of any EOF analysis is arbitrary, combining all the layers into a latitude-height cross section requires some *ad hoc* choices. Here and the rest of this thesis, we employ the following procedure. First, the sign convention here was chosen to create a vertically coherent structure from the stratosphere to the troposphere. More specifically, at approximately 50°S, the sign at each level was picked to match with the one above and below. Second, the amplitude was scaled to represent one standard deviation in the wind variability.

Interestingly, applying the procedure in picking the sign convention in this third method, the tropospheric part (under 100 *mb*) looks very similar to Fig. 3.5a and the stratospheric part looks very similar to Fig. 3.5b. However, unlike the previous two methods, this calculation does not show how statistically correlated the different levels are "connected" with one another. For instance, Fig. 3.5a shows a correlation between 500 *mb* and 300 *mb*. Such an inference cannot be made by this third method.

Although we could find the vertical coherence by examining the correlation between the leading PCs of each level, we instead follow the method used in Baldwin and Dunkerton (2001). Here, we look at the leading PC as a function of lag and pressure and see whether there are any coherent structures. Using the leading PC, which will also be referred to as the annular mode index, AMI, Fig. 3.6 is constructed by compositing the events where the AMI at 10 *mb* exceeds 0.8 standard deviations. As shown in the bottom panel, the stratospheric AMI has roughly the same sign everywhere such that the value peaks at about 5mb and generally decreases away for almost all lags.

In the troposphere, however, the AMI has the same sign only for certain lags; more precisely, only roughly between lags 20 and 65 days do they statistically (at the 95 percent confidence interval) have the same sign as the stratosphere. The literal interpretation of this figure is that whenever there's an anomalous stratospheric event, the troposphere follows with the same sign some time afterward. In addition to this feature being similar to observations (cf. Baldwin and Dunkerton 2001), the lags between -25 day and 0 day show the same-signed

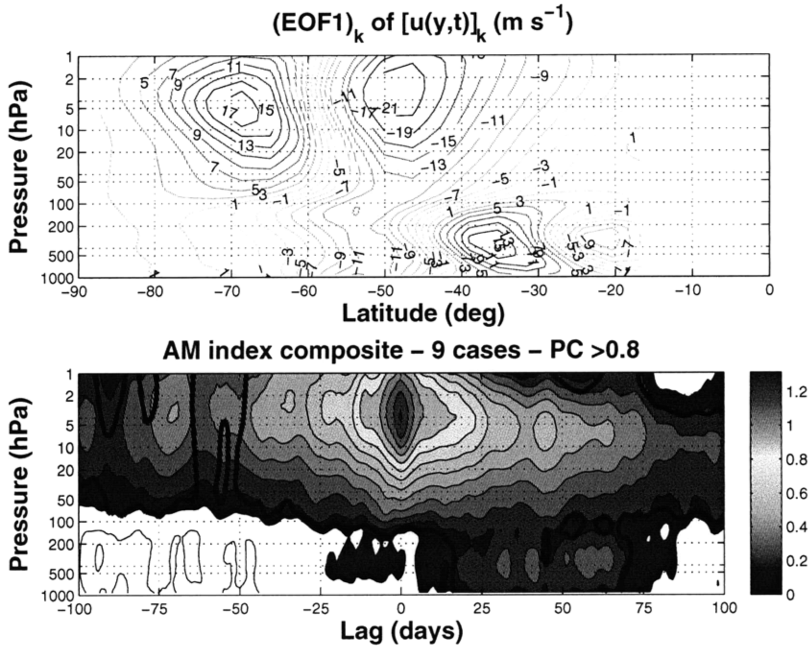

Figure 3.6: Top panel: Level-by-level leading EOF of [u] (top) - same as Fig. 3.5c. Bottom panel: Composites of the annular mode index (AMI) as a function of pressure and lag. When the AMI at $p = 10mb$ exceeds 0.8 standard deviations, composites before and after this time are made and represent day zero. Contour intervals are every 0.1, with the zero contour omitted and values greater than zero filled. The black line marks the region where the AMI composite is statistically significant away from zero at the 95 percent confidence interval.

anomaly in the troposphere, though they are not statistically significant greater than zero. As discussed in Section 1.2, this could suggest what happens in the troposphere during the approximate lag of -15 days causes *both* the anomalous stratospheric event at lag = 0 day, as well as the tropospheric signal at lags between 20 and 65 days.

So with the first and third methods suggesting there is indeed a coupling between the troposphere and stratosphere (but not the second method), the fourth method uses regressions. We first obtain the first PC, PC1, of zonal-mean zonal wind at a specified pressure level and use that time series with the full zonal-mean zonal wind anomalies to obtain a spatial regression pattern. In equation form, this can be simply written as the following.

$$[u](y,p,t) = PC1_k(t) \cdot u_{reg}(y,p) \tag{3.3}$$

where k is the particular level of constant pressure. In Fig. 3.5d, PC1 from the near-surface pressure level calculated from Fig. 3.5c is used. Besides the lobe at 80°S and the different magnitudes, the obtained regression pattern shows a spatial structure that is nearly identical to Fig. 3.5a. This method shows that the AMI at the surface seems tied with the AMI in the stratosphere.

To test this pattern's sensitivity to the choice of the vertical level at which PC1 was taken, Figs. 3.7a-c show three other choices: one also in the troposphere (500 *mb*), another in the lower stratosphere (50 *mb*) and one in the upper stratosphere (5 *mb*). The mid-tropospheric choice is qualitatively similar to Fig. 3.5d suggesting the regression patterns are similar when picking choices within the troposphere. This is not a suprising result given how vertically coherent structures from the leading EOF and PC depicted in Fig. 3.5a and Fig. 3.6 respectively.

However, the regression pattern changes when picking a timeseries from the stratosphere. Fig. 3.7b depicts the regression pattern when the AMI at 5 *mb* is used. Again, this picture is very similar to the one shown in Fig. 3.5b, where the vertical structures were equally weighted. However, in this case, there is a weak connection to the tropospheric mid-latitude region. This pattern would suggest that what happens at 5 *mb* is very weakly correlated to the troposphere, but is, not surprisingly, very well correlated with the rest of the stratosphere.

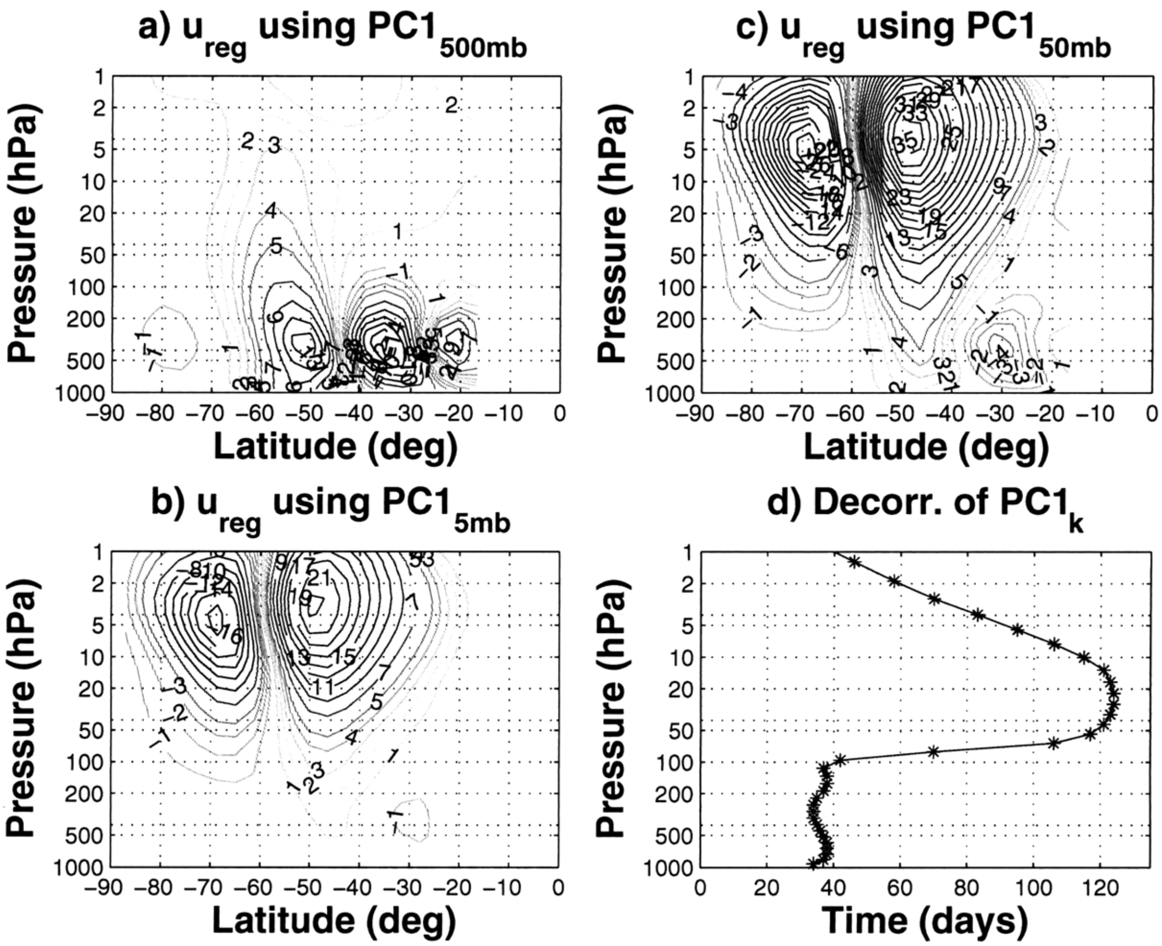

Figure 3.7: Regression patterns obtained using the leading PC at (a) 500 *mb*, (b) 5 *mb* and (c) 50 *mb*. In (d), the decorrelation time for the leading PC from the EOF analysis shown in Fig. 3.5c. The decorrelation time is the length in time it takes for the autocorrelation function to cross $1/e$.

Finally, picking a timeseries at an intermediate value, we choose the leading principal component at 50 *mb*. We use this timeseries with the zonal wind anomalies to find the regressed wind pattern shown in Fig. 3.7c. This calculation is the most dramatic example of the coupling between the troposphere and stratosphere. The spatial structure is representative of the superposition of the previous two figures and would suggest that whenever the stratospheric polar vortex moves equatorward, the tropospheric jet moves poleward at the same time.

The interpretation of Figs. 3.7a-c is that whatever changes occur at 500 *mb*, the anomalous activity is very similar to what happens elsewhere in the troposphere but only weakly in the stratosphere. Similarly, anomalous activity at 5*mb* coincides with the rest of the stratosphere, but not so much with the troposphere. However, in the lower stratosphere, the anomalous activity correlates to changes in both the stratosphere *and* the troposphere. This makes intuitive sense that the lower stratosphere is what is important in coupling the two layers.

The results of Figs. 3.7a-c seem to suggest the importance of resolving the lower stratosphere, consistent with some of the work described in Section 1.2. Whenever there is anomalous activity at that location, the circulations to both the stratosphere and troposphere are altered. We will come back to the importance of the lower stratosphere in Chapter 5.

An added benefit in calculating the principal component at each vertical level, we can perform an analysis in determining the typical timescale associated with each level. This is done by looking at the autocorrelation function for each of the principal components for each height. The length of time in which the autocorrelation function crosses the $1/e$ threshold is referred to as the decorrelation time and is shown in Fig. 3.7d. It is about 35 days everywhere in the troposphere, but, in the lower stratosphere, the decorrelation time sharply increases to about 120 days at a pressure level of 25 *mb* then decreases gradually towards the sponge layer. Compared to a similar setup, this figure is broadly characteristic of the results from Gerber and Polvani (2009).

From Fig. 3.6, we can see that after the anomalous stratospheric event, the troposphere follows the same sign and persists in that particular phase for 55 to 70 days. Another argument often made in the literature (*e.g.* Baldwin and Dunkerton (2001)) is how long the troposphere persists in that particular phase compared to the typical timescale. Here, in this case, with the decorrelation time roughly 35 days, Fig. 3.6 shows that the troposphere not only follows the same sign after the stratospheric event, but stays in that particular phase for one and a half to two times longer than the normal timescale. Since the stratosphere is known to have long time scales (cf. Fig. 3.7d) the relatively long persistence in the stratosphere would seem to suggest a stratospheric influence.

The bottom panel of Fig. 3.6 also suggests that the greatest stratospheric anomalies do not coincide with the greatest tropospheric anomalies. The changes that occur in the stratosphere do not induce instantaneous changes to the troposphere. The time it takes for the troposphere to respond are not accounted for in Figs. 3.5 and 3.7. Instead of regressing the instantaneous AMI with the zonal wind anomalies (which is shown in Figs. 3.5d and 3.7), we perform lag-lead regressions as shown below.

$$[u](y,p,t) = PC1_k(t+\tau) \cdot u_{reg}(y,p) \tag{3.4}$$

where τ is the AMI lag.

Fig. 3.8 shows the regression patterns with the different lags using the leading principal component from the surface EOF analysis. Comparing all of the panels in Fig. 3.8 with the zero-lag regression pattern (Fig. 3.5d) shows that there are considerably larger amplitudes in the stratosphere in the lagged cases. The further away from a lag of zero day the higher the ratio between that maximum stratospheric and tropospheric changes.

More interestingly, the coupling between the stratosphere and troposphere switches behavior between a lag of -20 days and 20 days. A positive lag reveals the equatorward lobe of the stratospheric dipole extending towards the poleward lobe of the troposphere. This suggests that when the eddy-driven shift shifts poleward, the stratospheric polar vortex intensifies and moves equatorward, similar to what was found in Figs. 3.5a-c and Figs. 3.7a-c. However, during negative lags, the poleward lobe in the stratosphere extends toward the poleward lobe in the troposphere. This means a poleward shift in the mid-latitude jet correlates with a poleward shift and weakening of the stratospheric polar vortex, a relationship not seen from Figs. 3.5a-c and Figs. 3.7a-c.

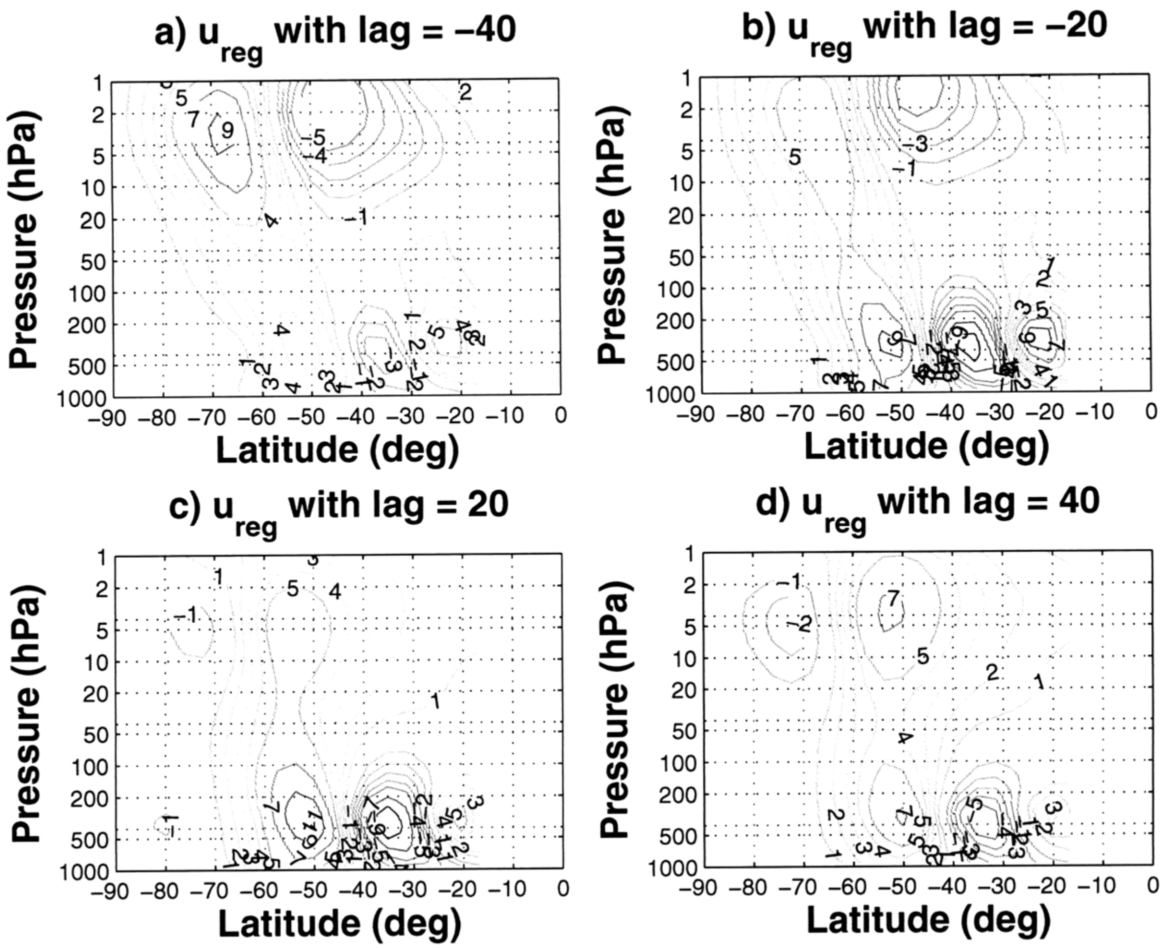

Figure 3.8: Regression patterns obtained using the leading PC from the surface with lags of (a) -40 day, (b) -20 day, (c) 20 day and (d) 40 day. Fig. 3.5d uses a lag of 0 day. Lag values correspond to (3.4) with negative lags corresponding to the AMI preceding the zonal-mean zonal wind data.

Despite all the different patterns, Fig. 3.8a would seem to be the most appropriate in describing the stratosphere-troposphere coupling. The bottom panel of Fig. 3.6 suggests that the troposphere needs about 25 days to respond to changes from the stratosphere (with another 15 days for the greatest signal). Therefore shifting the tropospheric AMI earlier (*i.e* negative lags) would best match the stratospheric activity while maintaining the tropospheric signal.

In summary, depending on the methodology, different patterns emerge as the leading mode of variability. Since we are interested in the coupling between the stratosphere and troposphere, generating a height-latitude plot is unavoidable. This simplest way is to perform an EOF analysis of the zonal-mean zonal wind. However, this is hampered by the choice of the vertical weighting scheme performed on the covariance matrix (Figs. 3.5a-b). One way to avoid any weighting is finding the leading principal component of the zonal-mean zonal winds at the surface and regressing this time series with the full data. The problem with this method is sensitivity to the choice in the pressure level at which the leading PC is taken (Fig. 3.7). Finally, we argued that the changes in the troposphere do not respond instantaneously to the changes in the troposphere (Fig. 3.6). In other words, if a stratospheric signal were being sent towards the troposphere, this signal would take some time to reach the surface. Thus, we suggested that regressing the tropospheric AMI with negative lag (of 40 days) would work best at describing the coupling when stratospheric changes are likely inducing changes in the troposphere.

3.3 Response to external forcings

In the last section, calculations using various methods were performed to describe the model's internal variability. While the results were sensitive to the precise methodology, all the cases (Figs. 3.5 and 3.7) showed that both the tropospheric and stratospheric jet oscillated. Depending on the methodology, most showed that whenever the mid-latitude jet shifted poleward (equatorward), the stratospheric polar vortex predominately shifted equatorward (poleward) as well.

To test this statistical claim, two separate types of forcings will be applied. Following

Polvani and Kushner (2002), the first type uses thermal forcings by varying the γ parameter (cf. (2.6) and Fig. 2.6.) In the second type of forcing, we apply external momentum forcings which are switched on smoothly over a period of 20 days, then held fixed. The climatology is then compiled for the subsequent 5,000 days.

Although this is similar to the works of Song and Robinson (2004), Ring and Plumb (2007) and Chen and Zurita-Gotor (2008), varying the height of the stratospheric momentum forcings in the presence of a polar vortex have not been performed to the knowledge of this author. In light of our results from the previous section, applying momentum forcings at different heights may be important in diagnosing what is important in the stratosphere-troposphere coupling. In all of these experiments, only the stratosphere is perturbed; this simplifies the interpretation on whether changes in the stratosphere can indeed affect changes in the troposphere, at least in the context of this simple model.

3.3.1 Momentum perturbations

In this section, we will explicitly apply an external momentum forcing to the momentum equations. These forcings are not meant to represent anything physical, but instead are used as a way to perturb the climatology. The response can then be examined by taking the difference between the climatologies, one from the forced and the other from the unperturbed case.

Steady angular momentum forcings are applied to both hemispheres. Using the control run, at the end of the 4000 day period, the forcing amplitude is applied linearly over a period of twenty days and its final value is then remain fixed. More specifically, an easterly forcing is added in the Northern Hemisphere, while a westerly forcing is applied in the Southern Hemisphere. By applying an equal and opposite momentum forcing at the same latitude in both hemispheres, the globally-averaged angular momentum is unchanged. Although we will be mainly focused on the Southern (winter) hemisphere, there is also the added benefit of performing two experiments in one.

This monopolar forcing is zonally symmetric, with a Gaussian profile in latitude with a full-width half-maxima of 15°. Vertically, the forcing is Gaussian in log-pressure with a

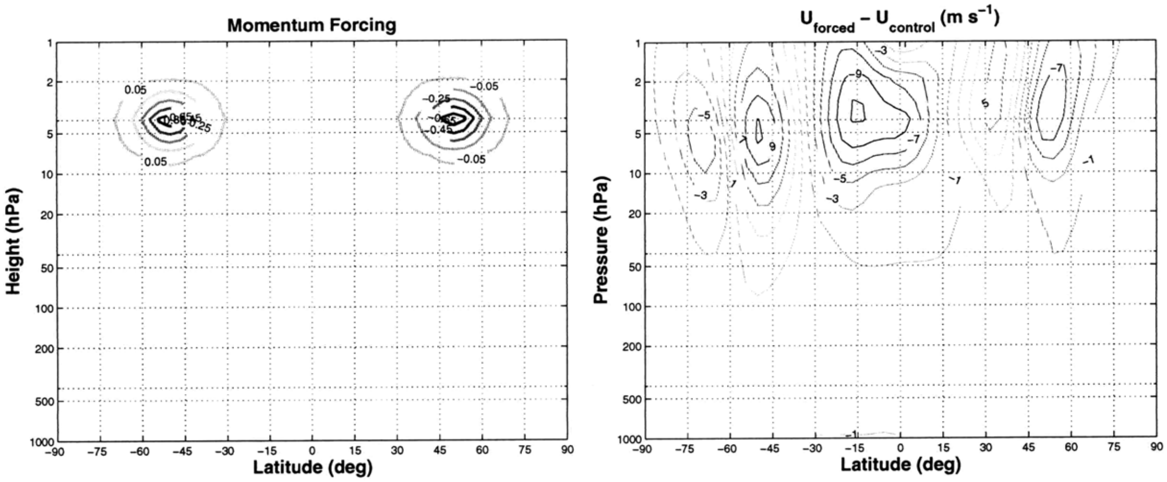

Figure 3.9: Left: Applied momentum forcing $m\ s^{-1}$ day^{-1} centered at $\pm$ 50° with a contour interval of 0.2 $m\ s^{-1}\ day^{-1}$ (0.05, 0.25, 0.45, ...) and the zero contour omitted. Right: Zonal wind response with a contour interval of 1 $m\ s^{-1}$ with the zero contour omitted.

half-maxima of about 2 km as shown in Fig. 3.9.

Similar to the works of Song and Robinson (2004), Ring and Plumb (2007) and Chen and Zurita-Gotor (2008), a monopolar forcing in each hemisphere resulted in a dipolar structure in the anomalous zonal winds away from the tropics in both hemispheres, depicted in the right panel of Fig. 3.9. More specifically, the response should be equal to the projection of the forcing onto the mode of the internal variability (cf. Ring and Plumb 2007; Ring and Plumb 2008).

However, unlike the aforementioned studies, the difficulty lies in precisely determining that mode of variability. As discussed in the previous section, depending on how you calculate the leading mode, the analysis varies. However, the spatial structure in the extratropical stratosphere does look similar to some of the calculations shown in Figs. 3.5 and 3.7. In particular, the response shown in Fig. 3.9 is qualitatively similar to that shown in Figs. 3.5b and 3.7b, where a positive (negative) lobe is equatorward (poleward) of 60°S, although the relative magnitudes are not similar. The lobe equatorward of 60°S (right panel of Fig. 3.9) is about twice as strong as its counterpart poleward of 60°S, while the EOF and regression analyses are comparable in strength. This could be a consequence of the easterly response in the tropics that was not taken into account during those two calculations.

However, the tropical stratospheric response may not be robust because anomalies here can persist for thousands of days. Unlike the extra-tropics, with the Coriolis parameter small, there is no geostrophic balance. As a result, there is very little constraint on temperatures. This is the same reason anomalies from the QBO can be long-lived as well.

In any case, Figs. 3.5b and 3.7b would seem to accurately predict that the extratropical response would be confined to the stratosphere and, in particular, the troposphere would remain largely unchanged. This result would seem consistent with Song and Robinson (2004). With their forcing near the upper stratosphere, the spatial pattern to the response had a similar shape to their leading mode of variability, which was also calculated from an EOF analysis with no mass weighting.

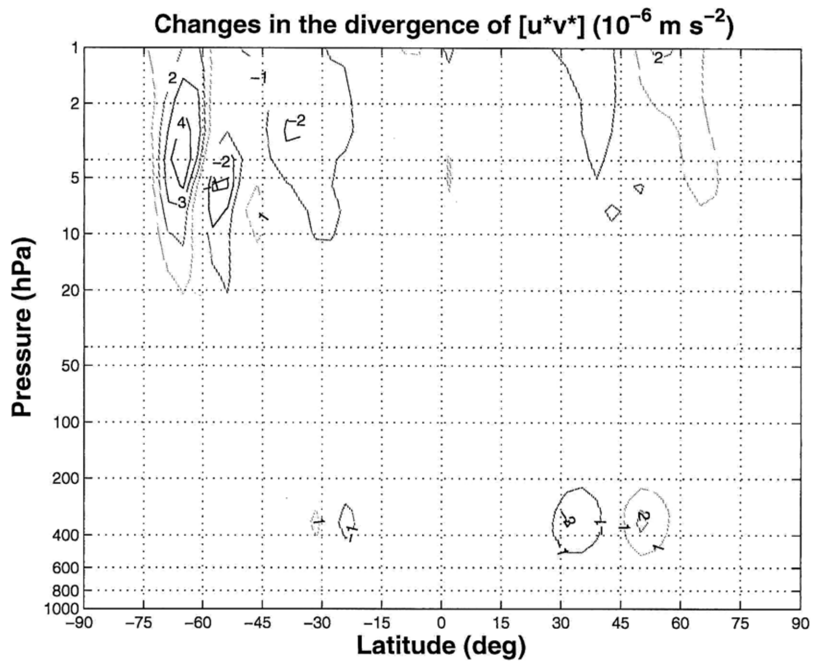

Figure 3.10: Changes in the latitudinal divergence of the eddy momentum flux from the control run with a forcing shown in Fig. 3.9.

However, unlike the Song and Robinson (2004) case, the response is localized only in the stratosphere, *i.e.* the forcing was evidently sufficiently weak and too far from the stronger eddy activity in the troposphere to trigger a response. But this doesn't prevent changes in the eddy activity associated with the stratospheric polar vortex. Fig. 3.10 shows the anomalous (forced - control) latitudinal divergence of the eddy momentum fluxes. Once again, the spatial pattern features a dipole pattern similar to the calculations shown describing the leading mode of variability shown in Figs. 3.5 and 3.7. More precisely, there is anomalous convergence equatorward of the polar night jet coincident with the eastward strengthening of the wind. Similarly, poleward of the jet, in regions where the wind has weakened, there is anomalous eddy momentum flux divergence. Once again, these characteristics are consistent with the eddy-zonal flow feedback ideas seen in the troposphere.

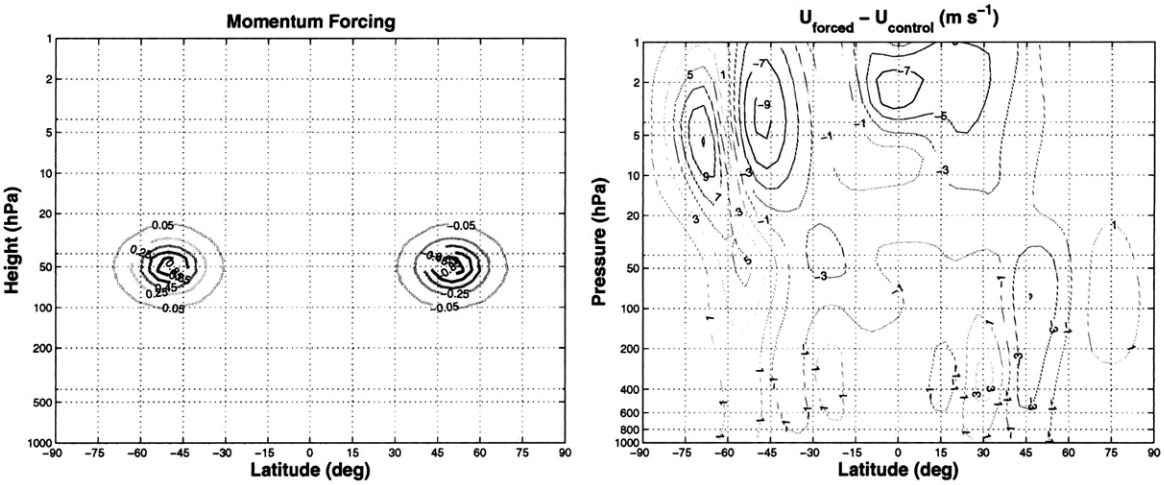

Figure 3.11: Same as Fig. 3.9 but with forcing centered at 50 hPa.

Having discussed a forcing in the upper stratosphere, the next will be presented at more intermediate level. The forcing shown in Fig. 3.11 has its center at the same latitude as Fig. 3.9, but near the lower stratosphere, at 50 hPa.

There are several points of interest. First, although virtually all the forcing is in the stratosphere, there is still a tropospheric response, albeit significantly weaker than the results from Polvani and Kushner (2002). The resemblance in the tropospheric spatial pattern to the annular modes seen in Figs. 3.5 and 3.7 appears to be consistent with theories of the eddy-zonal flow feedback ideas from Lorenz and Hartmann (2001). Through the stratospheric changes, an anomalous region of vertical shear in the stratosphere extends into the troposphere, providing an anomalous local source of baroclinicity. Owing to the curvature of the earth, there will be a net propagation of baroclinic activity equatorward of

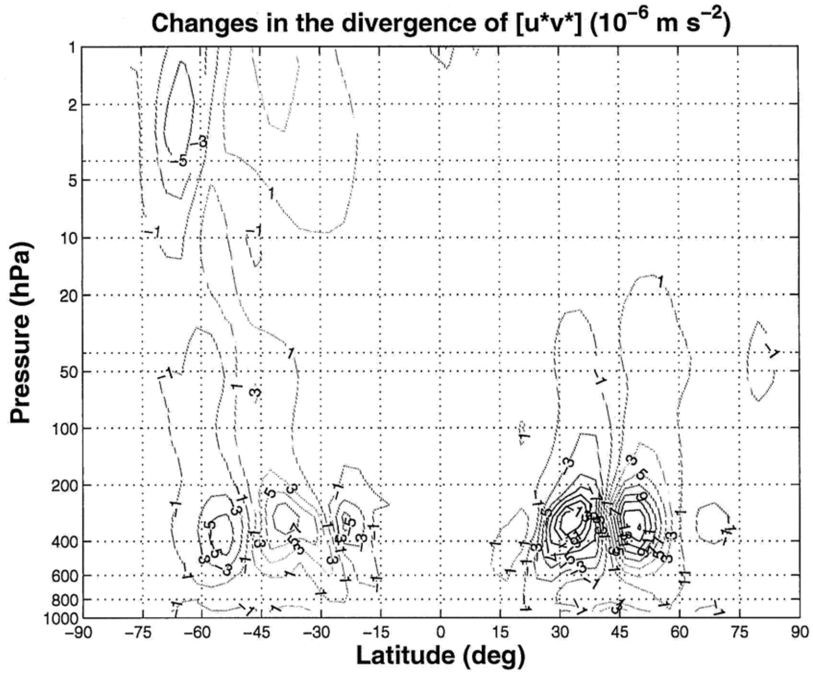

Figure 3.12: Same as Fig. 3.10 but with forcing centered at 50 hPa.

the jet, reinforcing and amplifying the anomalous vertical shear. Equatorward of this region, wave breaking will provide a westward torque and hence, the dipole structure seen in the mid-latitudes.

However, despite the variety of calculations performed in the last section, not one accurately predicted the response of both the troposphere and stratosphere. The closest one was Fig. 3.5d. Although the relative magnitudes were not representative of the response seen in Fig. 3.11, the poleward lobe of the tropospheric jet extending to the poleward side of the stratospheric polar vortex was representative of the structures calculated.

Secondly, there is a greater change in the tropospheric zonal-wind in the Northern Hemisphere than its southern counterpart, a surprising result since the winter hemisphere is associated with greater variability. But this is largely due to the timescale of the internal variability. The response depends not only on the projection of the forcing but also the e-folding time of the variability (cf. 1.4). Taking an autocorrelation of the principal component corresponding to Fig. 3.5a, the decorrelation time is 35 days. An analysis from the NH (not shown) shows that the timescale is 152 days. Since the internal variability of the leading mode in the NH is about 4 times bigger than the SH, assuming the projection of the forcing and the mode are identical between the two hemispheres, the response should also be larger by the same factor, consistent with the right plot of Fig. 3.11.

Thirdly, though the forcing was at the same latitude and also placed in the stratosphere, one might naïvely expect the same stratospheric signed dipole shown in Fig. 3.9. Instead, the stratospheric dipole pattern is of opposite sign (see Fig. 3.11). Consistent with the switching of sign, Fig. 3.12 reveals that the difference in the barotropic EP flux divergence has a similar dipole pattern as shown in the previous case (cf. Fig. 3.10), but here, the eddy momentum fluxes have organized in such a way that the barotropic component of the EP flux divergence is of opposite sign.

None of the statistical plots from the previous section would have accurately predicted the opposite sign except for the negative-lag regression plots shown in Figs. 3.8a-b. Only in those plots did the poleward tropospheric lobe extend to the poleward lobe of the stratosphere, reinforcing the argument made in the last section that Figs. 3.8a-b may be the most appropriate in detailing this stratosphere-troposphere coupling mode.

Note that unlike the previous case, there's a significant change in the tropospheric eddy activity. From this figure, we can infer that a change in the stratosphere ignited the tropospheric eddy feedback process responsible for the tripole pattern found in Fig. 3.12 and Fig. 3.11. This is consistent with the study of Song and Robinson (2004), who found that a momentum forcing in the stratosphere would induce a meridional overturning circulation, *e.g.* downward control, that extends partially into the troposphere. This would then project onto the annular modes, exciting the eddy-feedback producing the response shown in Fig. 3.11.

However, as discussed in section 1.2, Song and Robinson (2004) also found that planetary waves are needed to explain the tropospheric response. For completeness, we will show the eddy heat fluxes, which are largely dominated by the planetary waves in the stratosphere. Fig. 3.13a shows the time-average of this quantity in the control run (cf. Fig. 3.1). As expected, the source of the vertically propagating waves are generated near the surface, and the region of vertical propagation resides in both the troposphere and stratosphere.

Fig. 3.13b shows the changes in the eddy heat fluxes from the forcing that was centered at

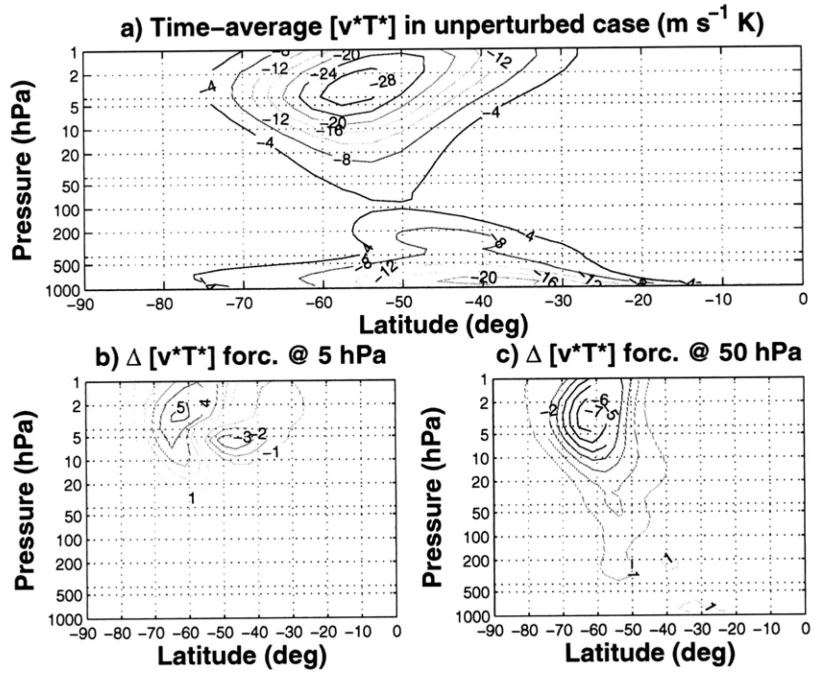

Figure 3.13: In (a), the eddy heat fluxes from the time-average of the unperturbed case. The climatological departure from (a) in the upper stratospheric momentum forcing case shown in Fig. 3.9 and (c) in the lower stratospheric momentum forcing case shown in Fig. 3.11.

5 hPa. Not surprisingly, the changes to the eddy heat fluxes are confined to the stratosphere only, consistent with the tropospheric response shown in Fig. 3.9. However, in the other case, interestingly, the *source* of the waves do not seem to have changed significantly (Fig. 3.13c), as one might expect given the tropospheric response. Instead, most of the changes in the eddy heat fluxes are centered in the mid- to upper- stratosphere decreasing towards the lower stratosphere and the upper troposphere. This would seem to suggest that there are more waves propagating away from the troposphere and into the stratosphere. This idea will be revisited in chapter 5.

3.3.2 Thermal perturbations

Instead of momentum forcings, in this section, we will alter the relaxation temperature profile, as performed by Polvani and Kushner (2002). The purpose of reproducing their work here is not only to review their findings, but also to motivate the results found in the next chapter.

Instead of having a cold polar stratospheric region, the equilibrium temperature profile has been perturbed in such a way that it is only a function of pressure, as shown in Fig. 3.14a. We will compare this to the equilibrium temperature profile from the control run, discussed in section 3.1 and shown again in Fig. 3.14b.

The resulting time-averaged zonal-mean zonal wind for no polar vortex and polar vortex cases are shown in Fig. 3.14c and Fig. 3.14d, respectively. As expected, with no temperature gradient in the equilibrium profile, the polar vortex has "turned off." The extratropical stratosphere in both hemispheres consists of either weak westerlies or easterlies. Besides the stratospheric changes, a comparison between Fig. 3.14c and Fig. 3.14d shows that the tropospheric circulation has changed. The tropospheric jet has shifted from approximately 43°S to 30°S, consistent with the work by Polvani and Kushner (2002).

To emphasize this last point further, Fig. 3.15a and Fig. 3.15b show the difference between the two experiments. Once again, the thermal perturbation is applied to the equilibrium temperature in the stratosphere only. This changes the climatological zonal-mean zonal winds. Note the monopolar forcing results in a monopolar change in the stratospheric

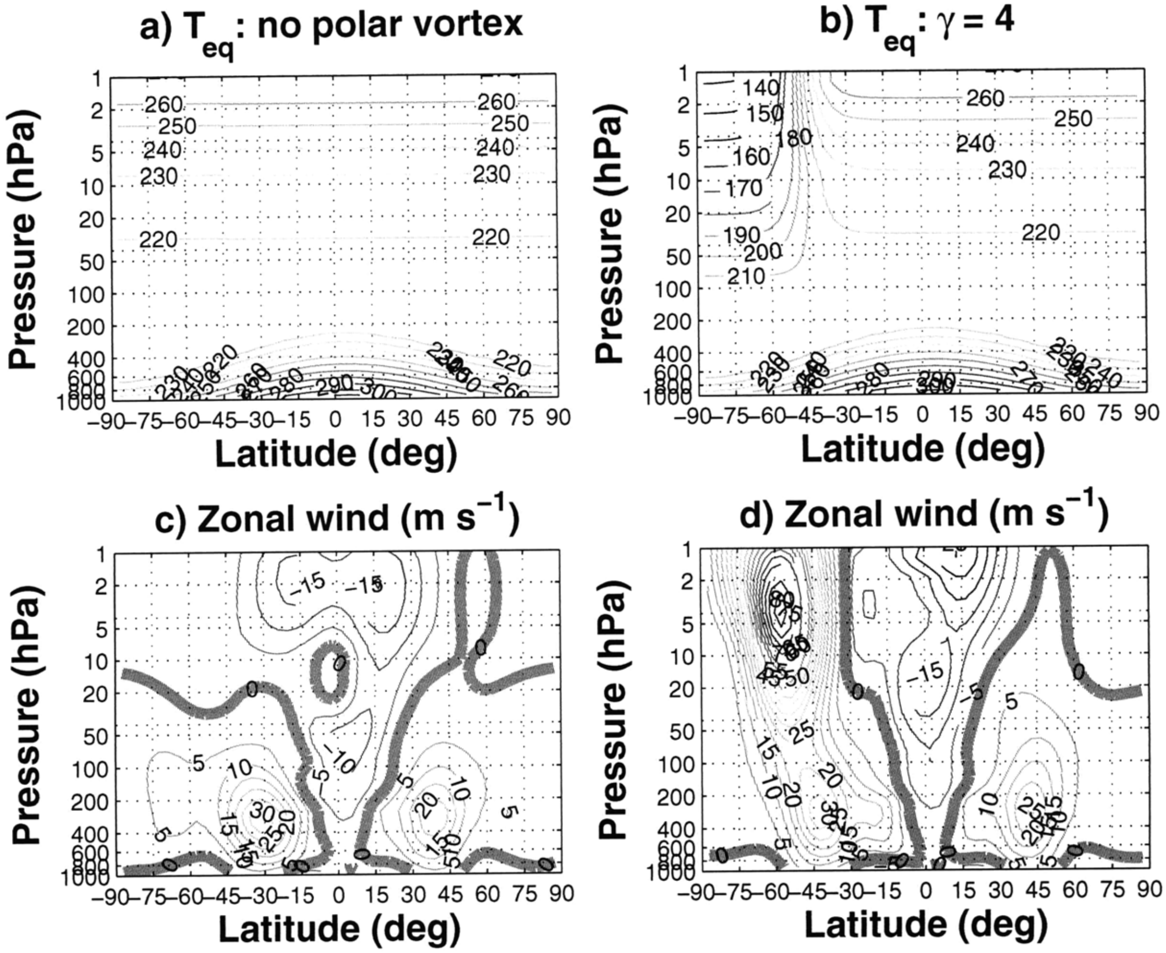

Figure 3.14: Equilibrium temperature profile for the (a) no polar vortex case and (b) $\gamma = 4$ case with a contour interval of 10 K. Climatological zonal-mean zonal wind for the (c) no polar vortex case and (d) $\gamma = 4$ case with a contour interval of 5 ms^{-1}. γ is an external adjustable parameter defined in (2.6)

zonal winds. However, in the troposphere, a different pattern emerges. The structure is reminiscent of the latitudinal "wobbling" of the tropospheric jet seen in observations (cf. Lorenz and Hartmann 2001). The most dramatic feature is shown in Fig. 3.15c. The peak of the surface westerlies shifted from 45°S to 32°S, even though imposed changes to the equilibrium temperatures were confined to the middle and upper stratosphere.

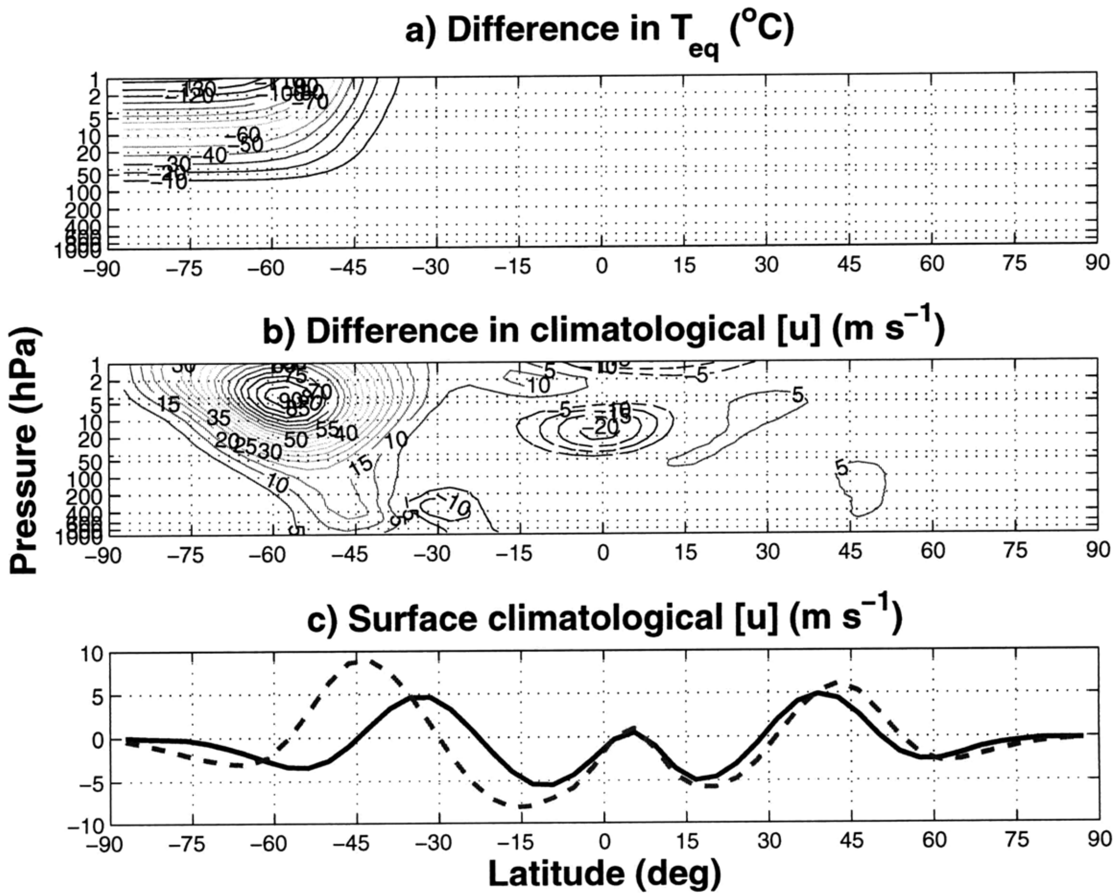

Figure 3.15: Difference plot of the (a) equilibrium temperature profile and (b) climatological zonal-mean zonal wind shown in Fig. 3.14. In (c), a comparison between the near-surface climatological zonal-wind for the two cases. Contour intervals for (a) are 10 K and (b) 5 ms^{-1} with the zero contour omitted.

3.4 Summary and discussion

In this chapter, we examined the climatology, the internal variability and the sensitivity to both momentum and thermal forcings of the strong polar vortex case in the Polvani and Kushner (2002) setup. The climatological stratospheric and tropospheric winds and the isolation of the polar vortex are all qualitatively representative of a Southern Hemisphere winter. We also showed that during the 12,000 day run that there were no major sudden warmings. This is not a suprising result since there is no topographical features to generate planetary waves, although if the model was run indefinitely longer, a sudden warming would eventually appear (cf. Kushner and Polvani (2005)).

Although there are no major sudden warmings, there is still variability in the stratosphere. The next section went into detail of the difficulties of generating an unambiguous picture of the leading mode of variability. Depending on the calculation method, various spatial patterns were generated. However, there were some gross features that appear to be robust: the annular modes in the troposphere and the dipole pattern in the stratosphere.

We then applied two momentum forcings in the stratosphere, one centered at 50 hPa and the other centered at 5 hPa. While there was virtually no tropospheric response to the applied upper stratospheric torque, the one in the lower stratosphere did result in changes. An analysis shows that the changes in the troposphere correspond to changes predominantly in the eddy momentum fluxes. Changes to the eddy heat fluxes were centered in the upper stratosphere, but did extend towards the upper troposphere.

The most dramatic example of the stratosphere affecting the troposphere was shown in the last section, as previously shown by Polvani and Kushner (2002). A thermal perturbation, localized in the stratosphere, is applied. Subsequently, the tropospheric jet shifted from 43°S to 30°S. In all of these experiments, even in this case where the stratospheric changes in the zonal-mean zonal wind were monopolar, the changes in the troposphere exhibited an annular mode response. However, we will in the next chapter that the strong response was a result of the tropospheric state residing between two regimes.

This suggests that the tropospheric response is mainly due to the eddy feedback processes, as suggested by previous work (*e.g.* Lorenz and Hartmann 2001, Song and Robinson 2004, and Ring and Plumb 2007). However, unlike these previous studies, the response from Fig. 3.11 had a different spatial structure than what the leading EOF indicated. Although the changes in the troposphere represented the typical annular mode response, and similarly, the dipole response of the stratospheric variability was similar to the EOF analysis from Figs. 3.5 and 3.5), the relationship between the two differed. From these calculations, an *equatorward* shift of the stratospheric polar vortex was correlated with a poleward shift of the mid-latitude jet. But the momentum forcing shown in Fig. 3.11 instead it is a *poleward* shift in the stratospheric vortex that is correlated with a poleward shift in the tropospheric eddy-driven jet.

Since an EOF analysis does not take into account the time-lag between the changes in the stratosphere and the presumed affects on the troposphere, a lag of the surface AMI is regressed onto the zonal-mean zonal wind data. If there is such a delay in the surface response, we can adjust the AMI to *precede* $[u]$. From Fig. 3.6, a lag of -40 and -20 days seem reasonable in describing the delay between the strongest stratospheric variability and the largest tropospheric response. Using these values, Fig. 3.8 shows a spatial structure reminiscent to the response from Fig. 3.11. A poleward shift in the mid-latitude jet corresponds with a poleward shift in the stratospheric vortex.

Using this lag-lead regression analysis has two main advantages: (1) a choice in the vertical weighting is avoided and (2) the time-lag between the strongest stratospheric and tropospheric signal is taken into account. Results from the response from our momentum forcing also suggests that the traditional EOF calculation may not be best at describing the leading mode of variability when the stratosphere and troposphere is coupled. Thus, in the absence of knowing the "correct" analysis, the work from these previous authors, suggesting the spatial structure of the internal variability to be the shape of the response may not be the right approach. Therefore, the focus will be on a more dynamical framework in understanding these changes, which will be discussed further in Chapter 5.

Chapter 4

Response to stratospheric forcing and its dependence on the state of the troposphere

The thermal forcing results presented in the last section and by Polvani and Kushner (2002), hereinafter referenced as PK, are especially dramatic: they found a large poleward shift (of about 10° latitude) and intensification (by almost 5 $m\ s^{-1}$) of the surface wind maximum in the southern (winter-like) hemisphere of a simplified GCM in response to imposed perturbations in the stratospheric equilibrium temperatures. However, as emphasized by Gerber and Polvani (2009) and as will be discussed further here, in the particular cases of PK, the decorrelation time of the model's leading annular mode is extremely long (200-500 days), compared with 10-20 days that characterize the observed annular modes in the atmosphere (Feldstein 2000). Simplified GCMs without topography typically produce decorrelation times several times larger than those observed (Gerber and Vallis 2007; Gerber and Polvani 2009), but those in the PK cases are long even by the standards of such models. One consequence of unrealistically long decorrelation times is that the fluctuation-dissipation theorem (discussed in Section 1.4) predicts unrealistically strong responses to external forcings.

In the next two sections, we will explore the reason for these extremely long decorrelation time scales and illustrate that the anomalous nature of the sensitivity of the climatological

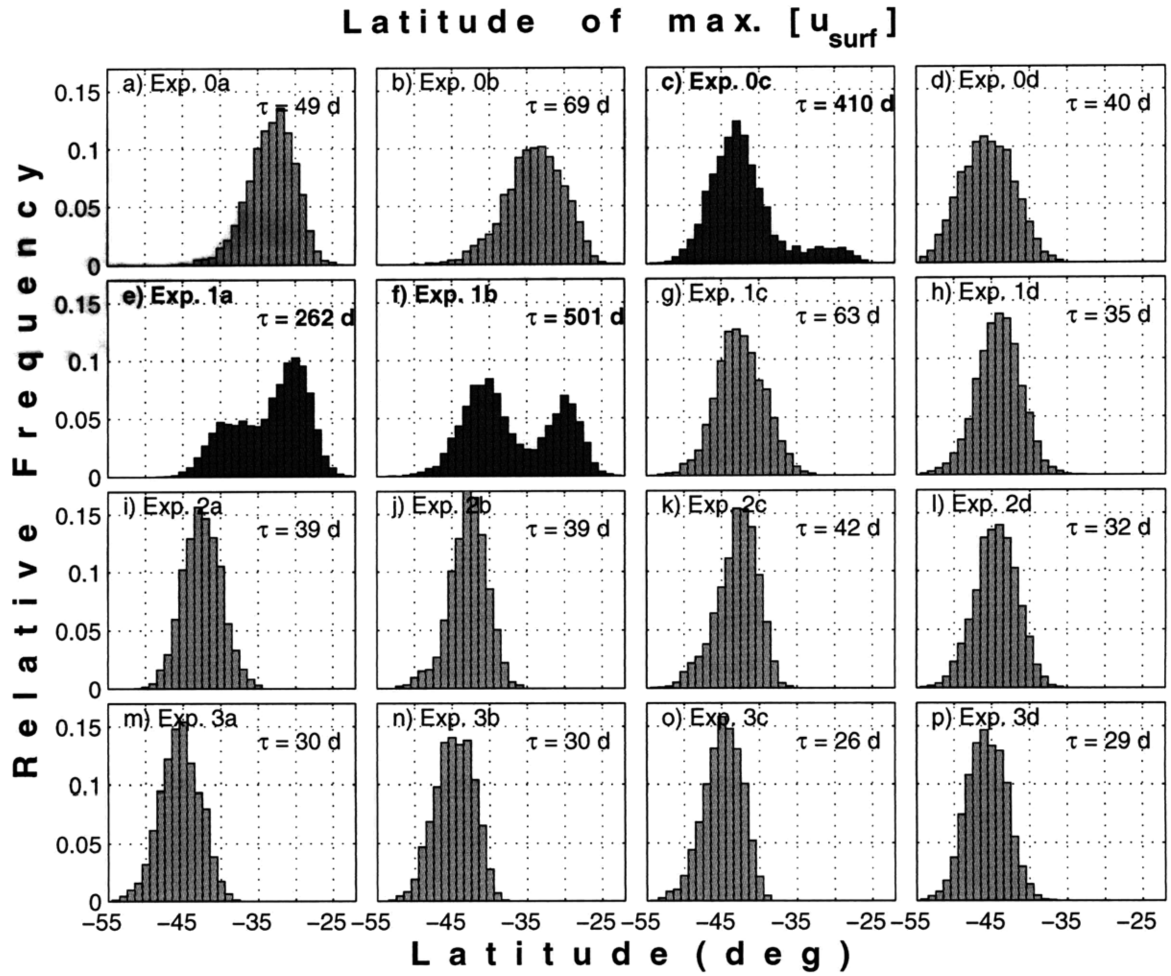

Figure 4.1: A relative histogram of the latitudinal location of the maximum daily-averaged near-surface zonally-averaged zonal winds for all model runs listed in Table 4.1. Histograms in bold are model runs where the decorrelation time for the leading principal component is greater than 200 days. Within each column, the same stratospheric equilibrium temperature profile is used, with polar vortex intensities (γ) increasing to the right. Within each row, the same tropospheric equilibrium temperature profile is used, with the magnitude of the equator to pole temperature difference increasing downward. Adapted from Chan and Plumb (2009). The second row are for the experiments from Polvani and Kushner (2002).

state in PK by investigating how the response to perturbed stratospheric equilibrium temperatures depends on the climatological state of the troposphere. Following PK, we define an equilibrium temperature (T_e) distribution in the troposphere like that of Held and Suarez (1994), but vary a single parameter to shift the latitude of the peak T_e between the equator and the summer subtropics. One such state is identical to that of PK. We show that the decorrelation time of the leading annular mode in the model's winter hemisphere is particularly long for this state. Modest changes in either direction of this tropospheric parameter reduce the decorrelation time considerably. Consequently, the response to changes in stratospheric T_e become much weaker than that found by PK. These results complement those of Gerber and Polvani (2009), who found the PK state and its annular mode decorrelation times to be very sensitive to model resolution. The long decorrelation time of the PK cases is a reflection of the fact that their tropospheric climatology sits at a transition at which the eddy-driven jet separates from the subtropical jet.

In the context of fluctuation-dissipation theorem, a discussion will follow in Section 4.2.3. In the final section, we will provide additional experiments to emphasize further how changes in the stratosphere and its affect on the troposphere is dependent upon the tropospheric state. In these cases, instead of changing the equilibrium temperature, changes to the topographic profile will be made. We will show that the response of the stratospheric forcing is dependent on not only the affects of the topography on the stratosphere, but also its affect on the tropospheric climatology. In this particular model, we will see that the strong response occurs only in a particular "window" of this climatology.

4.1 Dual regime behavior

As discussed in Section 3.1, one of the discrepancies between this model and what's found in observations is the location of the maximum winds in the upper troposphere during the winter months. We discussed how this difference could be a result of not capturing the right proportionality between the strength of the subtropical and eddy-driven jets. Perhaps due to the model's shortcomings in modeling tropical processes important to the maintenance of the subtropical jet, the leading mode of variability describes a "switching" in the location of the eddy-driven jet between the subtropics and in mid-latitudes.

This dual regime behavior can best be seen by producing a relative histogram of the location of the eddy-driven jet. Using the peak surface westerlies as a proxy (cf. Vallis 2006), Fig. 4.1 shows the relative frequency for the latitudinal location. Fig. 4.1h is for the control run where γ=4 (the strong polar vortex case.)

When the polar vortex decreases in strength, results from the last section and PK describe an equatorward shift of the jet. However, Fig. 4.1e-g suggest those tropospheric changes are not as straightforward. Instead of a systematic equatorward progression as the polar vortex case is reduced, the eddy-driven jet is actually switching to a different preferred region.

This emergence of the eddy-driven jet's preference around 30°S suggests there are dual regimes. This claim is further supported by looking at the timeseries of the relative angular momentum anomalies at 300 hPa (Fig. 4.2a) for the "no vortex" case. Notice the particular phase lasts for hundreds of days and then switches sign for a period of another hundred days.

4.2 Supplemental experiments with changes to tropospheric equilibrium temperatures

4.2.1 Setup

The leading mode of variability in observations do not indicate the eddy-driven jet switching between the subtropics and the mid-latitudes, nor the bimodal distribution for the meridional location of the surface westerlies, as indicated in Figs. 4.1e and 4.1f. The situation changes markedly when the tropospheric state is altered by changing the factor ϵ (see (2.3)). Combining the changes of both the tropospheric and stratospheric equilibrium temperature profiles, Table 4.1 describes the systematic changes to each experiment and the integrated number of days.

Runs 1a-d with $\epsilon = -10K$ are identical to those of PK, and the weak vortex cases 1a, 1b, are noteworthy for their very long decorrelation times (see Figs. 4.1e and 4.1f). In series 2 and 3, the tropospheric T_e maximum is shifted poleward of that in the cases of PK. For comparison with our other cases, the climatological zonal-mean zonal winds for runs

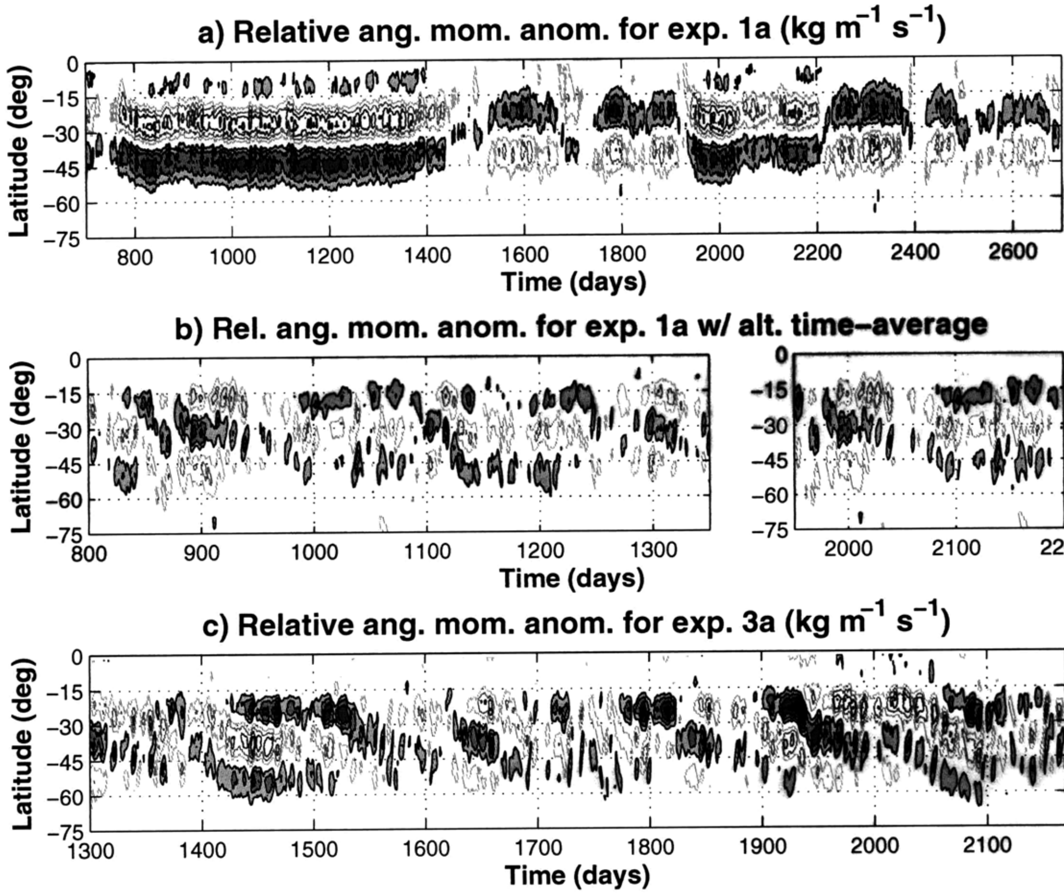

Figure 4.2: Timeseries of the relative angular momentum anomalies at P = 925 *mb*. The anomalies were subtracted from a time- mean, which included the entire dataset for a) exp. 1a and c) exp. 3a. (b) Departures from the time-mean of 1a, calculated by the time segment shown in the plot's abscissa. Filled (line) contours denote positive (negative) values and the zero contour has been omitted. (b) and (c) have the same contour intervals and are one-half of those in (a).

Exp.	Seasonal asy. (ϵ)	Polar Vortex (γ)	Run Dur. (days)
0a	0	No Vortex	5000
0b	0	$\gamma = 2$	5000
0c	0	$\gamma = 3$	10000
0d	0	$\gamma = 4$	5000
1a	-10	No Vortex	8000
1b	-10	$\gamma = 2$	10000
1c	-10	$\gamma = 3$	5000
1d	-10	$\gamma = 4$	8000
2a	-20	No Vortex	5000
2b	-20	$\gamma = 2$	4000
2c	-20	$\gamma = 3$	4000
2d	-20	$\gamma = 4$	5000
3a	-30	No Vortex	4000
3b	-30	$\gamma = 2$	4000
3d	-30	$\gamma = 3$	4000
3d	-30	$\gamma = 4$	4000

Table 4.1: List of model experiments. ϵ and γ terms are external parameters and are defined in (2.3) and (2.6).

1a,1b and 1d are shown in Figs. 4.3a-c. The large impact reported by PK of the strong vortex case 1d (with $\gamma = 4\ K/km$) onto the mean zonal winds is highlighted in Fig. 4.3d. In particular, this illustrates the annular-mode nature of the tropospheric response, as explicitly

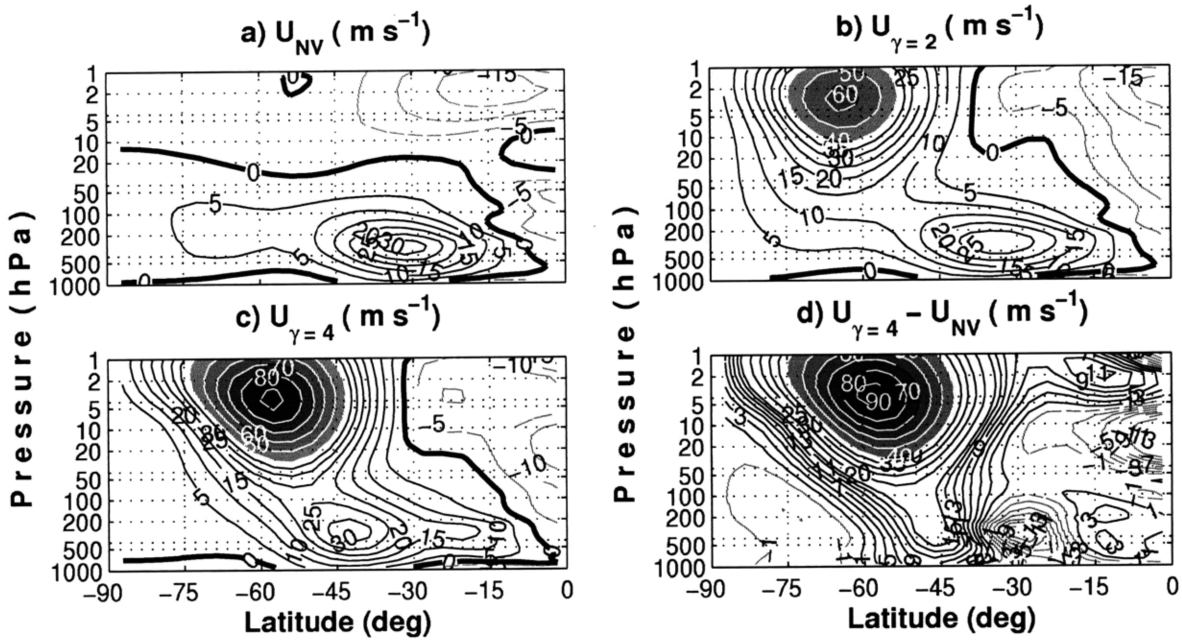

Figure 4.3: (a)-(c) Climatological zonally-averaged zonal winds for experiment 1a-1c. (d) Difference between (c) and (a). Values greater than 40 m s^{-1} are shaded.

demonstrated by PK.

Inspection of Figs. 4.3a-c reveals a change in the time-mean tropospheric jet, from a deep single jet centered near 35°S to a double structure comprising a deep jet near 45° with an almost-separated subtropical jet in the upper troposphere near 25°. In fact, the time-mean picture in the weak vortex cases 1a,b is rather misleading. Again, Fig. 4.1e-h shows a relative histogram of the latitudinal location of the maximum daily-averaged near-surface zonal-mean zonal winds for run 1a-d; the near bimodal distribution in case 1a reveals that in reality the eddy-driven surface wind maximum is fluctuating between locations at 30° and 40°. Case 1b brings out this dual regime behavior more clearly (Fig. 4.1f). There is in fact a minimum at the location of the time-mean jet. Thus, as discussed in Gerber and Polvani (2009), in the PK cases with a stratospheric weak vortex, the eddy-driven jet in the troposphere is actually teetering between two states. In one state, the eddy-driven jet merges with the subtropical jet, while in the other, the two are well separated.

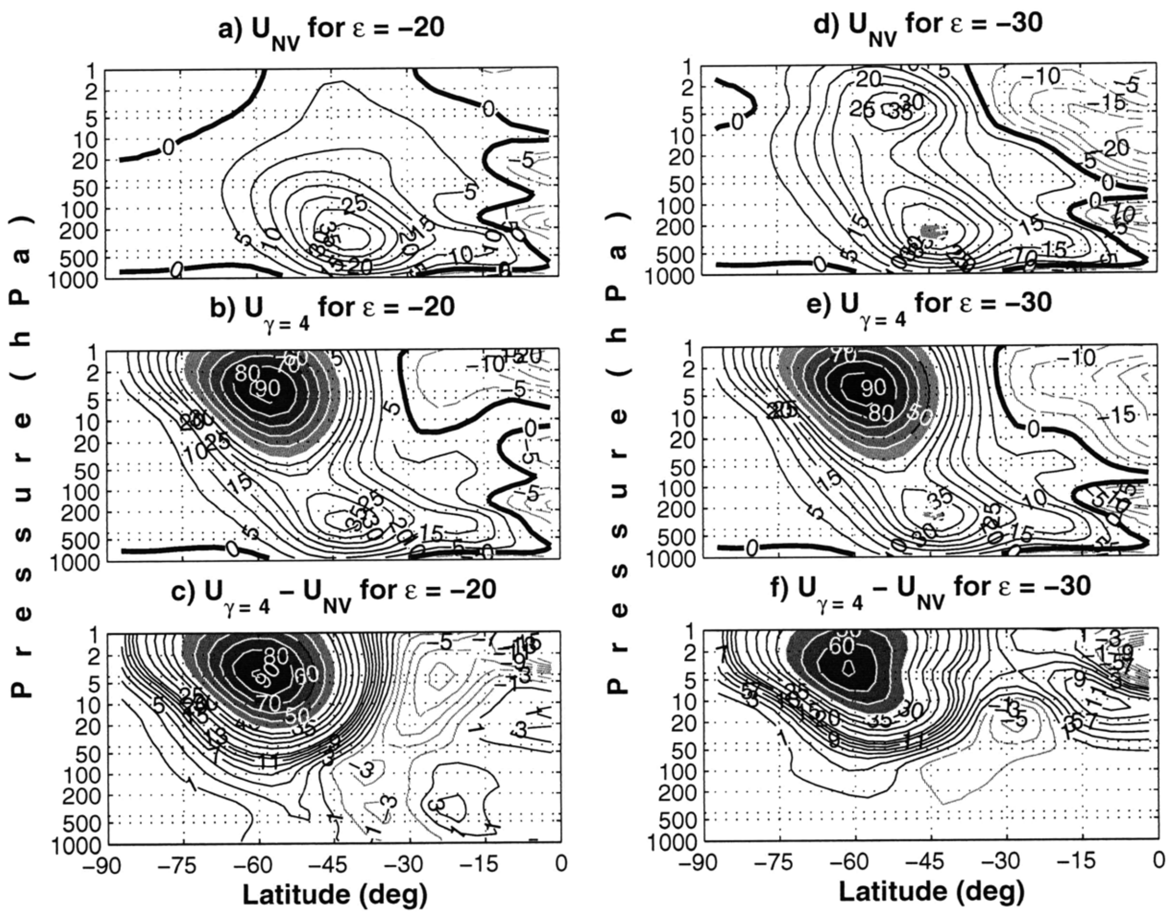

Figure 4.4: Climatological zonally-averaged zonal winds for (a) exp. 2a (b) exp 2b. (d) exp. 3a and (e) exp 3b. The difference between (b) and (a) is shown (c) and between (e) and (d) is shown in (f). For (a), (b), (d) and (e), contours are labelled every 5 m s^{-1}, the zero contour is thickened and values greater than 40 m s^{-1} are filled. For (c) and (f), values less than 20 m s-1 are contoured every 2 m s^{-1}, values between 20 m s^{-1} and 40 m s^{-1} are labelled every 5 m s^{-1}, values greater than 40 m s^{-1} are filled and contoured every 10 m s^{-1} and negative values are gray and dashed.

4.2.2 Results

Time-averaged zonal-mean zonal winds for the "no vortex" runs 2a and 3a, and the corresponding "strong vortex" runs 2d and 3d are shown in Fig. 4.4a-b and Fig. 4.4d-e. In each case, the tropospheric eddy-driven and subtropical jets are well separated in the time mean; in each case, the "teetering" behavior of runs 1a,b is absent, and the decorrelation time of the leading fluctuating mode is considerably shorter (see Fig 4.1i-j and 4.1m-n).

The contrasting behavior of the fluctuations in the near-surface tropospheric zonal flow is illustrated for the "no vortex" runs 1a ($\epsilon = -10\ K\ /\ km$) and 3a ($\epsilon = -30\ K\ /\ km$) in Fig. 4.2a and Fig. 4.2c, respectively. The long persistence of each of the two regimes evident in the location of the eddy-driven jet in case 1a contrasts with the more rapid (note the different time scales on the two plots), weaker, and occasionally poleward-propagating fluctuations in case 3a, similar to the cases found in an observational study by Feldstein (1998).

In fact, case 1a also shows more rapid fluctuations like those of case 3a, but these are masked in Fig. 4.2a by the larger long-lived anomalies. This is shown in Fig. 4.2b, whose anomalies are calculated from individual periods of run 1a when the surface jet is in its poleward position. Within this regime, a comparison with Fig. 4.2c shows the jet displays fluctuations similar in magnitude and time scale to those of run 3a. Thus, the persistent regimes seen in the PK case 1a do not replace the more rapid variations, but rather co-exist with them, and from this viewpoint, they constitute an additional mode of variability.

The impact on the time-mean zonal winds of changing the specification of stratospheric T_e "no vortex" to "strong vortex" for the cases with $\epsilon = -20\ K$ and $-30\ K$ is shown in Fig. 4.4c and 4.4f respectively. While in each case the changes to the stratospheric jet are comparable to the PK cases with $\epsilon = -10\ K$, the tropospheric impact is much weaker. This is made explicit in the comparison shown in Fig. 4.5b-d, showing the response of the surface zonal winds to the altered stratosphere for the three tropospheric states, and suggesting that the strong response found in PK is anomalous.

Although both experiments 2a and 3a were performed with a stratospheric relaxation profile that is isothermal in pressure, Fig. 4.4a and 4.4d exhibit westerlies in the stratosphere.

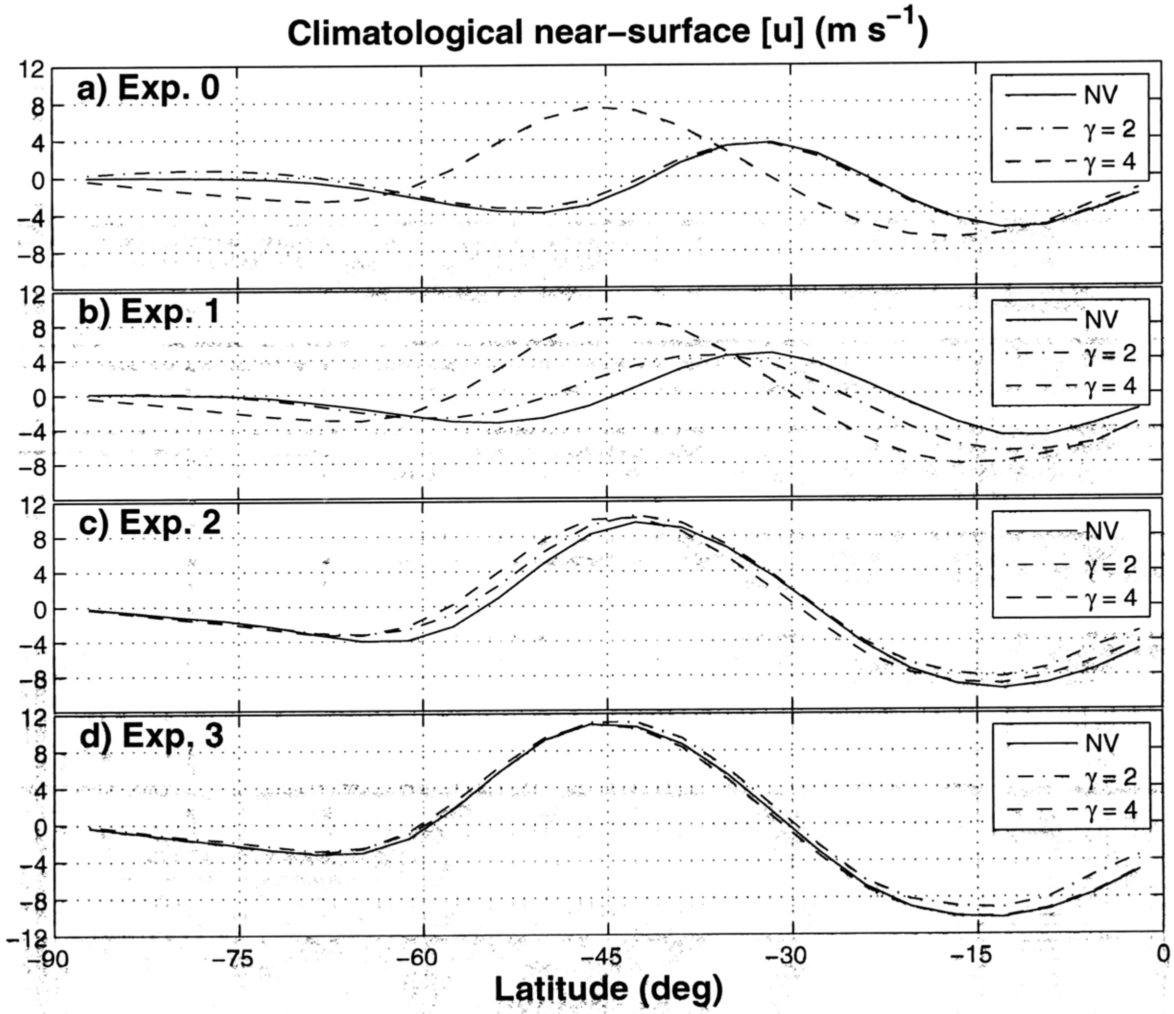

Figure 4.5: Climatological near-surface zonal-mean zonal winds for a) exp. 0, b) exp. 1, c) exp. 2. and d) exp. 3.

Further tests using T42 and T60 resolution exhibit the same property. We suggest the following as the reason for this behavior. As the magnitude of ϵ increases, the meridional temperature gradient increases, and hence the maximum tropospheric mid-latitude winds increase as well, as shown by comparing Figs. 4.3a, Fig. 4.4a and Fig. 4.4d. However, there is not enough compensating wave drag above the jet in exp. 2a and 3a (not shown) to reduce the increased vertical shear, allowing the mid-latitude winds to be more barotropic. In the extreme case of experiment 3a, with insufficient wave damping above the tropospheric jet and a meridional stratospheric equilibrium temperature gradient equal to zero, to a first-order approximation, the winds turn nearly barotropic throughout the lower two-thirds of the extra-tropical stratosphere. The reason for the insufficient wave drag above the jet appears to be related to the poleward jet position and an increase in meridional wave propagation (not shown). (Note that as $|\epsilon|$ increases, the jet shifts poleward, as shown in Fig. 4.5). As a result, the ratio between the wave drag above the jet and equatorward of jet decreases. Although the lack of wave drag can explain the westerlies in the stratosphere, this process does not explain the localized maximum wind speed at about 5 mb for exp. 3a. Since this particular characteristic does not affect our main results and appears to be resolution dependent (does not happen in our T42 and T60 cases), this property will not be discussed further. In any case, as the magnitude of ϵ increases, there does appear to be a robust propensity for the mid-latitude winds to be more barotropic (and hence stratospheric westerlies) above the jet, but a more thorough explanation is beyond the scope of this study.

Other simple models have demonstrated that gradually changing a single parameter (e.g. increasing the diabatic heating in the tropics) can change the location of peak eddy activity from one latitude to another (e.g. Lee and Kim (2003)). Consistent with Gerber and Polvani (2009), the evidence presented here is that this system is actually "teetering" between these two states. This is clearly demonstrated in Fig. 4.1f by the bimodal distribution of the eddy-driven jet's distribution in exp. 1b.

To demonstrate fully that $\epsilon = -10K$ lies in between two regimes, we perform an additional experiment with $\epsilon = 0K$ thus placing the tropospheric T_e maximum equatorward of that of the PK case. As shown in Fig. 4.1a, the distribution of the eddy-driven jet's location is unimodal and is unambiguously located either in the subtropics or in the mid-latitudes in case 3a and 0a respectively. A comparison with Fig. 4.1e shows that the control case of the PK setup indeed sat in between these two states.

There are other examples in the atmosphere that exhibit "regime behavior". For instance, using a primitive equation model, Akahori and Yoden (1997) showed that it was possible for there to be a bimodality in the frequency distribution of the eddy life cycle index. Using a weak surface drag value, the zonal-mean jet was located in high-latitudes and the life cycle of baroclinic eddies are predominantly characterized by anticyclonic breaking. Conversely, using a high drag value, the tropospheric jet shifts to the low latitudes with eddies being characterized by cyclonic breaking. But for an intermediate surface drag value, there was a bimodality in the frequency distribution function of this eddy life cycle index. In an observational example, Christiansen (2009) noted the bimodality in the winter stratospheric circulation: either strong or weak polar vortex winds existed, seldomly something in between.

We speculate the physical reasoning for this particular "regime behavior" and its associated long decorrelation has to do with this eddy-driven jet's preference for the two distinctly separate locations. Using the dynamical core of the GFDL GCM, Lee and Kim (2003) have shown that the location of the eddy-driven jet could exist in either region depending on the location of the greatest instability. In one regime, imposing sufficiently strong equatorial diabatic heating, the subtropical jet intensifies to the point where the strongest hemispheric baroclinicity resides in this region, and subsequently constrains the eddy-driven jet's location within the subtropics. However, with weak equatorial diabatic heating, the greatest instability would then be associated with the model's imposed equilibrium temperature, whose meridional gradient maximizes in mid-latitudes, resulting in the eddies organizing their activity in this region.

In the PK setup, we thus speculate that the instability in mid-latitudes and the subtropics are comparable in magnitude, teetering between these two regimes. If one region is slightly more unstable than the other, then this region is likely to be co-located with the greatest hemispheric baroclinic activity. However, at some point, when the eddy heat fluxes are sufficiently strong at reducing the local temperature gradient, the greatest baroclinic activity would then be reorganized from the subtropics to the mid-latitudes or *vice versa*. Such a transitional state would have characteristics of two separate regimes.

4.2.3 Applicability to Fluctuation Dissipation Theorem

Why does the tropospheric response differ so much between experiments? According to the fluctuation-dissipation theorem (FDT), the linear response to an imposed forcing is proportional to the projection of that forcing onto the system's natural modes of variability and to the decorrelation time associated with that mode, according to an equation of the form:

$$(Response \bullet mode) \sim decorrelation \times (forcing \bullet mode) \tag{4.1}$$

Although this equation has not been shown to be quantitatively precise in a simple GCM, the qualitative nature has been shown to be accurate (e.g. Ring and Plumb 2007, 2008; Gerber et al. 2008).

An obvious difference between the no vortex cases (experiments 2a and 3a with 1a) is the location of the jet. The change in the stratospheric equilibrium temperature profile resulted in the tropospheric jet shifting to the mid-latitudes. An important consideration is how that changed the stratospheric thermal forcing's projection onto the leading mode of variability. Presumably, with the change of the jet location, the mode structure will change as well. There is then the possibility that the inner product of the two decreased noticeably, and hence, could explain the significantly weaker response. Thus, we first determine whether the weak response can be explained by the poor projection of the forcing onto the mode. To determine the mode of variability for these thermally forced cases, we perform a similar analysis as that of Ring and Plumb (2008). First, the covariance of the zonal wind and temperature anomalies is obtained. Then, through singular value decomposition (SVD), we determine the leading pattern of the temperature variability. Fig. 4.6 shows a comparison between experiments 1 and 3 for the leading mode and the applied forcings. Note the perturbation is the same for both cases. As shown in Table 4.2, the forcing doesn't project less onto the leading mode, but instead the projection is actually greater in the ϵ = -30 case.

With the projection of the forcing onto the mode being larger, (4.1) suggests that a weaker response must be associated with a shorter decorrelation time. Indeed, as shown in the upper right corners of Fig. 4.1, the decorrelation time of experiment 3a is nearly ten

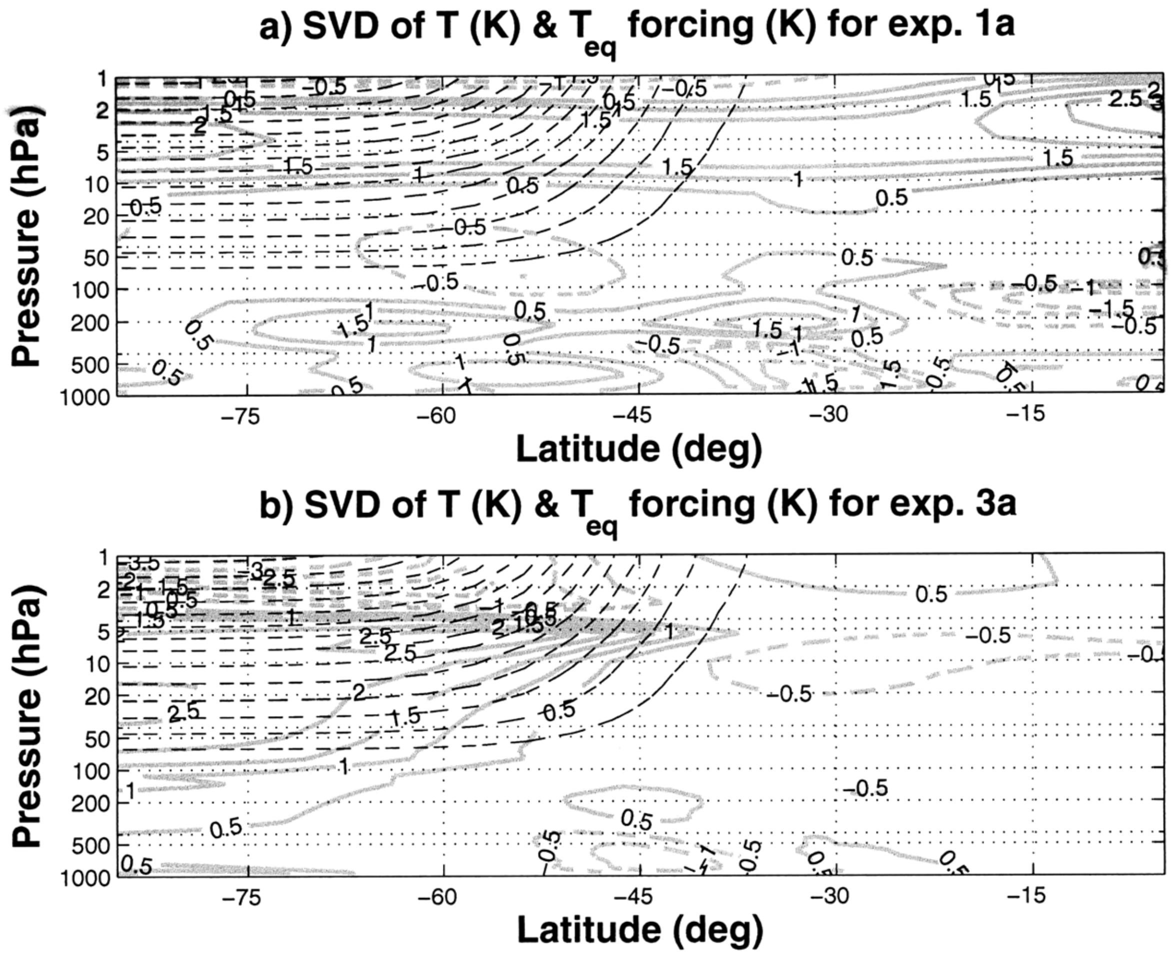

Figure 4.6: Leading spatial pattern of temperature anomalies (thick contours) and the thermal forcing (thin dashed countours) for exp. 1a (top) and for exp 3a (bottom). The thick contours were derived from the SVD of the covariance matrix between $[u]$ and $[T]$. The contour interval for the thermal forcing is 10 K.

times smaller than that of experiment 1a. Thus, in these experiments, the magnitude of the tropospheric response is controlled by the model's time scale of internal variability.

The dependence on the decorrelation time provides an explanation of the nonlinearity of the surface wind response found by PK to changing the parameter γ (their Fig. 2) and our Exp. 0 (Fig. 6a). As (3) makes clear, linearization of the response/forcing relationship about a basic state presumes that the characteristics of a mode - in particular, the modal structure and its decorrelation time- remain essentially unchanged by the perturbation. As Fig. 4.1 makes clear, in cases 2 and 3, the decorrelation time changes little under perturbations, but in case 1a and 1b, it is sensitive to the parameter γ, being especially large near $\gamma = 2$ and $\gamma = 3$ in case 0c- when the system is "on the edge" of switching from one jet location to the other – in which case (3) predicts nonlinearity in the response with the greatest sensitivity near $\gamma = 2$, as PK found.

Exp.	Forcing • mode (K)	Response • mode (K)
1	19	1117
3	54	1034

Table 4.2: Projection Calculations. The mode was calculated by first taking the covariance of the zonally-averaged temperature and the zonal-mean zonal wind anomalies. Then we take the leading non-dimensional SVD pattern and project both the forcing and the response. The forcing is defined to be the difference in the equilibrium temperature between the no vortex case and $\gamma = 4$. The response is defined to be the difference in the climatological zonal-mean zonal winds. Series 1 and 3 are described in Table 4.1.

4.2.4 Summary

In this section, we have demonstrated the sensitivity of the results obtained by Polvani and Kushner (2002) to the tropospheric state. As Fig. 4.1 makes clear, long decorrelation times are found to be in the cases when the latitudinal preference for the eddy-driven jet teetered between: (1) coexisting with or (2) being well separated from the subtropical jet. Modest changes to the tropospheric state removed this behavior and significantly reduced the decorrelation time to a more realistic value (from 250 days to 30 days). Consequently, the response to an identical forcing was much weaker than that found by PK (compare Fig. 4.3d with Fig. 4.4f). Consistent with fluctuation-dissipation theorem (FDT) and Gerber et al. (2008), the decorrelation time associated with the internal variability is equally as important as how the forcing projects onto the mode.

Previous work have shown that, qualitatively, FDT is a simple and effective way to predict climatological changes when tropospheric forcings have been prescribed (e.g. Ring and Plumb 2007, 2008; Gerber et al. (2008)). Using this framework, we have shown that FDT can also be used in a stratosphere-troposphere system where stratospheric forcings can be used to predict the qualitative response. Unfortunately, similar to those previous studies, we find that the quantitative accuracy of the FDT is limited. One of the issues in applying the FDT is the appropriate definition of the "modes" of the unforced system. Ring and Plumb (2008) argued for the use of principal oscillation patterns (POPs) rather than EOFs, to define the leading modes but, in their mostly tropospheric model, they found little difference between the structures of the leading POPs and EOFs. A model that includes the stratosphere, however, is likely to be more problematic, as the vertical structure of the leading EOFs is sensitive to how the covariances are weighted when calculating the EOFs. In this paper, we have followed Thompson and Wallace (2000) in defining how the vertical structure is weighted; we regard it as unlikely that our main conclusions here are unduly sensitive to this choice.

4.3 Supplemental experiments with changes to topographic profile

4.3.1 Setup

We have primarily followed the setup of Polvani and Kushner (2002) thus far. However, in their study, as well as Song and Robinson (2004), they have implicated the importance of planetary-scale waves in the stratospheric / tropospheric coupling, but yet neither models incorporated topography, a vital mechanism in generating wavenumbers 1 and 2 of sufficient magnitude as those seen in observations. Therefore, to supplement some of our results, we have added gaussian-shaped topographical profiles in the winter hemisphere.

The thermodynamic equilibrium profile used is identical to the ones studied in Chapter 3. More specifically, ϵ=-10 K and γ = 4 K/km, or equivalently, the strong vortex case of Polvani and Kushner (2002). Here, the only difference is the topographical profile.

As shown in Table 4.3, six "mountain" shapes were used. More specifically, variations to the height of the peak, the latitudinal location, the latitudinal and longitudinal widths were considered. The following equation is used to define the shape of the topography.

$$z_{surf} = ht \cdot exp\left[\left(\frac{max[0,(|\phi-\phi_0|-r_\phi)]}{w_\phi}\right)^2 - \left(\frac{max[0,(|\theta-\theta_0|-r_\theta)]}{w_\theta}\right)^2\right] \tag{4.2}$$

Although these external changes do not initially appear to be systematic, they can be grossly categorized into three categories: (1) "tall" mountains centered in the mid-latitudes, (2) "moderate" mountains centered in the mid-latitudes and (3) mountains centered in the sub-polar region.

As we will see, three different climatologies will exist and subsequently, three different behaviors, as seen by compositing the annular mode indices for weak vortex events (e.g. Fig. 3.6), will be shown.

4.3.2 Results

The first group of experiments have the highest topographies centered in the mid-latitudes. As shown in Fig. 4.7, the shape of the topography is primarily confined to the southern hemisphere with the ridge extending throughout the mid-latitudes. The W-E component of the mountain is mainly limited to 60 degrees of longitude.

The resulting climatological zonal-mean zonal wind is shown in the color shading of Fig. 4.8a. Unlike the cases presented in Chapter 3 where there was a flat topographical profile, the location of the tropospheric jet is no longer in the mid-latitudes, but instead shifted to

Exp. Name	γ (K/km)	ϵ (K)	$\phi_0(^\circ)$	$w_\phi(^\circ)$	$r_\phi(^\circ)$	$w_\theta(^\circ)$	$r_\theta(^\circ)$	ht. (m)
mt1	4	-10	-45	20	10	20	0	4500
mt2	4	-10	-45	8	0	70	0	4500
mt3	4	-10	-45	8	0	70	0	3500
mt4	4	-10	-45,-45	8,8	0	35,35	0	3000,3000
mt5	4	-10	-60	8	0	20	0	4000
mt6	4	-10	-70	20	0	60	0	4500

Table 4.3: Topographical setups. γ governs the stratospheric equilibrium polar temperature profile (see 2.6). ϵ controls the tropospheric equilibrium temperature profile (see 2.2). All other variables describe topographical profile driven by (4.2). ϕ_0 describes the center of the surface peak in the latitudinal direction. w_ϕ describes the half-width in the latitudinal direction. r_ϕ is the width of the latitudinal ridge. w_θ controls the half-width in the longitudinal direction. r_θ describes the ridge in the longitudinal direction. Ht. is the peak height. All trials contained only one mountain except for $mt4$, which had two mountains centered at $90^\circ E$ and $270^\circ E$.

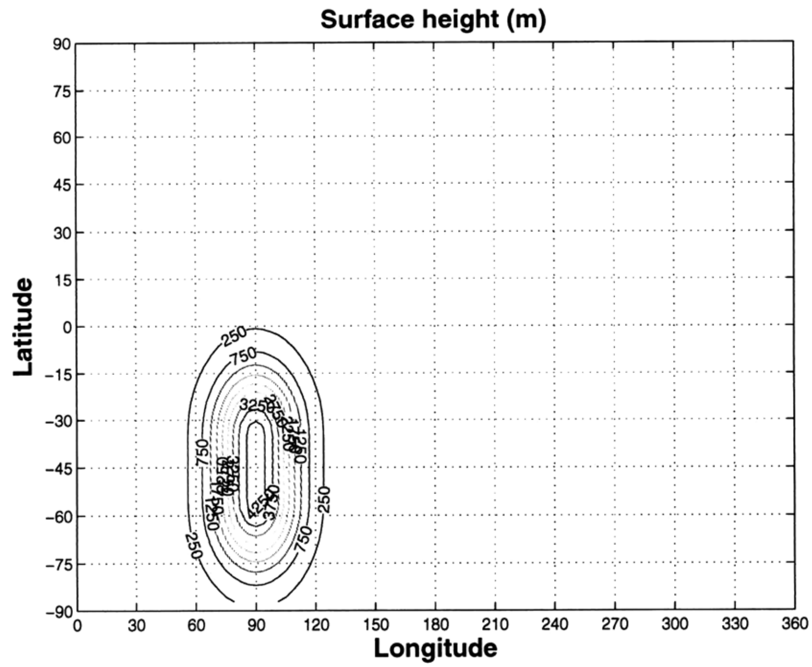

Figure 4.7: Topographical profile for $mt1$. Contour intervals are every $500m$ and start at $250m$. A full description can be found in Table 4.3.

30°S in the presence of a mid-latitude ridge.

Also comparing the case with no topography (Fig. 3.1), notice the stratospheric jet has shifted poleward from 58°S to 68°S and that the magnitude is also weaker. These two differences are consistent with the known effects of topography. Since there are more planetary waves in this model, more waves can travel into the stratosphere, dissipate and exert a drag on the polar vortex. As a result, it's not a surprise that the winds in the stratosphere are weaker. Secondly, the reason for the poleward shift in the stratospheric jet has to do with the location of the mountains. With the mountain ridge equatorward of the polar vortex, more waves would presumably break on the equatorward side than the poleward side. This would lead to a poleward shift in the peak of the stratospheric winds.

Including the mountain, the tropospheric jet shifted to 30°S, raising the possibility that the dual regime behavior, discussed in Section 4.1, is present. However, as shown in Fig. 4.8b, the timescales representative of the tropospheric annular mode variability are longer than observed, but typical of those in these simple models. Thus, in this particular case, the long timescales found in PK are not present under this setup. This is likely because the inclusion of a mountain has "pushed" the system away from the transition zone found in the previous section (cf. Fig. 4.1) and is now unambiguously in only one regime, significantly lowering the persistence of the annular mode index.

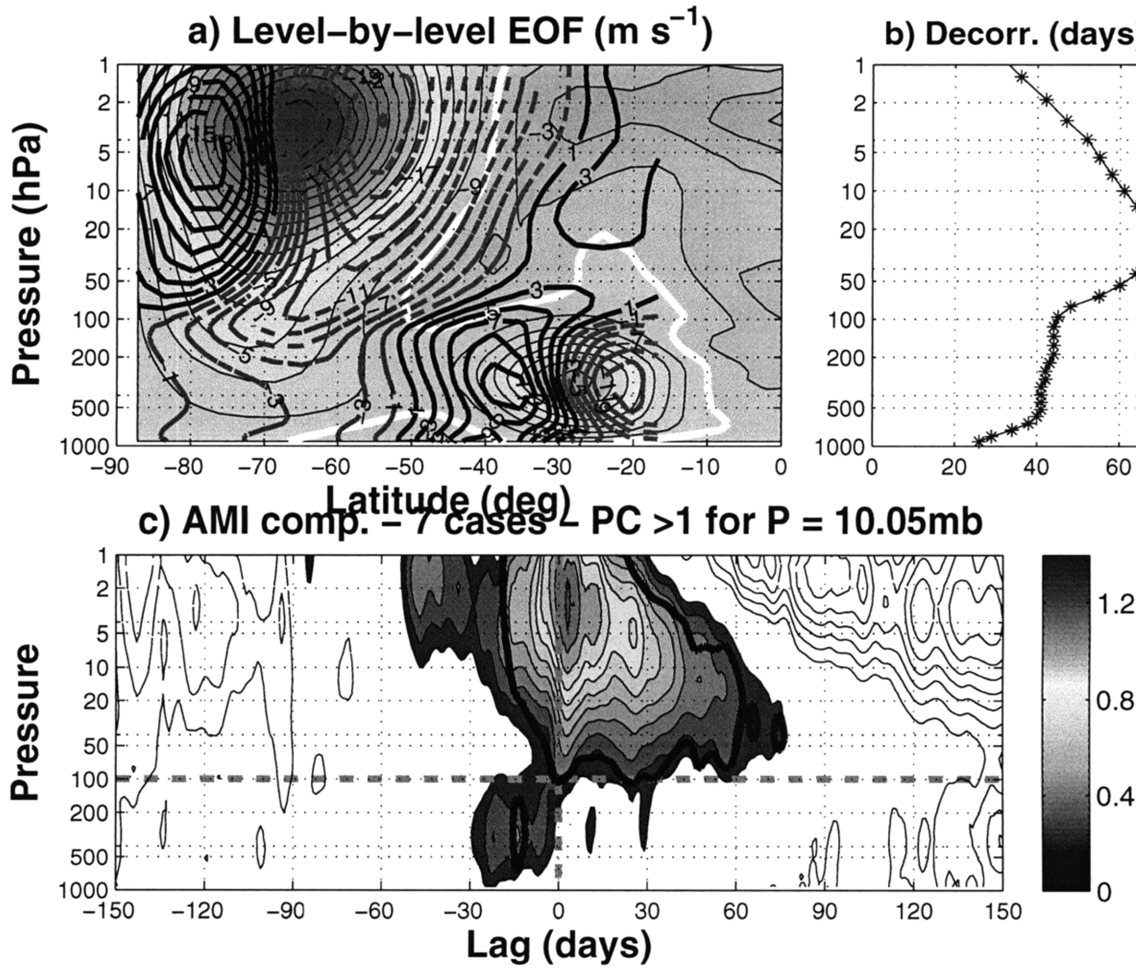

Figure 4.8: Characteristics of exp mt1. In (a), the time-average zonal-mean zonal wind is shaded in color and the thick contours are the level-by-level leading EOF of $[u]$ with the sign chosen to depict vertical coherence (cf. 3.2). In (b), the decorrelation time of the leading PC at each level. In (c), the annular mode index composite of weak vortex events. Filled contour intervals are every 5 $m\ s^{-1}$ in (a) with the zero contour in white. The lined contours are every 2 $m\ s^{-1}$, with positive values in black and negative values dashed in gray. Contour intervals in (c) are every 0.1, with the zero contour omitted and values greater than zero filled. The black line marks the region where the AMI composite is statistically significant above zero at the 95 percent confidence interval.

The increased variability in the stratosphere is also consistent with a model having topography. Comparing Fig. 3.5c with the thick contours shown in Fig. 4.8a, the maximum variability has increased by about ten percent. With larger amplitude waves reaching the stratosphere affecting the mean flow, the variability would also increase.

However, the biggest difference between the flat topography case seen in the last two chapters and that of exp. mt1 is the spatial pattern associated with the leading mode of variability. Instead of the poleward lobe of the tropospheric jet "connecting" to the equatorward lobe of the stratospheric vortex, the two are separated (Fig. 4.8a). This is fundamentally a different picture. Here a poleward shift (and a weakening) of the stratospheric polar vortex is correlated with a poleward shift of the tropospheric jet. This is *opposite* to what was described in Chapter 3 *and* opposite to what has been described in observations (e.g. Thompson and Wallace 2000).

The composite of the annular mode index as a function of lag and pressure during weak vortex events is also quite different. Fig. 4.8c shows that after the weak vortex event, the troposphere does not seem to respond. Once again, the behavior of this system is different from observations and from the case with flat topography. In those cases, a tropospheric signal is seen before the weak vortex event; the troposphere then follows the same-signed anomalies as those in the stratosphere. In this case, as measured by the AMI, there is no indication that the troposphere follows any changes in the stratosphere.

Since these annular mode index composites are statistically generated, they, themselves, cannot prove cause and effect. However, explicitly adding momentum forcings can either support or discredit the results from above. Fig. 4.9 shows the momentum forcing, its relation to the time-averaged winds, and its relation to the leading mode of variability. The forcing is centered at 50 mb with a peak value of -1 $m\ s^{-1}\ day^{-1}$. With a strong projection between the forcing and the stratospheric mode, we would expect a large response.

However, unlike the case with flat topography (cf. Fig. 3.11), Fig. 4.10 shows a suprising result. Although with the addition of topography and the expected stronger stratospheric response (note that stratospheric changes were twice as strong), there virtually no changes to the tropospheric circulation in the winter hemisphere. This would add further credence that a tropospheric response to a stratospheric perturbation depends largely on the tropospheric

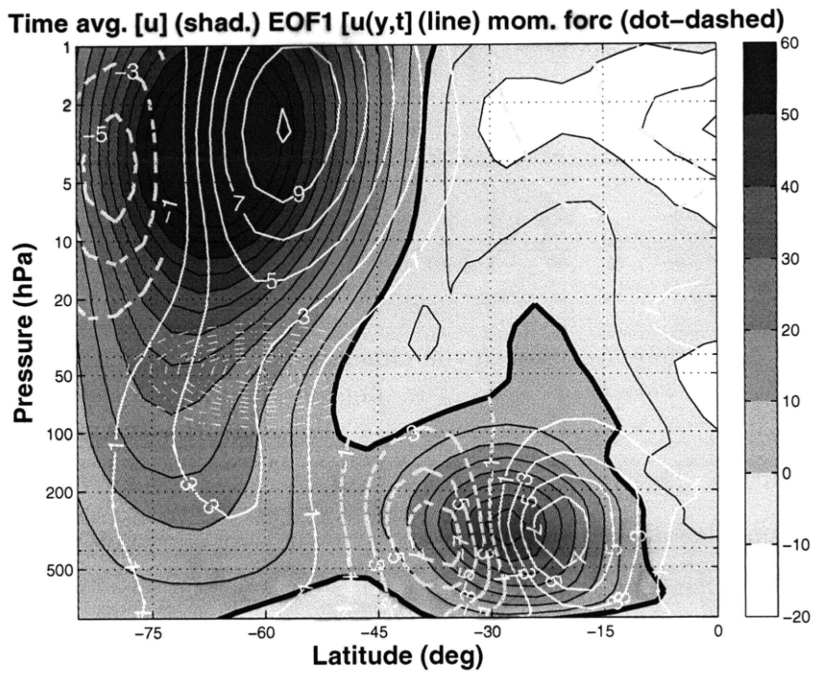

Figure 4.9: Similar to Fig. 4.8a. Here the thin white and gray lines represent the pressure-weighted leading EOF calculated by combining all the levels. White lines are positive and gray-dashed lines are negative. The thin dot-dashed line represent the momentum forcing. The peak value is - 1 $m\ s^{-1}\ day^{-1}$ with contours every 0.1 $m\ s^{-1}\ day^{-1}$.

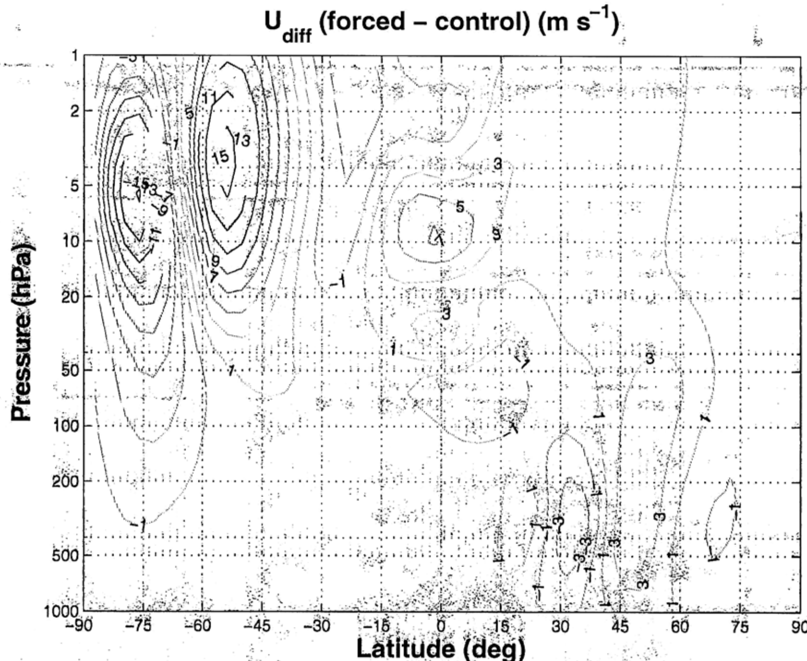

Figure 4.10: The difference between the climatological winds from the forced case (cf. Fig. 4.9) and the control case (Fig. 4.8) . The contours are every 2 $m\ s^{-1}$.

state. In addition, the stratospheric dipole is of the opposite sign. With a negative momentum forcing on the equatorward side, the resulting pattern is opposite to what is expected from the EOF pattern in Fig. 4.9.

Nevertheless, the momentum forcing has added further evidence that the troposphere does not respond to stratospheric changes in this case. As we will discuss in the next chapter, we suspect the winds are too weak in the mid-latitudes of the lower stratosphere. The waves above the mountains are likely too strong and as a result, reduce the vertical wind shear producing the weak winds. Decreasing the size of the large ridge from the mountains may alleviate this problem.

In exp. mt2, Fig. 4.11 shows that there is no longer a ridge and instead, the topography has been changed to a smoother Gaussian profile. Most of the mountain is also confined to the mid-latitudes. The climatological winds are similar to the previous case (see Fig. 4.8). One difference, is the increase in the mid-latitude lower stratospheric winds (Fig. 4.12).

Another difference is the stratosphere-troposphere coupling. Here, the poleward lobe

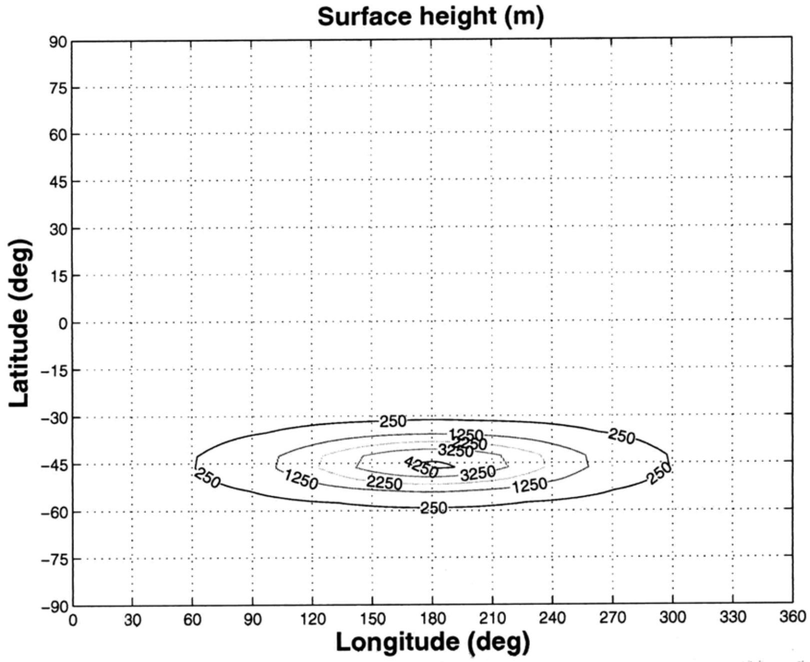

Figure 4.11: Topographical profile for mt2. Contour intervals are every $1000m$ and start at $250m$. A full description can be found in Table 4.3.

associated with the oscillation of the tropospheric jet "connects" with the variability of the stratospheric jet. In this case, similar to observations, a weakened polar vortex is correlated with an equatorward shift of the troposphere jet.

Fig. 4.12b shows that the timescale associated with the leading mode of variability as a function of height. Similar to that of the previous case, the decorrelation times are small in the troposphere and upper stratosphere and large in the lower- to mid-stratosphere. Again for this particular experiment, given the relative short timescales, the bimodal behavior seen in Polvani and Kushner (2002) is not a factor in this run.

Despite the difference in the behavior of the coupling, the annular mode index composite reveals a similar picture as the previous case (Fig. 4.8c). There's a robust tropospheric positive phase (as defined by Fig. 4.12a) before the weak vortex event. Again, afterwards, the troposphere does not follow the same sign as the stratosphere. Instead, the troposphere switches sign and turns negative. So, like the previous case, there's not a lot of confidence in suggesting a stratospheric influence on the troposphere.

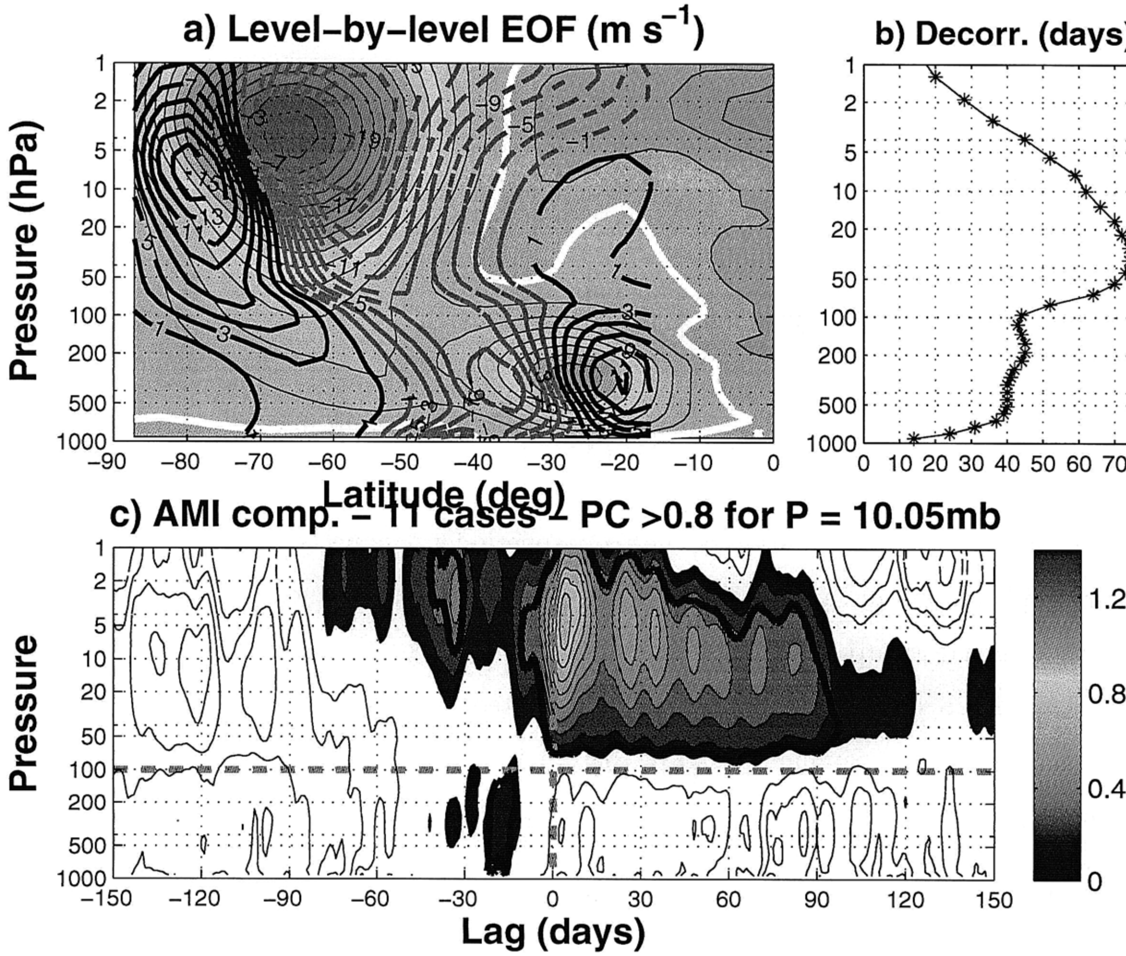

Figure 4.12: Same as Fig. 4.8, but for exp. *mt*2 instead.

As we will discuss in the next chapter, the mid-latitude lower stratospheric winds seem important. In an attempt to increase the lower stratospheric winds further, the next experiment decreases the height of the mountain. As shown Fig. 4.13, the peak height has been decreased to 3000m. Otherwise, everything else is the same as exp. $mt2$.

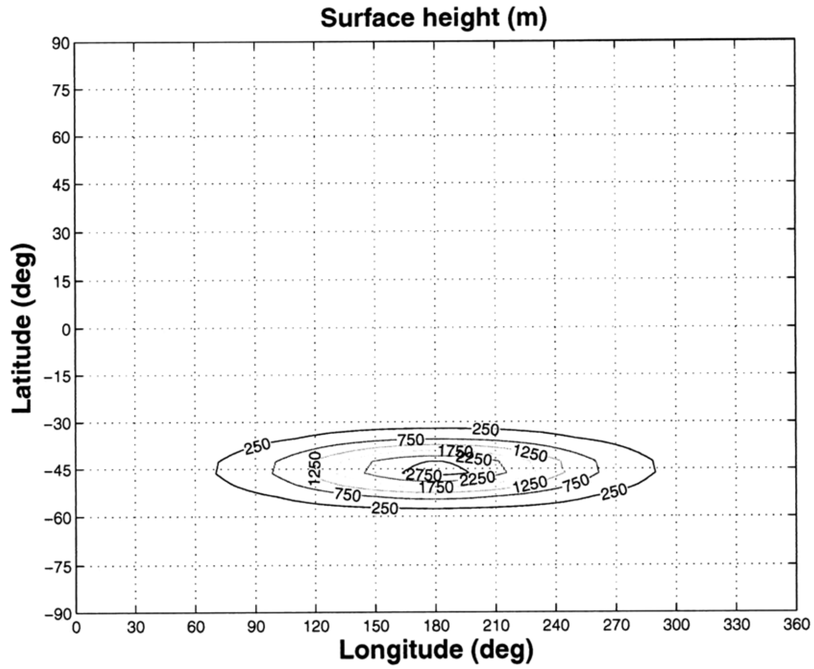

Figure 4.13: Topographical profile for $mt3$. Contour intervals are every 500m and start at 250m. A full description can be found in Table 4.3.

For exp. $mt3$, Fig. 4.14a shows that the mid-latitude lower stratospheric winds have increased to about 15 $m\ s^{-1}$, a big change from the easterlies of exp. $mt1$. In addition, the tropospheric jet has shifted poleward to approximately 35°S. As we have seen in Section 4.1, this could be indicative of the bimodal behavior that seems inherent in this parameter space. Fig. 4.14b confirms that the long timescales that were associated with the jet switching appears to have crept back into the model.

This is not completely surprising since the addition of the mountain would decrease the strength of the polar vortex. As shown in Fig. 4.1, reducing the winds from the strong polar vortex case in the Polvani and Kushner (2002) setup, brings you towards a transition zone between the eddy-driven jet in the subtropics and mid-latitudes. In addition, the "shorter" mountain does not seem to prevent the jet from "switching" as seen in the previous two experiments.

Given the unrealistically long timescales, examining the annular mode index composites may lead to exaggerated results. But for completeness, Fig. 4.14c shows both the troposphere and stratosphere exhibiting the same-signed anomalies. The most robust pattern (thick black line) shows that after the weak vortex event the troposphere has the same sign. However, although not statistically significant, the tropospheric AMI before the weak vortex event also persisted with the same sign for a nearly equal period of time, suggesting that tropospheric circulation did not change after the stratospheric event.

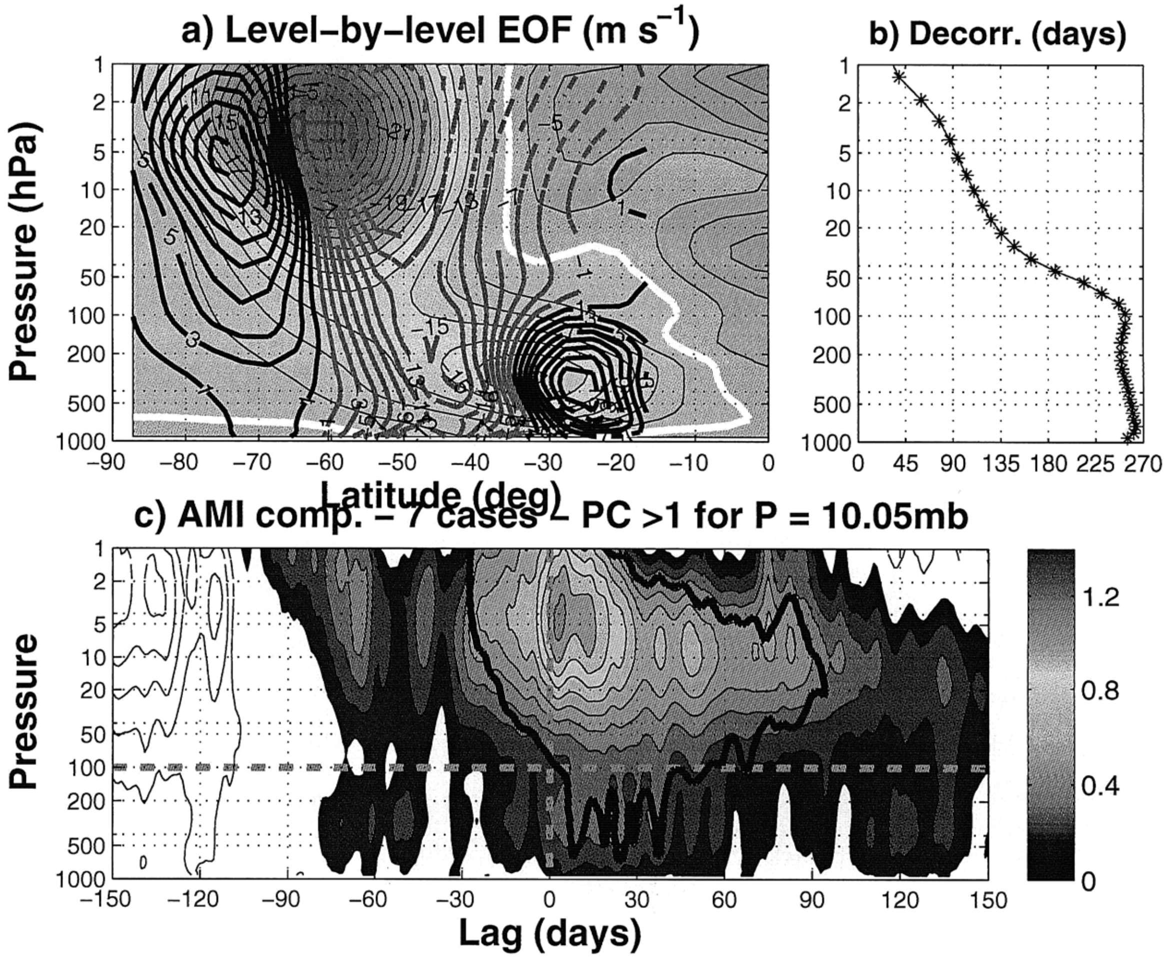

Figure 4.14: Same as Fig. 4.8, but for exp. *mt*3.

Ideally, for situations where changes in the stratosphere unequivocally impacts the troposphere, composites of the tropospheric AMI should exhibit an asymmetry. In other words, negative lags should exhibit vastly different behaviors than the positive lags. In this case, there is not a significant difference in the annular mode index (AMI) before and after a weak vortex event. Thus, in this setup, it is hard to argue a stratospheric influence.

However, in experiment mt4, the evidence is more compelling. Fig. 4.15 shows the topography profile consists of two mountains, but with the same topographic peak height and latitudinal extent as that of run mt3. A full description can be found in Table 4.3. So instead of a wavenumber one mountain, the shape is in the form of wavenumber two.

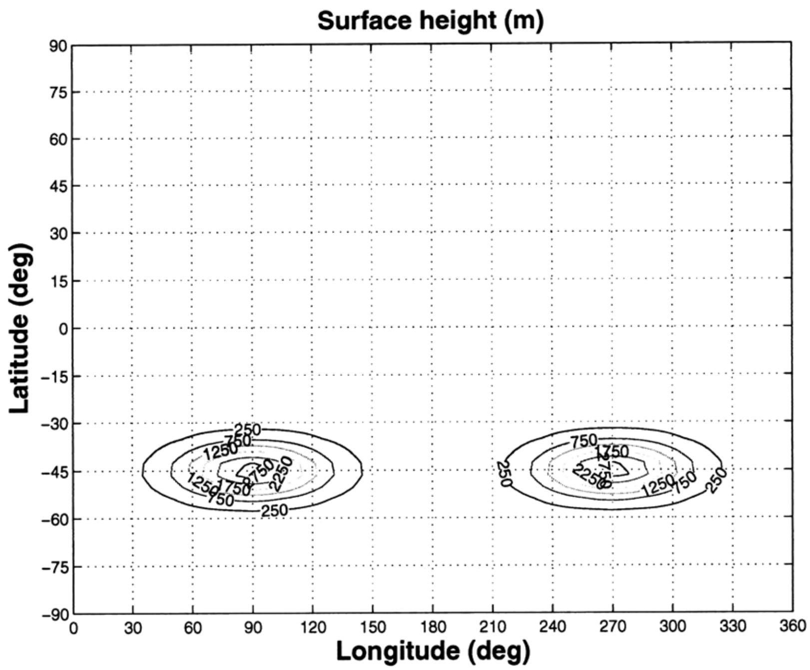

Figure 4.15: Topographical profile for $mt4$. Contour intervals are every $500m$ and start at $250m$. A full description can be found in Table 4.3.

The time-average zonal-mean zonal wind and the level-by-level EOF of [u] is shown in Fig. 4.16a. A comparison to Fig. 4.14a shows that the two are quite similar. However, a big difference is that the unrealistically long time scales associated with the dual regime behavior (seen in the last experiment) has nearly been reduced by a factor of three (Fig. 4.16b).

Most interestingly, under this setup, the composites of the annular mode index during weak vortex events show a clear asymmetry before and after a weak vortex event. Fig. 4.16c shows all negative values in the troposphere before and all positive values after the weak vortex event, suggesting a more definitive stratospheric influence on the troposphere.

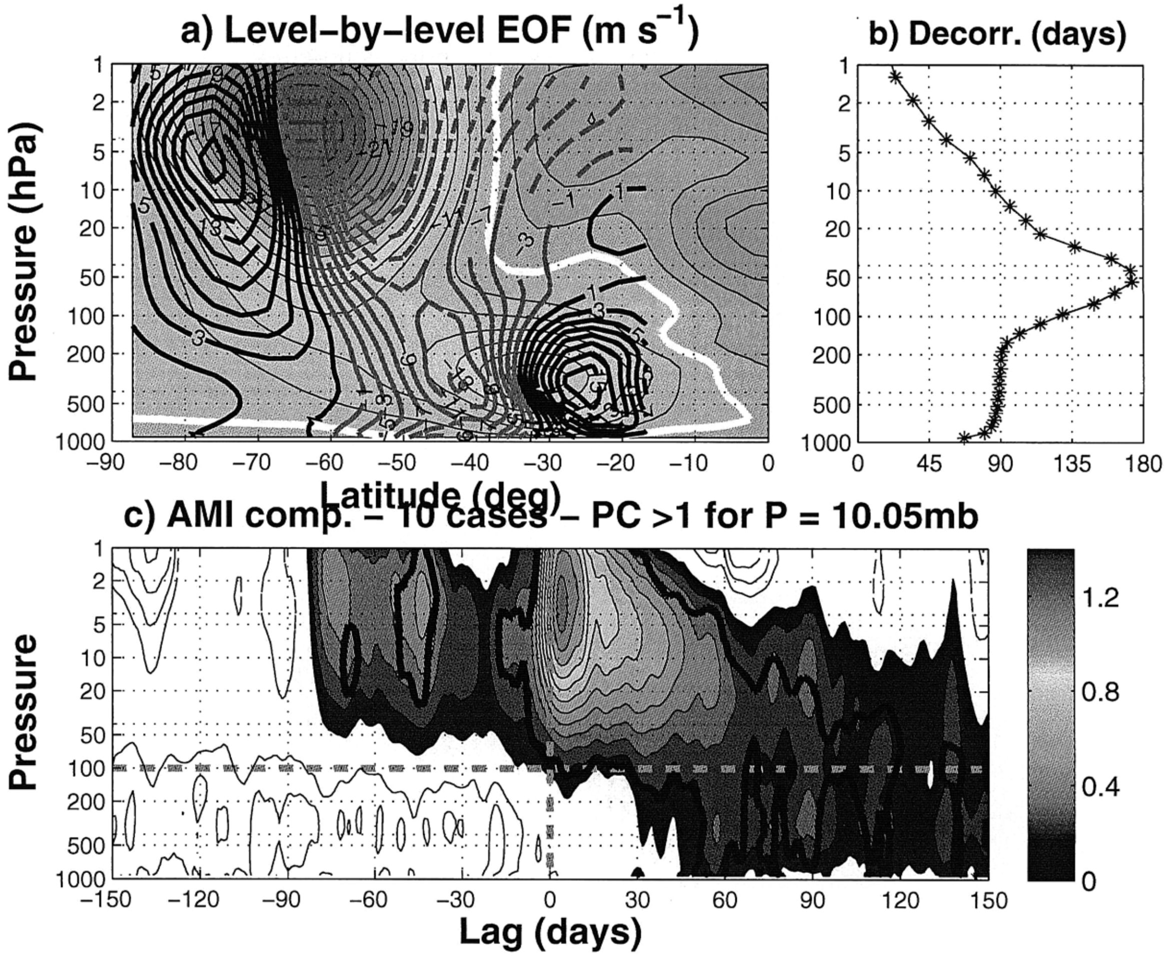

Figure 4.16: Same as Fig. 4.8, but for exp. *mt*4.

Including the case with flat topography (from Chapter 3), we have now seen in the three cases where the climatological mid-latitude lower stratospheric winds are of moderate westerly strength, there appears an increased likelihood in changes of the troposphere after weak vortex events. Is that always the case? To test this idea, we have shifted the mountains into the sub-polar region. In one case (Fig. 4.17) a small mountain and in the final experiment, a large mountain (Fig. 4.19) in the sub-polar region.

As shown in Figs. 4.18a and 4.20a, the mid-latitude lower stratospheric winds are ap-

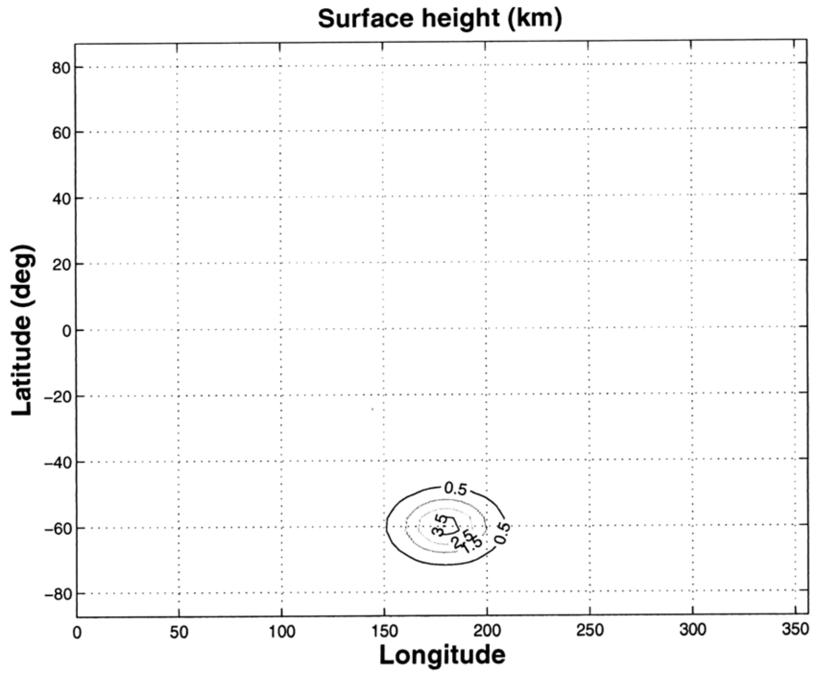

Figure 4.17: Topographical profile for $mt5$. Contour intervals are every $500m$ and start at $250m$. A full description can be found in Table 4.3.

proximately 20 $m\ s^{-1}$ in both cases. The leading EOF structures both have similar spatial pattern, and the vertical profile of the decorrelation times are qualitatively similar.

Unlike the mt4 experiment, in these two cases, there is no clear signal of a significant tropospheric change in the annular mode index after a weak vortex event (Figs. 4.18c and 4.20c). For exp. mt5, there is not any obvious asymmetry before and after a weak vortex event. For exp. mt6, the large mountain in the sub-polar region, the lack of a tropospheric signal is even more dramatic. The composites, in fact, show virtually no changes to the annular mode index before and after a weak vortex event.

4.3.3 Summary

In this section, we have attempted to reproduce the composites of the observed annular mode index (AMI) during weak vortex events, such as the ones produced by Baldwin and Dunkerton (2001) and Gerber and Polvani (2009). With the same stratospheric thermal equilibrium profile to each model run, depending on the location and amplitude of the

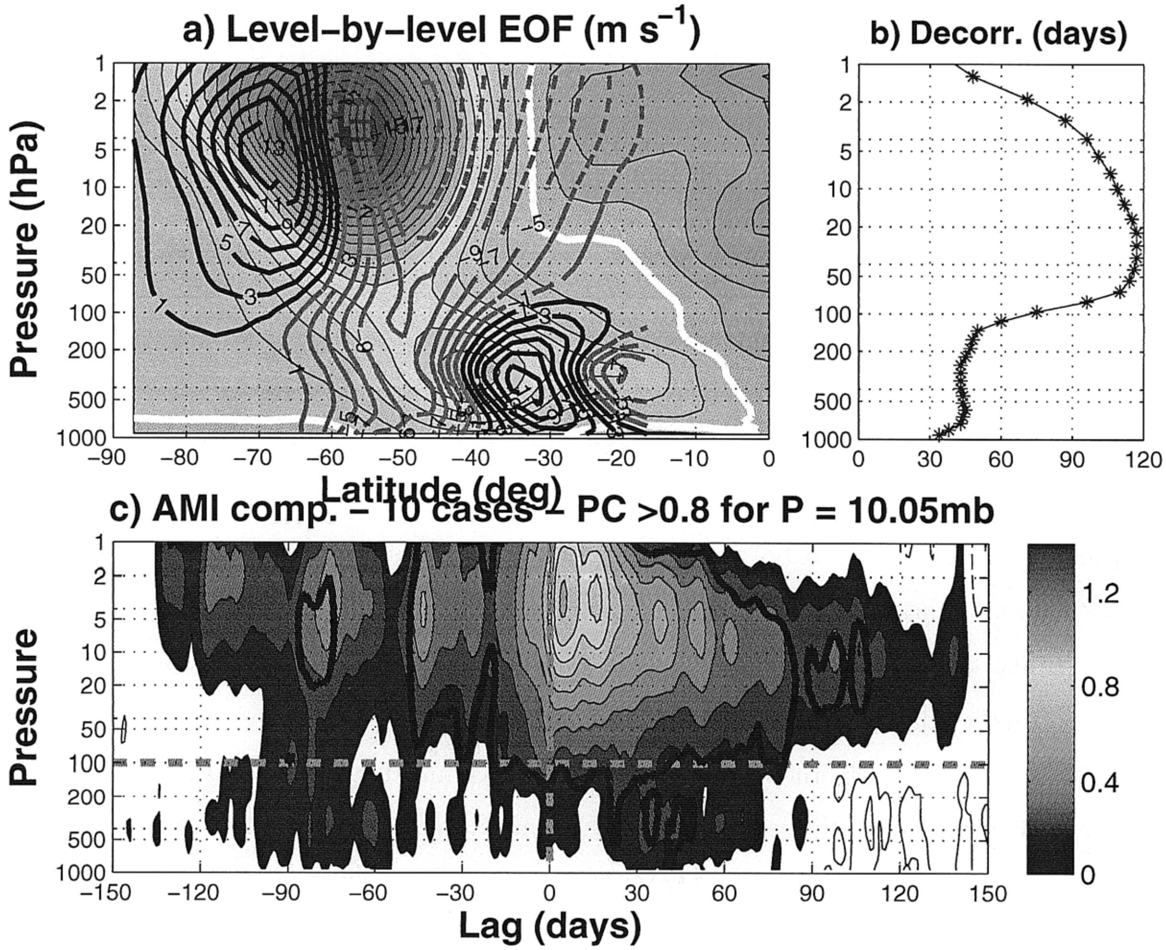

Figure 4.18: Same as Fig. 4.8, but for exp. *mt*5.

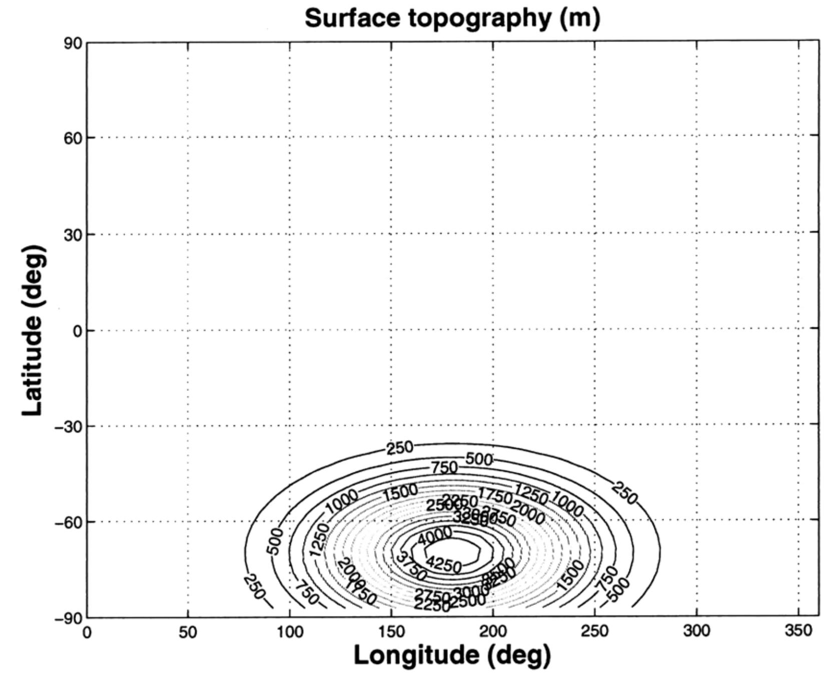

Figure 4.19: Topographical profile for $mt6$. Contour intervals are every $500m$ and start at $250m$. A full description can be found in Table 4.3.

specified topography, the tropospheric AMI composites exhibit three distinct characteristics before, during and after weak vortex events.

In the first group, when the mountains are placed in the mid-latitudes with large amplitudes, the anomalous tropospheric AMI values precede those of the weak stratospheric vortex (see Fig. 4.8c). However, there does not appear any changes in the troposphere after the large stratospheric change. In the second group, the mountains are again placed in the mid-latitudes, but this time with a one quarter reduction from the previous height. The changes to the composites of the AMI change remarkably. Preceding weak vortex event, the tropospheric AMI's are negative. Between lags of 0 to 30 days, the values are zero. Then starting at lag = 30 day and continuing for the next 90 days or so, the troposphere follows the same sign as the stratosphere (see Fig. 4.14c). In the third grouping, the mountain is shifted into the sub-polar region. The composites show that before, during and after the weak vortex event, the tropospheric AMI signal stay approximately near zero suggesting no stratospheric influence.

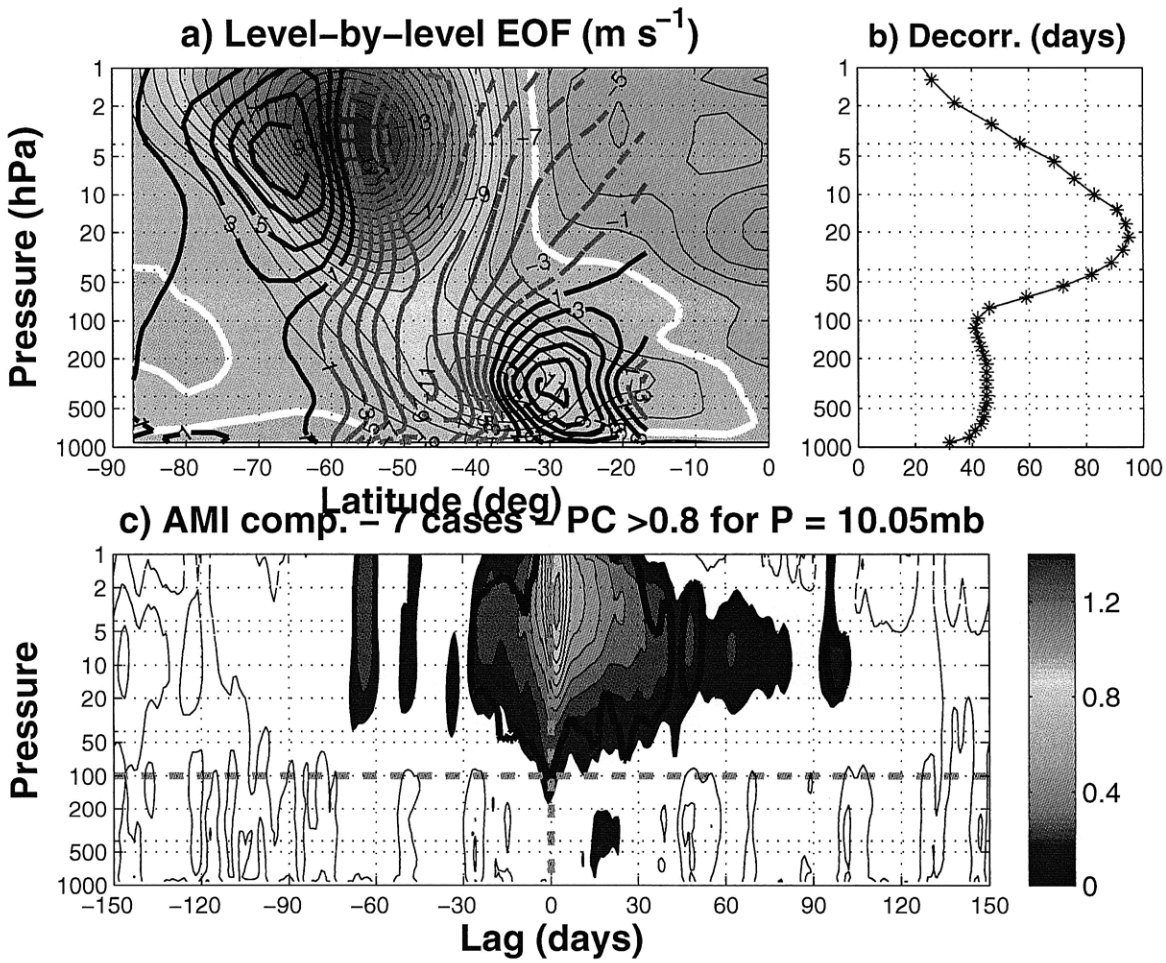

Figure 4.20: Same as Fig. 4.8, but for exp. *mt*6.

4.4 Summary

In this chapter, the sensitivities to the initial tropospheric state on the stratospheric influences are examined. Through systematic changes to the troposphere, we show that the same stratospheric perturbation do not lead to the same changes in the troposphere. Consistent with fluctuation-dissipation theorem, changes to the troposphere from stratospheric forcing was largely dependent on the timescale associated with the leading mode of variability. For long timescales, large responses were found. From Fig. 4.1, we see that the long timescales are associated with the transition zone separating two regimes. The eddy-driven jet is either (a) well-separated from or (b) co-exist with the subtropical jet. Large responses are only found in the parameter space where the jet teeters between these two regimes. Outside of this parameter space, applying the same stratospheric thermodynamic forcing, virtually no responses are found in the troposphere.

In an attempt to move away from this transition zone, we took two approaches. The first was to change the equilibrium temperature (T_{eq}) profile. Shifting the peak T_{eq} further into the summer hemisphere removed the dual regime behavior, with the eddy-driven jet located only in the mid-latitudes (and never in the subtropics.) Similarly, applying a sufficiently tall mountain in the mid-latitudes displaced the peak surface westerlies into the sub-tropics. This too removed the dual regime behavior and subsequently reduced the strong responses seen in previous studies (*e.g.* Polvani and Kushner 2002; Kushner and Polvani 2004.)

In an attempt to reproduce the annular mode index composites from observations (Baldwin and Dunkerton 2001), we've tried three separate types of mountain configurations. Varying the height and location, we found that the annular mode index (AMI) composites by Baldwin and Dunkerton (2001) during weak vortex events can only be reproduced when mountains are centered in the mid-latitudes and of intermediate heights. If the mountain heights are too tall or shifted into the polar region, following a weak vortex event, there is little or no change in the tropospheric AMI composites either cases.

In addition, a necessary but not sufficient condition was for the poleward dipole of the annular modes to be correlated with the strengthening/weakening and equatorward lobe of the stratospheric dipole. For example, in exp. $mt1$, plots of AMI composite showed no significant tropospheric response after a weak vortex event. A momentum forcing was placed in the center of variability in the lower stratosphere, yet there was virtually no tropospheric response. In this case, with the zero line poleward of 50°S in the lower stratosphere, any stratospheric changes may be too poleward to trigger the tropospheric eddy feedback responsible for the annular mode response. This example and others suggest the stratospheric influence has a dependence on the characteristics of the tropospheric climatology, which will be discussed further in the next chapter.

Chapter 5

Importance of the lower stratosphere and the planetary waves

In the last chapter, we showed that the response to changes in the stratosphere depended largely on the initial tropospheric state. In the first series of experiments, stratospheric thermal perturbations were applied to various winter-like profiles, one of which was identical to Polvani and Kushner (2002). As stated in Chan and Plumb (2009), the response was largely dependent on the tropospheric annular mode timescale. In the second series of experiments, variations of the topographical profile were applied, while applying the same equilibrium temperature profile in both the troposphere and stratosphere. Composites of the annular mode index during weak vortex events having characteristics of a stratospheric influence, as those seen from observations (cf. Baldwin and Dunkerton (2001)), depended largely on the topographical setup. A summary of the those experiments can be found in Table 5.1.

Table 5.1 suggest that the primary ingredients in which tropospheric anomalies follow stratospheric anomalies associated with a weak vortex event are that (1) the location shown in the third column has a climatological wind speed of greater than 10 $m\ s^{-1}$ and (2) a sufficient source of planetary waves in generating the weak vortex events needs to be generated in the mid-latitudes. The choice of 45°S and 100 mb was chosen because it qualitatively best exhibited the following two traits. Firstly, the latitudinal location was approximately halfway

Exp. Name	Mt. centered @ 45°S	U(45°S,100 mb) $\geq$ 10 $m\ s^{-1}$	Δ trop. AMI index
mt1	yes	no	no
mt2	yes	no	no
mt3	yes	yes	yes
mt4	yes	yes	yes
mt5	no	yes	no
mt6	no	yes	no

Table 5.1: Topographical setups. γ governs the stratospheric equilibrium polar temperature profile (see 2.6). ϵ controls the tropospheric equilibrium temperature profile (see 2.2).

between the stratospheric polar vortex and the tropospheric eddy-driven jet. Secondly, this is the latitude at which the maximum variance occurs from the EOF calculation at that level (Fig. 4.16). Finally, 100 mb was chosen because this was the approximate pressure level where the correlation from the tropospheric AMI values appear to drop off the most quickly (Fig. 5.1). As long as those characteristics are sufficiently met, the precise location is likely not important.

Fig. 5.2 adds further credence that the position picked is in the "pathway" region that connects the troposphere to the stratosphere. This plot shows the correlation between the zonal-mean zonal wind at 100 mb at the various latitudes in the abscissa with the location of the eddy-driven jet (or equivalently, the latitudinal location of the maximum surface westerlies.) As shown, a weak, but positive correlation exists in both the polar and tropical regions. However, in the mid-latitudes, an anti-correlation exists, with the largest absolute correlation near 45°S.

Although this correlation does not prove cause and effect, it does show that there is a statistical relationship between the strength of the lower stratospheric winds and the location of the eddy-driven jet. For strong winds, the peak of the surface westerlies (and the associated eddy-driven jet), ϕ_{max}, is near the mid-latitudes. While winds are close to zero

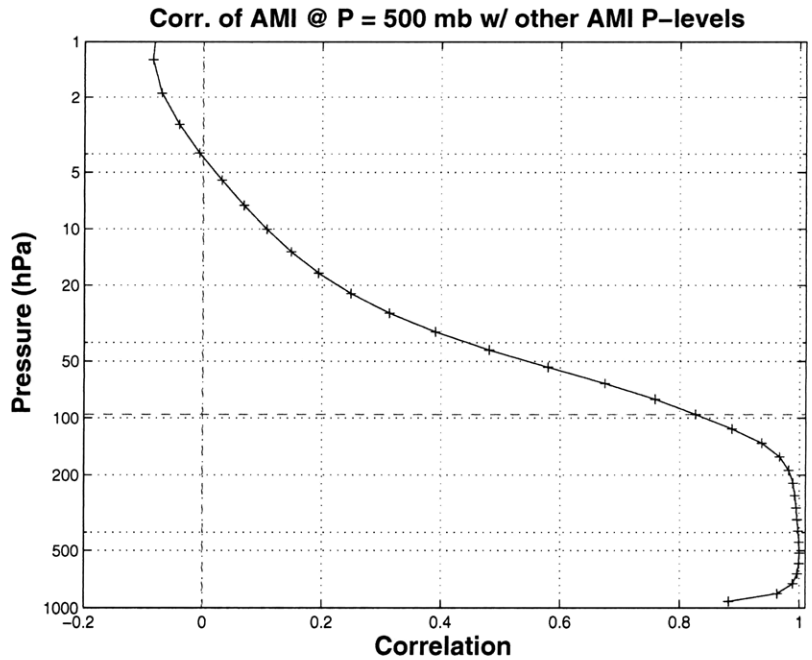

Figure 5.1: The correlation of the level-by-level AMI with the AMI at $p = 500\ mb$ for exp. $mt4$.

in this pathway region, the strongest surface westerlies will lie equatorward of its time-mean position. However, this correlation is an instantaneous one. Fig. 5.3 shows a time-lag of the latitudinal location of the maximum surface westerlies strength with the zonal-mean zonal winds. There is not much change to the correlation coefficient when lags of plus or minus eight days are used. The greatest correlation occurs near a lag of -2 day suggesting if there is a cause and effect, it is the changes to the location of the eddy-driven tropospheric jet that precede the strengthening or weakening of the lower stratospheric winds.

5.1 Lower stratospheric momentum forcings

In order to demonstrate the relationship of the strength of the lower stratospheric winds further with the position of the eddy-driven jet, we will explicitly alter the lower stratospheric winds and see if there is a change in the eddy-driven jet as described above. Using exp. mt3 as the "base" experiment, we alter the lower stratospheric winds by applying a momentum torque. As discussed in Section 3.3.1, these momentum torques are gaussian in log-pressure

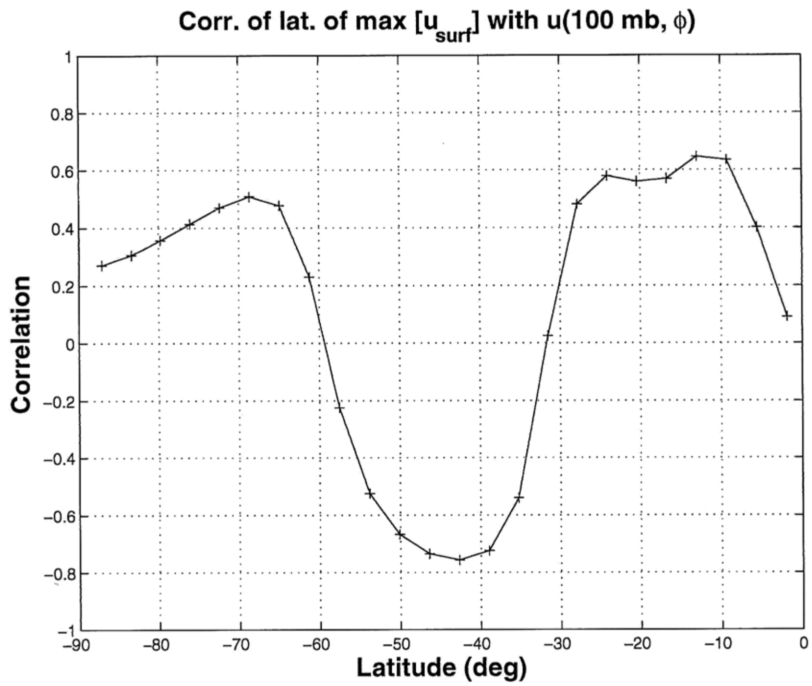

Figure 5.2: The correlation of the zonal-mean zonal wind at 100 *mb* with the latitudinal location of the maximum surface westerlies for various lags from from exp. *mt*4. A nine day running mean is applied to the latitudinal location of the maximum $[u_{surf}]$.

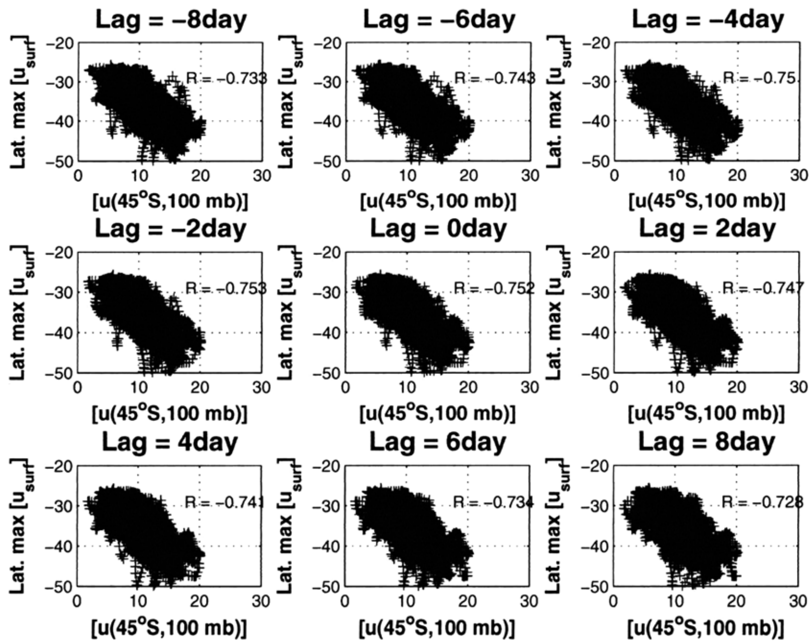

Figure 5.3: The correlation of the zonal-mean zonal wind at 100 mb and 45°S with the latitudinal location of the maximum surface westerlies at various lags.. A nine day centered-mean is applied to the latitudinal location of the maximum $[u_{surf}]$.

and in latitude and anti-symmetric about the equator.

As indicated in the third column of Table 5.2, the greater the torque, not surprisingly, the stronger the winds. The fourth column shows that there is a step-like jump in the eddy-driven jet. For weak winds (less than or equal to 7 $m\ s^{-1}$), the time-average position of the tropospheric jet is at 27°S; while for strong winds (greater than or equal to 15 $m\ s^{-1}$), the jet is located at 39.5°S.

A further examination of the annular mode index (AMI) composites of weak vortex events for each model run reveals a systematic change to its behavior. Figs. 5.4 - 5.9 show similar plots to ones described from the last chapter. The purpose of the plot is to see how the AMI composites evolve with different momentum forcings. In addition, this will give us a sense of the parameter space in which current observations lie.

As we can see from Figs. 5.4 - 5.6, the negative momentum forcings reduced the wind speeds in the lower stratosphere. But more impressively, the behavior of the internal variability has significantly changed. Instead of the tropospheric AMI values following the strato-

Exp. Name	Peak mom. forcing	U(45°S,100mb)	ϕ_{max}	Δ trop. AMI index
mom1	-1.5	4.9	-27.0	no
mom2	-1.0	5.2	-27.0	no
mom3	-0.5	7.0	-27.0	no
mt3	0	14.5	-40.0	yes
mom4	+0.5	15.0	-39.5	yes
mom5	+1.0	21.1	-39.5	no
mom6	+1.5	21.4	-39.5	no

Table 5.2: Momentum forcings applied to exp. mt3. The peak forcings are centered at 45°S, 100 hPa and are in units of $m\ s^{-1}\ day^{-1}$. U denotes the climatological zonal-mean zonal wind and ϕ_{max} represents the latitude of maximum surface westerlies. The background behind the applied torques are discussed in Section. 3.3.1

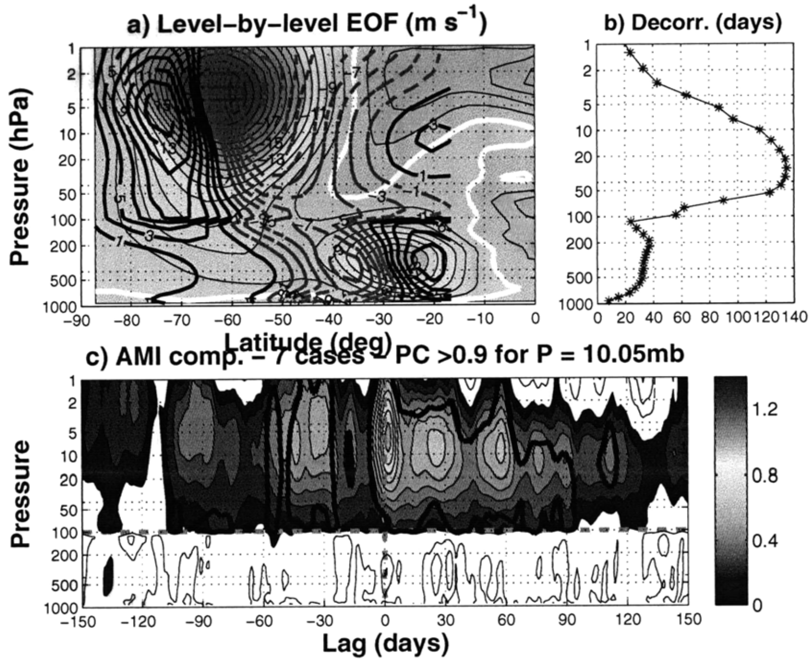

Figure 5.4: Characteristics of exp. mom1. In (a), the time-average zonal-mean zonal wind is shaded in color and the thick contours are the level-by-level leading EOF of $[u]$. In (b), the decorrelation time of the leading PC at each level. In (c), the annular mode index composite of weak vortex events. Filled contour intervals are every 5 $m\ s^{-1}$ in (a) with the zero contour in white. The lined contours are every 2 $m\ s^{-1}$, with positive values in black and negative values dashed in gray. Contour intervals in (c) are every 0.1, with the zero contour omitted and values greater than zero filled. The black line marks the region where the AMI composite is statistically significant away from zero at the 95 percent confidence interval.

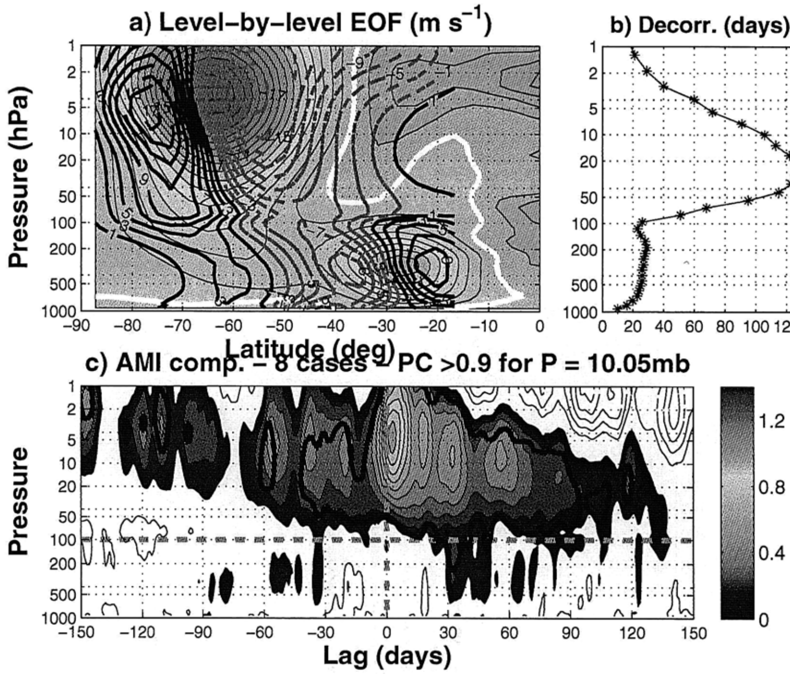

Figure 5.5: Same as Fig. 5.4, but for characteristics of exp. mom2.

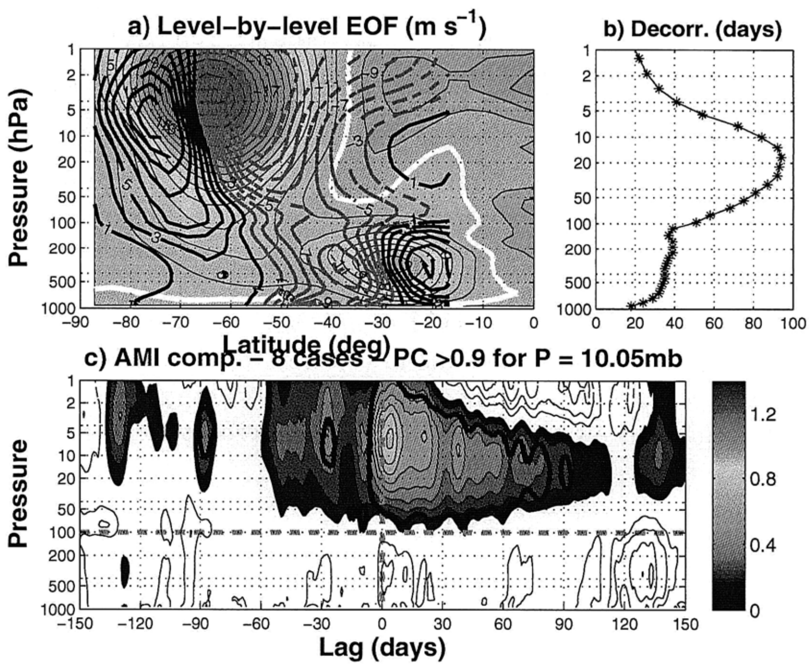

Figure 5.6: Same as Fig. 5.4, but for characteristics of exp. mom3.

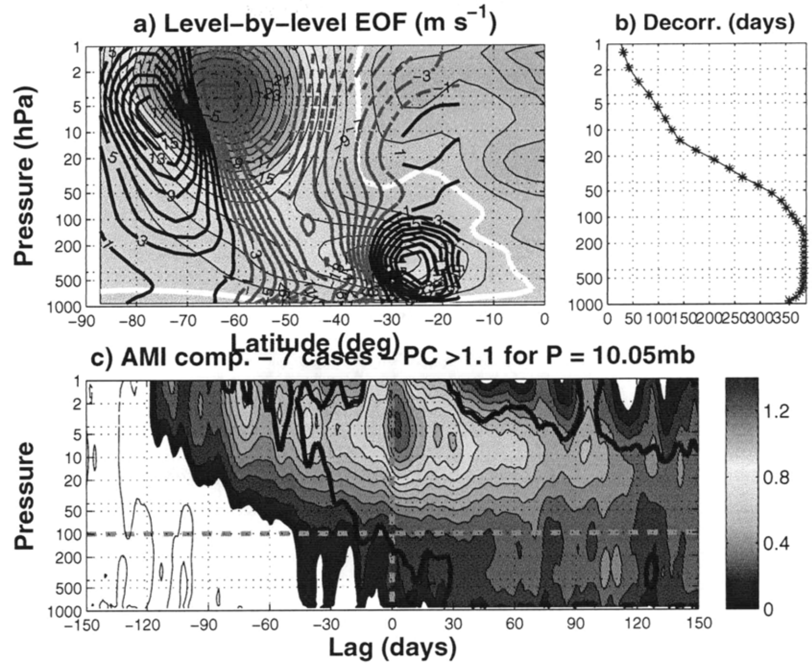

Figure 5.7: Same as Fig. 5.4, but for characteristics of exp. mom4.

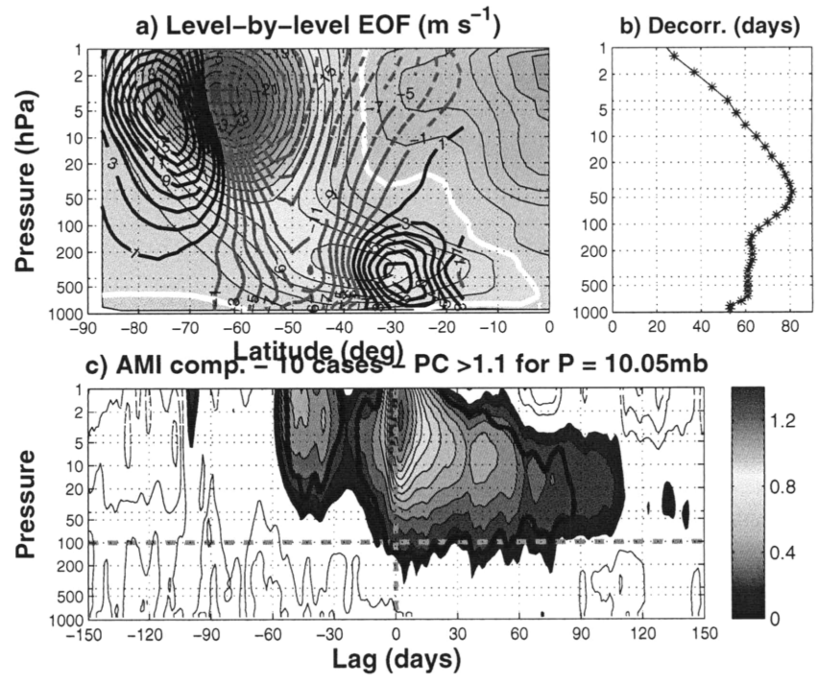

Figure 5.8: Same as Fig. 5.4, but for characteristics of exp. mom5.

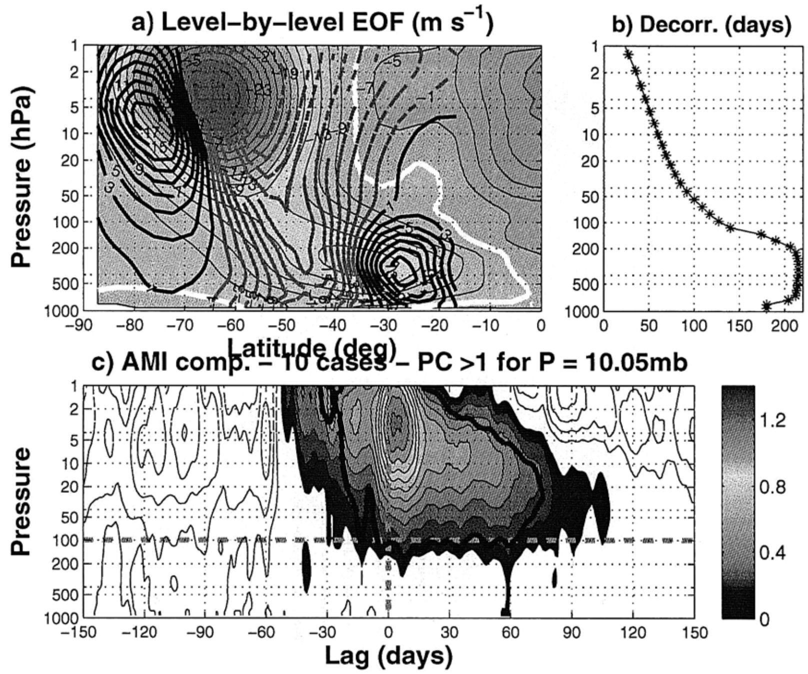

Figure 5.9: Same as Fig. 5.4, but for characteristics of exp. mom6.

sphere after a weak vortex event (recall Fig. 4.14), now it appears the tropospheric AMI no longer follows the same signed anomalies as those in the stratosphere.

Similarly, from Fig. 5.8 and Fig. 5.9, it appears that in both cases lag-lead composites of the AMI reveal a different picture than those in observations. During and after weak vortex events, there is no clear sign that the troposphere AMI has had any significant changes. These two experiments also suggest that there is little stratospheric influence.

With lower stratospheric winds of an intermediate value, only experiment mom4's and mt08's (the case with momentum forcing) internal variability seem to suggest a stratospheric influence. Fig. 5.7c shows that during and after weak vortex events, the tropospheric AMI is statistically always positive.

As a whole, there appears to be a "window" for stratospheric influence. For lower stratospheric winds less than 10 $m\ s^{-1}$, the peak surface westerlies reside in the subtropics, while for winds greater than 15 $m\ s^{-1}$, they shift to the mid-latitudes. This would suggest that it is only intermediate values (with characteristics of both regimes) that lie in a parameter space where the troposphere will be sensitive to changes in the stratosphere, at least for this model that uses the Polvani and Kushner (2002) equilibrium temperature profile.

5.2 Discussion

The previous section showed that two regimes existed. Certain wind speeds in the lower stratosphere seemed to determine where the transition between the eddy-driven jet in the subtropics or in mid-latitudes. The question here is:*how do the winds in the lower stratosphere "create" this bi-modal behavior found in the troposphere?*

Before we answer this question, as far as the published literature goes, it is important to point out that experiments with troposphere-only models (described in Section. 2.3) do not show any evidence of an eddy-driven jet being located in the subtropics. Including changes to the ϵ value (including zero), the surface westerlies always peak in the mid-latitudes.

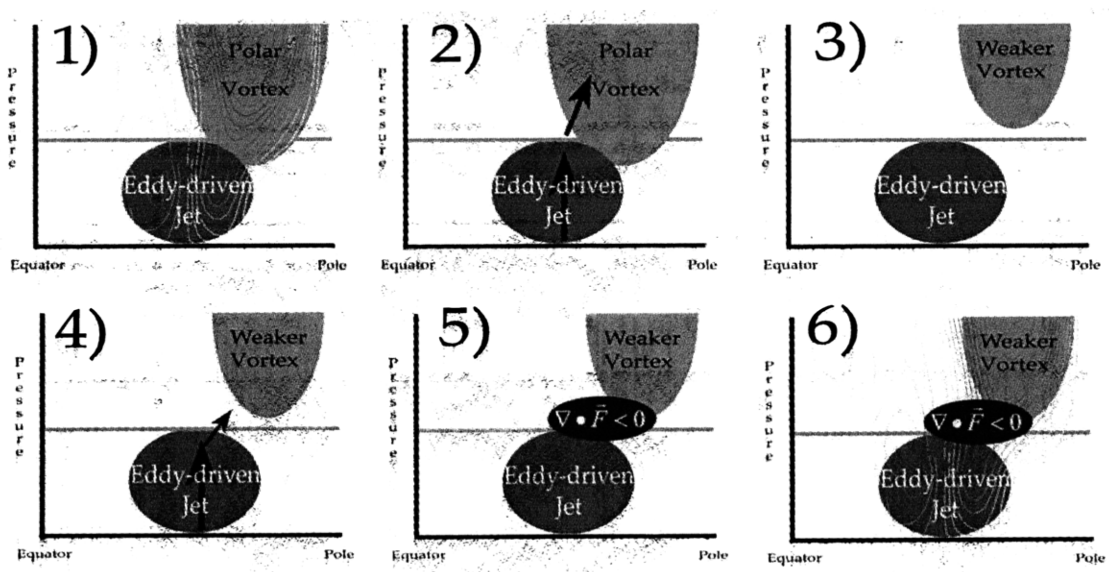

Figure 5.10: Schematic of the mechanism proposed. Shaded regions represent region of westerlies and arrows represent planetary waves. Thin contour lines describe the leading EOF of [u]. See text for details.

As shown in Fig. 5.10, we hypothesize that in the cases where the stratosphere impacted the troposphere the wave drag in the lower stratosphere is important in reducing the winds in the lower stratosphere, and through tropospheric eddy-feedback processes, shifts the eddy-driven jet equatorward. The full details of this mechanism is as follows. A pulse of planetary waves get sent from troposphere to the stratosphere (Fig. 5.10-2). Anomalously negative EP fluxes divergence reduces the zonal-mean zonal flow in the stratosphere (Fig. 5.10-3). When the next pulse of planetary waves get sent upward, there is an increased likelihood that the waves will break, since $u - c$ is closer to zero now (Fig. 5.10-4) and hence a wave drag will form (Fig. 5.10-5). This negative momentum forcing would then project onto the annular mode (Fig. 5.10-6). Through eddy-feedback processes, this will reinforce the mainly dipole structure seen in the troposphere of Fig. 4.16a, and in essence, driving the eddy-driven jet equatorward.

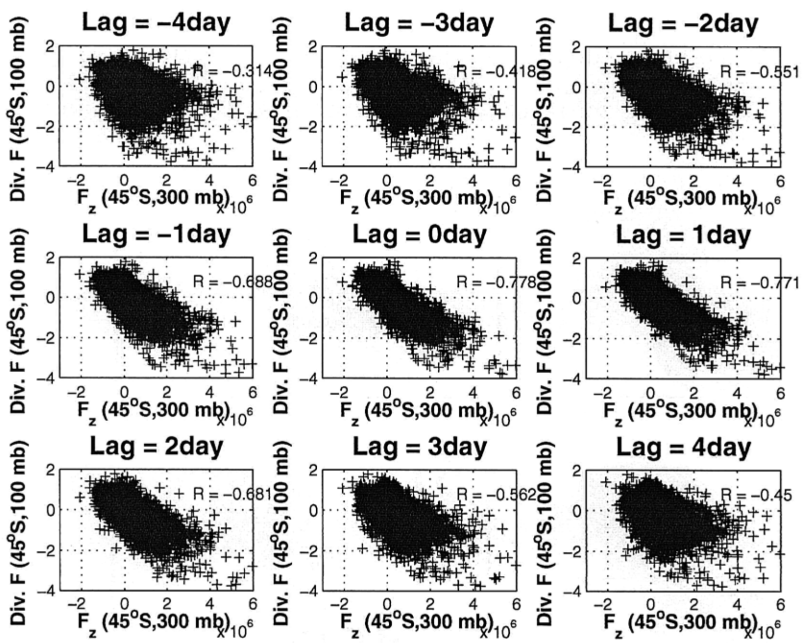

Figure 5.11: The correlation between the vertical component of the EP flux at 300 mb and the divergence of the EP flux at 100 mb and 45°S at various lags. Taken from exp. $mt4$.

The evidence supporting the first part of this mechanism is shown in Fig. 5.11. This is not a surprising result – the larger the planetary waves (as measured by the vertical component of the EP flux – see (3.2)) the greater the wave drag. The second part can be seen by comparing Fig. 5.12 with Fig. 5.13. Shortly before day zero, in the upper stratosphere, very strong wave drag preceded the sudden decrease in westerlies (similar to Polvani and Waugh 2004). Although the relationship is less obvious, the same is true in the lower stratosphere for a lag of -30 days.

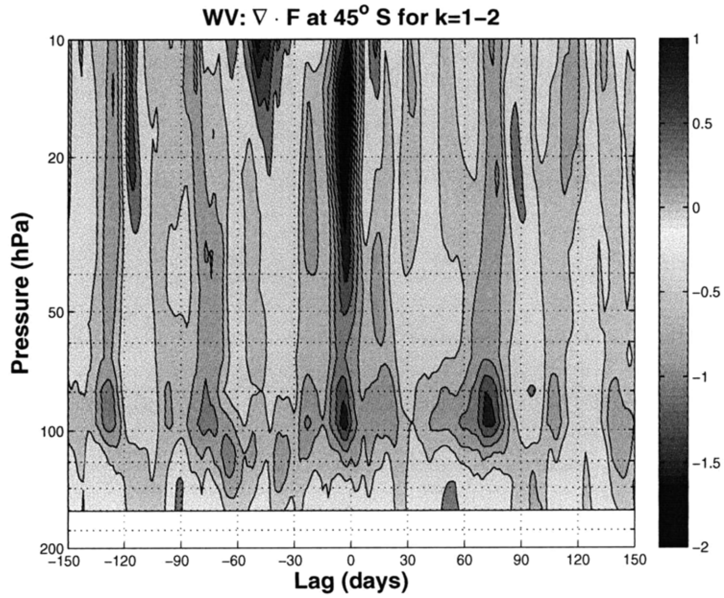

Figure 5.12: A composite of $\nabla \cdot F$ at 45°S during weak vortex events. The annular mode index was determined by performing the EOF of $[u(y,t)]$ level-by-level and taking the principal component. Day 0 is thus defined to be when the annular mode index at 10 mb first reaches 1 standard deviation.

In the third part of the mechanism described above, we can see that at a lag of about 70 days, there's another wave drag in the lower stratosphere (Fig. 5.12), which again reduces the winds further (see Fig. 5.13). Through eddy feedback processes (cf. Ring and Plumb (2007)), this negative momentum forcing reinforces the dipole straddling the tropospheric jet. Specifically, the winds will be reduced poleward of the time-mean jet, which is evident by comparing the mid- to upper-tropospheric winds before and after a lag of 30 days.

The key to this whole process is the reduction of the lower stratospheric winds so that the second pulse of planetary waves create a wave drag in the lower stratosphere. For instance, in Song and Robinson (2004), applying the same stratospheric momentum forcing to two separate cases produced different tropospheric responses than the control run. In the first case, doubling the stratospheric polar vortex winds, but using the same forcing greatly reduced the response. In a separate second case, applying the same forcing, but damping the planetary waves greatly again greatly reduced the tropospheric response. The interpretation

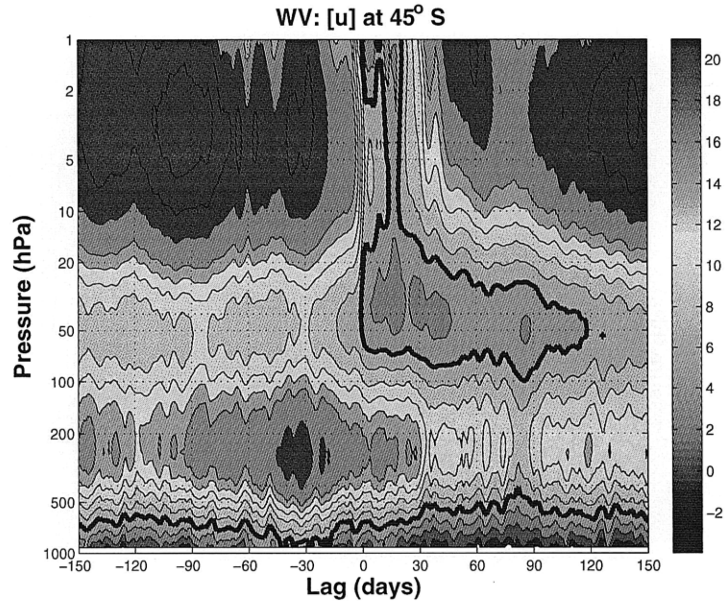

Figure 5.13: A composite of $[u]$ at 45°S during weak vortex events. The annular mode index was determined by performing the EOF of $[u(y,t)]$ level-by-level and taking the principal component. Day 0 is thus defined to be when the annular mode index at 10 mb first reaches 1 standard deviation.

was that planetary waves has an important in role in getting the stratosphere troposphere coupling correct.

The behavior of the wave drag in the extra-tropical lower stratosphere from the other three experiments is shown in Fig. 5.14. Comparing the other three, it appears experiment mt4 is the only one with the greatest wave drag for each experiment peaking shortly before day 0 and sometime thereafter. In the top panel, mom2, the case where a negative momentum forcing was applied to reduce the winds, there was also a peak wave drag immediately before day 0. Notice afterwards that there is no anomalous wave drag of that magnitude afterwards.

The second experiment we chose to compare was mom5. This was where we added a positive momentum forcing in the lower stratosphere to increase the winds. In this case, it appears there is in general greater wave forcing. However, there does not appear to be any obvious pattern to the wave drag before and after a weak vortex event, an indication that the EP flux convergence behaves independently of the changes to the lower stratospheric winds.

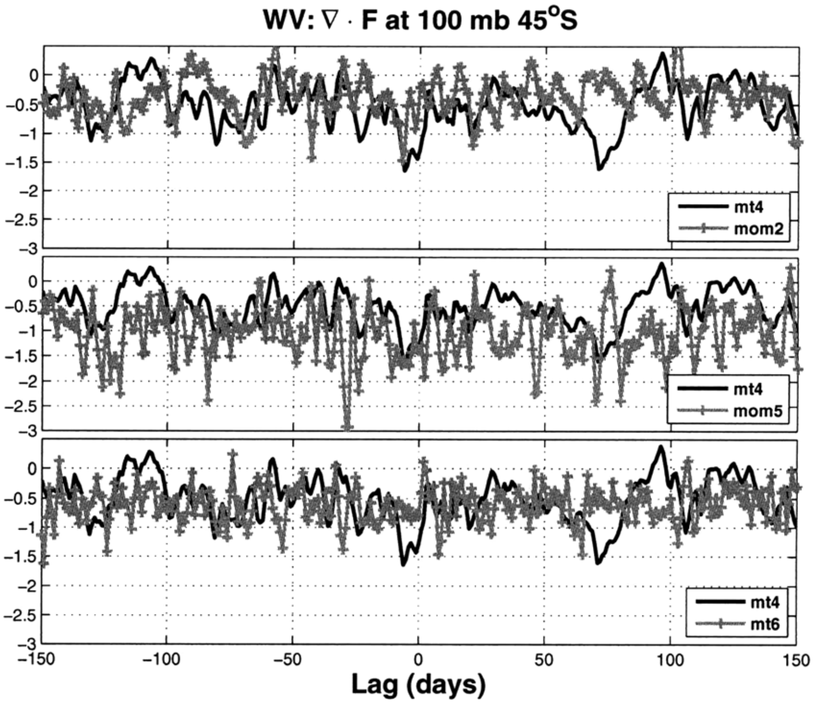

Figure 5.14: Composites of EP flux divergence for wavenumbers 1 and 2 at 100 mb, 45°S for four different experiments. All three plots show the run from mt4. Units are in $m\ s^{-1}$ day^{-1}.

In the fourth experiment, mt6, we chose one with no momentum forcing, but the lower extra-tropical stratospheric winds are as large as the previous experiment. With the mountains shifted to the polar region, there is still not much change to the behavior of the wave drag before and after a weak vortex event.

5.3 Summary

In these last two chapters, we looked at whether changes to the stratosphere led to changes in the characteristics of the troposphere. Using stratospheric weak vortex events as a "perturbation", an examination of the tropospheric behavior was made usually in the form of the annular mode index (AMI). We found that within only a certain parameter space did tropospheric same-signed AMI followed those in the stratosphere, similar to what is found in observations (cf. Baldwin and Dunkerton (2001)).

In general, our model results suggest that the lower extra-tropical stratospheric winds had to be in a certain "window" for the stratospheric influence to take place. More precisely, the distribution of the winds in this location had to span two regimes. As shown in Table 5.2, for high wind speeds the eddy-driven jet resides in the mid-latitudes, while for low winds speeds, the surface westerlies peak in the subtropics. From Fig. 5.3, for one particular run, we see that the correlation is greater than 0.75 for this relationship.

Of course the argument can be made that there is no causality from this statistical correlation. It is possible the eddy-driven jet shifts equatorward causing the mid-latitude winds in the stratosphere to decrease. However, results from the previous section suggest there is a possible mechanism by which there is a "control" in where the eddy-driven jet is located. We speculate that pulses of mid-latitude planetary waves propagating vertically now break in the presence of sufficiently weak winds. This forcing then projects onto the annular modes, and hence, reinforces the jet to shift equatorward. However, when the winds are sufficiently strong, planetary waves will not get dissipated there since the phase speeds are likely far from background winds.

The sensitivity of vertically propagating planetary waves and lower stratospheric winds was examined in greater detail by Chen and Robinson (1992). They found that for anomalously strong vertical shear across the tropopause, more wave activity is trapped into the troposphere. This finding is consistent with what we have found. During the initial weak vortex events, the lower stratospheric winds has weakened. However, relative to those changes, the tropospheric winds have not altered significantly (Fig. 5.13). With the increased vertical shear, less wave activity is entering the stratosphere, as indicated by the strong anomalous convergence of EP fluxes (Fig. 5.12). This forcing can then project onto the annular modes, allowing for the anomalous negative annular mode index to persist further.

This framework is consistent with the results from the last Chapter and summarized in Table 5.1. In the first two experiments, with climatological mid-latitudinal lower stratospheric winds being less than 10 $m\ s^{-1}$ and presumably similar planetary wave phase speeds, it is likely that during weak vortex events, there is significant change in the wave propagation and thus, no significant anomalous wave drag in the lower stratosphere. The middle two experiments lie in the transition region between the two regimes. With support from Fig. 5.12 and Fig. 5.13, they followed the mechanism described above.

It is interesting to note that the first two experiments had larger amplitude topographies than the second two. Intuitively, one might expect larger amplitude planetary waves would result in a stronger stratospheric influence. However, it is the intermediate height mountains that generated the greatest evidence of a two-way coupling and debunking this notion. It appears after some topographical height, the generated heat fluxes wipe out any meridional temperature gradient causing the westerly winds to be weak throughout the troposphere and into the lower stratosphere.

In the final two mountain experiments, we displaced the topographical profile into the polar region. Although the winds were in the window of stratospheric influence, during weak vortex events, composites of the AMI did not show any significant changes. We speculate the source of planetary waves is also important as they will likely influence where they break. Given the likelihood that the wave drag is more distant to the eddy-feedback processes in the mid-latitudes, it is likely the wave drag and its negative momentum forcing can no longer project onto the annular mode, hence tropospheric changes were weak.

An alternative way in explaining the large tropospheric response is through the decorrelation time of the tropospheric internal variability. Unrealistically large values were indicative of a transitional state between two regimes. When the amplitude of the topographies were extremely large, this pushed the tropospheric state far away from the transition zone and into one regime. However, when the topographic heights were lowered, the model reentered back into the transitional zone, and thus, small perturbations would give large responses.

Therefore, to capture the stratospheric role in determining a response to a forcing, an accurate representation of planetary wave propagation is needed. More specifically, the region where wave breaking occurs in relation to the eddy feedback is crucial. This mechanism is consistent with the ideas from Song and Robinson (2004) and Sigmond et al. (2008). The former found planetary waves and the latter found the strength of the lower stratosphere winds to be important. Here, our findings support how the two are related.

Chapter 6

Equatorward and poleward Propagation

6.1 Introduction

We have seen that during certain periods the internal variability of the zonal-mean zonal wind follow a systematic poleward propagation. Fig. 4.2c is an example of such behavior. This has also been noted to occur in observations by Feldstein (2000) and in modeling studies (*e.g.* Son and Lee 2006).

Varying a combination of tropical heating and high-latitude cooling in a tropospheric model, Son and Lee (2006) found a parameter space in which the internal variability can be classified into mainly three categories . When strong tropical heating is applied, the main variability is dominated by clear oscillations of the jet, similar to what is shown in Fig. 4.2a. However, when weak tropical heat forcing is applied explicitly, the behavior of the anomalies is no longer dominated by the annular modes. Instead, the variability can be best described as poleward propagation, similar to what is shown in Fig. 4.2c.

With the annular modes traditionally defined as the leading EOF, the second EOF is typically characterized as a pulsation or weakening. The importance of the second EOF is increased during these period of poleward propagation. Because the variability is no longer a simple oscillation, in order to capture the qualitative structure of the propagation, both

EOFs are needed.

There are significant implications to knowing when the variability is dominated by poleward propagation. Unlike the annular mode like variability where it is dominated by red-noise, poleward propagation is semi-periodic. This has significant implications for extended range weather forecasting. Using Fig. 4.2c as an example, a forecaster at 40°S, in the "middle" of the poleward propagation path, would have a higher-skilled forecast if they knew that mid-latitudes are being dominated by this variability. For instance, at $t = 1550$ *day*, there are anomalous westerly winds at this location. 100 days later the anomalous winds are westerly again, with below-average climatological values in between. Although the decorrelation time of the annular modes is only 30 days, prediction within this regime of 400 days is straightforward.

As noted, although this behavior is found in observations, there is no widely accepted explanation for the cause of this poleward propagation. Many plausible dynamical mechanisms have been proposed (e.g. James and Dodd 1996; Robinson 2000; Lee et al. 2007). However, a complete theory would also include the following two concerns. First, what controls the propagation speed? Second, how does the observed atmosphere "switch" from variability dominated by poleward propagation to one where the jet oscillations appear to be stochastic?

In Lee et al. (2007), they proposed that it was the synoptic waves that were responsible for driving the poleward propagation. If the eddy-driven jet is in the mid-latitudes, baroclinic waves would originate from this region and propagate equatorward. When they reach the critical latitude (when $u = c$) in the tropical region, the waves break and reduce the background winds; hence, the critical latitude will shift poleward. When subsequent mid-latitude waves form and propagate equatorward, they too will break at the critical latitude and once again shifting the region of wave breaking poleward and in essence, perpetuating this appearance of anomalies propagating poleward. Since waves cannot penetrate past the critical latitude, equatorward of this, in the absence of any dynamical forcings, the model's radiative relaxation causes the winds to return westerly again. So, in short, this mechanism is dependent on the eddy momentum fluxes in driving this variability.

Exp. Name	Ts. of EMF?	Ts. of EHF?	Ta. of EMF?	Ta. of EHF?
zsm1	yes	yes	no	no
zsm2	no	yes	yes	no
zsm3	yes	no	no	yes

Table 6.1: List of experiments using the zonally-symmetric model (zsm). Ts., Ta, EMF, EHF, τ is an abbreviation for timeseries, time-average, eddy momentum fluxes, eddy heat fluxes and the decorrelation of the leading mode of variability, respectively.

6.2 Relative roles of eddy heat and momentum fluxes

Mainly prompted by the results from the next section and the work of Lee et al. (2007), we will investigate whether eddy heat or eddy momentum fluxes are responsible in driving poleward propagation. The mechanism described by Lee et al. (2007) suggest that it is the eddy momentum fluxes that are crucial to the variability. As we will see in the next section, the eddy heat fluxes seemed largely responsible for driving the systematic migration in a zonally-rentrant oceanic GCM. So here, we will take a tropospheric-only model, as described in section 2.3.

Taking a model run where the variability has manifested as poleward propagation, we will calculate the eddy heat and eddy momentum fluxes. Using a zonally-symmetric version of the model, as described in section 2.4, we will then input these eddy statistics. Inputting only one of the timeseries (instead of both), we can determine which one can reproduce the poleward propagation.

The top panels of Fig. 6.1 and Fig. 6.2 shows the climatology of the full model and the zonally-symmetric model, respectively. In the latter experiment, we input both the timeseries of the eddy momentum and eddy heat fluxes, $zsm1$ (Table 6.1). The climatology for both models are nearly identical. Both have surface westerlies between 30°S and 55°S with the jet in the upper troposphere around 43°S. Although the magnitude of the subtropical

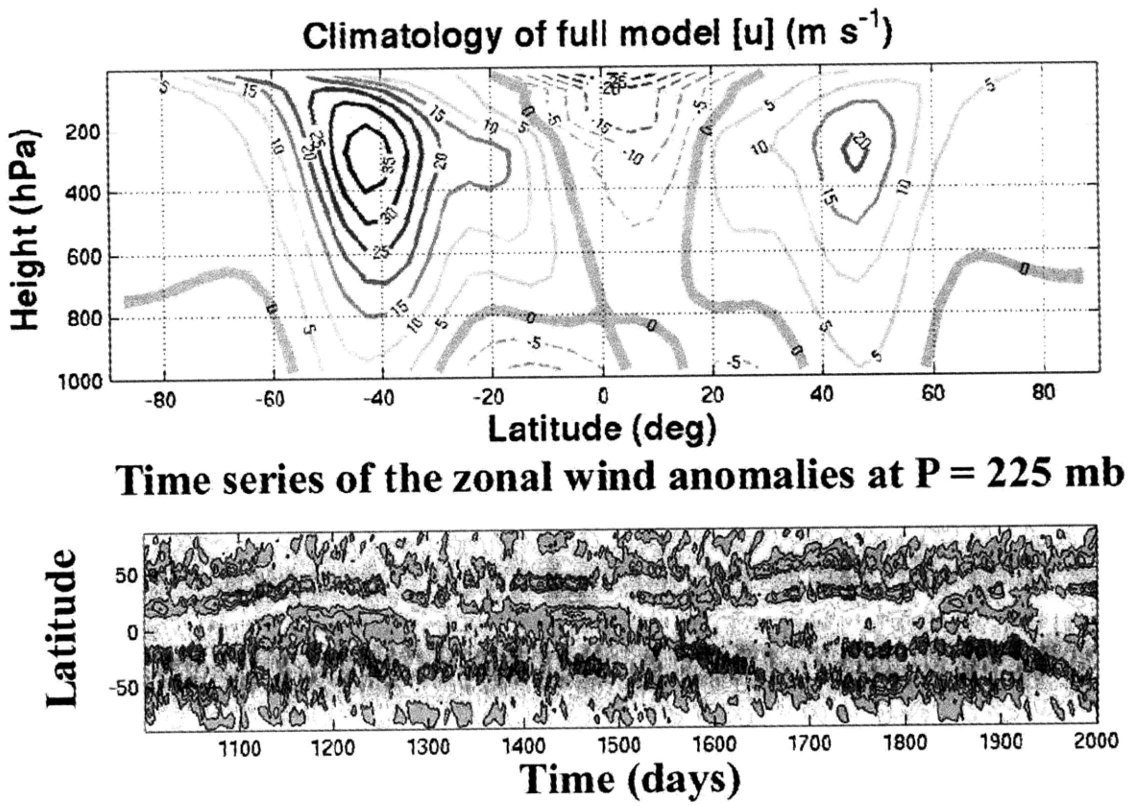

Figure 6.1: Full-model climatological zonal-mean zonal winds (top panel) and timeseries of the zonal-mean zonal wind anomalies (bottom panel). Units are in $m\ s^{-1}$. Contours are every 5 $m\ s^{-1}$ with the zero contour thickened for the top panel and every 2 $m\ s^{-1}$ with the zero contour omitted. .

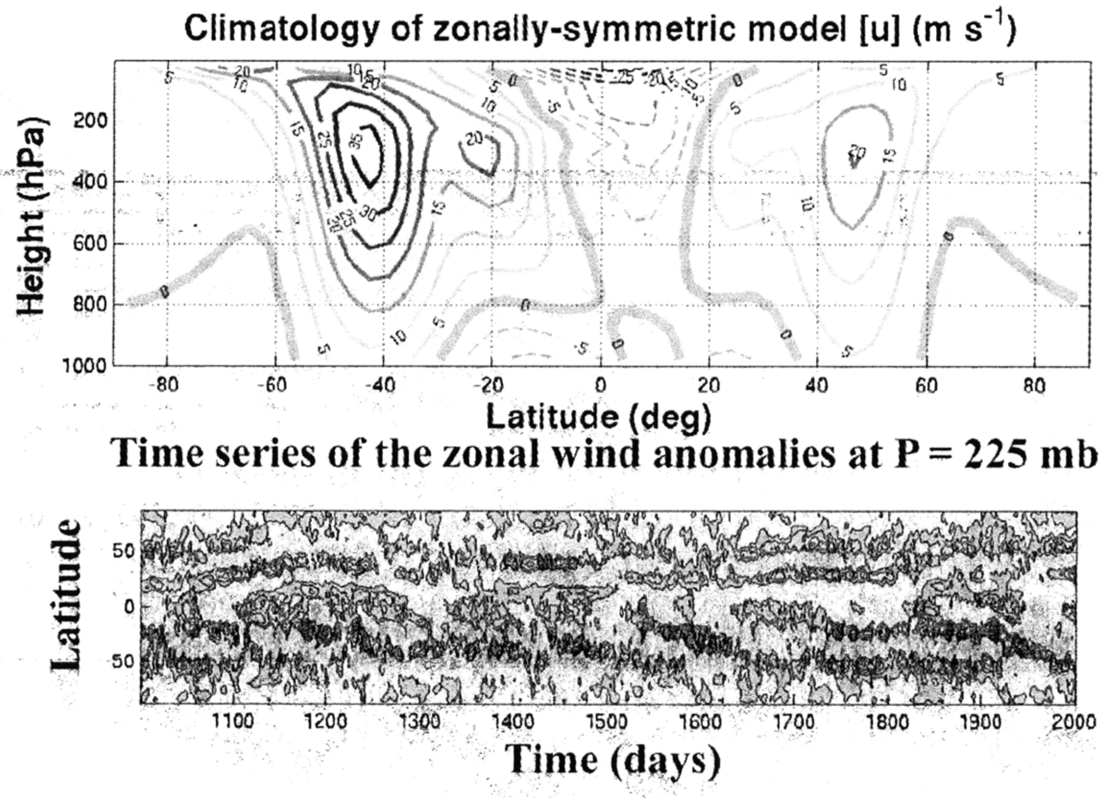

Figure 6.2: Same as Fig. 6.1, but for zonally-symmetric model instead.

jet is slightly stronger in the zonally-symmetric model, the maximum wind speed in the troposphere both peak at about 38 $m\ s^{-1}$.

Not only was the zonally-symmetric model (forced by the eddy statistics from the control run) able to reproduce the climatology of the full model, the anomalous activity was also captured. A comparison of the bottom panel of Fig. 6.1 and Fig. 6.2 show that they too are very similar. Not only are the magnitudes of the anomalous activity captured, but the structure as well. For instance, in between times of 1450 days and 1650 days, both models have poleward propagation during these times, an indication that the zonally-symmetric model has correctly reproduced the climatology and internal variability.

Instead of inputting both the timeseries of the eddy momentum fluxes *and* eddy heat fluxes into the zonally-symmetric model, we will choose one and force the model with the time-average of the other. This is indicated as exp. $zsm2$ and exp. $zsm3$ in Table 6.1 and allows for a direct comparison to examine how the internal variability would behave if the eddy heat or eddy momentum fluxes acted "alone." (We note that it is nearly impossible to perfectly separate the two since the eddy heat fluxes were likely strongly influenced by the eddy momentum fluxes in the full 3-dimensional model run, and *viceversa*. So while it is not precise to say that the components of the EP fluxes are perfectly independent of one another, we do suspect they are largely separated.)

A timeseries of the zonal wind anomalies in the upper troposphere in $zsm2$, the case where the evolution of the eddy heat fluxes and the time-average of the eddy momentum fluxes were explicitly forced, is shown in the middle panel of Fig. 6.3. For ease of comparison, the top panel of Fig. 6.3 is the same as the bottom panel of Fig. 6.1 and is from the full 3D model. Not surprisingly, in the absence of compensating momentum fluxes, in general, the magnitude of the anomalies are stronger than from the 3D model. In addition, the poleward propagation is not evident at any point in the simulation.

The same is true in $zsm3$. When inputting the evolution of the eddy momentum fluxes and the time-average of the eddy heat fluxes, there is no hint of poleward propagation (bottom panel of Fig. 6.3. In fact, the structure of the zonal wind anomalies appears much more annular mode like than that of the 3D run and certainly more so than that of $zsm2$, suggesting it may be heat fluxes that generates the poleward propagation.

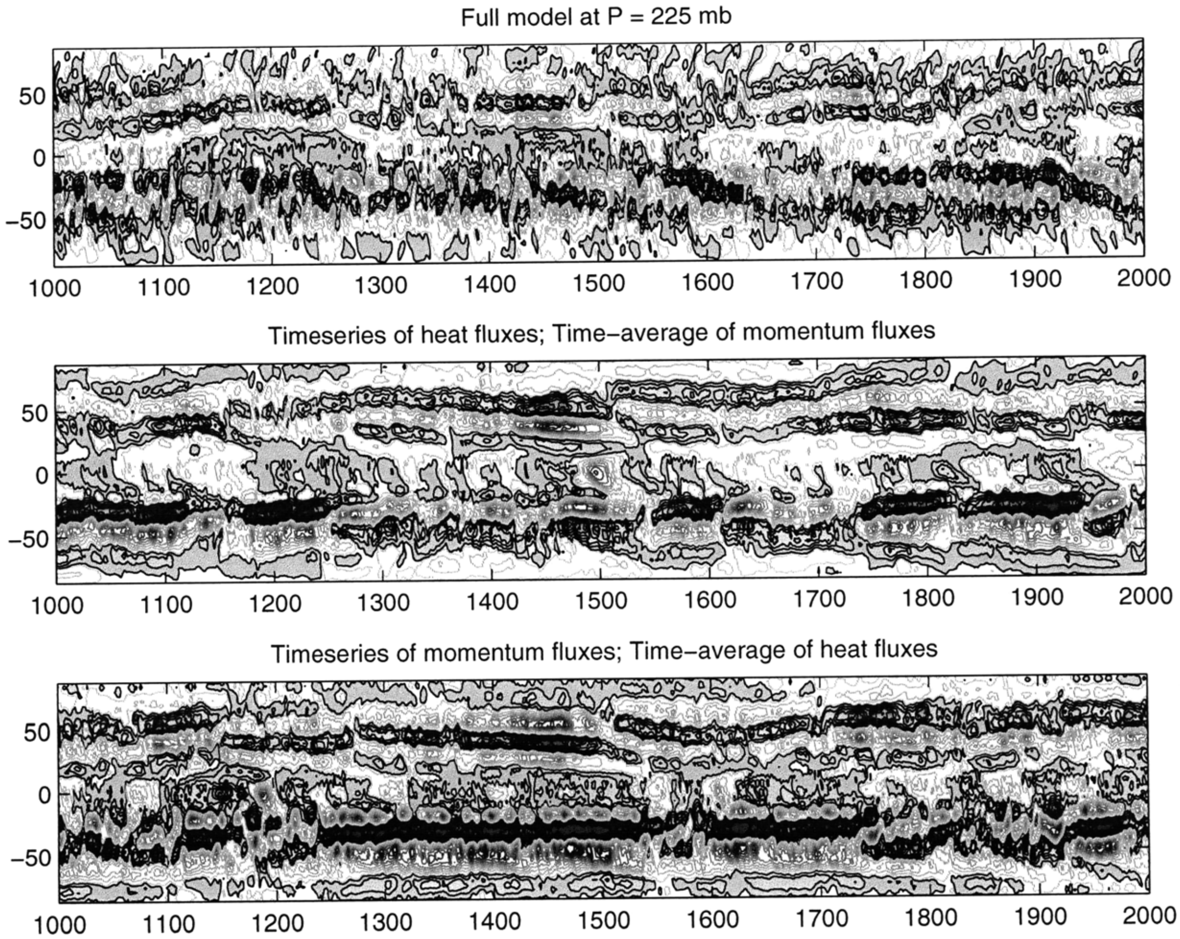

Figure 6.3: Time series of the zonal-mean zonal wind anomalies for $zsm1$ (top panel), $zsm2$ (middle panel) and $zsm3$ (bottom panel). The top panel is the same as bottom panel of Fig. 6.1. List of experiments and their characteristics are shown in Table 6.1. Here, the contour intervals are every 3 $m\ s^{-1}$, with the zero contour omitted and positive values filled.

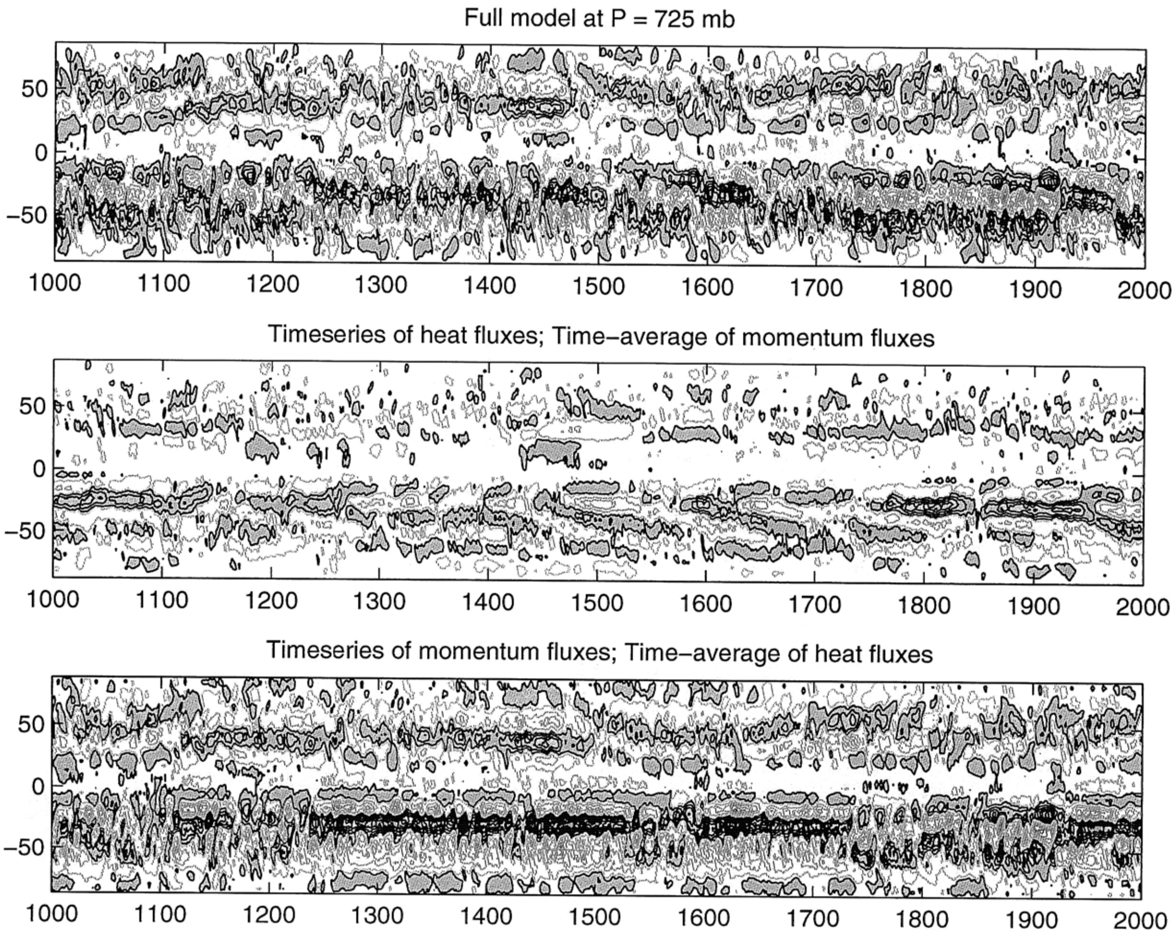

Figure 6.4: Same as Fig. 6.3, but for a pressure level of $725mb$. Contours are every $1\ m\ s^{-1}$ with the zero contour omitted and positive values filled

This can be better seen from the lower levels. Fig. 6.4 shows the wind anomalies at $725mb$ from the three model runs, with the middle panel matching the variability from the full model run best. This was the zonally-symmetric model that inputted the climatological value for the eddy momentum fluxes, while adding the daily variability of the eddy heat fluxes into the temperature equation Since the bottom panel, which incorporated the daily variability of the eddy momentum fluxes, did not exhibit any signs of poleward propagation, the conclusion here is that the eddy heat fluxes seem to be important in driving this type of variability.

The fact that $zsm2$ did not seem to capture the poleward propagation in the upper levels prevents us from being fully confident that it is the eddy heat fluxes that are important in driving the poleward propagation. However, eddy heat fluxes are typically strongest in the lower and weak in the upper troposphere. Thus, it may not be a surprise that the $zsm2$ was unable to capture this type of variability. However, the fact that $zsm3$ was unable to reproduce the poleward propagation in the upper levels is a bit concerning.

6.3 Equatorward migration in an oceanic GCM

Now that we have seen that eddy heat fluxes seem responsible for the migration of the zonal wind anomalies, we will take a closer look at the processes involved. For simplicity, we will use an oceanic, zonally-rentrant GCM discussed in section 2.5. In this section, we describe some characteristics of zonal jets in a model driven by a steady eastward wind stress which peaks in middle latitudes. The model simulation was run as a testbed for ideas on eddy transport, and its major, climatological, characteristics are described elsewhere (Cerovecki et al., 2009). As discussed in Chan et al. (2007), here, we will focus on the time variability of the zonal jets in the model. At any instant in time, the mean zonal flow comprises a dominant jet, together with two or three secondary jets, primarily on its poleward side. The main jet wobbles quasi-periodically, in a manner that appears similar to the "annular mode" behavior of atmospheric jets. At the same time, the secondary jets, poleward of the main jet, migrate systematically equatorward such that, once every period of the main jet's fluctuation, one secondary jet merges with the main jet, while another appears at the poleward flank of the secondary jets.

Multiple jets have long been understood to occur in wide domains, and demonstrated in models ranging in complexity from barotropic and shallow water through to two-level quasi-geostrophic and multilevel primitive equation models (*e.g.*, Williams, 1978; Panetta, 1993; Cho and Polvani, 1996; Lee, 2005). Such structures have been observed in jets in the ocean (*e.g.*, Roden, 2000) and in the atmospheres of Jupiter and Saturn (*e.g.*, Pater and Lissauer, 2001). A recent discussion of the dynamics of the formation of multiple jet structures, and factors controlling their width, can be found in Dritschel and McIntyre (2008). While most of these studies have not revealed any tendency for the jets to migrate, systematic equatorward migration of multiple jets, under some circumstances, has been described by Williams (2003) in a model of Jupiter's atmosphere.

There are two, related, points of interest in this section . First, the correspondence between the migration of the secondary jets and the oscillation of the main jet appears to be a manifestation of "annular mode" behavior in a multiple jet environment which, to our knowledge, has not been reported before. In fact, we shall show that most of the variance in the zonal flow is captured by two spatial structures, each of which projects onto both the main jet and the secondary jets and which, taken together, describe the simultaneous oscillation/migration pattern. Second, while the narrowness of the jets is maintained by eddy momentum fluxes (as has long been understood), their equatorward migration is a response to the eddy heat fluxes, which act to reduce the baroclinicity on the poleward flank of the jets and increase it on the equatorward flank. We speculate that this behavior is ultimately determined by the latitudinal gradient of thebackground static stability.

The structure of this section is as follows. The time-averaged features is presented in the next section, followed by an analysis of the spatial and temporal variability. Finally, properties of the baroclinic eddies, their effect on the zonal mean flow and, in particular, their relation to the migration of the secondary jets are discussed in section 4.

6.3.1 Time-averaged statistics

Despite the deformation radius increasing monotonically from about 10 km at 40°S to about 100 km at 15°S, the length scale of the forcings, shown in Fig. 2.10, are more than one to two orders of magnitude larger than the Rossby radius of deformation. With such a broad forcing, it is not surprising that multiple jets emerge (Panetta 1993). Fig. 6.5 shows the time-mean zonal flow. A strong eastward jet (herein after the "main jet") is located at 17°S, while a weaker westward flow on its equatorward side. Poleward of the main jet is another eastward jet at about 26°. We shall see in what follows that this is the time-averaged remnant of several, time-dependent secondary jets.

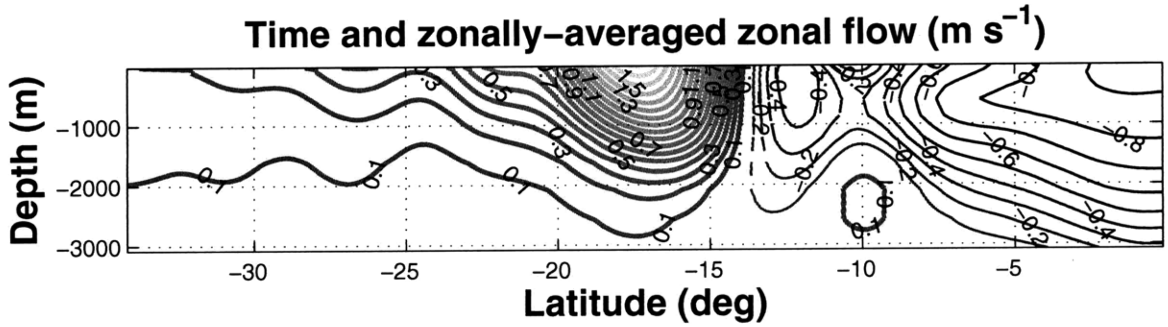

Figure 6.5: Time and zonally-averaged zonal flow. Contour interval is 0.1 m s^{-1}. Zero contour is omitted.

Fig. 6.6 shows the time-averaged density and potential vorticity (PV) distributions. Poleward of 12°S, PV is homogenized along isopycnals in the near-adiabatic interior. This region of homogenized PV coincides with the region of baroclinic eddy activity (Cerovecki et al. 2009). PV gradients do appear in the non-adiabatic region near the surface, as is evident in Fig. 6.6, but the contribution in the surface "PV sheet" (Bretherton 1966) associated with the surface temperature gradient is not visible on the figure. To illustrate this point in the presence of multiple migrating jets, we show in Fig. 6.7(a) a snapshot of the zonally-averaged zonal flow, and (b) the quasi-geostrophic PV gradients integrated through the top 165 m (including the surface PV sheet) and (c) the quasi-geostrophic PV gradient at a typical interior level. As shown, the surface PV gradient dominates. Consistent with the arguments of Dritschel and McIntyre (2008), each jet is associated with a sharp eddy-transport barrier.

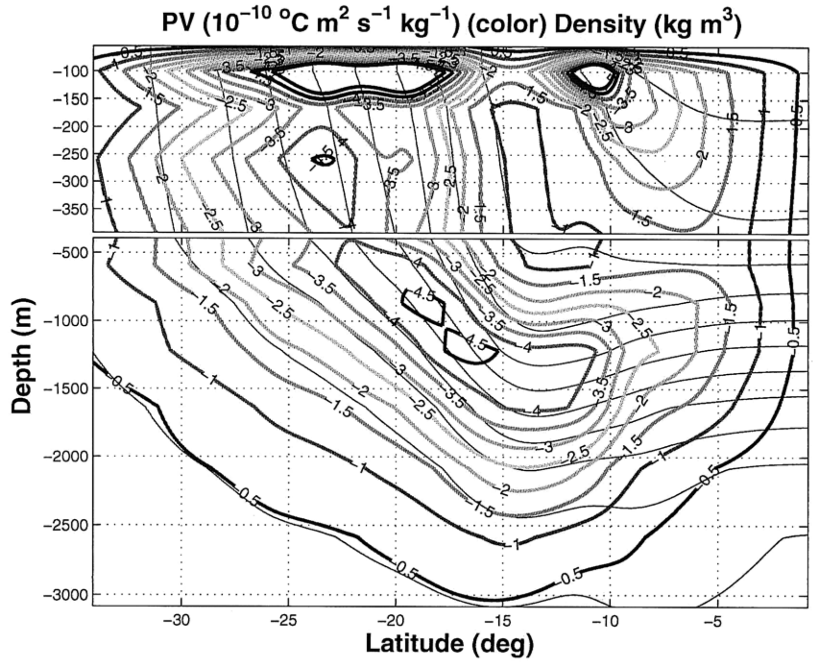

Figure 6.6: Time-averaged quantities of Ertel's potential vorticity (thick line) and isopycnals (thin line) with a contour interval of 0.5 x 10^{-10} °C m^2 s^{-1} kg^{-1} and 0.5 kg m^{-3}, respectively. Note the top 400m has been enlarged.

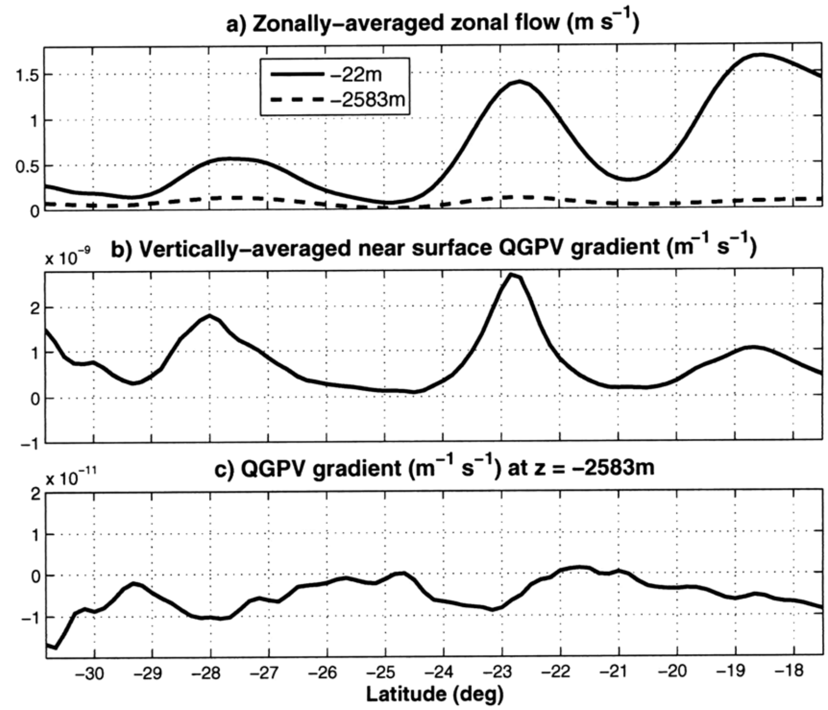

Figure 6.7: Snapshot for year 1052 of (a) the zonally-averaged zonal flow near the surface and in the interior (b) the vertically-averaged (top 165m) quasi-geostrophic potential vorticity gradient and (c) the interior quasi-geostrophic potential vorticity gradient. The vertical scale of (b) and (c) are different. Note that the near-surface gradient shown in (b) includes the contribution from the surface temperature gradient in the surface "PV sheet" and, in fact, is dominated by that contribution.

There are multiple PV "steps", i.e. the gradients are concentrated at each jet, and weak everywhere else. However, in our case the PV steps are manifested not in the interior, but rather in strong, localized gradients of surface temperature.

The static stability varies greatly in depth and in latitude, as indicated in Fig. 6.8. At any particular depth, the stability at all depths monotonically increases equatorward up to approximately 20°S. As for the whole domain, several extrema are present. Perhaps, the most obvious is located between $-15°$ and $-10°$ above a depth of 750m, a region associated with mode water formation (Cerovecki and Marshall 2008).

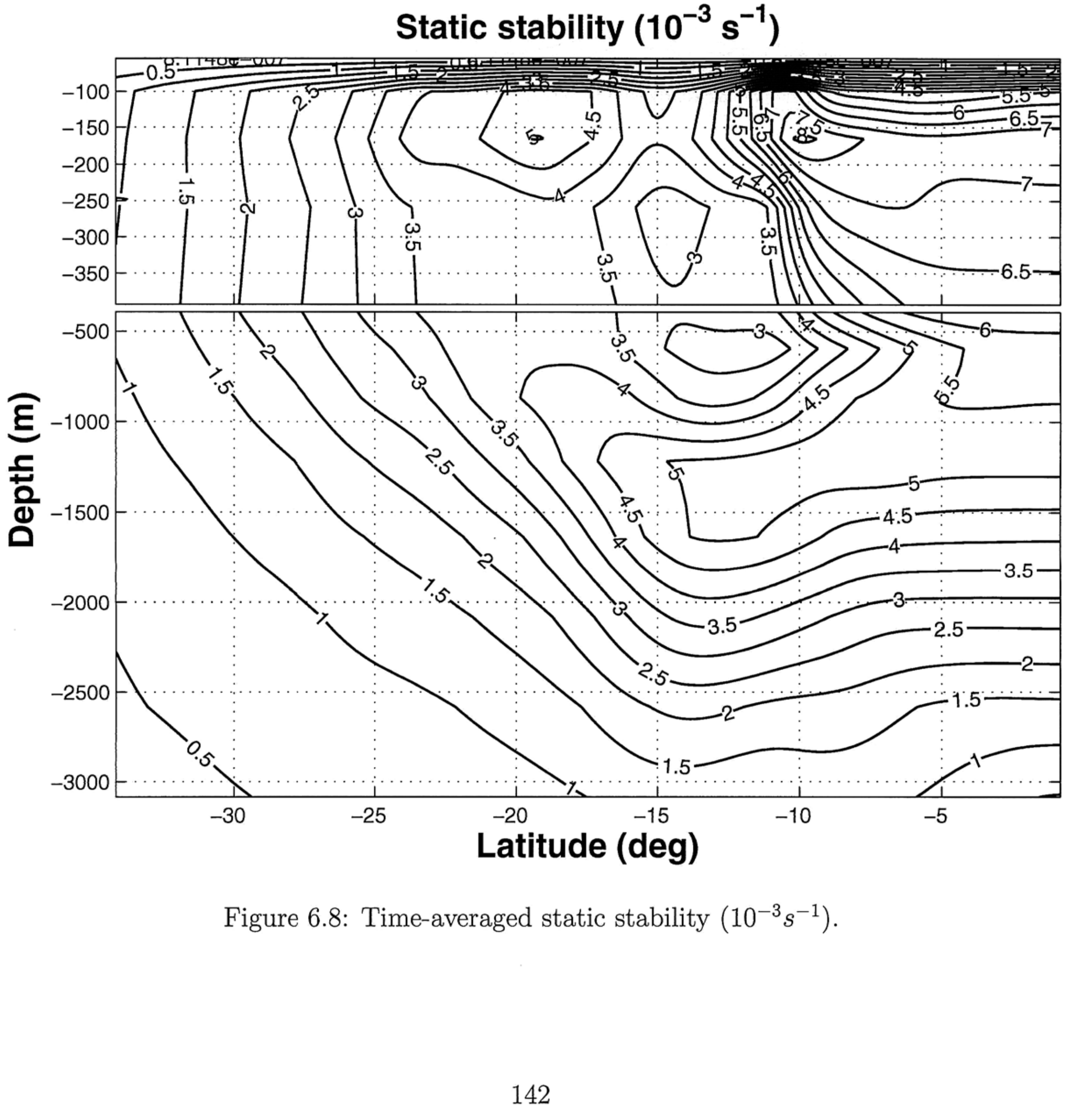

Figure 6.8: Time-averaged static stability ($10^{-3}s^{-1}$).

6.3.2 Description of Variability and EOF Phases

Fig. 6.9 shows the annual-mean zonal flow, year by year over a nine year period. While the main jet oscillates meridionally, two to three secondary jets migrate equatorward and each eventually merges with the main jet. Fig. 6.10 shows the vertically-integrated, zonally-averaged zonal flow anomalies as a function of latitude and time. The equatorward migration is clearly seen poleward of the primary jet, in particular, between 20°S and 35°S. From the emergence of the secondary jet around 30°S to the time it takes to reach the primary jet varies from 8 to 12 years and is a robust feature of this model.

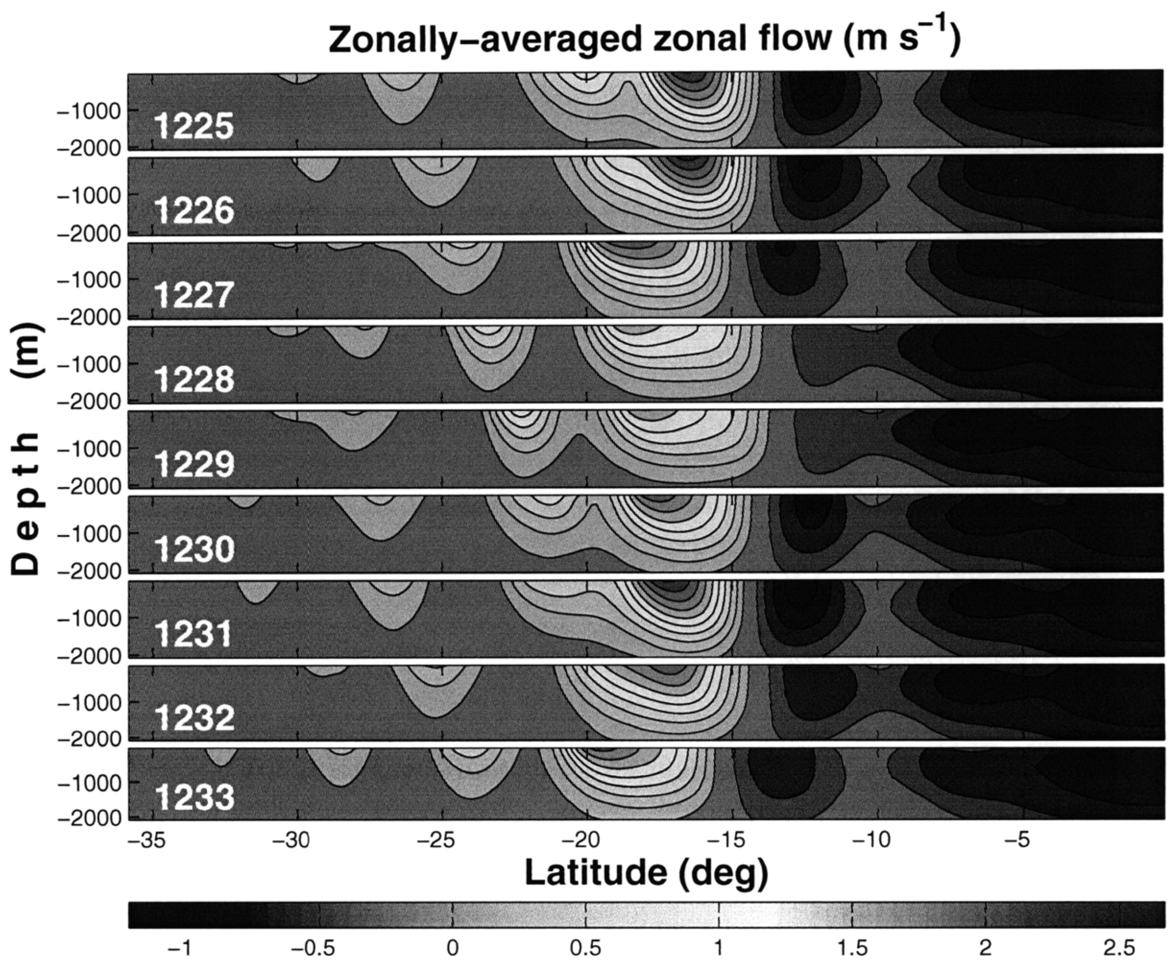

Figure 6.9: Timeseries of the annually- averaged zonally- averaged zonal flow. Time stamps (in years) are located on bottom left corner of each plot. Contour interval is 0.25 m s^{-1} and the zero contour is omitted.

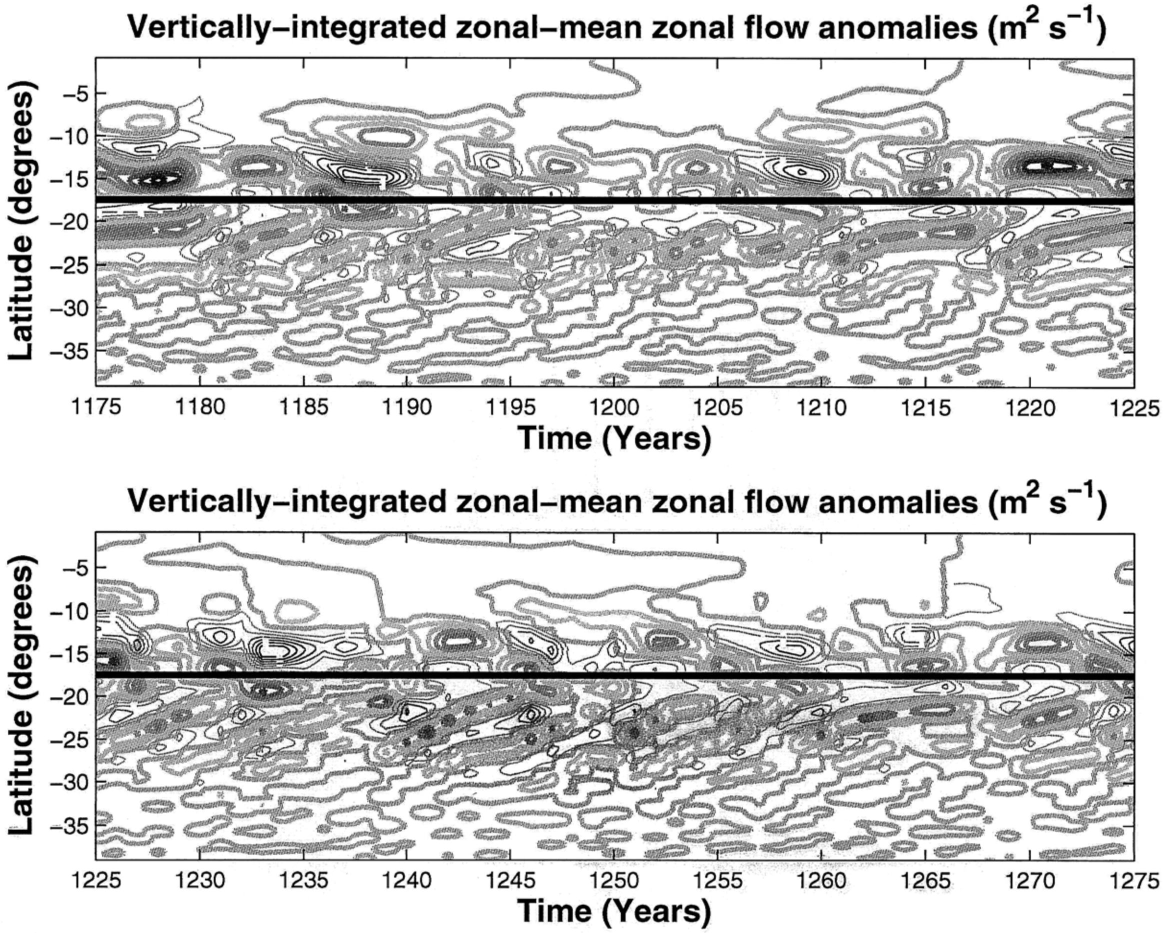

Figure 6.10: Time series of the anomalous vertically-integrated zonally-averaged zonal flow. Positive contours start at 20 and increase in increments of 200. Negative contours (dashed lines) start at -200 and are also in increments of 200. Thick black line represents the time-averaged position of the main jet.

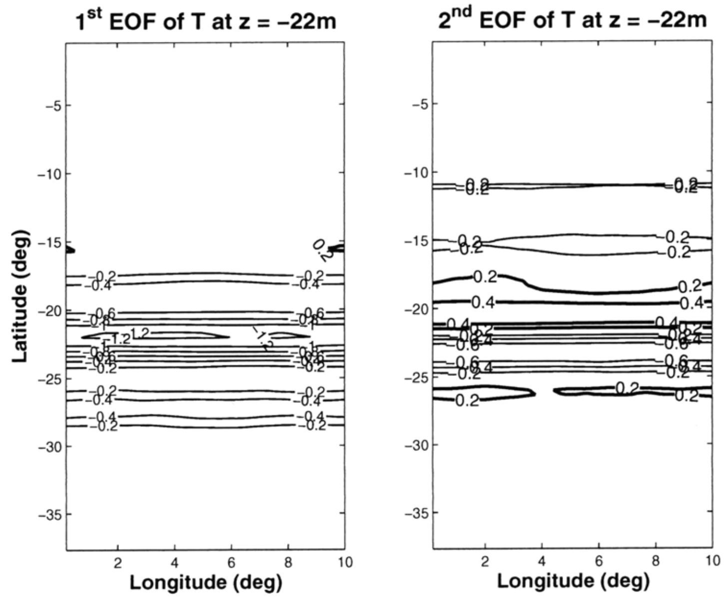

Figure 6.11: The leading two EOFs of the annually-averaged temperature at the surface layer. The percent variance is shown in the bottom left corner.

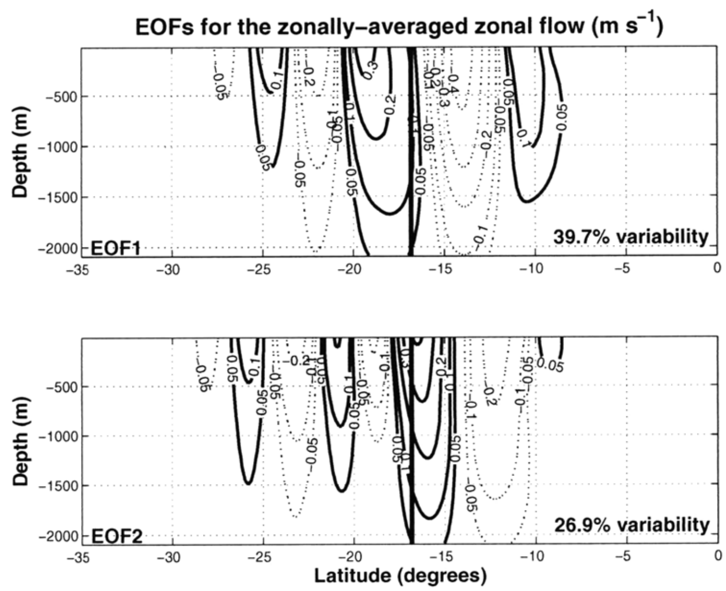

Figure 6.12: The leading two EOFs of the annually-averaged zonal-mean zonal flow. Solid (dashed) lines represent positive (negative) values. Note the nonuniform contour interval. Vertical black line indicates position of the time-averaged jet. The percent variance is shown in the bottom right corner.

Although less obvious, there is some evidence of zonal flow anomalies propagating poleward between $-10°$ and $-15°$. Compared to the equatorward migration at higher latitudes, the poleward propagation occurs less systematically and over a shorter range. Because of its close proximity to the main jet, entangling its influence with the zonal flow anomalies itself become difficult. Consequently, our discussions of propagating zonal flow anomalies will mainly focus on the region of systematic equatorward propagation between $-20°$ and $-30°$.

The spatial and temporal variability of the entire time series can be best quantified by the use of empirical orthogonal functions (EOFs). The data were weighted to account for the decrease in area around latitude circles toward the pole, but were not weighted to account for the varying layer depths. This will not be important as we are mostly interested in the horizontal variations of the zonal flow. Using the North et al. (1982) test, the first and second EOFs are-well separated.

Fig. 6.11 shows the horizontal structure of the leading two EOFs of the annually-averaged surface temperature. With the model forcings independent of longitude, it comes as no surprise that there is little longitudinal variability. Thus, for the remainder of the paper, we consider zonal-mean budgets and explicitly examine the variability of the zonally-averaged zonal flow.

As shown in Fig. 6.12, EOF1 displays an "equivalent barotropic" structure with maximum absolute anomalies at 19°S and 14°S. The vertical black line represents the time-averaged location of the primary jet's maximum value (17.2°S). By comparing the mode's spatial structure and the mean location of the jet, EOF1 describes meridional fluctuations of the main jet, or in other words, it captures the jet "wobbling" in the north-south direction. This mode constitutes the largest amount (39.5 percent) of the total variability. In EOF2, the maximum anomalies are almost coincident with the mean location of the jet. Therefore, this mode indicates the intensifying and weakening of the main jet. Given the structure of the EOFs in Figs. 6.11 and 6.12, therefore, the spatial variability near the primary jet appears to be analogous to the atmospheric annular modes; the leading mode describes oscillations of the main jet, while the second mode captures its enhancement (*e.g.* Lorenz and Hartmann 2001) just as it does in the atmospheric eddy-driven jet.

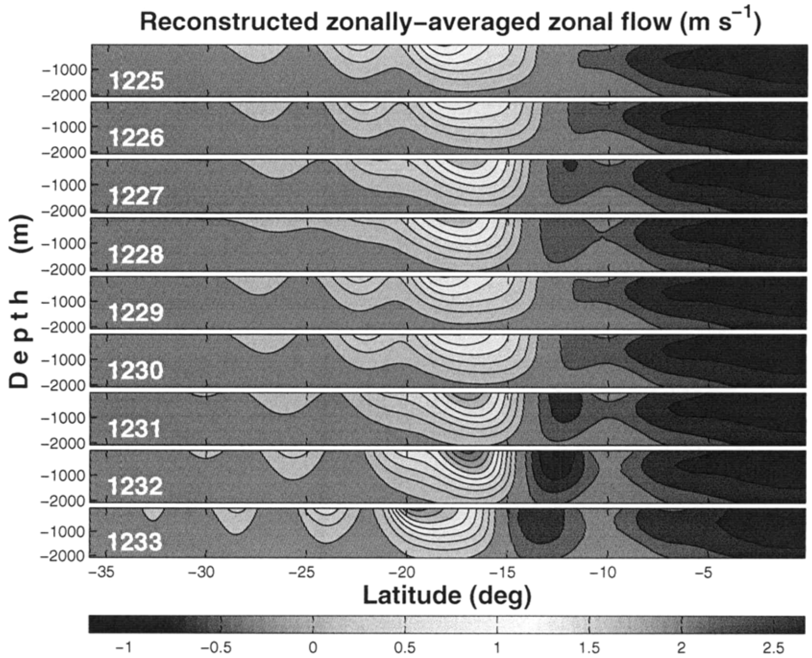

Figure 6.13: Time series of the reconstructed zonal flow using the leading two EOF modes and the time-averaged zonal flow.

Unlike the atmospheric case, there is an obvious non-dipole structure in both modes; poleward of 20°S, three to four more additional extrema are present. These features capture the migrating secondary jets, with EOF2 comparable in magnitude with, and in quadrature with, EOF1 in this region. Thus EOF2 must account for more variance than is typical in the atmospheric case. Higher order components are weaker with EOF3 capturing eleven percent and successive EOFs less than four percent; therefore, as Fig. 6.13 shows, the evolution of the zonal flow is well captured by the first two EOFs (*cf.* Fig.6.9).

The principal component captures the temporal variations associated with the spatial pattern of the EOFs. For instance, when the primary jet is displaced poleward (equatorward), the principal component associated with EOF1, PC1, will be positive (negative). Similarly, when the zonal flow at the primary jet is anomalously positive (negative), the principal component associated with EOF2, PC2, will be positive (negative).

Now that we have established how well the variability in the zonal average of $u(y,z,t)$ is represented by the two EOFs, we define the following four phases (shown in Table 6.2)

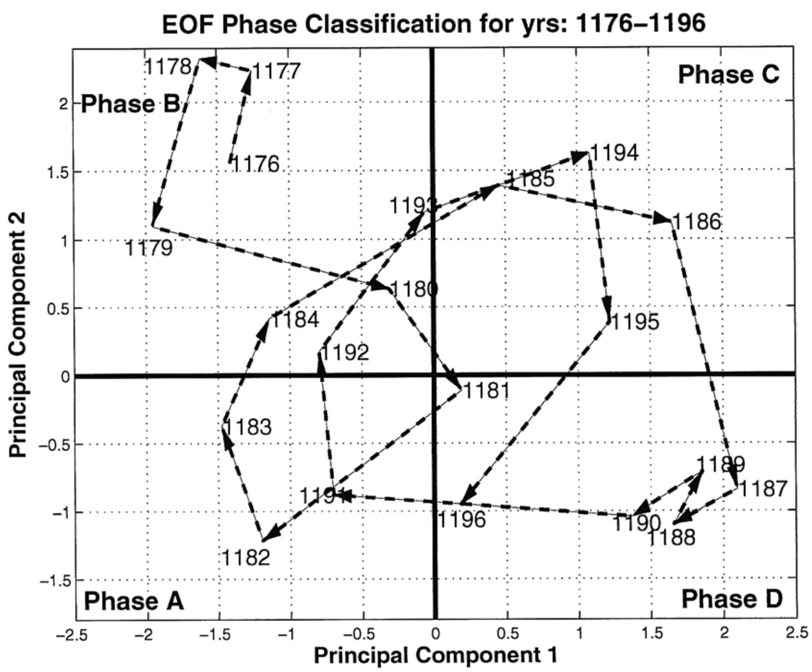

Figure 6.14: The timeseries of the leading two principal components in PC space. The EOF phases are described in Table 6.2 and labelled in each quadrant. Each point is a one year average.

	Phase A	Phase B	Phase C	Phase D
PC1	Negative	Negative	Positive	Positive
PC2	Negative	Positive	Positive	Negative
Displacement	Equatorward	Equatorward	Poleward	Poleward
Strength	Decreasing	Increasing	Increasing	Decreasing

Table 6.2: Physical characteristics of the primary jet in the four EOF phases.

to capture both the temporal and spatial variability. For instance, we define Phase A as PC1<0 and PC2<0, Phase B as PC1<0, PC2>0, etc. A graphical representation of the four phases is shown in Fig. 6.14, as well as an example of a twenty-one year time series in the PC space. Throughout the 313-year time series, there is a sense of generally clockwise rotation, such that the following sequence occurs: Phase A $\rightarrow$ Phase B $\rightarrow$ Phase C $\rightarrow$ Phase D and then repeats back to Phase A. Since the secondary jets migrate, the principal components of both modes need to change sign to allow the secondary jets to advance equatorward and hence, this sequence is ultimately dictated by the behavior of the secondary jets.

	Phase A	Phase B	Phase C	Phase D
Prior to Phase A	–	7%	29%	64%
Prior to Phase B	85%	–	15%	0%
Prior to Phase C	16%	79%	–	5%
Prior to Phase D	19%	6%	75%	–
Prior to High Zonal Index	26%	74%	–	–
Prior to Low Zonal Index	–	–	39%	61%

Table 6.3: Statistical results on the conditions prior to the onset of each phase and zonal index.

Now that we have defined these four phases of the oscillation, we can thus describe the evolution of the structure of the zonal mean state as well as eddy fluxes by compositing all years associated with each phase. When analyzing migrating jets, a time-average would "smooth" out its spatial structure. However, by defining these four phases, we will now be able to capture and examine the migrating jets. An example, which will be discussed in greater detail later, is shown in Fig. 6.20. The sequence shows that the primary jet wobbles, while the secondary jets migrate equatorward, precisely the behavior shown in Fig. 6.9. We can think of this sequence as a typical eight year cycle with each phase representing roughly two years.

Table 6.3 shows how closely the sequence was followed. Each change in phase is followed by the correct phase at least sixty-four percent of the time, e.g. the conditions prior to the onset of Phase A were correctly described to be in Phase D sixty-four percent of the time and incorrectly by Phase B or C thirty-six percent of the time. Similarly, Phase A described the PC space prior to Phase B eighty-five percent of the time. This shows that these pre-conditions are not symmetric, e.g. there is a stronger relation between Phase A and Phase B than there is between Phase D and Phase A.

Given the results in Table 6.3 and Fig. 6.20, there is a correlation between the strengthening of the main jet and the arrival of the migrating jets. When the secondary jet is closest (Phases B and C), there is also an intensification of the primary jet (see Table 6.2). The implication is that as the migrating jet approaches, the main jet intensifies then displaces poleward (Phase C), the side of the approaching secondary jet. Conversely, in Phases A and D, where the strength of the main jet decreases, the closest secondary jet is further away. One last statistical result worth mentioning, brings attention to the duration of each phase. For our 313-year model study, Phase A constituted 95 years in total, nearly twenty percent more than any other phase. Concurrent with anomalous weak eddy activity, the low zonal index (i.e. when PC1 is negative) lasting for longer durations appears consistent with the study done by Feldstein and Lee (1996), who examined the zonal index of the atmospheric jet in an aquaplanet.

6.4 The role of eddies in the flow evolution

The zonal flow anomalies shown in Fig. 6.10 are observed to persist on time scales that are larger than the frictional timescale associated with the bottom drag. Eddy-mean flow interaction is the only process capable of maintaining these anomalies.

The zonal momentum equation for quasi-geostrophic motion can be written as:

$$\frac{\partial[u]}{\partial t} - f[v] = -\frac{\partial[u'v']\cos^2\phi}{a\cos^2\phi\partial\phi} + \frac{\partial[\tau]}{\partial z} \tag{6.1}$$

where square brackets represent zonal averages, primes denote deviations therefrom, τ represents the applied forcing and the bottom friction. Integrating the entire column, we obtain:

$$\frac{\partial < [u] >}{\partial t} = -\left\langle \frac{\partial[u'v']\cos^2\phi}{a^2\cos^2\phi\partial\phi} \right\rangle + [\tau_{surf}] - [\tau_{bot}] \tag{6.2}$$

where vertically-integrated values are represented by angle brackets, the Coriolis force vanishes owing to mass conservation, τ_{surf} is the applied wind forcing shown in Fig. 2.10a; the bottom stress, τ_{bot}, is calculated in the model as:

$$\tau_{bot} = 2A_z\frac{u_{bot}}{\delta_{bot}} + C_D u_{bot}\sqrt{\frac{1}{2}(u_{bot}^2 + v_{bot}^2)} \tag{6.3}$$

where A_z is the vertical viscosity, u_{bot} and v_{bot} is the zonal and meridional velocity, respectively, at the bottom of the ocean; δ_{bot} is the thickness of the bottom layer, C_D is the bottom drag coefficient. (For specific values, see Cerovecki et al. 2009.)

The time-averaged momentum budget is discussed in Cerovecki et al. (2009). The three terms on the right-hand side of (6.2) must balance. The wind stress is balanced, on the broad scale, by bottom drag as shown in Fig 6.15. However, there are spatial variations in the latter on the jet scale that do not correspond to features in the wind stress; rather, these variations balance the convergence of eddy momentum fluxes (e.g. Held 1975; Ioannou and Lindzen 1986.)

Since we are interested in the equatorward migration of the zonal flow anomalies, we will here examine departures from the time mean of (6.2). Since the wind forcing was held constant in time, there is only a three-way balance between the vertically-integrated flow

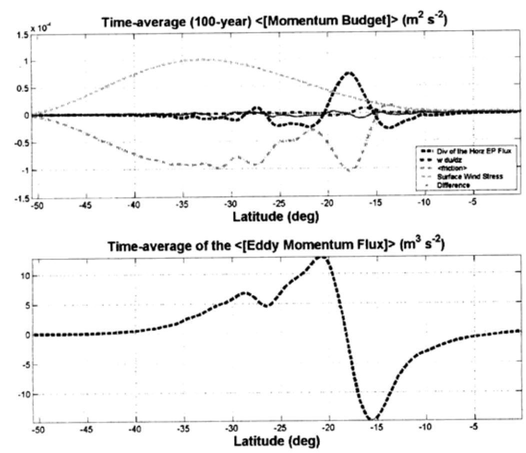

Figure 6.15: (a) Time-averaged quantities of the vertically- integrated zonally- averaged zonal momentum budget. Adapted from Cerovecki et al. (2009) (b) Time average of the vertically-integrated eddy momentum flux $< [u'v'] >$.

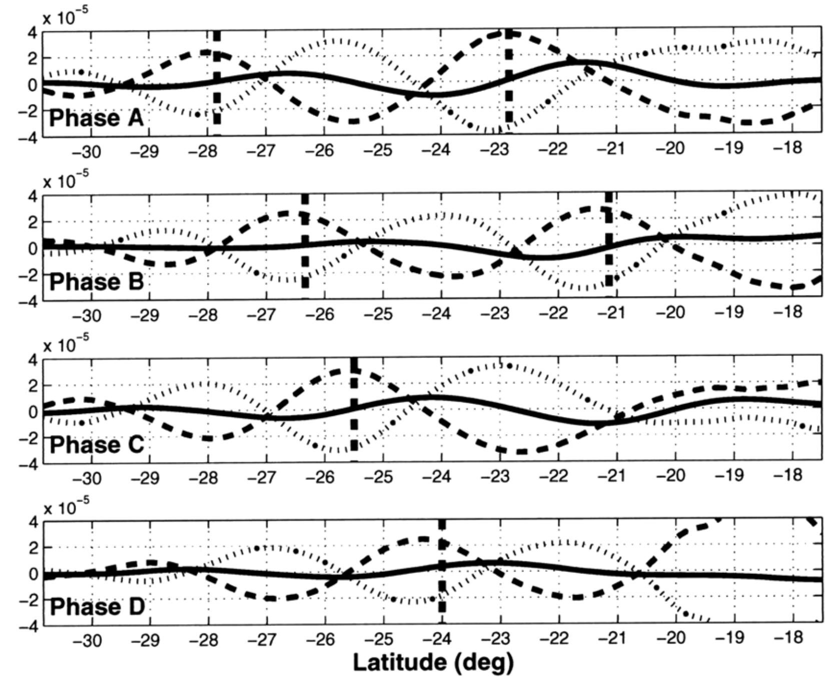

Figure 6.16: Anomalous quantities of the vertically-integrated zonally-averaged zonal momentum budget for each EOF phase composite labelled at the bottom left corner of each plot. Solid line is the flow tendency; long-dashed line is the eddy momentum flux convergence; vertically-dashed line is the friction. Vertical dashed lines correspond to the maximum positive zonal flow anomalies.

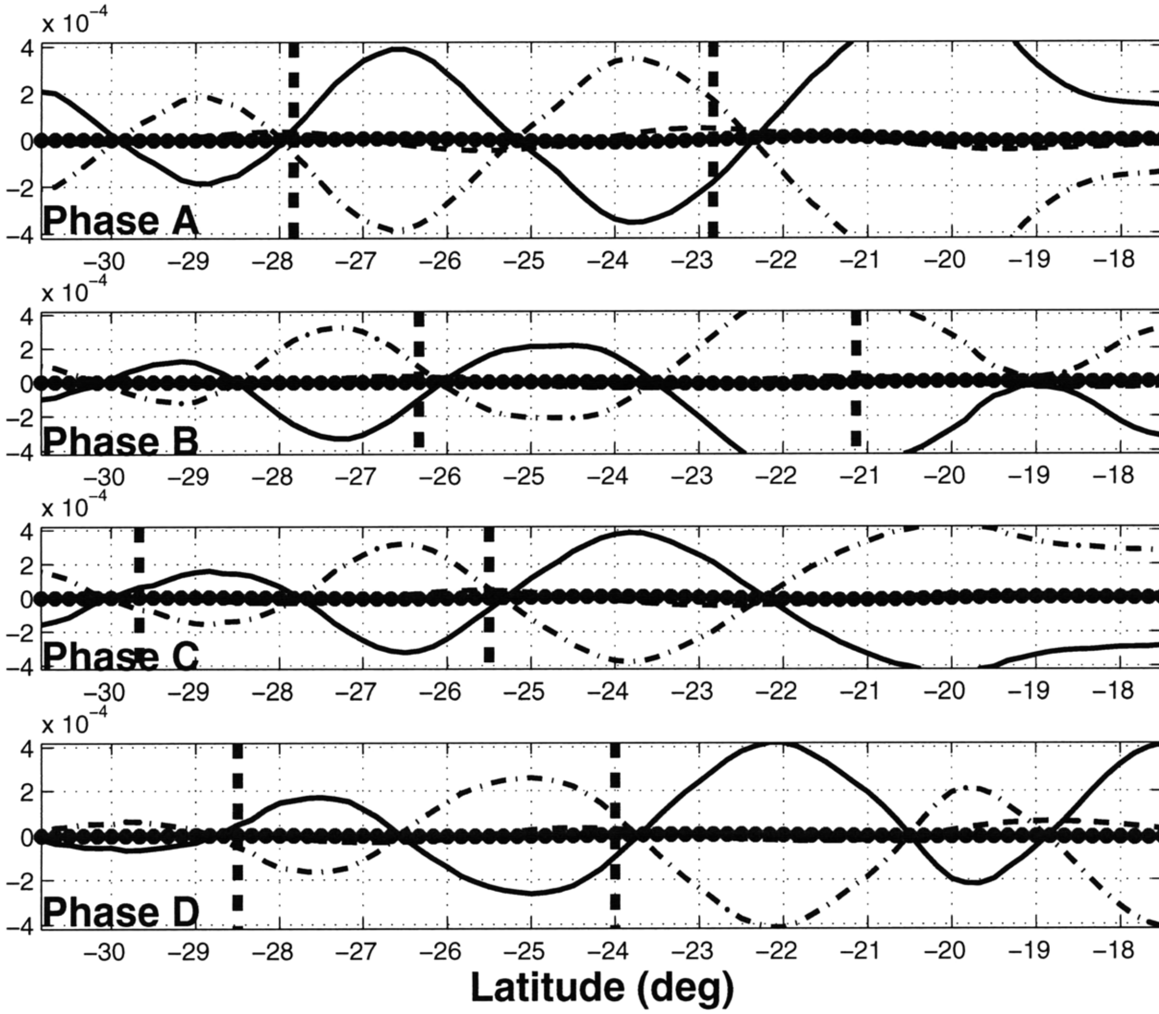

Figure 6.17: Anomalous quantities of the vertically-integrated TEM equation for each phase. The vertical integral was taken from the surface to a depth of 1600m. Solid line is the divergence of the vertical component of the EP flux; long-dashed line is the divergence of the horizontal component of the EP flux; dotted line is the flow tendency; and the dot-dashed line is the Coriolis force. Vertical dashed lines correspond to the maximum positive zonal flow anomalies.

tendency, anomalous convergence of the eddy momentum flux, and the anomalous bottom drag. After taking departures from the time-averaged state, Fig. 6.16 shows composites of each phase as described in the previous section. There is a quasi-steady balance between the bottom drag and the divergence of the Reynolds' stress, the flow tendency being weak and virtually negligible compared to these two terms. The vertically-integrated zonal flow anomalies are therefore sustained against friction by the anomalous convergence of eddy momentum fluxes. Note that there is no obvious latitudinal bias in the momentum flux convergence. Thus, another approach is needed to explain why the jets are migrating equatorward.

In order to understand fully the effect of the eddies on the mean flow, we use the transformed Eulerian mean (TEM) approach. This allows us to consider simultaneously the effects of the eddy momentum and heat fluxes (we shall in fact see that the heat budget plays a large role in the jet migration). The quasi-geostrophic TEM equations are (Andrews and McIntyre 1976):

$$\frac{\partial [u]}{\partial t} - f[\widetilde{v}^*] = \nabla \cdot \mathbf{F} + \frac{\partial \tau}{\partial z} \tag{6.4}$$

$$\frac{\partial [T]}{\partial t} + [\widetilde{w}^*]\frac{\partial T}{\partial z} = Q \tag{6.5}$$

where Q represents diabatic effects,

$$\mathbf{F} = (F_y, F_z) = \Big(-[u'v'], f\frac{[v'T']}{[T_z]} \Big) \tag{6.6}$$

is the Eliassen-Palm (EP) flux vector (*e.g.* Edmon et al. 1980), and

$$\widetilde{v}^* = [v] - \frac{\partial}{\partial z}\frac{[v'T']}{T_z} \tag{6.7}$$

$$\widetilde{w}^* = [w] + \frac{\partial}{\partial y}\frac{[v'T']}{T_z} \tag{6.8}$$

is the residual circulation.

Once again, since we are interested in the departures from the time-mean, (6.4) can be simplified. Away from the surface, we may neglect Q because there are no significant diabatic effects in the interior. Since the applied wind stress is constant in time, its anomalous value is always zero. Further, the bottom friction can be neglected when we focus our attention between the surface and the top 1600m (where the activity is strongest). Thus, (6.4) and (6.5) can be rewritten as:

$$\frac{\partial [u]}{\partial t} - f\,[\tilde{v}^*] = \nabla \cdot \mathbf{F} \tag{6.9}$$

$$\frac{\partial [T]}{\partial t} + [\tilde{w}^*]\,\frac{\partial [T]}{\partial z} = 0 \tag{6.10}$$

where all the above terms represents deviations from the time-average.

Near the surface, we invoke Bretherton's PV sheets (Bretherton 1966), exploiting the equivalence between an inhomogeneous boundary temperature distribution and a delta function PV anomaly just inside an isothermal boundary. Then both F_z and $[\tilde{w}^*]$ vanish at the boundary, and the divergence of EP fluxes are concentrated in the surface PV sheet.

Accordingly, we first vertically integrate each of the terms in (6.9) through the top 1600 m for each phase of the evolution; the results of doing so are shown in Fig. 6.17. There are three important features to note. First, the flow tendency is essentially a residual; the local momentum budget for each phase is a quasi-steady balance between the anomalous divergence of the EP fluxes and the TEM Coriolis term. Second, the baroclinic component $\partial F_z/\partial z$ dominates over the barotropic component $\partial F_y/\partial y$ in the divergence of the EP flux. Third, the anomalous EP flux divergence is out of phase with the secondary jets; the strongest anomalous convergence lies on the poleward flank, while the strongest anomalous divergence occurs on the equatorward flank. The reason behind the spatial structure of $\nabla \cdot \mathbf{F}$ will be discussed further in the next section.

The anomalous $\nabla \cdot \mathbf{F}$ thus creates an anomalous residual circulation as shown in Fig. 6.18 (and schematically illustrated in Fig. 6.23b). On the poleward (equatorward) flanks of an anomalous eastward jet, the EP flux is convergent (divergent), producing a poleward (equatorward) residual flow. By conservation of mass, near the jet cores, the anomalous residual flow must rise and, in between the jets, must sink.

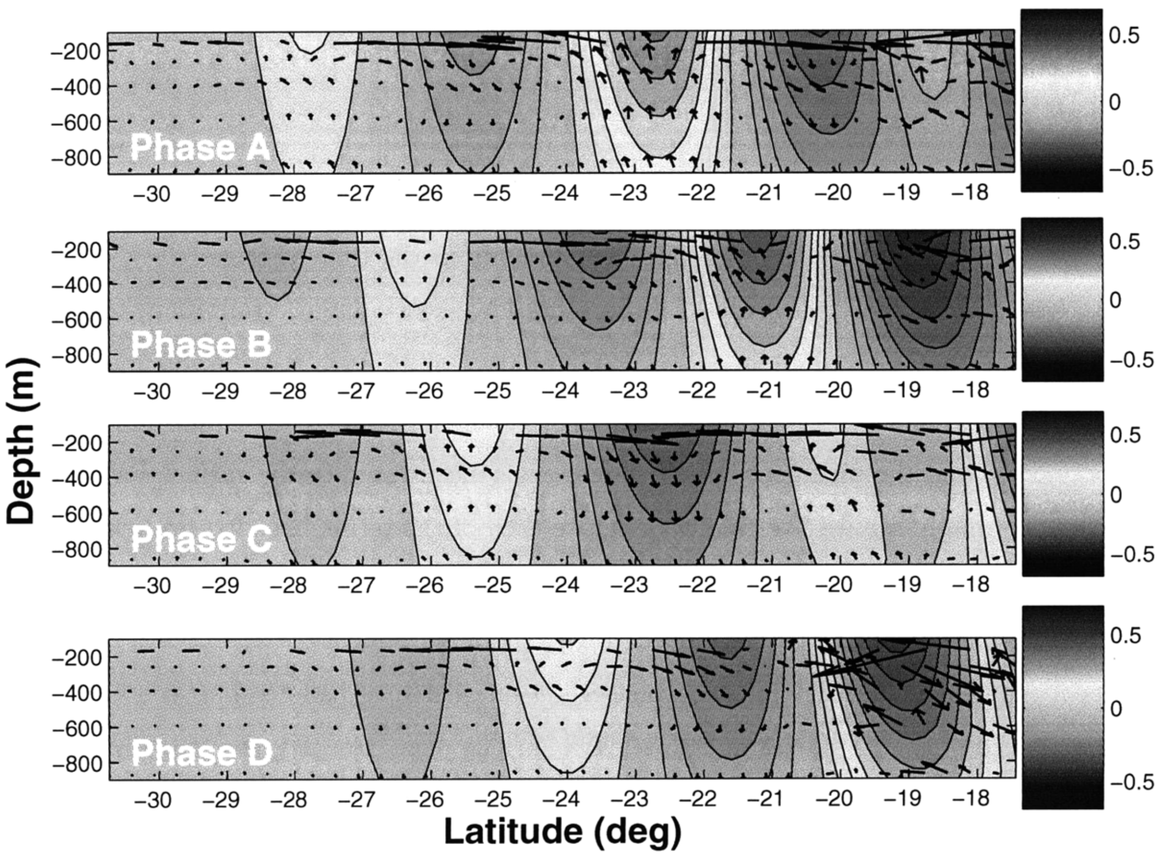

Figure 6.18: Anomalous residual circulation (vector) plotted over anomalous zonal flow (color) for each phase. The vectors are scaled the same for each plot, with the largest vector corresponding to 1.33 cm sec^{-1}.

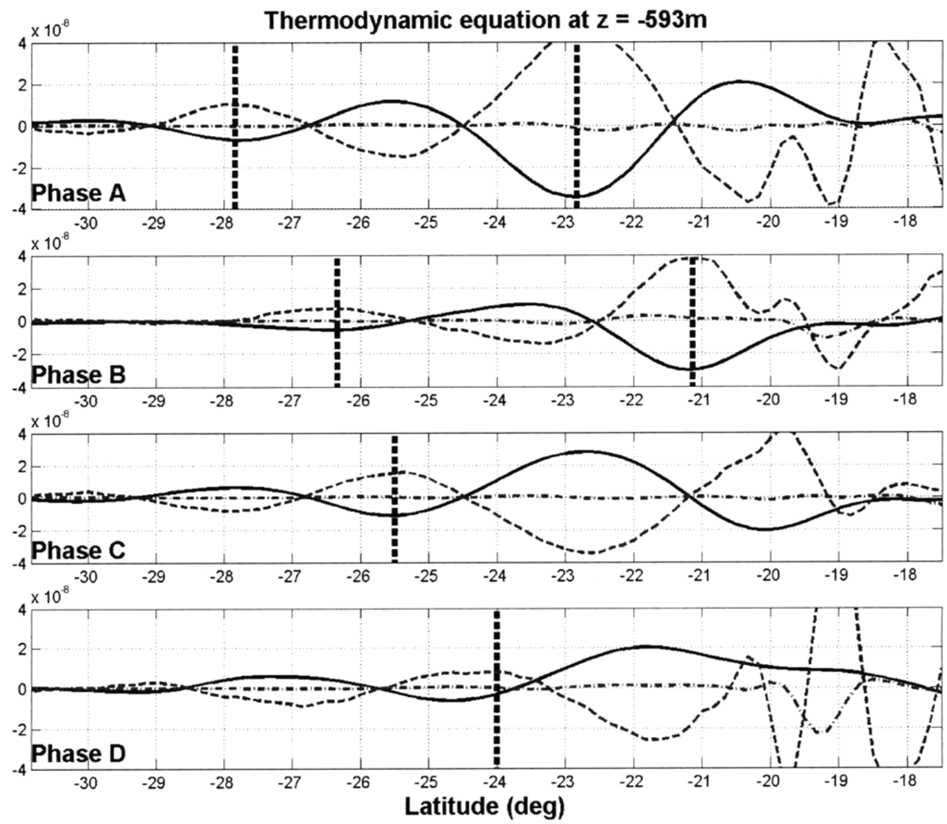

Figure 6.19: Anomalous quantities of the transformed Eulerian mean thermodynamic equation (^{o}C s^{-1}) at z=-593m. Solid line is the temperature tendency; long-dashed line is the residual vertical advection of the vertical temperature gradient; dot-dashed line is the residual meridional advection of the meridional temperature gradient. Vertical dashed lines correspond to the maximum positive zonal flow anomalies.

From (6.10), the rising residual circulation implies the temperature tendency is a local minimum near the secondary jets (see Fig. 6.19). Therefore, the time tendency for the meridional temperature gradient is positive on the equatorward flank and negative on the poleward flank, thus encouraging equatorward migration of the baroclinic zone. From the thermal wind relation, vertical shear will increase (decrease) on the equatorward (poleward) side, furthering the equatorward jet migration. Thus, this pattern of strong/weak baroclinic jets moving equatorward is ultimately dictated by the pattern of the EP flux divergence.

c. EP fluxes

We have seen, therefore, that the equatorward migration of the secondary jets is a consequence of the structure of $\nabla \cdot \mathbf{F}$, in particular, the fact that the anomalous near-surface EP flux convergence is located on the poleward flank of each eastward jet, rather than at the jet center, as one might naïvely expect. This finding, in turn, begs the question, why are the fluxes organized in this way?

Before examining the anomalous EP fluxes, we show in Fig. 6.20 the total EP fluxes for each of the four phases described in section 6.3.2. In all cases, equatorward of 12°S, where the isopycnals are relatively flat, little to no eddy activity is observed. However, eddies are ubiquitous poleward of 12°S. In all phases, the flux is upward (i.e. eddy heat flux is poleward), consistent with baroclinic instability being the source of the eddies. Comparing the different phases, both the eddy heat flux and eddy momentum flux are more dominant in the high index phases C and D than in the low zonal index phases A and B.

Since our interest is in the time-varying jets, we now focus on the anomalous EP flux vectors (i.e. departures from the time-mean) shown in Fig. 6.21. In general, where there are positive zonal flow anomalies, the baroclinic component of the flux is enhanced (more upward). However, upon a closer examination, the maximum of F_z is not coincident with the jet and is not symmetric: there is a poleward bias. From (6.6), the asymmetry must exist in the anomalous zonally-averaged eddy heat flux or in the static stability. (We presume that variation in Coriolis parameter across these narrow jets is too small to be of significance.) In fact, as Fig. 6.22 demonstrates, the composites of each phase indeed show that there is a

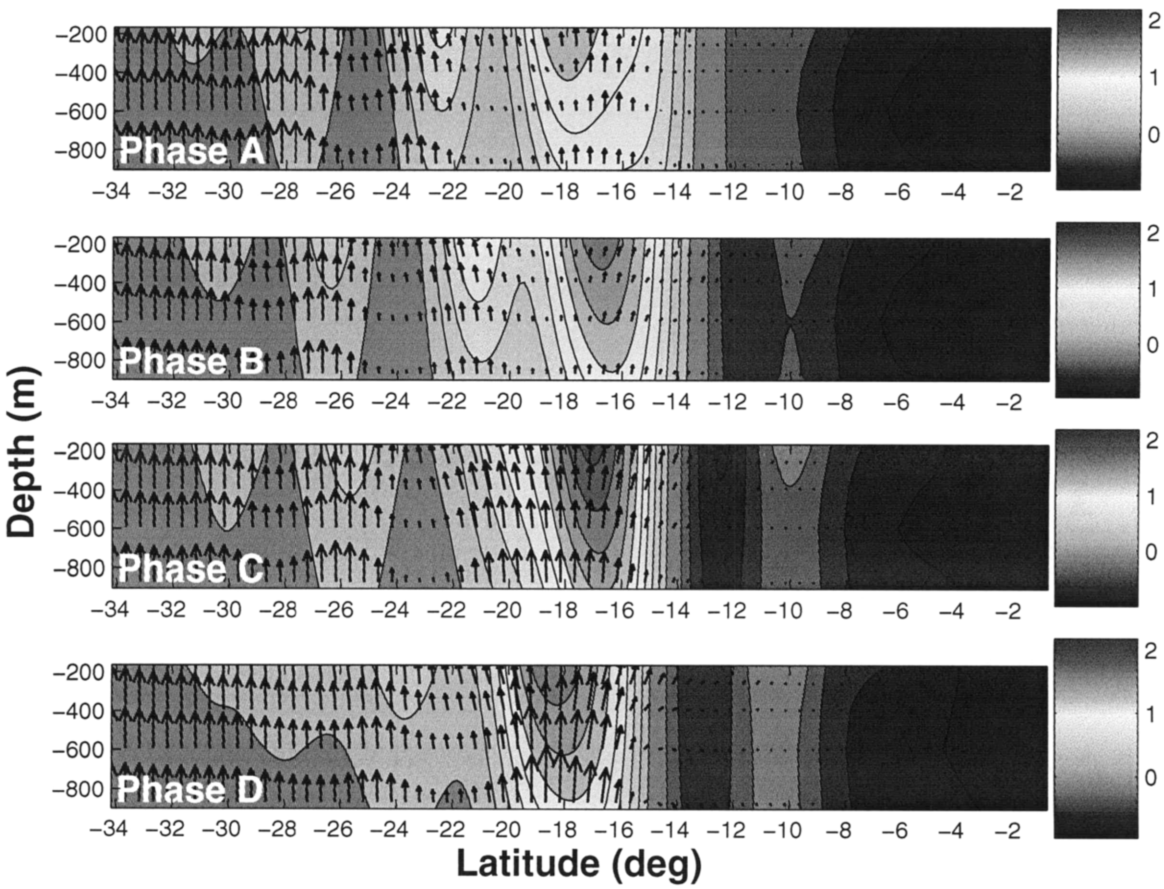

Figure 6.20: The total EP flux vectors for each EOF phase composite (labelled on bottom left corner) along with the zonally-averaged zonal flow. The vectors are scaled the same for each plot.

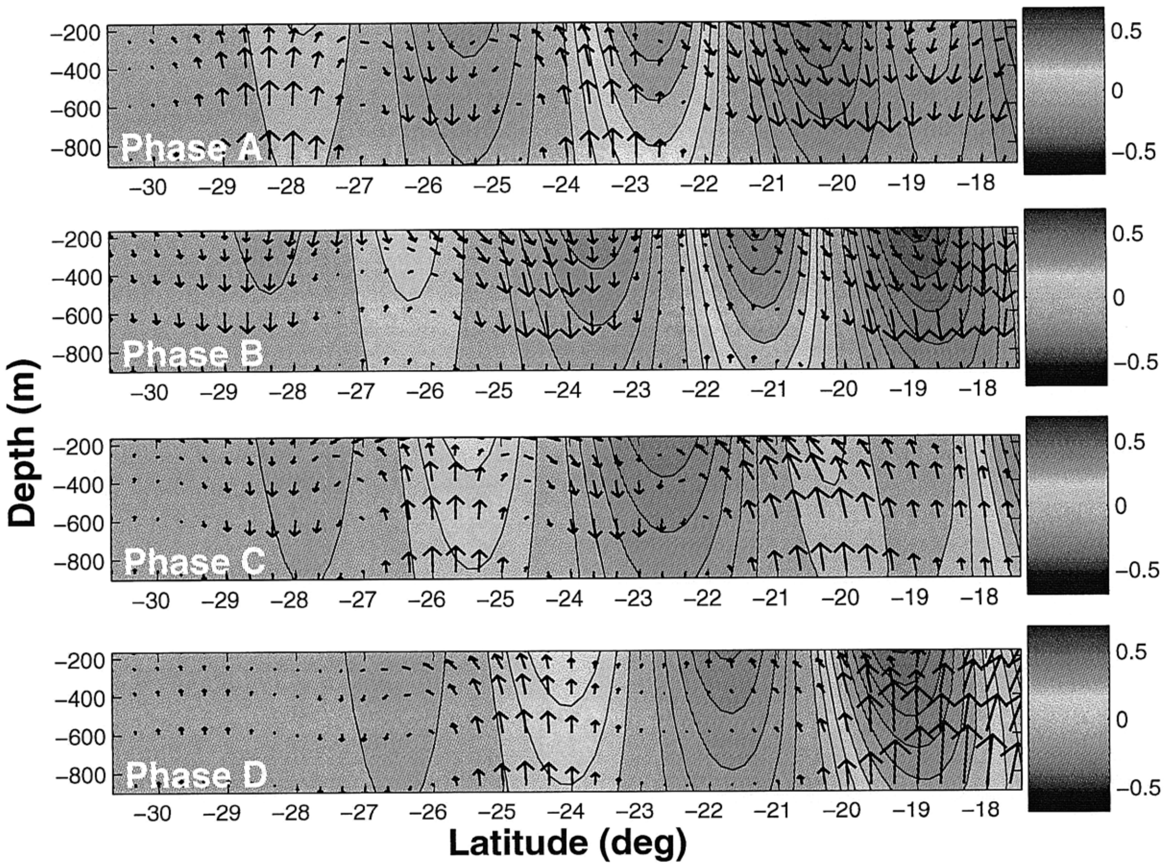

Figure 6.21: Anomalous EP flux vectors for each EOF phase composite are plotted over the zonally-averaged zonal flow anomalies. Each phase is labelled at the bottom left corner of plot. The vectors are scaled twice as large as Fig. 6.20 and are the same for each plot.

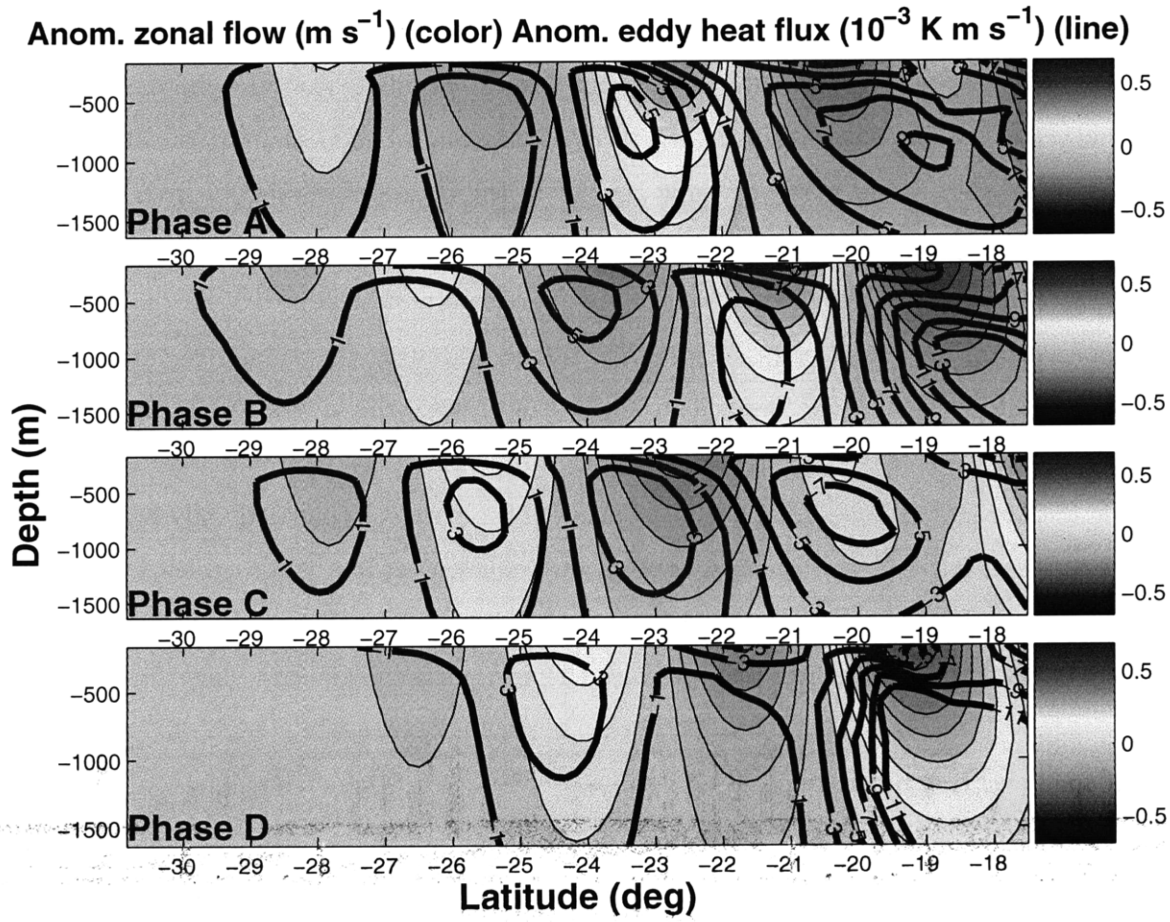

Figure 6.22: Anomalous eddy heat flux (line) is plotted over zonal flow anomalies (in color). Each phase is labelled at the bottom left corner of plot.

robust poleward bias in the anomalous eddy heat flux.

Why are the largest poleward eddy heat fluxes located poleward of the eastward zonal flow anomaly? We speculate that the implied asymmetry in baroclinic eddy activity is consistent with a bias in the Eady growth rate (Eady 1949), defined to be:

$$\sigma \propto \frac{fU_z}{N}. \tag{6.11}$$

We use σ as a local measure of instability, and speculate that the upward EP fluxes of baroclinic eddies will maximize where σ is greatest. The Coriolis parameter varies only by a factor of between five to eight percent in the region of interest over the typical width (about 2 degrees) of the jets. The vertical shear is essentially symmetric about the secondary jets. However, the buoyancy frequency, N, varies systematically with latitude in the region poleward of the main jet (see Fig. 6.8). In the migrating jet regime, N varies from thirty percent to over fifty-five percent over the length scale of the jets, with smaller values on the poleward side. Thus, the absolute magnitude of the Eady growth rate is larger on the secondary jets' poleward flank, consistent with the stronger poleward eddy heat fluxes there. Therefore, with N increasing monotonically equatorward in the migrating jet region, we speculate that, in the absence of any other asymmetries, the latitudinal variation in the background static stability may produce the asymmetry in the eddy heat fluxes.

6.4.1 Discussion

Drawing all these results together, the nature of the interaction between the eddies and the evolving jets is summarized schematically in Fig. 6.23. In the absence of any latitudinal asymmetries in the background state, one might expect the situation depicted in frame (a), the EP fluxes being symmetric about the jet, with divergence beneath the jet and convergence at and near the surface. Given our finding that the time derivative in (6.9) is negligible, the consequence is a pumping of the residual flow poleward at and near the surface, and equatorward at the bottom, generating a circulation cell as shown. The residual upwelling and downwelling therefore produce cooling on the equatorward flank, and warming on the poleward flank, of the jet, thereby reducing the baroclinicity at the jet core, and enhancing it at the flanks. This symmetric pattern would induce no tendency of the baroclinic zone, and the consequent jet, to migrate.

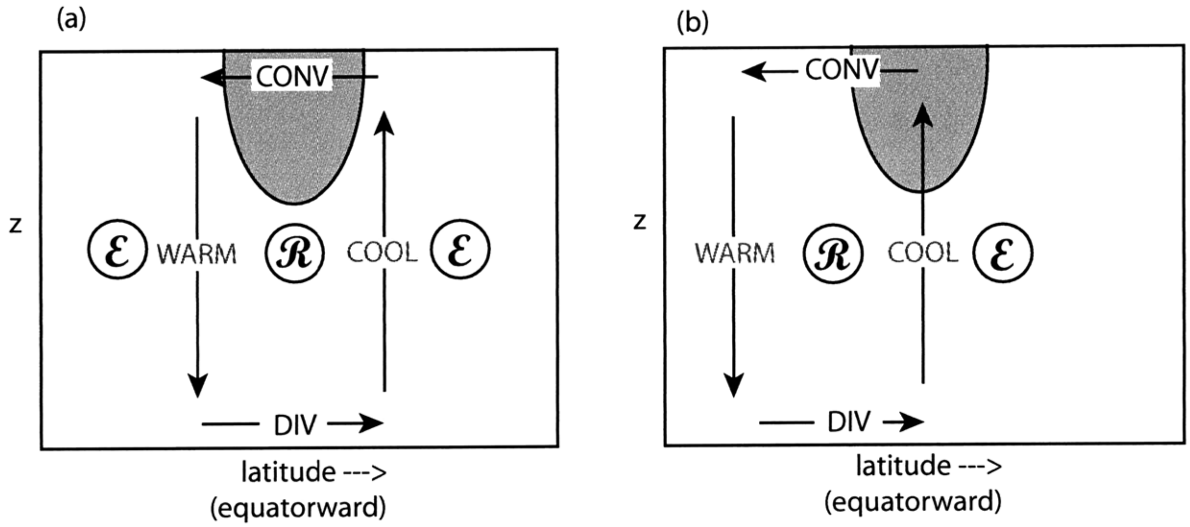

Figure 6.23: Schematic depiction of the interaction between baroclinic eddies and a localized jet. In frame (a), the baroclinic eddy activity is assumed to be symmetric about the jet; in (b), it is stronger on the poleward flanks of the jet, presumed to be a consequence of a general poleward decrease of static stability. 'CONV' and 'DIV' denote convergence and divergence, respectively, of the baroclinic EP fluxes; 'COOL' and 'WARM' indicate the local temperature tendencies attributable to the induced residual circulation, thus reducing ($\mathcal{R}$) and enhancing ($\mathcal{E}$) the local zonal mean baroclinicity. (Note that the southern hemisphere is depicted; the equator is to the right.) See text for discussion.

Consider now frame (b), in which we assume that the baroclinic eddy activity is displaced poleward of the jet as a consequence of basic state static stability increasing equatorward in the background state. The residual circulation cell is, accordingly, displaced poleward with respect to the jet, thus producing tendencies of reducing baroclinicity on the poleward flank, and enhancing it on the equatorward flank, leading to equatorward migration of the baroclinic zone and therefore of the jet itself.

6.4.2 Summary

As was shown in Fig. 6.9, multiple zonal jets emerge when extremely broad buoyancy and wind forcing are applied to the surface of the model ocean. Although both forcings are constant in time, there is significant variability in the zonally-averaged zonal flow (see Fig. 6.10). Between 15°S and 20°S, the main eastward jet oscillates meridionally, while between 20°S and 35°S, secondary (weaker) jets systematically migrate equatorward. An EOF analysis describes the leading mode as an equivalent barotropic structure with the largest anomalies 3° north and south of the primary jet's time-averaged position, thus describing north-south fluctuations of the main jet, in a manner qualitatively similar to atmospheric behavior (*e.g.* Thompson and Wallace 1998). However, unlike the atmospheric case, the two leading EOFs are in quadrature in the region of the secondary jets where, together, they capture the jets' migration.

The secondary jets are maintained against bottom friction by convergence of the eddy momentum fluxes. However, it is the eddy heat fluxes (or equivalently, the vertical component of the EP fluxes) that control their equatorward migration. Although the anomalous convergence of the eddy momentum flux is nearly symmetric along the jet axis, convergence of the baroclinic (vertical) component of the EP flux is not. The vertical EP flux dominates locally and is stronger on the poleward flank of the jets (see Fig. 6.17), leading to the jets' equatorward migration. We speculate that the asymmetry in the vertical EP flux is consistent with larger Eady growth rates associated with smaller values of static stability on the poleward side of the jets.

6.5 Summary

We have seen that in the oceanic GCM that the eddy heat fluxes were asymmetric with respect to the zonal flow anomalies and likely responsible for driving the systematic migration. Given the slope of the tropopause, above the boundary layer, at all heights, the static stability of the atmosphere increases poleward (Peixoto and Oort 1992). Assuming no other asymmetries, larger Eady growth rates would be larger on the equatorward side and a similar argument discussed above would hold.

However, since the deformation radius is about an order of magnitude larger in the atmosphere, the variations in the Coriolis parameter is now important. Since f is zero at the equator and large near the pole, the Eady growth rate will oppose the asymmetry from the static stability. Thus it is no longer clear if the mechanism seen in the ocean model would be applicable in the Earth's atmosphere.

Nonetheless, the work from section 6.2 suggest the eddy heat fluxes are important in driving the poleward propagation. Using a model run characterized by this type of variability, daily variations of eddy heat and momentum fluxes were calculated. Then, using a zonally-symmetric model, these terms were added explicitly to the zonal wind and zonal temperature tendency equations, respectively. This two dimensional model was able to capture both the climatology and the internal variability.

Two further zonally-symmetric trials were explored. The first contained the timeseries of the eddy momentum fluxes, but the *climatological* eddy heat fluxes, while the second, had the timeseries of the latter and the time-averaged value of the former. When the two dimensional model included the variations of the eddy momentum fluxes, no poleward propagation was present. However, when the variability of the eddy heat fluxes were inputted, the poleward propagation appeared. The interpretation here is that any mechanism involved in describing the poleward propagation must involve the eddy heat fluxes. As a result, the mechanism described above cannot be ruled out.

Chapter 7

Observational Perspective

As we have seen in Chapter 4, large responses to a perturbation occurred because the modelled troposphere teetered between two regimes. By lying in a transitional state, marginal forcing can bring about high amplitude non-linear changes to the tropospheric circulation. In that chapter, the two distinct regimes consisted of the eddy-driven jet being located either in the mid-latitudes or in the subtropics. This was clearly seen by the bimodal frequency distribution of the peak surface westerlies (cf. Fig. 4.1f).

We point out that the jet oscillation described by the annular mode is fundamentally different than the variability found in the transition zone. While the annular modes describe the latitudinal shifts of the mid-latitude jet, the non-unimodal distribution found (albeit in a particular region of the model's parameter space) in this thesis suggests that there may be an additional underlying mode in the atmosphere. In the first section, we question whether this dual regime behavior can be found in observations.

In the second section, we use observations to confirm our findings from Chapter 5. There, we found that the lower stratospheric winds needed to be sufficiently weak in order to trigger an equatorward shift in the tropospheric jet. So in the final section we will use observation data to determine whether this relationship will hold.

The following two section uses daily National Centers for Environmental Prediction - National Center of Atmospheric Research (NCEP-NCAR) Reanalysis data that extends from 1 January 1948 to 31 December 2007 (Kalnay et al. 1996). For the Southern Hemisphere, we confined our use from 1 January 1979 to 31 December 2007. We used data that was spaced on a 2.5° x 2.5° latitude - longitude with 17 pressure levels (1000, 925, 850, 700, 600, 500, 400, 300, 250, 200, 150, 100, 70, 50, 30, 20 and 10 mb.)

For the first part of the study, we also used the surface NCEP-NCAR reanalysis and several indices: daily Northern Annular Mode (NAM), Southern Annular Mode (SAM), North-Atlantic Oscillation (NAO) and Pacific-North American (PNA). The former two are from the same dataset as that of Baldwin and Dunkerton (2001) and spans from 1958 to 2006. Finally, both the NAO and PNA indices were derived by the National Climate Prediction Center and spans from 1950 to 2008. Since these indices could be generated at any level, we picked 500 mb as the choice to represent the troposphere. At any tropospheric pressure level, any of these indices are well-correlated with any other level in the troposphere. Thus our results will not be sensitive to the particular height we choose, as long as we picked any height below 200 mb.

7.1 Observational evidence of dual regimes?

The bimodal distribution in the model's location of the peak surface westerlies (cf. Fig. 4.1) took place under a winter setup. Thus, we will examine the winter months of December, January and February. Again, the purpose of examining the location of the peak surface westerlies is to determine the latitude of the eddy-driven jet. We have assumed that the strongest surface westerlies correspond to the largest region of eddy momentum flux convergence. Thus we have used the peak surface westerlies as a proxy to find the location of the eddy-driven jet.

In the model, the relationship with the surface westerlies is strictly true in the absence of mountain drag and in the zonal average. The results from Chapter 4 did meet those criteria. However, some minor problems lie in the observational data because of the presence of topography and ocean basins. So we will again perform a zonal average, but, to test for robustness, we will also include an analysis of different sectors. Following Eichelberger and Hartmann (2007), the Atlantic basin is defined between 60°W to 0°W and the Pacific sector is defined between 150°E to 240°E.

We will first examine if the zonally-averaged eddy-driven jet persists at one period and "jumps" to another, analogous to what was seen in the model (*e.g.* Fig. 4.2a). Fig. 7.1 tracks the daily latitudinal location of the peak surface westerlies as a function of time for two winter seasons. In both of these examples, for about ten days, the eddy-driven jet appears to switch between the mid-latitudes and the subtropics, with very few instances of something in between, suggesting there might be bimodal behavior.

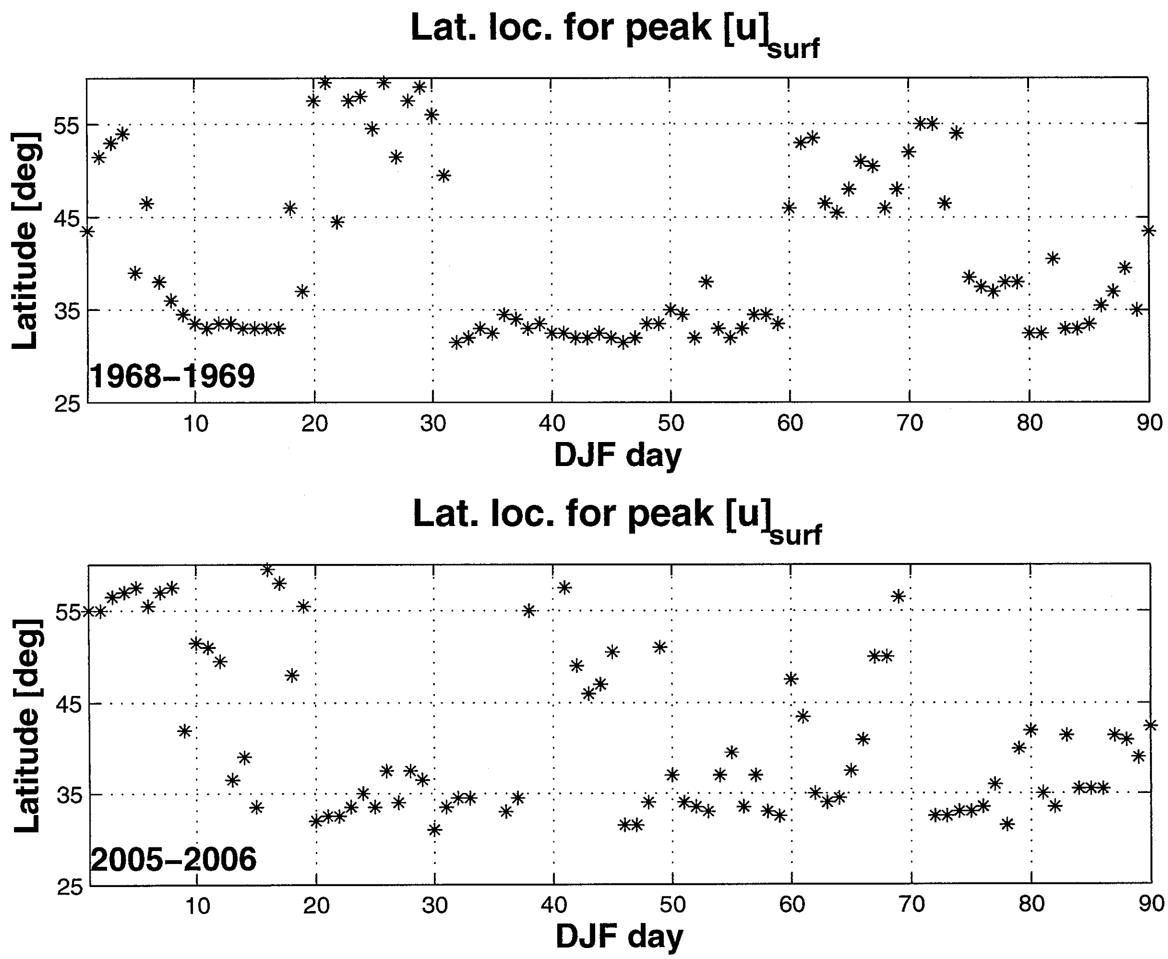

Figure 7.1: Daily latitudinal location of the zonally-averaged peak surface westerlies for the 1968-1969 (left panel) and the 2005-2006 (right panel) winter seasons averaged.

Fig. 7.2 shows the relative frequency of the peak surface westerlies for each individual winter month. What is most striking is, again, the bimodal distribution. The increased frequency in the eddy-driven jet being located away from the mid-latitudes and into the subtropics during the late winter months is not a gradual shift, but instead what we consider a regime shift. The jet either oscillates in the mid-latitudes or in the subtropics, but seldomly in between these two regions.

Before and after the winter months, the distribution is unimodal centered in the mid-latitudes (not shown), just like the model experiments (cf. Fig. 3.1). But during the winter months, Fig. 7.2 suggests that the seasonal forcing brings about a setup that could bring the eddy-driven jet into the transitional state that straddles between the two regimes.

To show how robust this bimodal feature in the latitudinal location of the peak surface westerlies, each season is plotted in Figs. 7.3-7.5. If the latitudinal location of the peak surface westerlies is indeed an accurate proxy to the location of eddy driven jets, then these plots suggest that the eddy-driven jet is never solely in the mid-latitudes or only in the **subtropics** during the winter months. Instead, they reside in one region for a certain period of time before "jumping" to another.

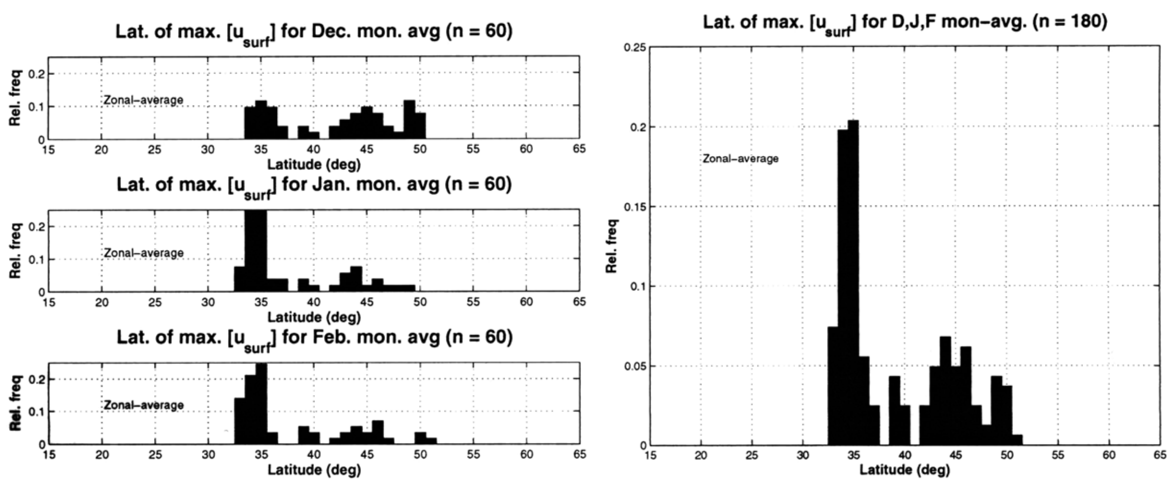

Figure 7.2: A relative histogram of the latitudinal location of the maximum daily-averaged surface zonally-averaged zonal winds for the labelled winter month (left panel) and the aggregate (right panel).

As a result of the dual preference for the peak surface westerlies in either the subtropics and the mid-latitudes, there can be large "jumps" over short periods of time. Fig. 7.6 shows the relative histogram of the maximum latitudinal shift from the previous 10-day averaged position to the following 10-day averaged position over the course of the winter season. As

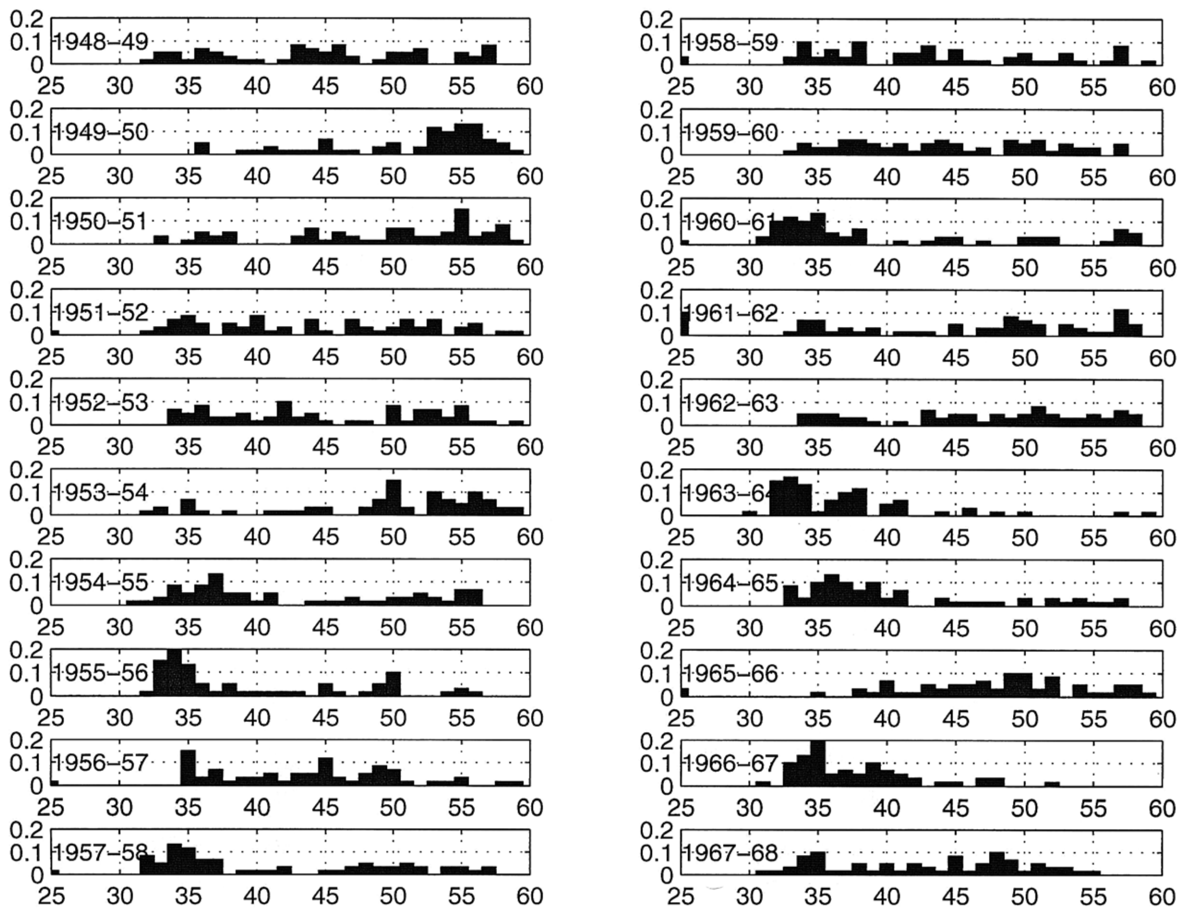

Figure 7.3: A relative histogram of the latitudinal location of the maximum daily-averaged surface zonally-averaged zonal winds for the labelled winter season.

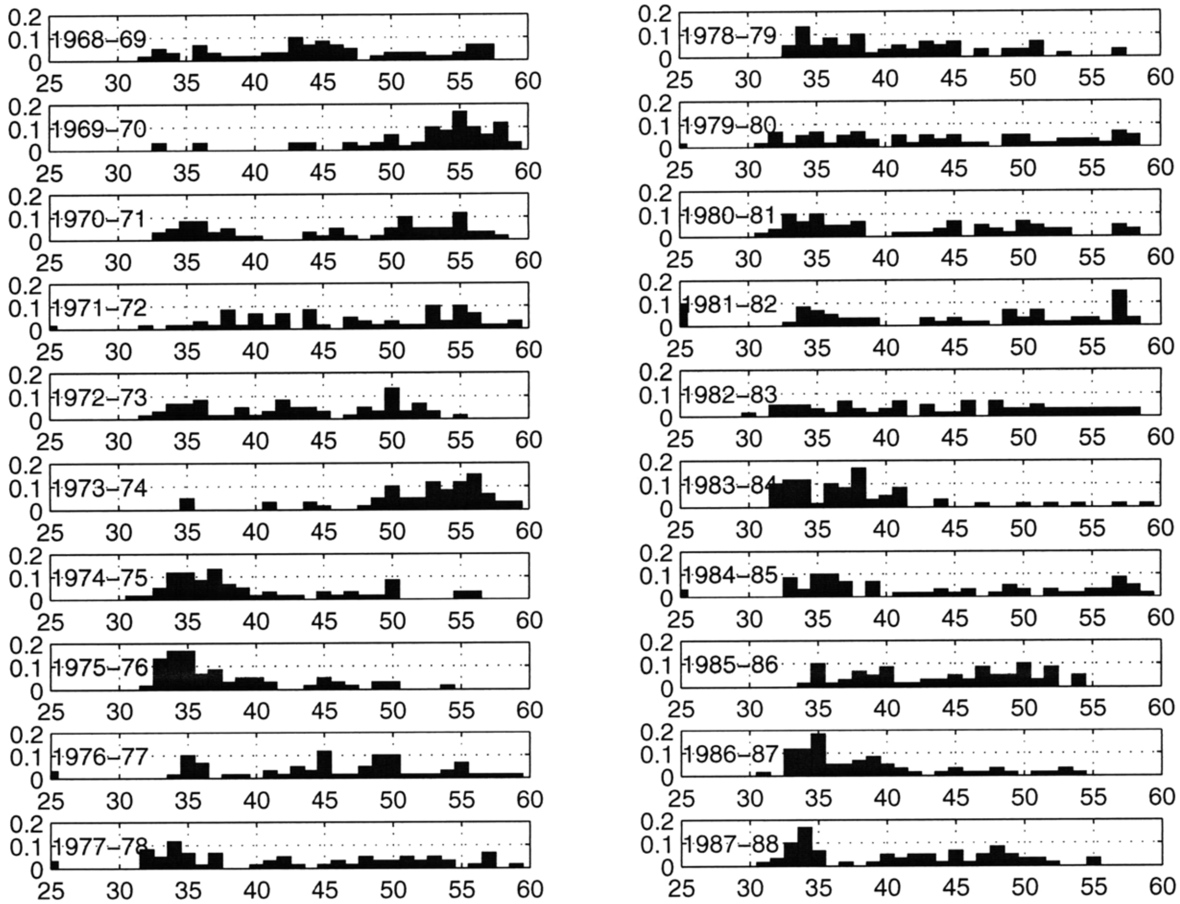

Figure 7.4: A relative histogram of the latitudinal location of the maximum daily-averaged surface zonally-averaged zonal winds for the labelled winter season.

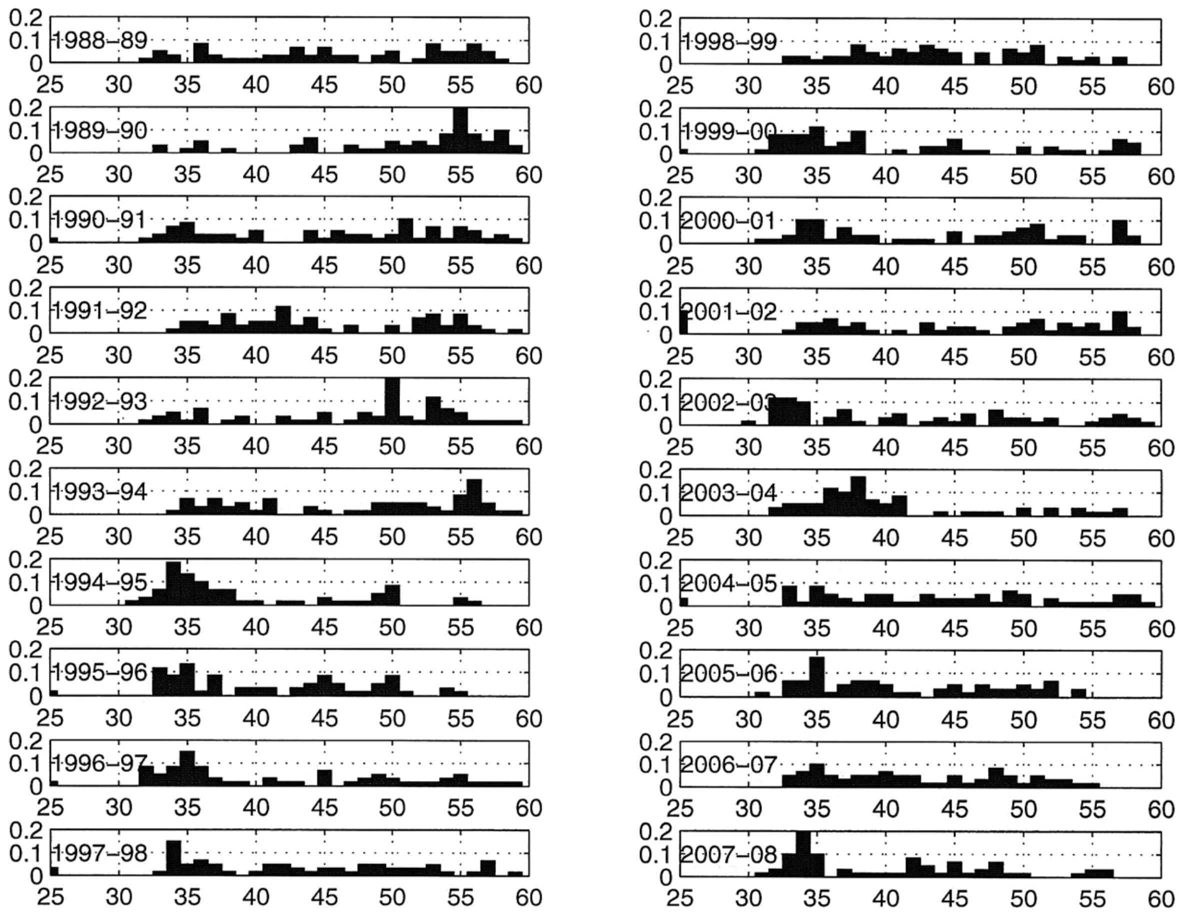

Figure 7.5: A relative histogram of the latitudinal location of the maximum daily-averaged surface zonally-averaged zonal winds for the labelled winter season.

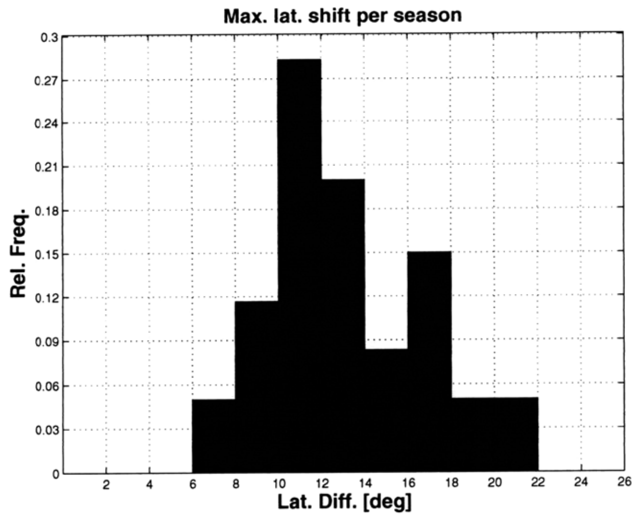

Figure 7.6: A relative histogram of the maximum absolute latitudinal shift in the peak surface westerlies per season. The shift is defined to be the difference in the average latitudinal location in the preceding and following 10 days. See text for details.

shown, most of the seasons, for at least a ten day average, the jet shifts at least 10 degrees from the previous ten days.

Since the decorrelation time of the annular modes is about 10 days, one would expect a much smaller shift in the jet. However, with a typical maximum value for each season greater than 10 degrees, the traditional picture of the eddy driven jet simply oscillating between a mean state is likely too simple during the winter season.

Alternatively, the dual regime behavior could be attributed to the different characteristics between the two ocean basins. At any given time, one region could dominate one part of the distribution in the zonal-average. For example, the Pacific sector could have contributed to the subtropical portion of the frequency distribution, while the Atlantic region could have been responsible for the peak of mid-latitude surface westerlies. However, once we decompose the zonal average into these basins, we find that the bimodal shape (Fig. 7.7) still holds, in large part. There is another maxima in the distribution located around 40°N for December and January over the Pacific basin, that was not present in the zonal-average.

While in the Atlantic sector, the separation between the wave-driven jet being located either in the mid-latitudes or the subtropics is the most dramatic. During the 5,475 days of

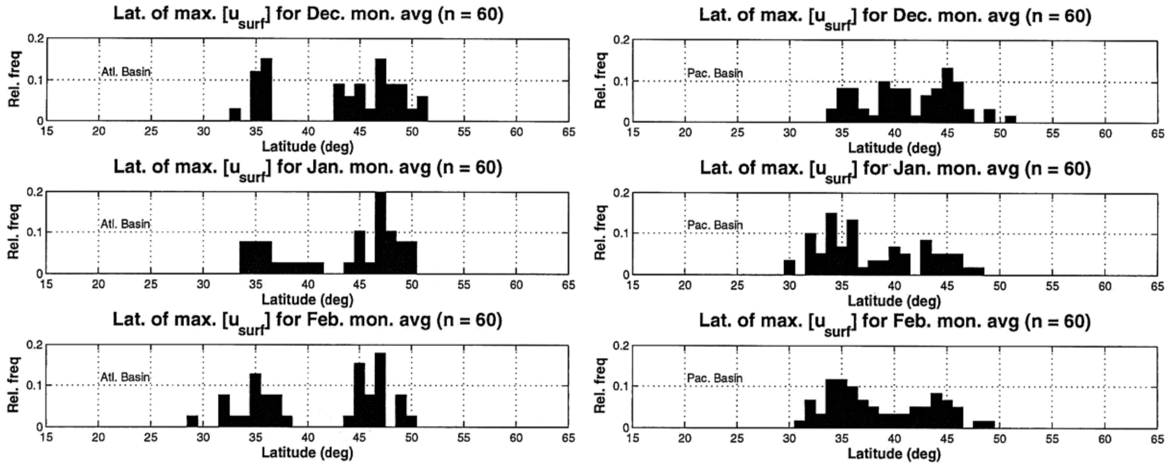

Figure 7.7: A relative histogram of the latitudinal location of the maximum daily-averaged surface zonally-averaged zonal winds for the labelled winter month for the Atlantic (left panel) and the Pacific (right panel) basin.

interest, less than two percent of the time did the eddy-driven jet center between 38°N and 42°N. The rest of the time, the location of the peak surface westerlies lay either equatorward or poleward of that minima.

If the atmosphere did lie between two separate states, a bimodal distribution would show up not only in the peak surface westerlies as indicated above, but also in the leading mode of variability. Thus we will proceed with analyzing the Northern annular mode (NAM) index. A relative histogram was generated for each month and is shown on the top panel of Fig. 7.8. The distributions are certainly not bimodal for every single month of the year. However, the shape of the distributions varies greatly between the seasons. Between May and September, there is a clear peak near the middle. (We note that the seasonal cycle of the corresponding spatial structures of these modes have been removed.)

During the winter months, the peak has greatly flattened. From September to January, the peak frequency dropped by more than a half. This flatness in the relative histogram persists until March, the month with least obvious unimodal shape. This is coincident with the typical stratospheric final warming events.

So while an obvious bimodal distribution was not present in the NAM, for certain months, there was no clear unimodal shape either. While the NAM captures the greatest variability,

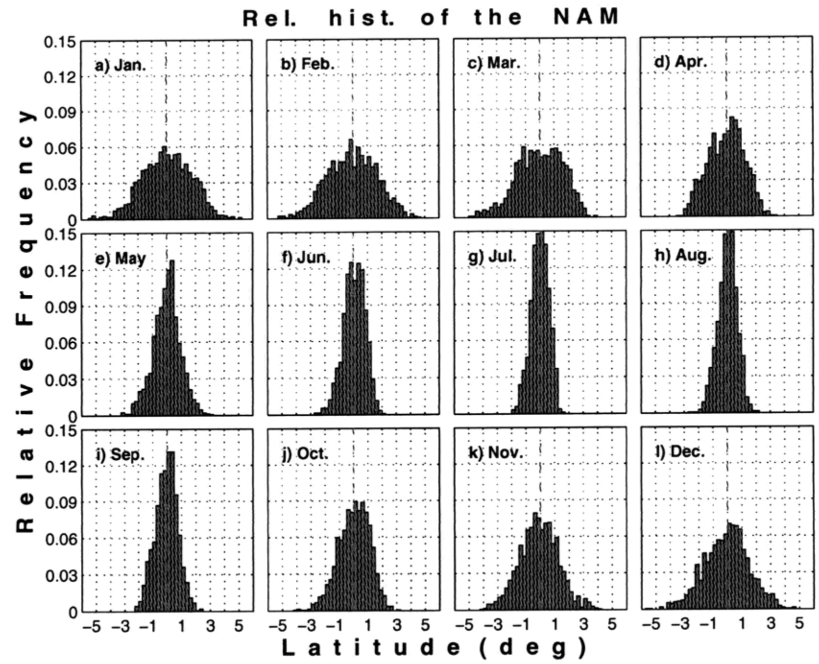

Figure 7.8: A relative histogram of the daily NAM indices for each individual month. The vertical dashed line represents an index value equal to zero.

it doesn't capture all. There is the possibility that there could be interference between the NAO and PNA patterns and they themselves could capture the dual regime behavior seen in Chapter 4.

The top panel of Fig. 7.9 shows the distribution of the NAO indices for each month. Again, there is no obvious bimodal structure, with all the months having their peak frequency close to zero. However, unlike the NAM indices, the distributions are less symmetrical during the winter months. Especially for January and April, a "shoulder" develops along the flanks.

These skewed distributions are even more pronounced in the PNA indices (bottom panel of Fig. 7.9) during the cold seasons. For example, about forty-eight percent of the indices lie between 0 and +1, while only thirty percent lie between -1 and 0. Given this skewness, it is difficult to rule out two separate regimes. There is the possibility that there are two peaks with different amplitudes, away from zero, such that when summed together gives the shoulder-like shape.

Another approach in looking for an eddy-driven jet coexisting in two regimes is looking

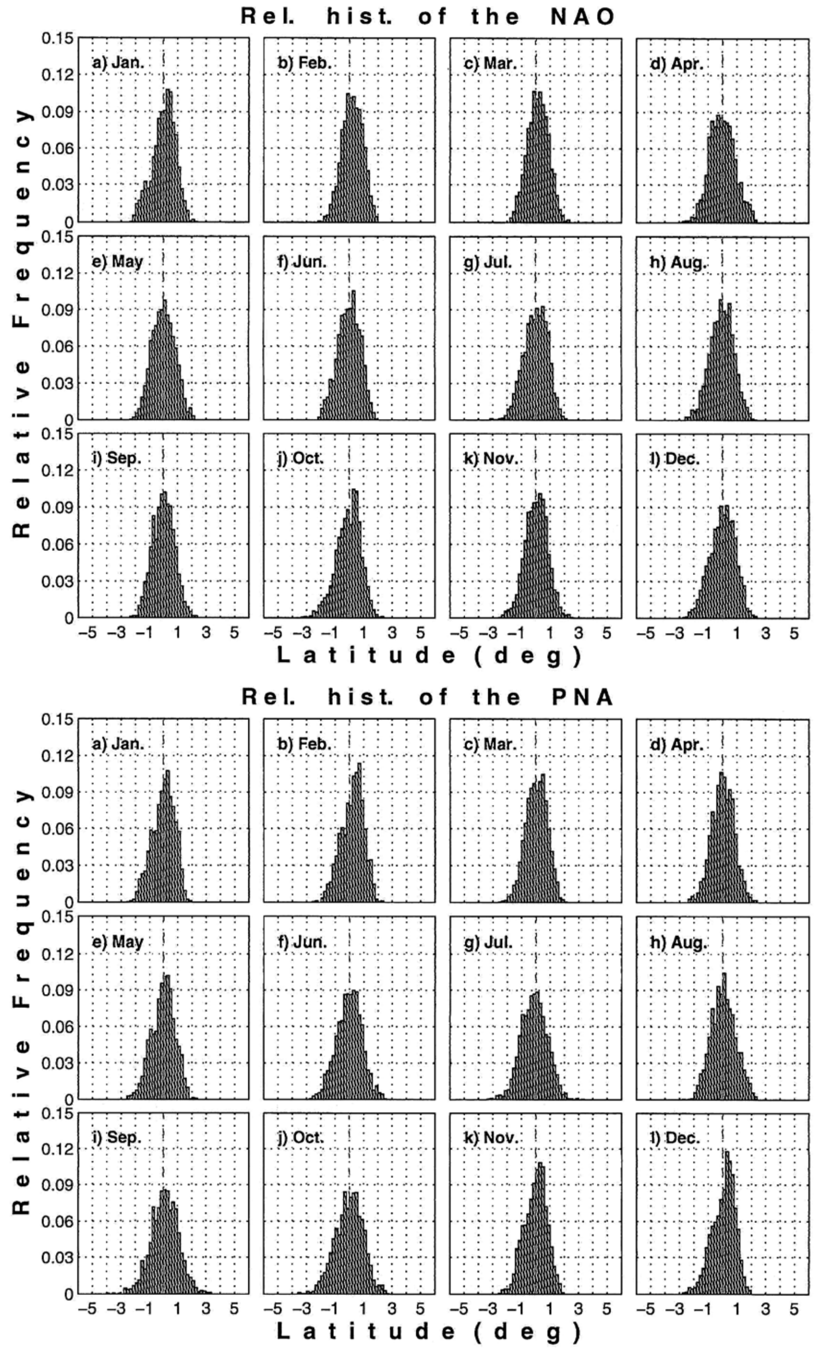

Figure 7.9: A relative histogram of the daily NAO (top panel) and PNA (bottom panel) indices for each individual month. The vertical dashed line represents an index value equal to zero. Each dataset consists at least 48 years of data.

at the eddy momentum fluxes, since the annular modes and its associated oscillation can be thought of as a pulsation of these fluxes. For example, with anomalous poleward eddy momentum fluxes coincident with the jet, there will be a convergence of momentum on the poleward flank of the jet driving a poleward shift. However, if the wave-driven jet were to be in a truly different state, then the peak of the eddy momentum fluxes would likely shift as well. Thus we will test if the peak eddy momentum fluxes exhibit a latitudinal shift between the time-average and an anomalously weak state.

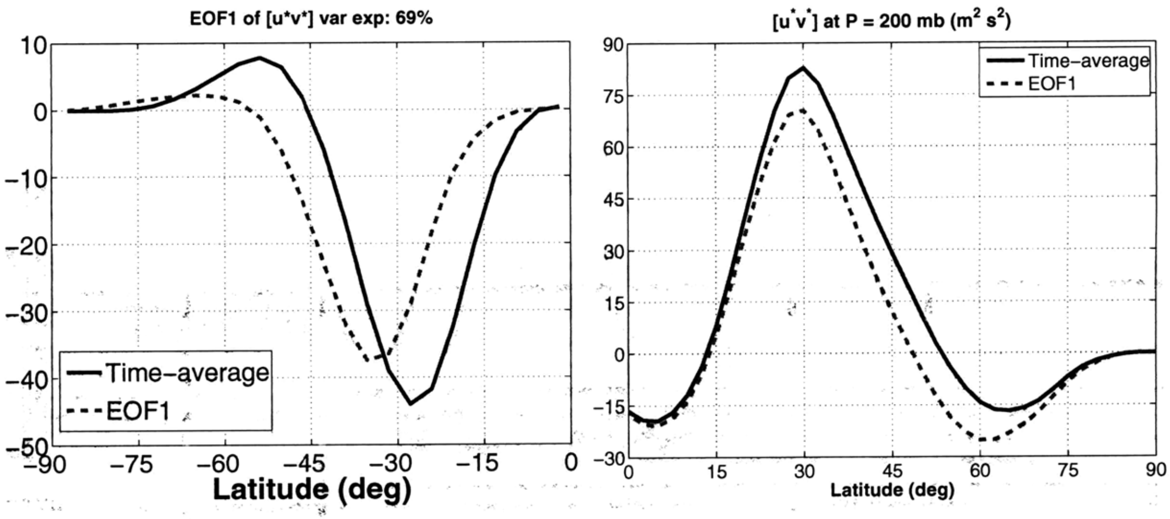

Figure 7.10: Left panel: Time-average (blue solid line) and weak (dashed-green) eddy momentum fluxes at 200 *mb* for model exp. 1b (cf. Table 4.1). Right panel: same as left panel, but from the NCEP-NCAR reanalysis.

As a comparison, the left panel of Fig. 7.10 shows the time-average of $[u^*v^*]$, with the peak slightly equatorward of 30°S. To get an anomalously weak state, we utilize an EOF analysis of these fluxes. After normalizing to represent one standard deviation, the spatial pattern is added to the time-average and is shown as the dashed-green in the figure. As shown, a weak state corresponds to a poleward shift of about 7°. This suggests that eddies are not only getting stronger or weaker, but also they are being displaced latitudinally, presumably due to a different regime. With the strongest eddy fluxes typically ± 7 degrees of 28°S at any given time, the two different locations support our case that two separate regimes were found.

This contrasts the behavior found in observational data. The right panel of Fig. 7.10

shows the time-average eddy momentum fluxes and the corresponding weak state. Here, the eddies are simply intensifying or weakening with no significant shift in the peak. So even though both cases will exhibit latitudinal shifts in the jet, the way eddies produce this variability were different. In the model that lay in a transition zone between two regimes, the center of the strongest eddy activity varied between two locations; while in observations, the center of the strongest eddy activity remained the same, suggesting the atmosphere does not have that dual regime behavior.

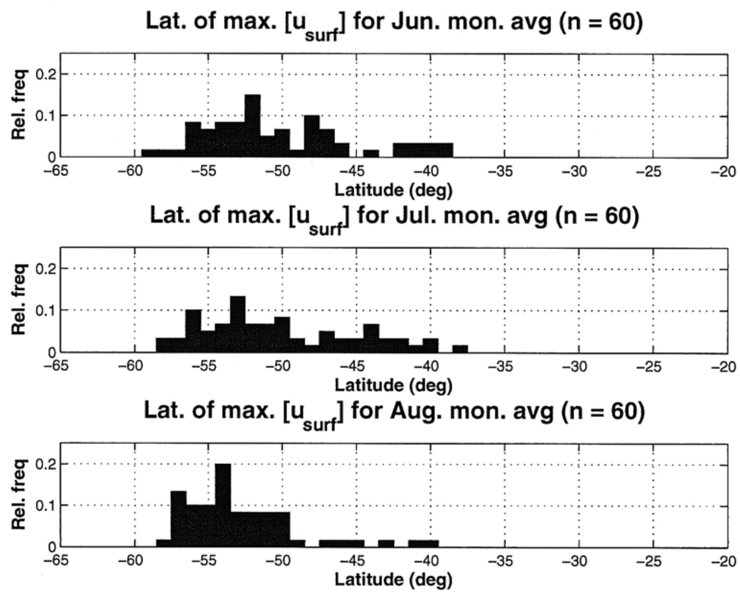

Figure 7.11: Same as the left panel of Fig. 7.2, but for the Southern Hemisphere and its respective winter months of June, July and August.

For completeness, we perform the same analysis for the Southern Hemisphere. Fig. 7.11 shows the frequency distribution of latitudinal location of the peak surface westerlies during the winter months. In June and July, the eddy-driven jet is clearly never in the subtropics and resides in the broad region between 40°S and 60°S. There is also no obvious peak during any of these months. Thus, it is not clear where the center of this presumed unimodal structure would even be.

Finally, Fig. 7.12 shows the distribution of the SAM indices for each month. Again, the shape for most months is Gaussian-like. However, for certain months, the peak of these distributions appears to be away from zero. In fact, for May and July, there appears to

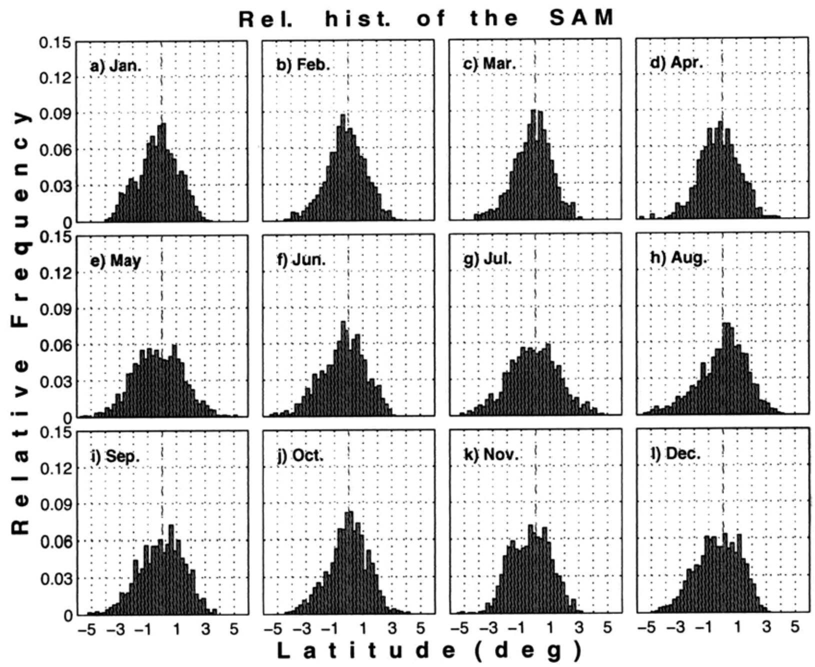

Figure 7.12: Same as Fig. 7.8 but for the Southern Annular Mode index for each month.

be a local minima at zero; while in November, the climatological month in which final stratospheric sudden warming takes place, there are subtle hints of a bimodal distribution.

Nonetheless, there are no obvious clues to suspect that the atmosphere exhibits the same dual regime behavior as that of the particular model in Chap. 4. While we saw evidence of the peak surface westerlies shift from the mid-latitudes to the subtropics, this was likely not a consequence of the eddies reorganizing themselves elsewhere (cf. Fig. 7.10). Thus, we can conclude that if there were to be this extra mode, it is too weak to detect in the presence of the strong annular mode signal.

7.2 Stratosphere/Troposphere Coupling

As we had mentioned in the previous section, stratospheric sudden warmings have been connected to changes in the troposphere. Fig. 7.13 shows a month-by-month EOF analysis of $[u(y,p,t)]$, poleward of 20°N. Seasonal variations of the data were removed by taking out the climatological average. This was determined by first taking an average for each day of the year, then a two-week centered mean was applied to smooth out the variations. The zonal-mean zonal wind data is then subtracted from this climatological average.

After this calculation is performed, not surprisingly, the greatest stratospheric variability is during the winter season and as shown, a weakening of the polar vortex, likely due to these sudden warming events, is correlated with an equatorward shift in the tropospheric jet consistently through the fall and winter months. Compared to the climatological winds, for almost all of the non-winter months, the leading EOF patterns show the variability in the troposphere as the typical oscillation of the mid-latitude jet, which has been well-documented (e.g. Yu and Hartmann 1993; Akahori and Yoden 1997; Eichelberger and Hartmann 2007). However, during the winter months, this relationship is only partially true. In addition to the latitudinal movement, there is also a component related to the intensification and weakening for the months of January, February and March.

Fig. 7.14 shows the same analysis for the Southern Hemisphere (SH). While we used the entire dataset (1948 - 2007) for the Northern Hemisphere (NH), only years between 1979 - 2007 will be shown for the SH. (Before 1979, the analysis showed a coupling with the stratosphere that was fundamentally different than what's shown in Fig. 7.14 – a stratospheric dipole emerged, but this data is likely unreliable because of the scarcity of observations before the satellite era.) An EOF analysis of each half of the 1979 - 2007 data showed the variability was robust.

There are noticeable differences between the two hemispheres. First, there is stratospheric variability throughout the year. Even during the summer months, amplitudes of 3 $m\ s^{-1}$ in the lower stratosphere are not uncommon. But this is likely due to tropospheric eddy activity driving changes that extend into the stratosphere.

Secondly, the greatest stratospheric variability does not coincide with the middle of winter. In the NH, with a peak amplitude of 14 $m\ s^{-1}$, January had the largest variability. This is not a surprise because stratospheric sudden warmings (SSW) occur typically around that time of the year (Charlton and Polvani 2007). In addition, they happen roughly every other year, which contributes to the large variability during those months, as indicated in Fig. 7.13. In the SH, the peak amplitude is found in November. Except for 2002, there haven't been any observations of a SSW, and hence variability is lower than the NH. Another reason

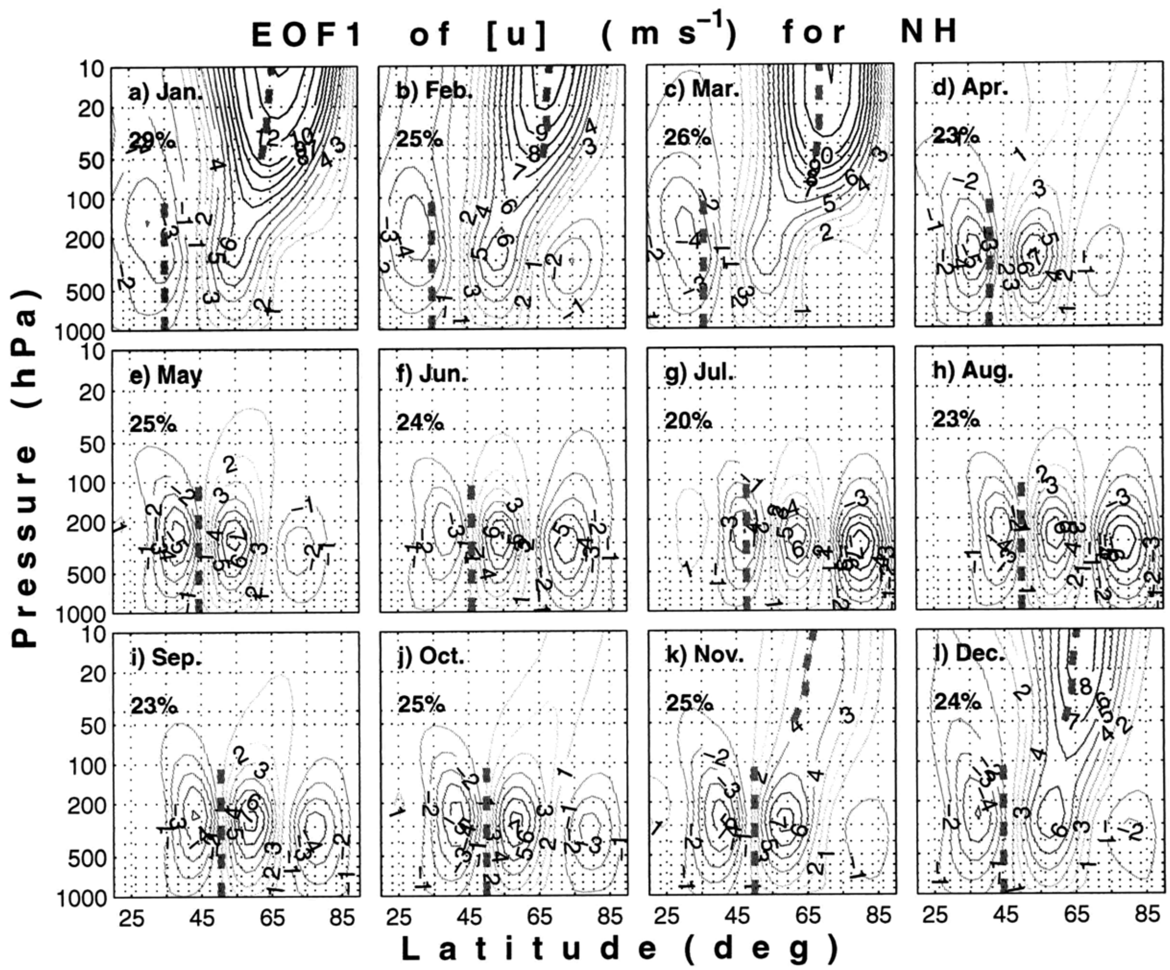

Figure 7.13: The leading EOF of daily zonally-averaged zonal wind data for each month. Vertical dashed gray line represents the climatological mean position of the peak surface westerlies between 100 hPa and the surface. Above 100 hPa, the gray line shows the latitudinal position of the maximum monthly-averaged $[u]$. Contour intervals are every 1 m s^{-1} up to 10 m s^{-1}. For values greater than 10 m s^{-1}, contours are every 2 m s^{-1}. The zero contour is omitted. The month and the percent of variance explained is displayed in the top left for each plot.

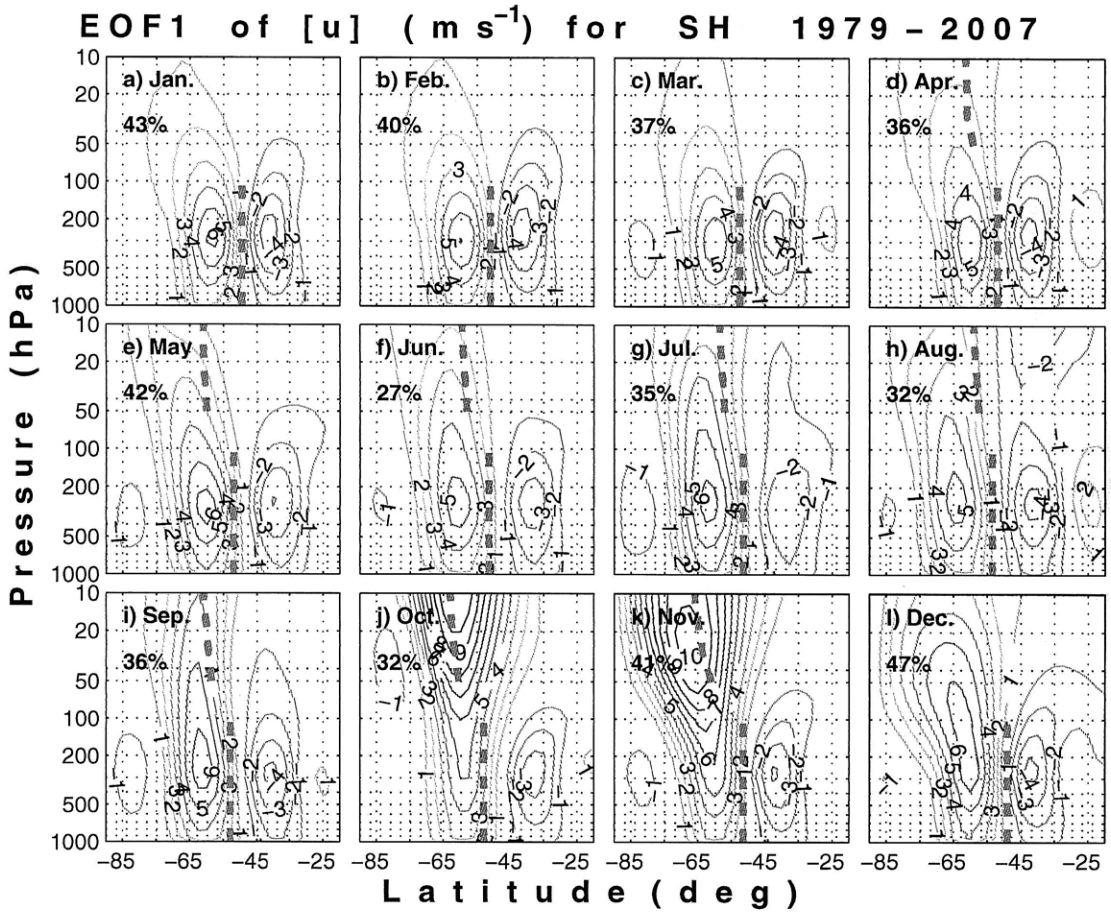

Figure 7.14: Same as Fig. 7.13 but for the Southern Hemisphere.

is due to the strong stratospheric winds; planetary waves can no longer penetrate into the stratosphere, which then minimizes the variability. As a result,, the greatest variability in the stratosphere coincides with the stratospheric final warming, which takes place in the spring.

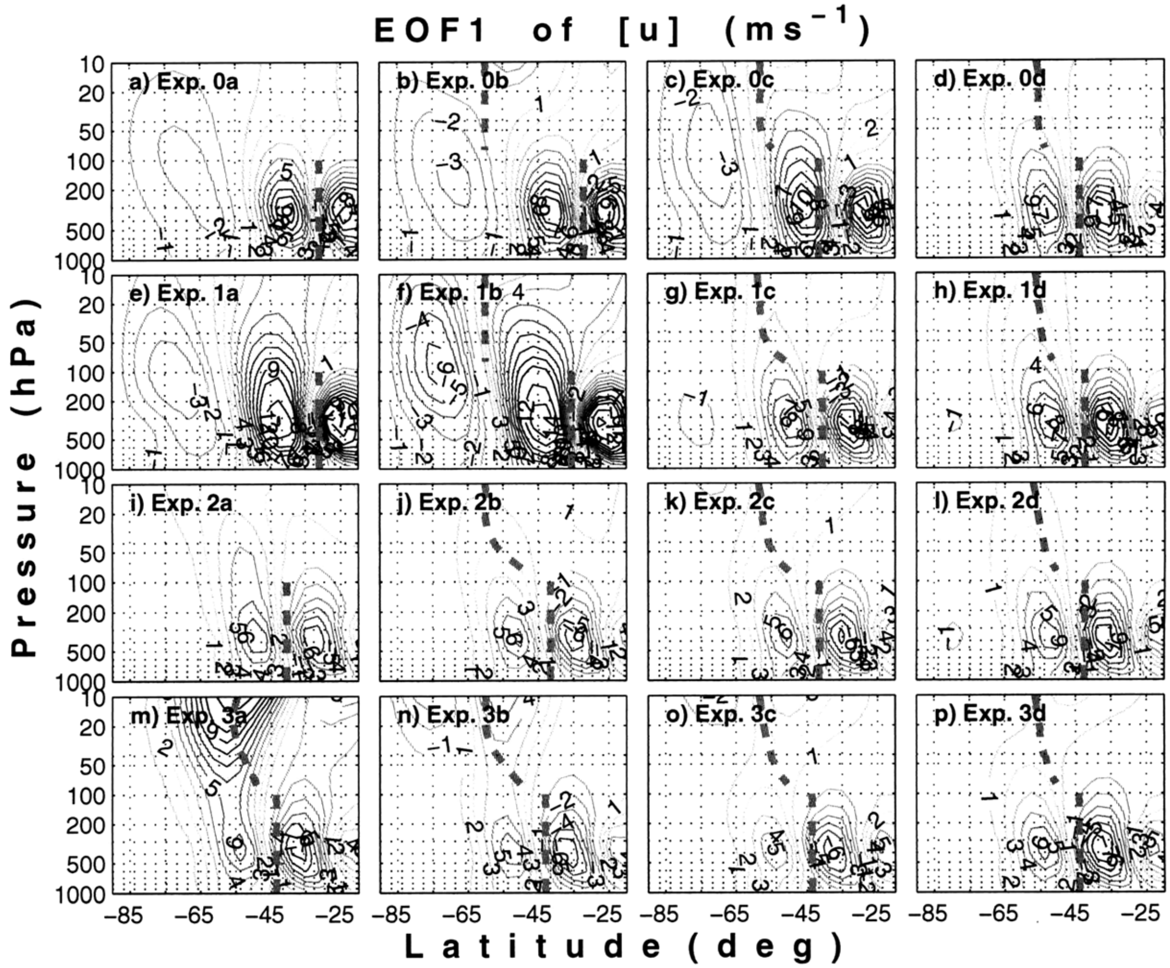

Figure 7.15: The leading EOF of daily zonally-averaged zonal wind data for each model experiment listed in the top left corner. Vertical dashed gray line represents the monthly mean position of the peak surface westerlies between 100 hPa and the surface. Above 100 hPa, the gray line shows the latitudinal position of the monthly-averaged maximum $[u]$. Contour intervals are every 1 $m\ s^{-1}$ up to 10 $m\ s^{-1}$. For values greater than 10 $m\ s^{-1}$, contours are every 2 $m\ s^{-1}$. The zero contour is omitted. Within each column, the same stratospheric equilibrium temperature profile is used, with polar vortex intensities (γ) increasing to the right. Within each row, the same tropospheric equilibrium temperature profile is used, with the magnitude of the equator to pole temperature difference increasing downward.

So far, we have seen how the stratospheric and tropospheric variability behave (at least through an EOF analysis) between the NH and SH and under different seasonal forcings. This will make a good comparison to the model results obtained in Chapter 4, since systematic changes to the equilibrium profile were applied. The same EOF analysis was conducted for those model runs and is shown in Fig. 7.15.

The variability of the 16 model runs can be categorized into 4 main groups. The first group are the model runs in the top left corner. Especially in the cases with long decorrelation times (exps. 0b, 1a, 1b), there is a vertically coherent extratropical dipole that extends into the stratosphere that was not seen in observations (cf. Figs. 7.13 and 7.14). This again suggests that the two-state regime is not found in observations.

Excluding 2c, the second group are exps, 1c to 2d. Here, the extratropical variability is predominantly a dipole in the troposphere and a monopole in the stratosphere. With the stratospheric variability relatively weak and the shape very similar to those of Fig. 7.14a-f, this group closely matches the variability seen in the SH summer and fall seasons. Just like in the observations, this second group has the poleward lobe of the tropospheric variability extending into the stratosphere with a poleward slant, suggesting this part of the modelled parameter space is quite realistic.

However, in the third group (exps. 2c, 3b, 3c, and 3d), this is not the case. Instead of a monopole in the stratosphere, a weak stratospheric dipole emerges. It is not immediately clear from these experiments what controls the spatial structure. But nevertheless, these cases do not appear to be representative to those shown in observations.

The only experiment not discussed is that of exp. 3a. This was the case where the peak tropospheric equilibrium temperature was shifted the furthest into the summer hemisphere and the stratospheric equilibrium profile was only a function of pressure. With a very weak stratospheric temperature gradient, the extent to which the tropospheric jet was roughly barotropic nearly reached all the way to the stratopause. It turns out that the variability here closely matches the observations.

In exp. 3a, the observed NH and SH, the poleward lobe of the tropospheric dipole extends into the stratosphere. Also, the latitudinal location of stratospheric maximum winds coincides with the center of action. Interestingly, this was also the case where further stratospheric perturbation did not induce any noticeable tropospheric changes in exps. 3b-d (see Fig. 4.5). So even though exp. 3a's variability closely matched those of observations, this was the also the case where stratospheric influence was the weakest.

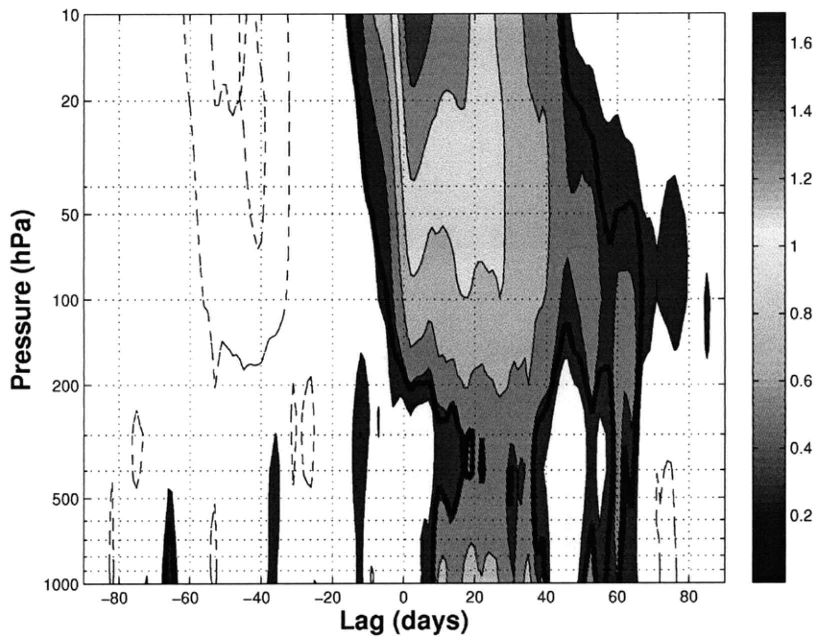

Figure 7.16: Composite of the time-height development of the anomalous NAM index during weak vortex events. Contours are every 0.25, with the zero contour omitted. Values greater than zero are filled, while dashed contours are negative. The black line marks the region where the NAM composite is statistically significant away from zero at the 95 percent confidence interval. Instead of compositing events when the NAM crosses 3 standard deviations at 10 hPa (*e.g.* Baldwin and Dunkerton 2001), instead, here, we take 1.5 standard deviations at the same pressure level.

Nonetheless, studies like Baldwin and Dunkerton (2001) suggest that changes in the stratosphere do indeed play a role in driving changes in the troposphere. Thus far, we have looked at instantaneous correlations between the two layers. If a particular cause led to a particular effect, looking at time-lag plot will reveal such a relationship. Fig. 7.16 shows the level-by-level NAM index composited during weak vortex events. Unlike in Baldwin and Dunkerton (2001), we define the onset of a weak vortex event to be when NAM drops below 1.5 standard deviations at 10 mb.

There were two points of interest raised in that particular study. First, the troposphere followed the same sign as that of the stratosphere after the stratospheric sudden warmings.

But secondly, the persistence of the NAM index after such an event persisted for an unusually long time (three to four times the typical NAM timescale of 10 days).

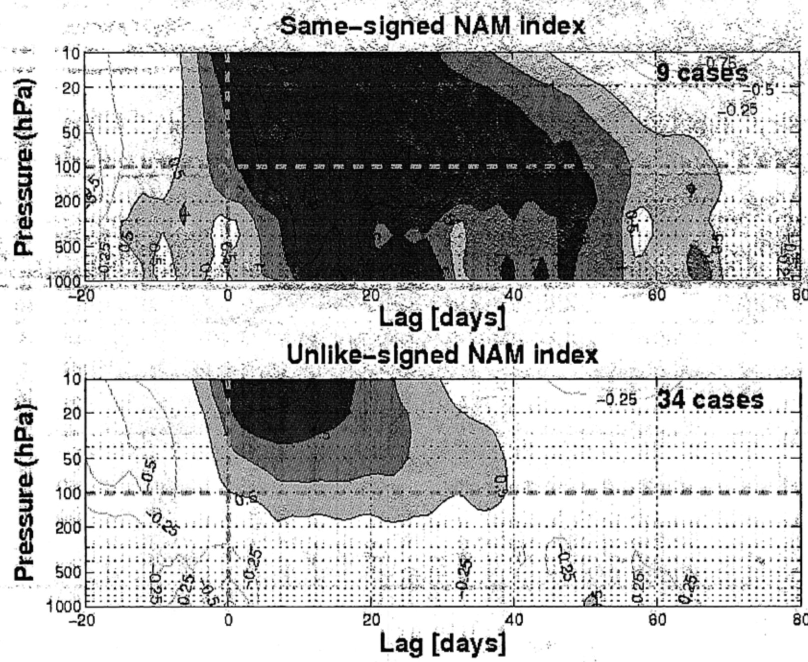

Figure 7.17: Composite of the time-height development of the anomalous annular mode index (AMI) for same-signed (top-panel) and unlike-signed (bottom-panel) tropospheric NAM winter events. Onset of events are defined as the day on which the AMI at 10 mb reaches 2 standard deviations. The same signed events are defined to be the cases when the average of the tropospheric NAM between a lag of 20 and 60 days has the same sign as the onset of the stratospheric NAM index. Conversely, for unlike signed events, the average of the tropospheric NAM between 20 and 60 days do not have the same sign. Filled contours denote positive values and the zero line has been omitted.

Using this long persistence, we can split the occurrences in Fig. 7.16. Same signed events are defined to be when the sign of the stratospheric NAM index at day zero is the same as the averaged tropospheric NAM index between a lag of 20 day and 60 days. These events will also be referred to as long-lived NAM anomalies, since they persist for an usually long time. Conversely, unlike-signed events are when the averaged tropospheric NAM index between 20 and 60 days do not have the same sign as the stratospheric NAM index at day zero.

As Fig. 7.17 shows, approximately only one quarter of these weak vortex events persist many times longer than the decorrelation time of the NAM index. Besides that, there are three main points of interest in describing the differences. First, the way we have defined these events do not preclude the tropospheric NAM index to follow the same sign as that of the stratosphere between lags zero and twenty days. Yet, as the bottom panel indicates, there is no tropospheric signal. This figure suggests that following weak vortex events, most of the time, the tropospheric NAM index does not follow the same sign.

Secondly, even though the upper stratospheric NAM index values start out similar in both cases, the amplitude of the anomalous NAM index in the lower to mid-stratosphere is much larger in the same-signed cases. Again, the way we have defined these events do not prevent the lower stratospheric NAM index to behave differently. Nonetheless, in the same-signed events, the lower to mid-stratosphere NAM indices are much larger.

The third and final point is perhaps the most interesting. The top panel of Fig. 7.16 show a tropospheric signal before the onset of the weak vortex events, while there is no such signal for the unlike-signed cases. Taken at face value, this implies that in order to get the same tropospheric NAM index to follow the same sign and persist for an unusually long period, there must be a tropospheric precursor. In other words, this figure suggests that between the lags of -20 and 0 day, the troposphere causes changes in the stratosphere *and* is also responsible for the persistent phase of the NAM index.

To test this idea, instead of compositing events when the NAM index drops below a certain threshold at 10 *mb*, we will use 500 *mb* pressure level instead. Similarly, we separate the cases into two categories: whether the averaged tropospheric NAM index between 20 and 60 days have the same sign as the onset of the NAM at 500 *mb*. As shown in Fig. 7.18., about one-third of the cases have this persistence in the phase of the NAM index.

The obvious difference between the two composites is the longevity of the phase of the NAM index. Of course, this is not a surprise since we have defined these composites to behave as such. However, a closer inspection reveals two other noticeable differences. First, the peak amplitude of the anomalous NAM index is stronger between days zero and twenty for the same-signed cases. Thus the long-lived NAM anomalies are associated with an anomalously strong onset. Secondly, there is a remarkable difference in the stratosphere. In the unlike-signed cases, there is virtually no change in the stratosphere. However, for the same-signed cases, there is a rather strong stratospheric signal coinciding with the peak NAM

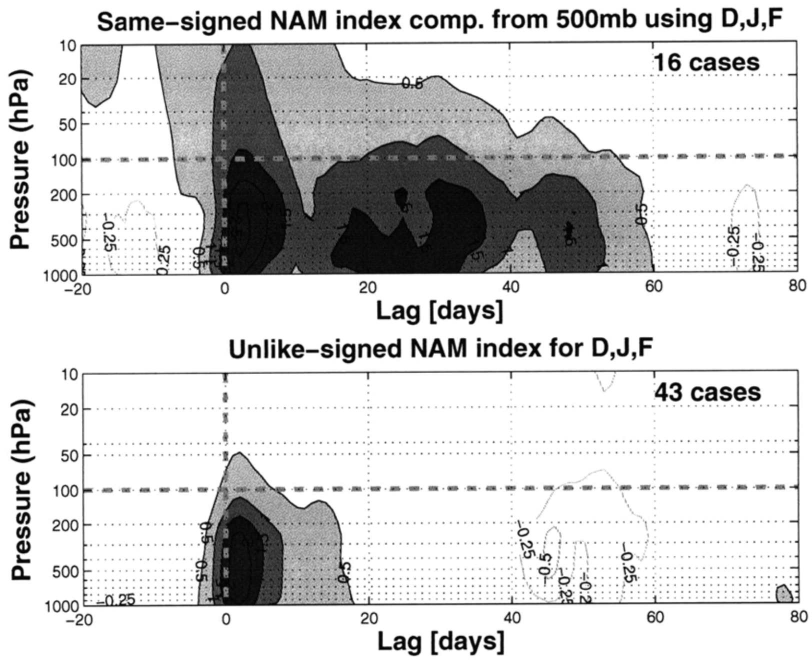

Figure 7.18: Same as Fig. 7.17, but the onset of these events are defined instead as the day on which the AMI at 500 *mb* reaches 2 standard deviations.

anomalies in the troposphere. So the key point of this figure is that when the NAM anomalies persist for much longer than the typical timescale, there is an accompanying change in the stratosphere. When the NAM anomalies persist for the usual 10 days, there is no change in the stratosphere.

The difference between the panels in Figs. 7.17 and 7.18 brings us back to the importance of the lower- to mid-stratosphere. We have seen that in this part of the stratosphere changes need to happen for the long-lived NAM anomalies. Fig. 7.19 shows the composited zonal-mean zonal wind at 100 *mb* and 60°N from Fig. 7.17. We picked this point because it is a good representation of both the lower stratosphere and is located near the latitudinal center of variability (cf. Fig. 7.13).

Before a lag of +5 day, both cases have an approximate same value. But after this time, they diverge quickly and are significantly different for another 30 days. This is consistent with what we had alluded to in Section 4.3. For the long-lived same-signed anomalies to persist, the lower stratospheric winds have to be sufficiently weak. In the absence of these lower stratospheric changes, the troposphere does not appear to respond to changes from

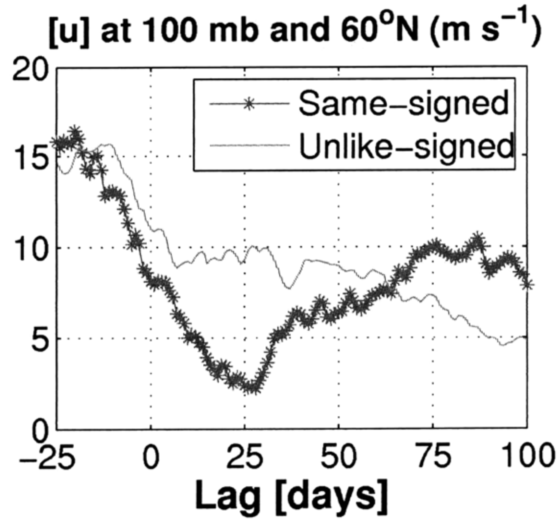

Figure 7.19: Composites of [u] at 100 mb and 60°N from the events defined in Fig. 7.17.

the upper stratosphere, consistent with our findings from Chapter 5.

7.3 Summary

We have provided an observational perspective on the topics covered in the previous chapters. In the first part, we looked at the possibility of an "underlying mode", where the eddy-driven jet shifted between two regimes, either (1) coexisting with or (2) being well separated from the subtropical jet. We noted that the frequency distribution of the peak surface westerlies during the winter months had a similar bimodal shape as that of the modeling results that lay in the transitional zone between these two states. Decomposing the zonal-average, a similar bimodal distribution is found the Atlantic and Pacific basins.

However, a frequency distribution of the NAM index, a respresentation of the leading mode of variability, did not show any obvious signs of a dual regime. A closer inspection of the late fall and winter months did show a flatter distribution, with no clear peak especially in March. Furthermore, relative histograms of the wintertime PNA and NAO show subtle signs of asymmetry. In January, both of these indices develop a "shoulder" on the negative side of the distribution.

It is common to consider the leading mode of variability as a simple jet oscillation, centered around one reference state (usually a climatological average). This would lead to a distribution that would be Gaussian-like and be centered at zero. Figs. 7.8 and 7.9 suggest this concept may not be entirely true during the winter months. With the peak away from zero, it is possible the jet is simply oscillating about its climatological position, and in this case, the idea of the annular mode variability would still hold. However, with a shoulder present in the distribution, there is the added possibility that the jet is oscillating about *two* reference states, a fundamentally different perspective than what is typically associated with the annular modes.

In the second part, we looked more closely at this tropospheric variability and its extension into the stratosphere. Coinciding with the non-Gaussian like distributions, comparing the spatial pattern (Fig. 7.13) with the climatological winds showed that indeed the variability is not a simple jet oscillation during the winter months. For all other cases, in both hemispheres, the variability can be considered a jet "wobble" from a reference state.

Nonetheless, mid-latitude tropospheric variability during the winter months seems correlated with the stratospheric NAM. So, similar to Baldwin and Dunkerton (2001), we composited a level-by-level NAM index during weak vortex events. However, here, we separate these cases into two categories: (1) where the tropospheric anomalous NAM index follow the same sign as the stratospheric NAM index 20 days after the onset and persist for a period of time much longer than the typical timescale and (2) where the tropospheric anomalous NAM index did not have the same sign as the stratospheric NAM index 20 days after the onset.

The first type constituted only a quarter of the cases and the composite looked virtually identical to that of Baldwin and Dunkerton (2001). However, for the second composite, there was virtually no tropospheric signal. These composites suggest there had to be a tropospheric precursor, and in addition, there had to be a sufficiently strong change in the lower stratosphere in order to get the long-lived NAM anomalies. Fig. 7.19 showed that the lower stratospheric winds were similar in the two composites right before the onset. However, after the onset of the weak vortex event, the winds from the two composites diverged greatly, with the lower stratospheric winds being much weaker in the cases of the long-lived tropospheric NAM anomalies.

Results from Chapter 5 suggested that as the winds decrease, there is a positive feedback between the wave breaking and the mean flow. When the winds get sufficiently weak, more waves will break because the background winds will approach their phase speeds. The increased wave drag would then project onto the annular modes and perpetuate the particular phase of the NAM. The positive feedback stops once radiative relaxation, above the wave breaking, restores stronger westerly winds, decreasing the likelihood of any further wave breaking.

Chapter 8

Conclusion

In this thesis, we have investigated the extratropical tropospheric responses (if any) to changes in the stratosphere. Using the same stratospheric forcings in a simple GCM, we explored how changes to tropospheric state altered the tropospheric response. So simple ideas such as downward control (cf. Haynes (2005)) have to be ruled out since these mechanisms would suggest the responses would be identical regardless of the tropospheric behavior.

One of the questions posed in the introduction was why there were such large responses in these simple models, compared to what was found in observations. As discussed in Chapter 4, we have found that these models had a timescale of internal variability that is too large, and in one extreme case, an order of magnitude larger than that of observations. As suggested by fluctuation-dissipation theorem, the model was overly sensitive to any external perturbations, and hence produced results larger than that of observations. Modest changes to either the tropospheric equilibrium temperature profile or to the topographical profile resulted in a timescale associated with the leading mode of variability similar to that of observations. Subsequently, the surface response went from 5 $m\ s^{-1}$ to about 0 to 1 $m\ s^{-1}$, similar to that of observations.

Between all the experiments and observations, our overarching theme has been the strong connection between the lower stratospheric mid-latitude winds and the position of the mid-latitude jet. Another question posed in the introduction was what the dynamical mechanism was in communicating stratospheric wave drag to a change in the tropospheric circulation.

We have argued that the lower stratospheric winds are crucial in determining whether there is a stratospheric influence, or more precisely, whether the tropospheric NAM anomalies become unusually persistent.

As suggested by Fig. 7.17 and the work of Chapter 5, if the sudden warming is large enough, the lower stratospheric winds can decrease to the point where waves no longer penetrate into the stratosphere. As a result, there is an anomalous wave drag in this region and can project onto the tropospheric annular modes. Thus, as long as the lower stratospheric winds remain sufficiently weak, the negative phase of the NAM will persist.

Our idea is similar to that of Song and Robinson (2004). In their work, they suggested planetary waves were important to generating the troposphere response. Here, we argue that planetary waves are needed to apply a wave forcing that can project onto the annular mode and perpetuate the negative phase of the annular mode. To support this claim, we ran model experiments with a mountain centered in the mid-latitudes and another in the polar region. Although both exhibit similar climatological winds and variability during a weak vortex event in the lower stratosphere, there is virtually no tropospheric signal for the latter case (see Fig. 4.20). We argued that the wave drag is likely more distant from the eddy-feedback processes in the mid-latitudes, and thus the wave drag can no longer project onto the annular mode, and hence, there are no noticeable tropospheric changes.

Both our modeling results and observations (Baldwin and Dunkerton 2001) show a time-lag between the onset of the weak vortex event and a tropospheric signal. The mechanism described here appears consistent with this finding. It takes at least several days for negative anomalies at 10 hPa to makes its way to the lower stratosphere. Then time is needed for the waves to respond to this weakening of winds in the lower stratosphere. Then there is some time for the tropospheric eddies to "feel" the wave forcing, before the eddy feedback perpetuates and amplify the tropospheric response. As a result, there is some considerable time between the tropospheric response and the onset of the stratospheric extreme event.

This time-lag is likely the reason why the lag-regression analysis between the surface annular mode index with the zonal-mean zonal wind resulted in the largest amplitudes in the stratosphere. There were only weak amplitudes (2 $m\ s^{-1}$) when a lag of zero is used (Fig. 3.5d). However, when a lag of 40 days is used, the amplitudes in the stratosphere are about four times larger (Fig. 3.8).

As Chapter 3 described, there were many difficulties in describing the stratosphere / tropospheric coupling. EOF analysis required some sort of weighting, which greatly affected the result. So given the time delay in the mechanism described above, a lag-lead regression of the surface annular mode index would make the most sense. In addition, projecting all the different "modes" calculated in Chapter 3 with an experiment run with a momentum forcing, only this time-lag approach predicted the correct shape of the response (see Fig. 3.11). Thus, we argued the best way to define the coupling was to use this lag-lead regression.

No matter what calculation was used, the strongest coupling occurred with the tropospheric state that lay in the transition zone between two regimes. As we saw in Fig. 4.1, the long timescales associated with the leading mode was the result of the model's eddy-driven jet teetering between (1) coexisting with or (2) being well separated from the subtropical jet. In Chapter 7, we noted that this bimodal behavior was not easily detected from the distributions in the NAM or SAM indices. We found Gaussian-like distributions in the NAO and PNA indices during the non-winter months as well. However, between November and March, both indices have a distinct asymmetry. Although the distributions were skewed, it was difficult to argue the atmosphere was in a bimodal state.

Increases to the equilibrium temperature gradient removed the long timescale. In its place, the variability changed from that of the bimodal "jet switching" variability to poleward propagation. While the eddy momentum fluxes associated with the eddy feedback are responsible for the persistence of the annular mode, as we discussed in Chapter 6, we looked at the increased importance of the role of the eddy heat fluxes when the variability is dominated by poleward propagation. Using a zonally-symmetric model, we inserted the eddy momentum and eddy heat fluxes from the control run and reproduced both the variability and climatology. When only the timeseries of the eddy momentum fluxes were input (along with the climatological eddy heat fluxes), the 2D model was unable to capture the poleward propagation. However, when the eddy heat fluxes were inserted (along with the climatological eddy momentum fluxes) into the zonally-symmetric model, the variability was captured, albeit only in the mid-levels. Therefore, the evidence from Chapter 6 suggests the mechanism responsible for this type of variability must include the role of the eddy heat fluxes.

8.1 Implications for Climate Change

As we had discussed in the introduction, through anthropogenic forces and the stratospheric ozone depletion, there will be continued changes in the stratosphere. Both lead to an increase in the temperature gradient, so through the thermal wind relation, an increase in the lower stratospheric winds is expected. Through the work of this thesis and the references listed in the introduction, whenever the lower stratospheric winds increase, the eddy-driven jet will shift poleward. Specifically in this thesis, our modeling work suggests that changes in the troposphere are materialized only when the wind speeds are in a certain window, *i.e.* the relationship described above is nonlinear. For instance, if the winds get too strong, the poleward trend of the surface westerlies would cease.

However, in the northern hemisphere, the poleward trend in surface westerlies have been mitigated by the polar surface warming. As shown by Ring and Plumb (2008) and Butler et al. (2009), the warming projects onto the annular mode, but of opposite sign, meaning an equatorward shift of the jet. With the reduction of the mid-latitude temperature gradient, work by Lee et al. (2007) suggests there is a propensity for the eddy-driven jet to coexist with the subtropical jet. In addition, with the poleward expansion of the Hadley circulation (Son et al. 2008), there will likely be an increase in the subtropical jet. According to Lee et al. (2007), this climate trend would also increase the chance of the eddy-driven jet to shift into the subtropics.

Since the variability indicates the eddy-driven jet is mainly in the mid-latitudes (cf. Fig. 7.13), with the increased likelihood of the wave-driven jet being shifted into the mid-latitudes, our work suggests that this may lead to an increase in the timescale of the annular mode. The modeling work produced a parameter space showing the frequency distribution of where the eddy-driven jet resided (Fig. 4.1). With the eddy-driven jet's preference to be in the mid-latitudes under this current climate, we speculate that as the vertical wind shear increases in the subtropics, the probability that the atmosphere will be enter into the transition zone found in the modeling study increases. As a result, the timescale associated with the variability would subsequently increase.

8.2 Suggestions for Future Work

In this thesis, there was great difficulty in determining the precise cause and effect of the wave drag and the reduction of wind speeds in the lower stratosphere. Did one cause the other or *vice versa*? There is also the complication arising of interpreting the noisiness of $\nabla \cdot \mathbf{F}$ (*e.g.* Fig. 5.14). To avoid this issue, one could run a model with planetary wave drag "shut off" in the lower stratosphere. Planetary and synoptic waves would be decomposed at each time step, but the zonal-mean flow reaction to planetary wave drag would be turned off in the region of interest (with synoptic waves being untouched.) Since planetary wave generation in the troposphere and wave breaking in the upper stratosphere should remain unaffected, weakening of the polar vortex should still occur. This setup would allow one to test the importance of planetary wave drag in the lower stratosphere and whether this projection upon the annular modes is the key in driving a tropospheric response.

This thesis also explored a model's tropospheric state teetering between an eddy-driven jet coexisting with or being well-separated from the subtropical jet. As we discussed in the last section, with the poleward expansion of the Hadley circulation and the surface polar warming, there is an increased likelihood of the observed atmosphere shifting closer into the transition zone, as depicted from the model's parameter space (cf. Fig. 4.1.) Using these two forcings, simulations can be performed and be differed from each other by a poleward expansion of the Hadley circulation and a polar surface heating. A parameter space can be generated with one type of forcing on x-axis and the other on the y-axis. Similar to Lee and Son (2005), an analysis could be performed to look at the jet position, even though we expect both forcings to contribute to an equatorward shift, but instead an analysis of the decorrelation time of the annular modes could be performed to see whether these climate forcings could interact and dramtically increase the timescale.

There would be large implications in an atmosphere with a greater persistent annular mode. Responses from climate forcings could get larger, as this thesis has shown. However, a more persistent annular mode would make better predictions of the jet stream's position, for instance. Nonetheless, the impact of climate change on this annular mode timescale merits further research.

Bibliography

Akahori, K. and S. Yoden, 1997: Zonal flow vacillation and bimodality of baroclinic eddy life cycles in a simple global circulation model. *J. Atmos. Sci.*, **54**, 2349–2361.

Andrews, D. G. and M. E. McIntyre, 1976: Planetary waves in horizontal and vertical shear: The generalized Eliassen-Palm relation and the mean zonal acceleration. *J. Atmos. Sci.*, **33**, 2031–2048.

Baldwin, M. P., 2003: Comment on tropospheric response to stratospheric perturbations in a relatively simple general circulation model by Lorenzo M. Polvani and Paul J. Kushner. *Geophys. Res. Lett.*, **30**, doi:10.1029/2003GL017 793.

Baldwin, M. P. and T. J. Dunkerton, 1999: Propagation of the Arctic Oscillation from the stratosphere to the troposphere. *J. Geophys. Res.*, **104**, 30 937–30 946.

Baldwin, M. P. and T. J. Dunkerton, 2001: Stratospheric harbingers of anomalous weather regimes. *Science*, **294**, 581–584.

Baldwin, M. P. and D. W. J. Thompson, 2009: A simplified annular mode index based on zonal-mean data. *submitted to Quart. J. Roy. Meteor. Soc.*

Bretherton, F. P., 1966: Critical layer instability in baroclinic flows. *Quart. J. Roy. Meteor. Soc.*, **92**, 325–334.

Butler, A. H., D. W. J. Thompson, and R. Heikes, 2009: The atmospheric response to climate change-like thermal forcings in a simple general circulation model. Part one: Steady-state experiments. *submitted to J. Atmos. Sci.*

Cerovecki, I. and J. C. Marshall, 2008: Eddy modulation of air-sea interaction and convection. *J. Phys. Oceanogr*, **38**, 65–83.

Cerovecki, I., R. A. Plumb, and W. Heres, 2009: Eddy transport and mixing in a wind- and buoyancy-driven jet on the sphere. *J. Phys. Oceanogr*, **39**, 1133–1149.

Chan, C., 2006: Annular modes in a multiple migrating zonal jet regime. M.S. thesis, M.I.T, Cambridge,MA.

Chan, C., R. A. Plumb, and I. Cerovecki, 2007: Annular modes in a multiple migrating zonal jet regime. *J. Atmos. Sci.*, **64**, 4053–4068.

Chan, C. J. and R. A. Plumb, 2009: The response to stratospheric forcing and its dependence on the state of the troposphere. *J. Atmos. Sci.*, **66**, 2107–2115.

Charlton, A. J. and L. M. Polvani, 2007: A new look at stratospheric sudden warmings. Part I: Climatology and modeling benchmarks. *J. Climate*, **20**, 449–469.

Charney, J. G. and P. G. Drazin, 1961: Propagation of planetary-scale disturbances from the lower into the upper atmosphere. *J. Geophys. Res.*, **66**, 83–109.

Chen, G. and P. Zurita-Gotor, 2008: The tropospheric jet response to prescribed zonal forcing in an idealized atmospheric model. *J. Atmos. Sci.*, **65**, 22542271.

Chen, P. and W. A. Robinson, 1992: Propagation of planetary waves between the troposphere and stratosphere. *J. Atmos. Sci.*, **49**, 2533–2545.

Cho, J. Y.-K. and L. M. Polvani, 1996: The emergence of jets and vorticies in freely evolving, shallow-water turbulence on a sphere. *Phys. Fluids*, **8**, 246–262.

Christiansen, B., 2009: Is the atmosphere interesting? A projection pursuit study of the circulation in the northern hemisphere winter. *J. Climate*, **22**, 1239–1254.

Dritschel, D. and M. McIntyre, 2008: The Phillips Effect and the resilience of eddy-transport barriers. *J. Atmos. Sci.*, **65**, 855–874.

Eady, E. T., 1949: Long waves and cyclone waves. *Tellus*, **1**, 35–52.

Edmon, H. J., B. J. Hoskins, and M. E. McIntyre, 1980: Eliassen-Palm cross-sections for the troposphere. *J. Atmos. Sci.*, **37**, 2600–2615.

Eichelberger, S. and D. Hartmann, 2007: Zonal jet structure and the leading mode of variability. *J. Climate*, **20**, 5149–5163.

Feldstein, S. and S. Lee, 1996: Mechanisms of zonal index variability in an aquaplanet GCM. *J. Atmos. Sci.*, **53**, 3541–3556.

Feldstein, S. B., 1998: An observational study of the intraseasonal poleward propagation of zonal mean flow anomalies. *J. Atmos. Sci.*, **55**, 2516–2529.

Feldstein, S. B., 2000: The timescale, power spectra and climate noise properties of teleconnection patterns. *J. Climate*, **13**, 4430–4440.

Fu, Q., C. M. Johanson, S. G. Warren, and D. J. Seidel, 2004: Contribution of stratospheric cooling to satellite-inferred tropospheric temperature trends. *Nature*, **429**, 55–58.

Furtado, J. C., 2005: On the balanced response of the troposphere to variability in the extratropical stratosphere. M.S. thesis, Colorado State University, Fort Collins, CO.

Gerber, E. P. and L. M. Polvani, 2009: Stratosphere-troposphere coupling in a realively simple AGCM: The importance of stratospheric variability. *J. Climate*, **22**, 1920–1933.

Gerber, E. P. and G. K. Vallis, 2007: Eddy-zonal flow interactions and the persistence of the zonal index. *J. Atmos. Sci.*, **64**, 3296–3311.

Gerber, E. P., S. Voronin, and L. M. Polvani, 2008: Testing the annular mode autocorrelation timescale in simple atmospheric general circulation models. *Mon. Wea. Rev.*, **136**, 1523–1536.

Gillett, N. and D. W. J. Thompson, 2003: Simulation of recent southern hemisphere climate change. *Science*, **302**, 273–275.

Hartmann, D. L., J. M. Wallace, V. Limpasuvan, D. W. J. Thompson, and J. R. Holton, 2000: Can ozone depletion and global warming interact to produce rapid climate change? *Proc. Nat. Acad. Sci*, **97**, 1412–1417.

Haynes, P., 2005: Stratospheric dynamics. *Annu. Rev. Fluid. Mech.*, **37**, 263–293.

Held, I. M., 1975: Momentum transport by quasi-geostrophic eddies. *J. Atmos. Sci.*, **32**, 1494.1497.

Held, I. M. and M. J. Suarez, 1994: A proposal for the intercomparison of the dynamical cores of atmospheric general-circulation models. *Bull. AM. Meteorol. Soc.*, **75**, 1825–1830.

Hurrell, J. W. and H. van Loon, 1997: Decadal variations in climate associated with the North Atlantic Oscillation. *Climate Change*, **36**, 301–326.

Ioannou, P. and R. S. Lindzen, 1986: Baroclinic instability in the presence of barotropic jets. *J. Atmos. Sci.*, **43**, 2999–3014.

James, I. N. and J. P. Dodd, 1996: A mechanism for the low frequency variability of the mid-latitude troposphere. *Quart. J. Roy. Meteor. Soc.*, **122**, 1197–1210.

Kalnay, E., et al., 1996: The NCEP/NCAR 40-year reanalysis project. *Bull. AM. Meteorol. Soc.*, **77**, 437–471.

Kraichnan, R. H., 1958: Irriversible statistical mechanics of incompressible hydromagnetic turbulence. *Phys. Rev.*, **109**, 1407–1422.

Kraichnan, R. H., 1959: Classical fluctation-relaxation theorem. *Phys. Rev.*, **113**, 1181–1182.

Kushner, P. J. and L. M. Polvani, 2004: Stratosphere-troposphere coupling in a relatively simple AGCM: The role of eddies. *J. Climate*, **17**, 629–639.

Kushner, P. J. and L. M. Polvani, 2005: A very large, spontaneous stratospheric sudden warming in a simple AGCM: A prototype for the southern-hemisphere warming of 2002? *J. Atmos. Sci.*, **62**, 890–897.

Kushner, P. J. and L. M. Polvani, 2006: Stratosphere-troposphere coupling in a relatively simple AGCM: Impact of the seasonal cycle. *J. Climate*, **19**, 5721–5727.

Lee, S., 2005: Baroclinic multiple zonal jets on the sphere. *J. Atmos. Sci.*, **62**, 2484–2498.

Lee, S. and H. Kim, 2003: The dynamical relationship between subtropical and eddy-driven jets. *J. Atmos. Sci.*, **60**, 1490–1503.

Lee, S. and S.-W. Son, 2005: The response of westerly jets to thermal driving in a primitive equation model. *J. Atmos. Sci.*, **62**, 791–810.

Lee, S., S.-W. Son, K. Grise, and S. B. Feldstein, 2007: A mechanism for poleward propagation of zonal mean flow anomalies. *J. Atmos. Sci.*, **64**, 849–868.

Leith, C. E., 1975: Climate response and fluctuation dissipation. *J. Atmos. Sci.*, **32**, 2022–2026.

Lorenz, D. J. and D. L. Hartmann, 2001: Eddy-zonal flow feedback in the southern hemisphere. *J. Atmos. Sci.*, **58**, 3312–3327.

Marshall, J., A. Adcroft, C. Hill, L. Perelman, and C. Heisey, 1997a: A finite-volume, incompressible Navier-Stokes model for studies of the ocean on parallel computers. *J. Geophys. Res.*, **102**, 5753–5766.

Marshall, J., C. Hill, L. Perelman, and A. Adcroft, 1997b: Hydrostatic, quasi-hydrostatic, and nonhydrostatic ocean modeling. *J. Geophys. Res.*, **102**, 5733–5752.

Matsuno, T., 1970: Vertical propagation of stationary planetary waves in the winter northern hemisphere. *J. Atmos. Sci.*, **27**, 871–883.

Matsuno, T., 1971: A dynamical model of the stratospheric sudden warming. *J. Atmos. Sci.*, **28**, 1479–1494.

Meehl, G. A., J. W. Hurrell, and . H. van Loon, 1998: A modulation of the mechanism of the semiannual oscillation in the southern hemisphere. *Tellus*, **50**.

Namias, J., 1950: The index cycle and its role in the general circulation. *J. Meteor.*, **7**, 130–139.

North, G. R., T. L. Bell, R. F. Cahalan, and F. J. Moeng, 1982: Sampling errors in the estimation of empirical orthogonal functions. *Mon. Wea. Rev.*, **110**, 699–706.

Panetta, R. L., 1993: Zonal jets in wide baroclinically unstable regions: persistence and scale selection. *J. Atmos. Sci.*, **50**, 2073–2106.

Peixoto, J. P. and A. H. Oort, 1992: *Physics of Climate.* Springer, 564 pp. pp.

Perlwitz, J. and N. Harnik, 2003: Observational evidence of a stratospheric influence on the troposphere by planetary wave reflection. *J. Climate*, **16**, 3011–3026.

Perlwitz, J. and N. Harnik, 2004: Downward coupling between the stratosphere and troposphere: The relative roles of wave and zonal mean processes. *J. Climate*, **17**, 4902–4909.

Plumb, R. A., 1977: The interaction of two internal waves with the mean flow: implications for the theory of the quasi-biennial oscillation. *J. Atmos. Sci.*, **34**, 1847–1858.

Plumb, R. A. and K. Semeniuk, 2003: Downward migration of extratropical zonal wind anomalies. *J. Geophys. Res.*, **108**, doi:10.1029/2002JD002 773.

Polvani, L. M. and P. J. Kushner, 2002: Tropospheric response to stratospheric perturbations in a relatively simple general circulation model. *Geophys. Res. Lett.*, **29**, doi:10.1029/2001GL014 284.

Polvani, L. M. and D. W. Waugh, 2004: Upward wave activity flux as precursor to extreme stratospheric events and subsequent anomalous surface weather regimes. *J. Climate*, **17**, 3548–3554.

Riehl, T., C. Yeh, and N. E. LaSeur, 1950: A study of the variations of the general circulation. *J. Meteor.*, **7**, 181–194.

Ring, M., 2008: Annular mode-like responses to external forcings in a simple atmospheric general circulation model. Ph.D. thesis, M.I.T, Cambridge,MA.

Ring, M. J. and R. A. Plumb, 2007: Forced annular mode patterns in a simple atmospheric general circulation model. *J. Atmos. Sci.*, **64**, 3611–3626.

Ring, M. J. and R. A. Plumb, 2008: The response of a simplified GCM to axisymmetric forcings: applicability of the fluctuation-dissipation theorem. *J. Atmos. Sci.*, **65**, 3880–3898.

Robinson, W. A., 2000: A baroclinic mechanism for the eddy feedback on the zonal index. *J. Atmos. Sci.*, 415–422.

Roden, G., 2000: Flow and water property structures beween the Bering Sea and Fiji in the summer of 1993. *J. Geophys. Res.*, **105**, 28,595–28 612.

Rossby, C. G., 1939: Relations between variations in the intensity of the zonal circulation and the displacements of the semi-permanent centers of action. *J. Mar. Res*, **2**, 38–55.

Sigmond, M., J. F. Scinocca, and P. J. Kushner, 2008: Impact of the stratosphere on tropospheric climate change. *Geophys. Res. Lett.*, **35**, doi:10.1029/2008GL033 573.

Simmons, A. J. and D. M. Burridge, 1981: An energy and angular-momentum conserving vertical finite-difference scheme and hybrid vertical-coordinates. *Mon. Wea. Rev.*, **109**, 758–766.

Solomon, S., 1999: Stratospheric ozone depletion: A review of concepts and history. *Rev. Geophys.*, **37**, 275–316.

Son, S.-W. and S. Lee, 2006: Preferred modes of variability and their relationship with climate change. *J. Climate*, **19**, 2063–2075.

Son, S.-W., S. Lee, S. B. Fledstein, and J. E. T. Hoeve, 2008: Time scale and feedback of zonal mean flow variability. *J. Atmos. Sci.*, **65**, 935–952.

Song, Y. and W. A. Robinson, 2004: Dynamical mechanisms for stratospheric influences on the tropopshere. *J. Atmos. Sci.*, **61**, 1711–1725.

Thompson, D. W. J., J. C. Furtado, and T. G. Shepherd, 2006: On the tropospheric response to anomalous stratospheric wave drag and radiative heating. *J. Atmos. Sci.*, **63**, 2616–2629.

Thompson, D. W. J. and S. Solomon, 2002: Interpretation of the recent southern hemisphere climate change. *Science*, **296**, 895–899.

Thompson, D. W. J. and J. M. Wallace, 1998: The Arctic Oscillation signature in the wintertime geopotential height fields. *Geophys. Res. Lett.*, **25**, 1297–1300.

Thompson, D. W. J. and J. M. Wallace, 2000: Annular modes in the extratropical circulation. Part I: Month-to-month variability. *J. Climate*, **13**, 1000–1016.

U.S. Standard Atmosphere, 1976: U.S. Government Printing Office. *Washington, D.C.*

Vallis, G. K., 2006: *Atmospheric and Oceanic Fluid Dynamics: Fundamentals and Large-Scale Circulation.* Cambridge University Press, 745 pp.

Wilks, D. S., 2005: *Statistical Methods in the Atmospheric Sciences.* Elsevier Science and Technology Books, 467 pp.

Williams, G., 1978: Planetary circulations: 1. Barotropic representation of Jovian and terrestrial turbulence. *J. Atmos. Sci.*, **35**, 1399–1426.

Williams, G. P., 2003: Jovian dynamics. Part III: Multiple, migrating, and equatorial jets. *J. Atmos. Sci.*, **60**, 1270–1296.

Yu, J.-Y. and D. L. Hartmann, 1993: Zonal flow vacillation eddy forcing in a simple GCM of the atmosphere. *J. Atmos. Sci.*, **50**, 3244–3259.